Title
Development of Metallic Magnetic Calorimeters for Nuclear Safeguards Applications

Author
Bates, Cameron Russell

Publication Date
2015

Development of Metallic Magnetic Calorimeters for Nuclear Safeguards Applications

by

Cameron Russell Bates

A dissertation submitted in partial satisfaction of the

requirements for the degree of

Doctor of Philosophy

in

Engineering - Nuclear Engineering

in the

Graduate Division

of the

University of California, Berkeley

Committee in charge:

Professor Kai Vetter, Chair
Dr. Stephan Friedrich
Professor Karl Van Bibber
Professor Adrian Lee

Spring 2015

Development of Metallic Magnetic Calorimeters for Nuclear Safeguards Applications

Abstract

Development of Metallic Magnetic Calorimeters for Nuclear Safeguards Applications

by

Cameron Russell Bates

Doctor of Philosophy in Engineering - Nuclear Engineering

University of California, Berkeley

Professor Kai Vetter, Chair

Many nuclear safeguards applications could benefit from high-resolution gamma-ray spectroscopy achievable with metallic magnetic calorimeters. This dissertation covers the development of a system for these applications based on gamma-ray detectors developed at the University of Heidelberg. It demonstrates new calorimeters of this type, which achieved an energy resolution of 45.5 eV full-width at half-maximum at 59.54 keV, roughly ten times better than current state of the art high purity germanium detectors. This is the best energy resolution achieved with a gamma-ray metallic magnetic calorimeter at this energy to date. In addition to demonstrating a new benchmark in energy resolution, an experimental system for measuring samples with metallic magnetic calorimeters was constructed at Lawrence Livermore National Laboratory. This system achieved an energy resolution of 91.3 eV full-width at half-maximum at 59.54 keV under optimal conditions. Using this system it was possible to characterize the linearity of the response, the count-rate limitations, and the energy resolution as a function of temperature of the new calorimeter. With this characterization it was determined that it would be feasible to measure ^{242}Pu in a mixed isotope plutonium sample. A measurement of a mixed isotope plutonium sample was performed over the course of 12 days with a single two-pixel metallic magnetic calorimeter. The relative concentration of ^{242}Pu in comparison to other plutonium isotopes was determined by direct measurement to less than half a percent accuracy. This is comparable with the accuracy of the best-case scenario using traditional indirect methods. The ability to directly measure the relative concentration of ^{242}Pu in a sample could enable more accurate accounting and detection of indications of undeclared activities in nuclear safeguards, a better constraint on source material in forensic samples containing plutonium, and improvements in verification in a future plutonium disposition treaty.

To Mom and Dad

Contents

List of Figures

List of Tables

Acronyms

ADR Adiabatic Demagnetization Refrigerator.

C-API C-Application Programming Interface.

DMSO Dimethyl Sulfoxide.

FLL Flux Locked Loop.

FRAM Fixed energy, Response function Analysis with Multiple efficiencies.

FWHM full-width at half-maximum.

GM Gifford-Mcmahon.

HPGe High-Purity Germanium.

HRGS High Resolution Gamma-ray Spectrometry.

IAEA International Atomic Energy Agency.

LLNL Lawrence Livermore National Laboratory.

MGA Multi-Group Analysis.

MMC Metallic Magnetic Calorimeter.

NDA Non-Destructive Assay.

NEP Noise Equivalent Power.

NPT Treaty on the Non-Proliferation of Nuclear Weapons.

PMDA Plutonium Material Disposition Agreement.

PWR Pressurized Water Reactor.

RF Radio Frequency.

RKKY Ruderman-Kittel-Kasuya-Yosida.

RRP Rokkasho Reprocessing Plant.

RSD Relative Standard Deviation.

SQUID Superconducting Quantum Interference Device.

SRS Stanford Research Systems.

TES Transition Edge Sensor.

UNAEC United Nations Atomic Energy Commission.

Acknowledgments

For everyone who has supported me with their encouragement, technical guidance, and sage advice I am eternally grateful. I cannot hope to list each and every person that has made this work come to fruition.

I would like to convey my great appreciation for those who served on my committee. Firstly, I would like to thank Prof. Kai Vetter, my dissertation chair and academic advisor, for providing guidance in times of difficulty and willingness to go out of his way to make sure my experience at Berkeley was as smooth as possible. I would not have been able to undertake this endeavor if it had not been for Stephan Friedrich who gave me the unique opportunity to be a part of this project and constantly pushed me to help me grow as a scientist. I also cannot thank Prof. Karl van Bibber enough for his even-handed wisdom in times of apparent crisis. Lastly, I would like to thank Prof. Adrian Lee, whose astute inquiries led me to think about the fundamental limits of cryogenic detectors in a new, more complete way.

My colleagues at LLNL deserve my utmost thanks. Their mentorship and assistance in helping me to develop my technical skills was extraordinary. To Jonathan Dreyer, who generously donated his time to teach and assist me, and provided me a sounding board to bounce ideas off of, I cannot thank you enough. I have greatly enjoyed our time working together. To Owen Drury, who has a level of patience and attention to detail that I have been constantly awed by, thank you. In addition to those who I worked with daily I must also thank others at LLNL who provided their technical assistance, including Marianne Ammendolia, Jan Batteux, GP Carosi, Sergey Pereverzev and Roger Henderson. A special thank you to Ross Williams who mentored me during my first internship at LLNL and opened my eyes to the incredible work available at the national labs.

To my colleagues from the University of Heidelberg, this dissertation would not have been possible with your generosity and hospitality. A special thanks to Christian Pies and Daniel Hengstler: your patience with my German and your willingness to explain technical aspects to me multiple times were greatly appreciated. Thank you also to Andreas Fleischmann, Loredana Gastaldo, and Christian Enss for welcoming me into your research group and treating me like one of your own students.

Thank you to Steve Boyd and Robin Cantor for always being a phone call away when I needed help debugging SQUID issues and understanding MMC theory.

Thanks also to everyone who was on this journey with me. To Patricia Schuster, I am honored to have such a brilliant, supportive friend. To Anthony Scopatz, thank you for renewing my faith in the pursuit of knowledge when I became disillusioned. Ross Barnowski, Andy Haefner, Ryan Pavlovsky, Caleb Roecker, Joseph Curtis, Anders Priest, Anagha Iyengar, and Francisco Ponce, your candid conversation and camaraderie were greatly appreciated.

Thanks to everyone who I had the pleasure to work with during my time spent at LBL, including Paul Barton, Mark Amman, Mark Bandstra, and Lucian Mihailescu.

Thanks to Lisa Zemelman, Kris Petersen, and Nancy Reason. All of you made what seemed like impossibly large amounts of bureaucracy seem trivial.

My family deserves special thanks for instilling in me the perseverance and willingness to step out of my comfort zone to achieve my goals. To my dad, your dedication to both your job and the

constant pursuit of new solutions to problems inspired me to become a scientist. To my mother, your patience and constant encouragement has pushed me to aim high and not settle for anything less than achieving my goals. To Kathleen, thank you for being supportive during this endeavor and I wish you the best of luck in your own.

To Beth, I am not sure there are words to express how grateful I am to have you in my life. Thank you for your understanding when I spent nights and weekends in the lab, traveled to Germany without you, and came home after a rough day frustrated and stressed.

This dissertation was made possible in part by the U.S. Department of Energy Office of Nonproliferation Research and Development under grant LL12-MagMicro-PD2Ja.

The author wrote this dissertation in support of requirements for the degree Doctor of Philosophy in Nuclear Engineering at the University of California, Berkeley. The research is funded in part by the LLNL Graduate Scholars Program, and is not a deliverable for any United States government agency. The views and opinions expressed are those of the author, and do not state or reflect those of the United States government or Lawrence Livermore National Security, LLC.

Chapter 1

Introduction

1.1 Introduction

The first measurable quantities of plutonium were produced at what was then called the Berkeley Radiation Laboratory in 1940 [1] by Glenn T. Seaborg and his colleagues. In the following year, it was determined that one of the isotopes, ^{239}Pu, was fissionable and thus could be suitable for a nuclear explosive device [1]. This led the scientists to withhold all scientific publications on the discovery and basic properties of plutonium. This realization also stimulated in the US the development of a massive Pu production program for use in the Manhattan project. Beginning with the Trinity test on July 16th, 1945 and continuing today, the world has known of the security concerns surrounding production and separation of this material. Concerns about the fundamentally new level of destruction that could be wrought immediately led to a plethora of plans to control the use of nuclear technology. Different administrations in the US and abroad have taken very different approaches to this problem. These have varied from total secrecy, to tacit acceptance of proliferation, to the generally assumed norms of today's international non-proliferation regimes, which lie somewhere in between [2]. This chapter will cover some important parts of the history of the control of fissile materials, present some of the unique challenges for the international safeguards regime, and propose how ultra-high resolution gamma-ray spectrometers could provide a solution to these challenges.

1.2 History of International Safeguards

The very first resolution passed by the United Nations General Assembly after its formation in 1945 was the establishment of a commission to deal with the problems created by the discovery of atomic energy [3]. This became the aptly named UN Atomic Energy Commission (UNAEC). Concurrent with the formation of this commission was a report commissioned by the US Secretary of State to develop a plan for international control of atomic energy. This plan included having an international body manage all fissile material production and storage [4]. A modified version was presented to the UNAEC, but due to an unrealistic set of concessions that were demanded from Russia it was ultimately rejected [5]. The UNAEC continued to convene up until the testing of the first Soviet nuclear device in 1949. This test effectively stymied conversation on international cooperation regarding nuclear energy until President Dwight D. Eisenhower rekindled the concept in his famous "Atoms for Peace" speech on December 8, 1953 [6]. While many still argue the merits of this concept with respect to non-proliferation, his speech proposed the concept of an international atomic energy agency. This speech was the basis for the statute that governs the International Atomic Energy Agency (IAEA), which entered into force on July 29, 1957 after eighteen countries had ratified the IAEA statute. The IAEA promoted the peaceful use of atomic energy and gave countries access to nuclear energy technology with the condition that the technology would be monitored by international inspectors to ensure it was not being used for military purposes [6].

Until the Treaty on the Non-Proliferation of Nuclear Weapons (NPT) entered into force in 1970, accession to the IAEA was done voluntarily by states looking to access nuclear technology from the United States or Western Europe. The NPT codified participation in the IAEA as a requirement for all non-nuclear weapons states developing nuclear energy [6]. This requirement significantly expanded the purview of the IAEA into something more closely resembling the modern safeguards regime.

Between the 1970s and 1990s, the IAEA was primarily focused on verifying activities at declared nuclear facilities. This was done by verifying material balance sheets and keeping track of items using tamper evident seals. This remained the extent of the IAEA's purview until the early 1990s when it was discovered that both Iraq and North Korea had been out of compliance with the NPT by undertaking activities at undeclared facilities [6]. The discovery prompted the development of the IAEA Additional Protocol, which gave inspectors complimentary access to universities and other buildings at research centers that performed nuclear related research. It also allowed for environmental sampling. Environmental sampling in concert with modern uranium and plutonium mass spectrometry makes it possible to detect undeclared activities by the trace amounts of uranium and plutonium that are released into the environment. These techniques can detect plutonium at the part per quadrillion ($1/10^{15}$) level, or a few hundred atoms per gram of material [7].

1.3 Plutonium Issues Today

Today, the concerns about plutonium are not limited to non-nuclear weapons states diverting material for military purposes. In the aftermath of the terrorist attacks on September 11, 2001 it became clear that terrorist groups had the ability to undertake operations on US soil. This, along with evidence that al-Qaeda was interested in acquiring weapons of mass destruction [8], adds a new element to the need to control plutonium. Directly related to this issue is concern about the disposition of excess weapons grade plutonium in Russia and the United States. In order to address the issues it is necessary to be able to accurately characterize the plutonium in a sample. This is a core component of materials protection control and accounting, the basis of nuclear safeguards programs. These safeguards not only help to prevent insiders or governments from diverting material, but also help prevent and track thefts of nuclear material by criminal or terrorist organizations. One of the unique properties of plutonium, which makes characterization easier, is that all of its isotopes are radioactive. This makes it possible to characterize plutonium by measuring the characteristic gamma-rays given off by each isotope. The isotopes of plutonium that are produced in non-negligible quantities in nuclear reactors range in mass from 238 to 242 atomic mass units. The measurement of four of these five isotopes using gamma-ray spectroscopy is one of the most common methods of characterizing both known and unknown plutonium samples. The only isotope that cannot be directly measure with gamma-ray spectroscopy is ^{242}Pu. The lines from this isotope cannot be measured directly with existing tools because they are weak and too close to neighboring plutonium lines that are stronger in most samples. This is a concern because as fuel remains in a reactor longer more ^{242}Pu is produced and if it cannot be directly accounted for it can limit both the operator's and inspector's ability to accurately characterize the plutonium sample making it easier to divert material without being caught. A measurement system with a high enough resolution to directly measure the ^{242}Pu would have an impact in all three areas. The problems and potential impact will be discussed below. Specifics of how plutonium isotopic measurements are performed today and potential improvements will be discussed in detail in the following chapter.

Safeguards

Today we are approaching a new era of safeguards with both increased use of nuclear energy globally and the possibility of large reprocessing facilities being built in non-nuclear weapons states. Together with modern technologies that greatly reduce the technological and financial barriers to reprocessing, this creates the possibility to greatly increase the number of states pursuing nuclear technology [9]. The reasons for pursuing reprocessing today are typically a combination of energy security, prestige, and waste minimization. The expansion of this technology presents a fundamental challenge for the IAEA as the two reprocessing facilities in Japan consume 20 percent of the IAEA's total safeguards budget [10]. These facilities and the safeguards issues they pose will be discussed in more detail in the following chapter. The need to monitor these facilities at a reasonable cost drives the demand for unattended on-line monitoring systems [11]. These systems often employ high-resolution gamma-ray spectroscopy to assay the material. As discussed previously, plutonium can be characterized by measuring the different gamma-rays produced by different isotopes and ^{242}Pu's gamma-rays cannot be directly measured with current systems. These systems therefore can be limited in their ability to determine total plutonium mass due to the inability to measure ^{242}Pu. This problem becomes larger when fuel spends longer amounts of time in a reactor. ^{242}Pu can make up five to ten percent of the total plutonium mass in spent fuel discharged from a modern reactor and a small error in the model for ^{242}Pu can mean a large error in the predicted total plutonium mass. In the case of a malicious actor, the formula used to calculate the ^{242}Pu fraction could be leveraged to divert material. While reactor grade plutonium is typically not considered usable for a militarily effective nuclear weapon, it could theoretically be used to create an improvised nuclear device [12].

Plutonium Disposition

Plutonium disposition faces the same basic problem as nuclear safeguards in terms of accounting for fissile material. Ideally, there would be even higher standards for uncertainty in plutonium isotopics, as not just total plutonium mass but the actual isotopics would be important to verify that it was military excess that was being dispositioned and not just reactor grade material. This sort of verification could be done in a manner similar to that used for the blend down monitoring system, a system which verified isotopics of weapons grade uranium using a mix of gamma-ray and neutron detectors [13].

Nuclear Forensics

The third application of plutonium isotopics is the field of nuclear forensics. This field can be split into two parts typically referred to as: pre-detonation and post-detonation. These terms refer to situations in which material is interdicted before a radiological dispersal device or nuclear device is detonated and after a device is detonated. The two primary advantages of the type of detector

Table 1.1: Timeline for investigation of intercepted nuclear material. Adapted from [14]

Technique	24 hours	1 week	1 month
Radiological	Estimated total activity Dose rate Surface Contamination		
Physical characterization	Visual Inspection Radiography Photography Weight Dimension Optical Microscopy Density	SEM XRD Organics	TEM
Traditional forensic analysis	Fingerprints, Fibers		
Isotope analysis	α-spectroscopy γ-spectroscopy	Mass spectrometry (SIMS, TIMS, ICP-MS)	Radiochemical separations and mass spec. for trace impurities: Pb stable isotopes
Elemental/chemical		ICP-MS XRF ICP-OES	GC/MS

developed for this work are that it is non-destructive and that it could allow for a shorter time between receiving a sample and getting high fidelity results for plutonium isotopics. The standard times for nuclear forensic analysis of a sample have been reproduced in table 1.1. This table shows that it would take on the order of one week to get mass spectrometry data. An array of microcalorimeters could theoretically achieve similar levels of precision in isotopic ratio in less than 24 hours. Post-detonation samples may have too much activity from short-lived isotopes for microcalorimeters to provide a viable alternative. More study of this specific case would be needed in order to determine its practicality.

1.4 Metallic Magnetic Calorimeters

Cryogenic gamma-ray detectors with operating temperatures of $\sim$0.1 K have been developed for several decades. Different detector technologies have been used to attain an energy resolution of $<$100 eV full-width at half-maximum (FWHM) at energies of up to 100 keV, including Si and Ge thermistors [15, 16, 17], superconducting transition edge sensors (TESs) [18, 19], and more recently, metallic magnetic calorimeters (MMCs) [20, 21]. This work focuses on MMCs, as their more linear response and normal metal construction may make it possible to operate them at higher count rates and sum multiple spectra without significant degradation.

Metallic magnetic calorimeters have been under development for the past twenty years, but most of their applications have focused on soft X-ray spectroscopy for basic physics and astronomy applications [22, 23, 24, 25]. Recently, the University of Heidelberg has developed a new MMC sensor specifically designed to measure hard X-rays. This sensor achieved a resolution of 62 eV FWHM at 18 mK [21]. The device used in this dissertation is based upon the same design with improvements to increase the linearity and uniformity of the response at higher energies.

1.5 Dissertation Outline

This thesis demonstrates the direct measurement of ^{242}Pu in a mixed isotope plutonium sample. It demonstrates how the linearity of MMCs enables summing many spectra with minimal degradation in resolution. Chapter 2 will discuss the production of plutonium in the fuel cycle and possible diversion scenarios in more detail. Chapter 3 discusses a fundamental thermodynamic model of a micro-calorimeter, its limitations and progress to a complete model of the MMC used in this work. Chapter 4 discusses the fabrication of metallic magnetic calorimeters and improvements made to this process. Chapter 5 covers the experimental apparatus used for the measurements and the improvements that were made to the systems at LLNL. Chapter 6 covers the data acquisition system developed for this work and the analysis software used to convert the digitized waveforms into spectra. Chapter 7 covers the initial measurements of this MMC detector at the University of Heidelberg, followed by characterization performed at LLNL, and finally measurements of a mixed isotope plutonium source containing significant amounts of ^{242}Pu. Chapter 8 discusses the implications these measurements have for future measurement systems and the steps needed to make this system a practical tool for plutonium isotopic analysis.

Chapter 2

Plutonium Isotopics

2.1 Introduction

Measurements of plutonium isotopics are important to international fuel cycle verification, verification of plutonium disposition, and nuclear forensics. Plutonium is an unavoidable byproduct of a uranium based fuel cycle. Plutonium can be used both for the development of nuclear explosive devices and for the production of energy. In order to ensure that material ostensibly produced for the latter is not used for the former, it is necessary to safeguard this material. One important component of safeguards is non-destructive assay (NDA). Non-destructive assay is comprised of many different techniques including but not limited to: gamma-ray spectroscopy, densitometry, X-ray fluorescence, neutron spectroscopy, neutron coincidence counting, and bulk calorimetry. These techniques all share the common property that they do not affect the item that is being assayed. This makes them desirable for safeguards use as it helps to minimize the burden on the operator of the nuclear facility. Three of the tools most relevant for plutonium assay today: gamma-ray spectroscopy, neutron coincidence counting, and bulk calorimetry are discussed in more detail in this chapter. This chapter also discusses how plutonium is produced, how it is safeguarded today, and how MMCs could improve this. In addition, it covers how MMCs could play a role in nuclear forensics and plutonium disposition verification.

2.2 Plutonium in the Nuclear Fuel Cycle

Plutonium is a byproduct of all commercially operating nuclear reactors in the world today. It is produced when a neutron in the reactor is absorbed by a ^{238}U nucleus in the following reaction

$$^{238}\mathrm{U} + {}^{1}_{0}n \rightarrow {}^{239}U^{*}$$

The $^{239}U^{*}$ then beta-decays to ^{239}Pu. This ^{239}Pu can subsequently undergo further capture reactions to produce other heavier isotopes of plutonium. As the fuel spends more time in the reactor, larger fractions of these heavier plutonium isotopes are produced. The production pathways for the primary trans-uranic components of spent fuel are shown in figure 2.1.

It is possible to simulate the relative abundances of different plutonium isotopes in a reactor as a function of burn-up, ie. the amount of energy a specific starting mass of uranium has produced. In a simplified model, the reactor remains on until the desired burn-up is achieved. This provides a notional concept of the isotopic abundances as a function of burn-up. Figure 2.2 shows the plutonium isotopics as a function of burn-up in a Pressurized Water Reactor (PWR) modeled using the CAIN software package [27]. Americium is included due to the short half-life of ^{241}Pu.

These concentrations have been simulated for a variety of common reactor types using CAIN. The results of those simulations are shown in table 2.1. These burn-ups are typical for modern fuel cycles and demonstrate the variation in relative concentration of ^{242}Pu from different reactor types.

Understanding the isotopics of plutonium is important because only some isotopic compositions are usable for nuclear weapons and these are not consistent with the isotopic compositions in used nuclear fuel. In order to be readily usable for nuclear weapons, plutonium must contain less than 20 percent ^{239}Pu [11]. In a commercial nuclear reactor, this is only the case at the very

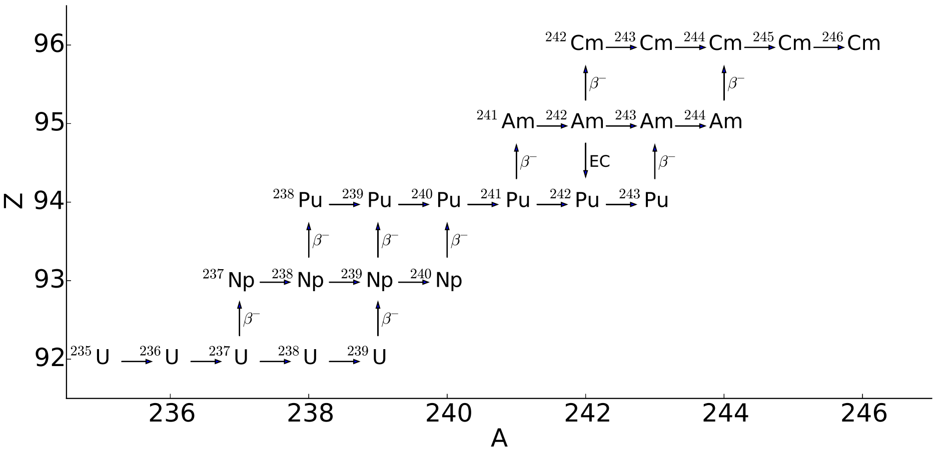

Figure 2.1: A plot of the production pathways for common trans-uranic isotopes in a reactor. Adapted from the Passive Nondestructive Assay Manual [26].

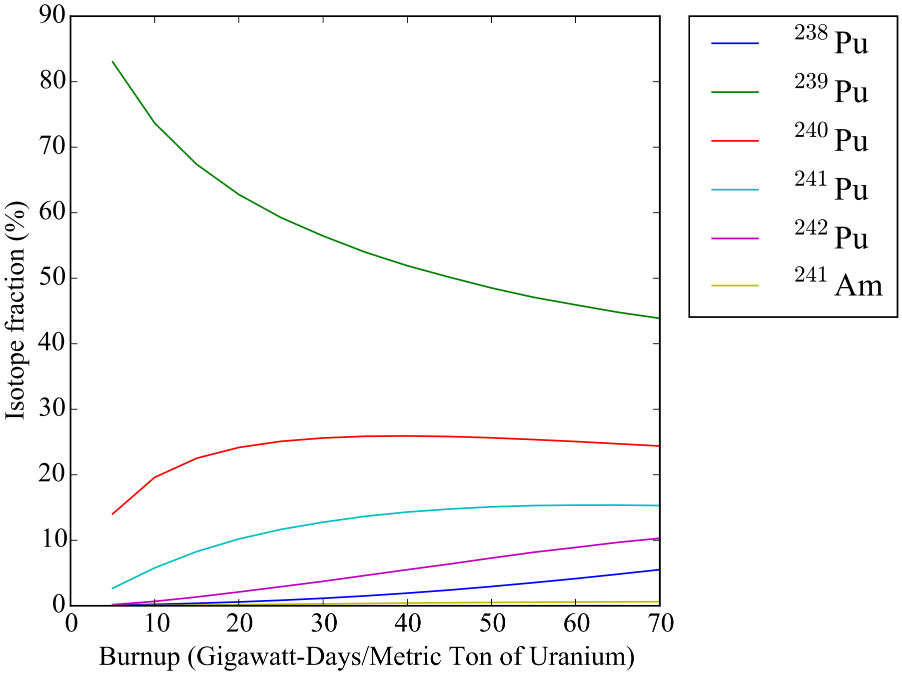

Figure 2.2: A plot of Pu concentration as a function of burn-up in a PWR calculated using CAIN [27].

Reactor	burn-up	^{238}Pu	^{239}Pu	^{240}Pu	^{241}Pu	^{242}Pu
PWR	30	1.1	56.6	25.7	12.8	3.7
	45	2.4	50.4	26.0	14.8	6.4
	65	4.8	45.1	24.9	15.5	9.7
BWR	30	1.2	55.7	25.9	13.1	4.1
	45	2.7	49.5	26.0	14.9	6.9
	65	5.5	44.2	24.7	15.3	10.3
Magnox	7	0.3	59.8	28.2	9.0	2.7
CANDU	25	0.7	46.5	34.4	10.0	8.5

Table 2.1: Plutonium isotope fraction as a function of burn-up for several different reactor types [27].

beginning of the fuel cycle. Removal of fuel that has only been in the reactor for a short time or a history of operating a reactor for very short periods at full power are both possible indicators that fuel is being diverted for military uses.

In order to verify that this has not occurred, the IAEA has to determine how much time the fuel has spent in the reactor. This is typically done by measuring the Cherenkov light from the assembly in a spent fuel pool which is proportional to a function of the burn-up and cooling time [11]. In addition, spectroscopic measurements using high-purity germanium (HPGe) detectors can be made to measure total gamma-ray activity as well as intensities of specific decays and ratios of different decays. These make it possible to constrain the burn-up of the fuel but do not directly quantify uranium or plutonium masses or isotopic ratios. More accurate information about the masses of trans-uranic isotopes can only be determined by dissolving the fuel and separating the actinides from the rest of the chemical components. This is undesirable both due to the burden on the commercial operator and because the physical integrity of the fuel element provides an excellent way to ensure no diversion has taken place.

There are two primary types of fuel cycles employed by states with nuclear power industries today. The first type of fuel cycle is known as an open or once-through fuel cycle. In this fuel cycle the uranium is enriched, fabricated into fuel, and put into the reactor. After the fuel is used, it is initially moved to a cooling pool in the reactor building. Once it has cooled enough to be removed from the water while retaining structural integrity, it is placed into dry cask storage. Finally, it is placed in a geologic repository for final disposition. In this system, limited destructive assay of a small subset of the fuel is typically more feasible than any passive assay of the fuel in order to verify the isotopic composition.

In the second type of fuel cycle, commonly known as a closed fuel cycle, the cycle is the same up to the point that the fuel leaves the spent fuel pool. In a closed fuel cycle, the spent fuel is sent to a reprocessing facility. At the reprocessing facility the fuel is chopped into pieces and dissolved. After it is dissolved, the fuel goes through a separation process to separate the uranium and plutonium from the rest of the elements. In the PUREX process developed by the United States, uranium and plutonium each are separated and end up in a nitric acid solution [28]. Ideally,

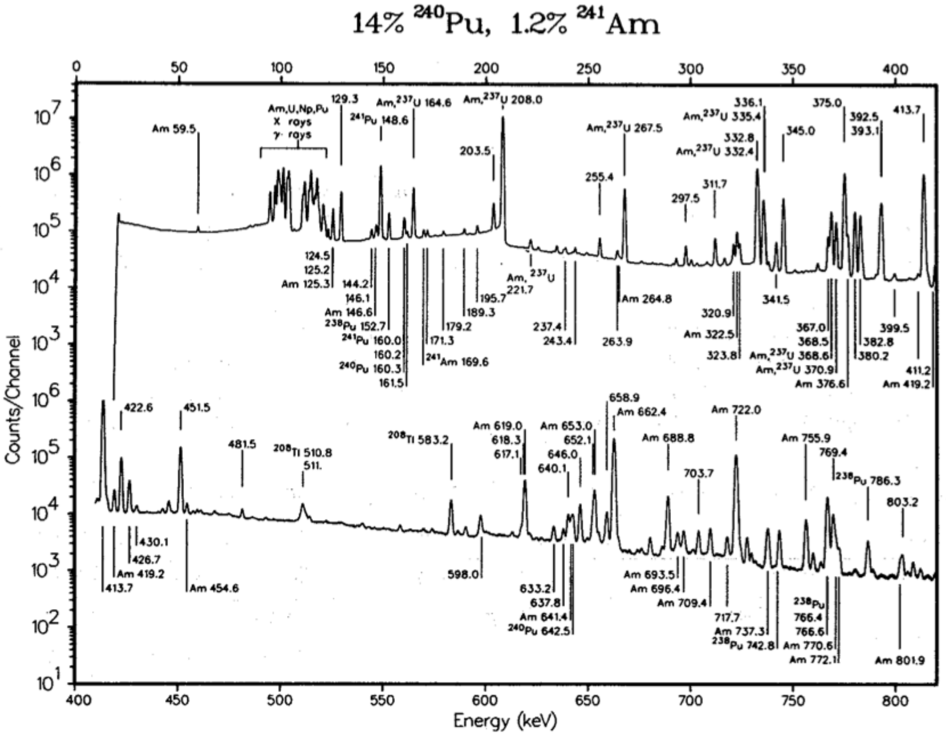

Figure 2.3: Gamma-ray spectrum of a plutonium sample from the Passive Nondestructive Assay Manual [26].

it would be desirable to measure the plutonium in the spent fuel before it is physically chopped and dissolved, but that is currently not possible. Once it has been separated it is possible to measure the plutonium isotopics using high resolution gamma-ray spectroscopy with a HPGe detector. In order to perform the measurement, a sample is placed in front of the detector and counted until there are a statistically significant number of gamma-rays detected from the plutonium. A sample spectrum collected from plutonium is shown in figure 2.3. From this type of spectra it is possible to determine the isotopic composition of most of the major isotopes of plutonium with only a few percent error. The analysis of the spectra will be discussed in more detail in subsequent sections. The one major plutonium isotope that can currently not be directly measured with non-destructive assay is ^{242}Pu. This quantity has to be modeled, and the uncertainty in the quantity is a primary driver in the uncertainty in the total plutonium mass in a measured item.

Up until the last decade, the only countries that have attempted large scale reprocessing of spent fuel within their country have been states possessing nuclear weapons. This status quo could change in the future as many rising powers seek to acquire indigenous reprocessing capabilities for energy security and as a demonstration of the technical capabilities of their country. This expansion of reprocessing capabilities presents a technical challenge for the international safeguards regime, which it cannot adequately cope with in its current form.

Japan is expected to be the first state without nuclear weapons to utilize large scale reprocessing with the reprocessing facility in the Rokkasho prefecture. As it is slated to begin operations in late 2014 to early 2015, it is a good example to demonstrate the challenges it poses to the IAEA safeguards regime.

The Rokkasho Reprocessing Plant (RRP) is a large facility designed to take spent fuel from light water reactors and convert it into mixed oxide fuel. This is done by removing the plutonium from the spent fuel and mixing it with enriched uranium to produce new fuel. This facility is capable of processing up to 800 metric tons of spent fuel per year [11]. Of this fuel, roughly 8 metric tons are plutonium. A 1 percent error in the total measured mass is equivalent to 80 kg of plutonium per year or 10 significant quantities of plutonium. A significant quantity is defined as the amount of special nuclear material that, if diverted, indicates it is no longer possible to exclude the possibility that a state is manufacturing a nuclear explosive device [29]. It is very challenging to verify the total plutonium to less than 1 percent error. In order to meet their safeguards obligations, extensive destructive analysis is currently required, which requires an on-site destructive analysis laboratory [11].

While safeguards have been successfully implemented at RRP, the burden on the IAEA has been very large. Some of these costs can be attributed to the fact that it is the first facility that can process over 100 tons of heavy metal per year in an NPT signatory state that was not a nuclear weapons state. The two reprocessing plants in Japan have been quoted as taking up to 20 percent of the IAEA safeguards budget [10]. This is not sustainable in the future if other non-nuclear weapons states decide to pursue reprocessing. South Korea has already shown interest in developing a pyroprocessing plant, where the fuel is dissolved and chemically separated in a molten salt [30]. Future safeguarded reprocessing plants will need both a more streamlined approach to safeguards as well as new technologies to reduce inspector burden. Improved plutonium isotopic analysis with gamma-ray spectrometers is one avenue to reduce this burden.

2.3 Plutonium Disposition

Plutonium Material Disposition Agreement

The plutonium material disposition agreement (PMDA) is an agreement between the United States and the Russian Federation concerning the management of plutonium that has been withdrawn from military programs [31]. It is seen as a step towards reducing the total fissile material stockpiles that are weapons usable. Due to both technical and political issues, neither country has begun disposition of the agreed upon plutonium, but it will be necessary to verify the contents of the blended plutonium mixture when the terms of this treaty are enacted.

Fissile Material Cutoff Treaty

In addition to the PMDA, there is another international agreement that is currently being discussed that would limit production and eventually limit stockpiles of fissile material. This is known as the Fissile Material Cutoff Treaty [32]. Initially, it would be important to verify the isotopics of plutonium produced by reactors that could then be used for producing weapons grade material. Eventually, it would also be necessary to verify the disposition of plutonium and that it had been properly blended or immobilized.

Plutonium disposition and plutonium isotopics

An important component of any plutonium material disposition regime would be the verification of the mass and type of plutonium that was being disposed. As was previously discussed, depending on the fidelity of isotopics that is desired, quantification of ^{242}Pu may be necessary to ensure the declared material is being disposed. The only currently available method to quantify ^{242}Pu requires destructive assay. Destructive assay may not be possible in a disposition regime due to concerns about secrecy and a non-destructive assay method that could be performed on-line would be desirable. In the "Megatons to Megawatts" agreement between the Russian Federation and the United States regarding the disposition of Russian highly enriched uranium an on-line system sfor monitoring uranium enrichment was used [13]. Ultra-high resolution gamma-ray spectroscopy with Metallic Magnetic Calorimeter (MMC)s could provide a similar capability in a future plutonium disposition regime.

2.4 Plutonium Characterization for Nuclear Forensics

As discussed in chapter 1, the third area in which rapid non-destructive assay of plutonium could be beneficial is in the area of nuclear forensics. It could be particularly useful in cases in which destructive assay is not possible or in cases in which there is a limited amount of time to analyze a sample. This could occur either in a pre-detonation scenario when there are concerns about additional threats or in a post-detonation scenario when it is desirable to know the source of the plutonium as soon as possible. One additional scenario is that a high precision analysis is required, but destructive assay is not possible due to legal issues (ie. the sample is from a foreign country). One of the primary advantages that MMCs have over traditional γ-ray spectroscopy is their ability to directly measure low energy γ-rays that would be either too close to neighboring lines or too weak compared to the Compton continuum to be measurable with a HPGe detector. One specific limitation that will be discussed in detail in this work is the inability to directly measure ^{242}Pu in mixed isotope plutonium samples. In the case of pre-detonation nuclear forensics, the ^{242}Pu isotopic concentration could be used to identify reactor type and initial fuel enrichment and thus the possible source of the fuel [33].

2.5 Plutonium Characterization and Quantization

The standard tools for verifying a sample of plutonium are a neutron coincidence counter, a bulk calorimeter and high resolution gamma-ray spectrometry (HRGS), typically using an HPGe detector. These technologies are used in concert in order to determine both the total plutonium mass and the plutonium isotopic composition. Typically, the γ-ray spectrum of a sample is first measured using HRGS to determine its isotopic composition. This isotopic composition along with errors is then entered into the software that operates the neutron coincidence counter. The sample is then measured using the neutron coincidence counter. Based on a measurement of the coincident neutron rates it is possible to determine the total mass to an accuracy of less than a percent, if and only if the isotopics are accurate. The measured isotopics and mass are then compared against the operators' declared values for consistency. In the current inspection regime it is up to the discretion of the inspector what level of error to accept, but errors that are within the three times the uncertainty reported by the isotopic analysis code Fixed energy, Response function Analysis with Multiple efficiencies (FRAM) are typically deemed acceptable [34].

Calorimetry

One of the best understood non-destructive methods of plutonium assay is bulk calorimetry. This measures the total heat generated by an object. When combined with isotopics analysis gamma-ray spectroscopy, it can provide the most accurate non-destructive assay of plutonium [26]. This is due to the fact that specific radionuclides have well-known heat generation rates from their decay radiation. This makes it possible to calculate the total plutonium mass by using the known isotopics and the heat generation rate to constrain the total plutonium mass to less than 1 percent [26]. This method has the disadvantage that it requires hours to measure a single sample. The accuracy of this method is dependent on using a model of the ^{242}Pu concentration in order to calculate the total mass of plutonium. Due to the fact that ^{242}Pu has the smallest specific power output of all the plutonium isotopes, a large discrepancy in ^{242}Pu concentration from the declared value would be challenging to detect with this method.

Well coincidence counters

A neutron coincidence counter typically consists of an array of ^{3}He neutron detectors in known configuration with a moderator, typically plastic, to slow fission neutrons to thermal energies. It tracks how many events occur within a moving time window that is typically 10's of microseconds long. The higher the multiplication factor in the system, the higher the number of neutrons that will be measured on average in the time window. By comparing the number of singles with the number of double and triples - only one event in the time window versus two and three events within the time window - it is possible to determine the fissile content in the sample if the isotopics are known. Typically the value that is calculated is the effective ^{240}Pu mass, which is defined as :

$$^{240}Pu_{eff} =^{240} Pu + \gamma_{242} *^{242} Pu + \gamma_{238} *^{238} Pu$$

In this equation γ_{242} and γ_{238} are values derived from either the declared or the measured isotopics of the sample to take into account spontaneous fission neutrons from ^{242}Pu and ^{238}Pu. The even isotopes are important in this measurement, because they spontaneously fission at a much higher rate as shown in table 2.2. These spontaneous fissions make it possible to measure the fissile material in the system without an external neutron source.

Table 2.2: Spontaneous neutron yields for plutonium from PANDA [26].

Isotope	Number of Neutrons	Half-life	Spontaneous Fission Yield (n/s/g)
^{238}Pu	144	87.74 yr	2.59×10^3
^{239}Pu	145	2.41×10^4 yr	2.18×10^{-2}
^{240}Pu	146	6.56×10^3 yr	1.02×10^3
^{241}Pu	147	14.35 yr	5×10^{-2}
^{242}Pu	148	3.76×10^5 yr	1.72×10^3

Standard tools for plutonium isotopics measurements

As was mentioned previously, HRGS is the standard tool for plutonium isotopics measurements. This typically consists of some type of HPGe detector. Depending on the sample, either a thin planar HPGe will be used or a larger coaxial detector. The planar germanium has better performance at lower gamma-ray energies, typically 60-210 keV, and it also typically gives the most precise results if there is minimal shielding. If there is significant shielding or significant self-shielding due to the size of the item, a coaxial detector is preferable because it has higher efficiency at higher energies. It often has lower precision, however, due to the greater uncertainty in the efficiency curve because the gamma-ray lines are farther apart and because the lines are measured with poorer energy resolution.

Once the detector has been chosen, it is necessary to choose an analysis routine. The two most commonly used tools that are commercially available are Multi-Group Analysis (MGA) [35] (developed by Lawrence Livermore National Laboratory (LLNL)) and FRAM [36] (developed by Los Alamos National Laboratory). Both of these codes are designed to do a fit of the sum of the detector response to the plutonium gamma-rays in regions where the energy resolution results in significant line overlap of different gamma-ray lines. These codes combine known properties of the radioactive isotopes and the form of the efficiency of the detector to estimate the contribution to the measured response from each isotope. This is discussed in more detail later in this chapter.

Calculations of plutonium isotopics with traditional methods

If the geometry of a sample and detector setup is known, it is possible to calculate the actual amount of a given isotope based upon the observed photopeak in the detector, assuming that self-attenuation does not prevent gamma-rays from reaching the detector [37]. This is due to the fact that for any macroscopic quantity of atoms, the observed decay rate is constant [38]. Along with the decay rate of the parent λ, it is also necessary to know the rate at which the excited levels in the child nuclide are populated, so that the rates of each gamma-ray line are known. The rate for a specific photon is known as the branching ratio P. With this information and a well-understood detector geometry, it is possible to model the response of the detector as a function of source energy using a 3D Monte Carlo transport code such as Geant4 [39, 40]. The result of the modeling can be used to calculate a photopeak efficiency as a function of energy $\eta_{pp,abs}$. Combining these factors together, the equation to calculate the total number of atoms, N, of a specific isotope is:

$$N = \frac{I}{\eta_{pp,abs} P \lambda} \tag{2.1}$$

Where I is the number of counts per second recorded in the detector. Depending on the mix of isotopes in the sample, the total source strength may increase or decrease significantly during the count time if the decay constant of the isotope or its parent is less than two orders of magnitude larger than the count time. This contribution is ignored in this work as the half lives of the isotopes of interest are all greater than 10 years.

In most realistic counting situations, it is not possible to know a-priori the geometry of the source exactly. In this situation, self-attenuation and the exact source detector-geometry remain unknown, so it is not possible to determine the absolute mass of a given isotope with gamma-ray spectroscopy with high accuracy. However, in many situations, it is still possible to determine the isotopic ratio if peaks from different isotopes are close in energy and the relative detector efficiency can be determined. Since most plutonium isotopes give off a large number of gamma-rays, it is possible to use the gamma-rays at different energies to determine the relative detection efficiency of the detector. This is because the relative rates of two γ-rays from the same parent isotope are physical constants and the measured photopeak rates are therefore only affected by the relative detection efficiency at the two photopeak energies. Using these relative photopeak rates, it is possible to determine the relative efficiency curve by assuming a shape based on the physics of radiation transport. With a known relative efficiency curve, the ratio of the relative abundance of the two isotopes, N_1 and N_2, can be calculated using the following equation:

$$\frac{N_1}{N_2} = \frac{I_1 \eta_{2,pp,rel} P_2 \lambda_2}{I_2 \eta_{1,pp,rel} P_1 \lambda_1} \tag{2.2}$$

This is the core concept behind the two most common plutonium isotopic analysis codes: MGA and FRAM [35, 36]. These two codes differ in how they handle peak fitting, efficiency calculation, and user input. Due to the fact that MGA is limited to using pre-determined fitting regions with few user adjustable settings, it could not be used for this work, and will not be discussed in further detail. The two most important aspects of isotopics calculation in FRAM, efficiency calculation and peak-fitting, will be discussed below.

Efficiency calculations

There are many different approaches to efficiency calculations. These approaches can generally be divided into two primary types: physics-based models and empirical models. The FRAM analysis code can use either model based upon the measurement situation. The physics-based model fits the relative detection efficiency based on known material parameters of absorbers between the source and the detector in combination with a simple model for the photopeak efficiency as a function of energy. The empirical model fits a polynomial as a function of $\ln E$ in order to determine the relative efficiency.

The empirical model used in FRAM is of the following form:

$$\ln \eta_i = C_1 + C_2 E_i^{-2} + \sum_{j=1}^{3}(C_{j+2}(\ln E_i)^j) + \sum_{k=1}^{m} C_{k+5} + \sum_{l=1}^{n} C_{l+5+m} E_i^{-1} \tag{2.3}$$

In this equation, C_i are fitted constants. The total number of fitted constants that are used is a function of the number of photopeaks being fitted. The variables m and n are both equal to the number of photopeaks being used for the efficiency fit. The most recent version of FRAM can use multiple nuclides with multiple photopeaks each to constrain the efficiency on a per-isotope basis. This fitted model is then used to correct the area of each photopeak based on the efficiency.

The physics-based model that can be used in FRAM is a physical model that can take into account self-absorption in plutonium as well as up to three additional absorbers. This model consists of four primary components: self-attenuation in the source, attenuation in up to three layers of shielding between the source and detector, a simple model of detector efficiency, and a "correction factor" that can help to adjust for slowly varying effects [36]. This equation has the following form:

$$\begin{aligned} \eta = &\frac{(1-\exp(-\mu_{Pu}x_{Pu}))}{\mu_{Pu}x_{Pu}} * && \text{self-attenuation} \\ &\prod_{n=1}^{3}(\exp(-\mu_n x_n)) * && \text{absorber attenuation} \\ &(DetEff) * && \text{detector efficiency} \\ &\exp\left(\frac{d}{E}\right) * E^b c^{\frac{1}{E}} && \text{correction factor} \end{aligned} \tag{2.4}$$

In this equation μ_n refers to a mass attenuation coefficient, x_n refers to the thickness of the corresponding material. The terms c, b and d are parameters that can be fixed or fit to the data.

Peak fitting

In order to determine the total counts in a peak, it is necessary to fit the peak shape to a model. In FRAM, peaks are generally modeled as a Voigtian function with an exponential low energy tail. Since the peaks of interest in this work are all gamma-rays, the width of the Lorentzian part of the Voigtian function is set to zero, thereby making it a pure Gaussian. The fit equation then has the form:

$$p(E) = A * \exp(B(E-E_0)^2) + Tail(E) \tag{2.5}$$

where A, B, and E_0 are the amplitude, width, and centroid of the peak and $Tail(E)$ is an exponential function of the following form:

$$Tail(E) = A * \exp(C_1 + C_2 E + (C_3 + C_4 E)(E - E_0))(1 - \exp(-0.4 * B(E-E_0)^2)) \tag{2.6}$$

In this equation A, B, and E_0 are the same parameters as those used for fitting the peak and C_i are fitted parameters of the tail. This tailing function takes into account both small angle scatter between the source and the detector and intrinsic effects in HPGe detectors that cause the peak to be non-Gaussian. In addition to modeling the peak and a tailing function it is also necessary to model the background counts underneath the peak. This is typically modeled by a constant or linear function that is fitted along with the peak. The fit value of A along with the fit values of C_i can then be used to calculate the total number of counts to attribute to that peak. In many situations the fitting is more complicated due to line overlap, meaning multiple peaks have to be simultaneously fit, but the fundamental concept remains the same.

Methods of calculating ^{242}Pu concentrations

By using one of the efficiency models and fitting the measurable peaks in a gamma-ray spectrum from a plutonium source, it is possible to measure all the plutonium isotopes present in large quantities in the typical nuclear fuel cycle with an HPGe detector except ^{242}Pu. This is due to its comparatively long half-life of $3.735{*}10^5$ years, because it only has three gamma-ray lines, all with intensities of less than 0.1 percent per decay [41], and the two strongest lines have close neighbors that are an order of magnitude or more stronger.

Without being able to directly measure ^{242}Pu, it becomes necessary to use a model of ^{242}Pu based on the observed ratios of other isotopes [42]. One of the most commonly used models is implemented in FRAM, and has the form:

$$^{242}Pu = A \times \left[(^{238}Pu)^B + (^{239}Pu)^C + (^{240}Pu)^D + (^{241}Pu +^{241} Am)^E \right] \tag{2.7}$$

Constant	Value
A	1.58
B	0.5
C	-1.8
D	1
E	0.23

Table 2.3: Default parameters in FRAM used to calculate ^{242}Pu concentration.

This model depends on the user defining appropriate parameters for the constants $A - E$. The default values used are shown in table 2.3. A specific reactor type is not specified for these parameters so this is comparable with a worst-case, but realistic, scenario where an inspector has not appropriately configured FRAM for the specific facility they are in. A comparison of the computed value from the formula and the simulation of the ^{242}Pu fraction as a function of burn-up are shown in figure 2.4. In this case, differences between the actual ^{242}Pu and predicted value can be up to several percent in this worst-case comparison. Different formulae have been developed over the years to attempt to remedy this, but they all have deficiencies in samples that vary widely in burn-up, with relative errors of five to ten percent being common [43]. The core deficiency of

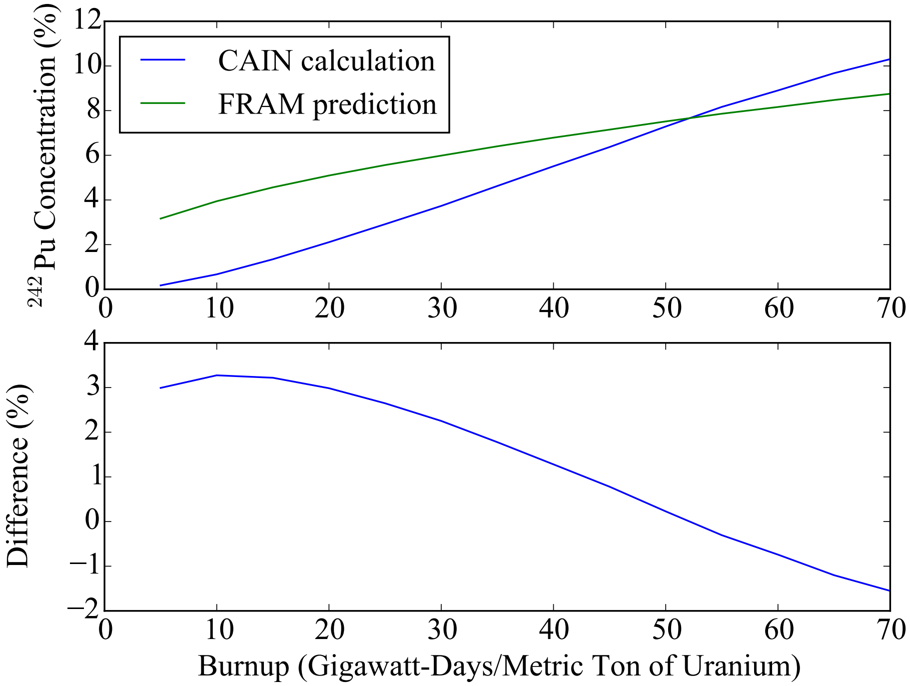

Figure 2.4: A comparison of FRAM's predicted ^{242}Pu concentration based on ratios of other isotopes in a CAIN simulation of a PWR to the ^{242}Pu concentration in that simulation [27].

any model-based approach is that it is necessarily dependent not only on the reactor type but also on the initial enrichment and flux profile of a given fuel element. Modern reactor core loading employs both a mix of initial enrichments and complicated core-shuffling which has the effect that different fuel elements will have different isotopic compositions, even within the same reactor. One implication of this is that the uncertainty in the ^{242}Pu concentration makes it difficult to verify initial fuel enrichment [33].

Direct measurement of ^{242}Pu

^{242}Pu has three characteristic gamma-rays that are given off during its alpha decay. These gamma-rays are rare for two distinct reasons. The first is that 76.49 percent of transitions go directly to the ground state of ^{238}U in a 0^+ to 0^+ transition. The second is that, of the 23.48 percent of decays that go to the 2+ excited state at 44.915 keV, almost all of them decay by internal conversion. These two factors lead to weak intensities, shown in table 2.4. This alone would not necessarily be a problem, but the two strongest lines are also very close to stronger gamma-rays from other plutonium isotopes. The differences in energy are on the order of 300 eV, which make them nearly impossible to distinguish with an HPGe detector. The second is that the line at 103.5 keV directly coincides with a plutonium X-ray line that will be significantly stronger than it would be in any

Energy (keV)	Intensity (%)
44.915	0.0373
103.50	0.00255
158.80	3.00E-4

Table 2.4: ^{242}Pu gamma-ray lines and intensities [41].

concentrated sample. The third problem is that in any sample with significant amounts of ^{241}Am present, the background from scatter could overwhelm the peak at 44.915 keV.

For the direct measurement of ^{242}Pu with ultra-high resolution gamma-ray detectors, which is the primary goal of this dissertation, the lines at 103.5 and 258.8 will be ignored as they are weak and the 103.5 keV line cannot be separated from the plutonium X-ray. The line at 44.915 keV, in comparison, is stronger and can be more easily separated from neighboring lines. In order to determine whether or not this measurement is feasible it is necessary to compare the locations and intensities of all the gamma-ray and X-ray lines in the spectrum to see if the ^{242}Pu line can be separated from them. In order to determine all of the gamma-ray lines and intensities, the web resource `http://www.nndc.bnl.gov/nudat2/` was used. Starting with this information, the number of gamma-rays per second per gram was calculated. The results are shown in table 2.5. From this table it is immediately clear that there are two lines, which could make measuring ^{242}Pu at 44.915 keV challenging. The first is the ^{240}Pu line at 45.244 keV, separated by 329 eV from the ^{242}Pu line and 69 times stronger than the ^{242}Pu line for the same amount of material. This is the line that is typically seen in plutonium samples at 45 keV. The second is the ^{241}Pu line at 44.86 keV, 55 eV away from the ^{242}Pu line, which is 58.9% of the intensity of the ^{242}Pu line for the same amount of material. The closer line would be much more difficult to separate but in many cases material used for reprocessing will likely be 30-50 years old, and by that point 75-90% of the ^{241}Pu will have decayed due to its 14 year half-life. At higher concentrations it would be necessary to either design the detector to have an energy resolution of less than 50 eV FWHM for good separation or to de-convolve the two peaks, which would increase the uncertainties in peak area.

In order to directly measure ^{242}Pu at 44.915 keV in the presence of either significant amounts of ^{240}Pu or ^{241}Pu, a detector with higher energy resolution than HPGe is needed. The two possible solutions to this are X-ray crystal spectrometers and micro-calorimeters. X-ray crystal spectrometers have an energy resolution of up to $10^4 \Delta E/E$ or less than 10 eV at 44 keV. These spectrometers have the drawback that they have very small solid angle acceptance. Very strong sources are therefore required to achieve good counting statistics, making it unsuitable for this application [44].

Micro-calorimeters

Micro-calorimeters have an energy resolution of 10's to a few hundred eV FWHM in this region and have much larger solid angle coverage in comparison to X-ray crystal spectrometers. This mix of high resolution and higher solid angle theoretically make it possible to directly detect ^{242}Pu. In order to demonstrate the feasibility of this measurement it is necessary to start with an idealized case. In general, the ability to quantify the ratio of two neighboring peaks is dependent on statis-

Isotope	Energy	Half-life (s)	Intensity (%)	Gammas/s/g	Ci/g
Pu239	40.41	7.61E+11	0.000162	3.72E+05	0.06203
Pu239	41.93	7.61E+11	0.000146	3.35E+05	0.06203
Pu238	43.498	2.77E+09	0.0392	2.48E+10	17.12
Pu241	44.2	4.51E+08	0.000004165	1.60E+07	103.8
Pu241	44.86	4.51E+08	8.33E-07	3.20E+06	103.8
Pu242	44.915	1.18E+13	0.0373	5.44E+06	0.003938
Pu240	45.244	2.07E+11	0.0447	3.75E+08	0.227
Pu239	46.21	7.61E+11	0.0000721	1.66E+05	0.06203
Pu239	46.68	7.61E+11	0.0000465	1.07E+05	0.06203
Pu239	47.6	7.61E+11	0.0000625	1.43E+05	0.06203

Table 2.5: Plutonium gamma-ray lines in the 40-50 keV region.

tics. For a known energy resolution, peak intensity, background and spacing between the peak centroids, it is possible to determine how accurately peaks and their ratios can be measured based on statistical analysis [45]. This is the first step in determining the resolution needed to separate the two plutonium lines. This work will focus on separating the ^{242}Pu line from ^{240}Pu line as it is not yet practical to separate the ^{241}Pu line from the ^{242}Pu with the current generation of MMCs.

These two lines are separated by 329 eV, and the relative intensity is related to the concentration of the two isotopes by the function

$$\frac{N_{^{242}Pu}}{N_{^{240}Pu}} = \frac{C_{^{242}Pu} * a_{^{242}Pu}}{C_{^{240}Pu} * a_{^{240}Pu}} \tag{2.8}$$

where C is the fraction of each isotope and a is the branching ratio of the gamma-ray line. It is possible to develop an analytical expression for the expected uncertainty in counts in a peak based upon a few assumptions. The basic assumptions needed are: a flat background, Gaussian shaped peaks, least-squares fitting of the data, and a known separation between the peaks. Based on these assumptions it is possible to derive the standard deviation σ of the number of counts in each peak [33, 46, 45]. The resulting equation has the form:

$$\sigma_1^2 = AU + BI_1 + CI_2 \tag{2.9}$$

$$\sigma_2^2 = AU + BI_2 + CI_1 \tag{2.10}$$

where

$$A = \frac{2\sqrt{\pi}}{1 - b^2} \tag{2.11}$$

$$B = \frac{2(1 - 2b^{\frac{7}{3}} + b^{\frac{10}{3}})}{\sqrt{3}(1 - b^2)^2} \tag{2.12}$$

$$C = \frac{2(b^{\frac{4}{3}} - 2b^{\frac{7}{3}} + b^2)}{\sqrt{3}(1 - b^2)^2} \tag{2.13}$$

$$b = \exp\left(\frac{-(E_1 - E_2)^2}{4\sigma_{det}^2}\right) \tag{2.14}$$

In these equations, σ_{det} refers to the energy resolution of the detector. Using these equations, it is possible to determine how many counts in peaks N_1 and N_2 are required for a given detector resolution and intensity ratio to achieve a desired statistical uncertainty. This can be used to determine the detectability of ^{242}Pu in the presence of significant ^{240}Pu. In order to determine the resolution and total number of counts needed, it is necessary to choose a representative ^{242}Pu $/^{240}$Pu ratio so that the relative intensities can be determined. The isotopics for a PWR with 30 gigawatt-days per metric ton uranium of burn-up was chosen from table 2.1 as it is a common fuel type and a common level of burn-up. Using this intensity ratio it is possible to plot the relative error as a function of counts in the ^{242}Pu peak for a variety of energy resolutions. Figure 2.5 shows that there is negligible advantage to having a detector resolution that is better than 150 eV FWHM, as long as there is no background and no ^{240}Pu. An understanding of the full spectrum and the maximum counting rate is required in order to determine the required counting time and to decide whether higher energy resolution is needed to better discriminate from background.

In addition, it is important to quantify the effects of a finite spectral background due to Compton scattering in a realistic geometry. For this, the Monte Carlo particle transport code Geant4 was used to estimate the background [39, 40]. This code allows the user to define a detector geometry and then simulate the transport of particles from the source to the detector. Since the primary measurement for this work was done with a source inside the cryostat, the geometry only includes the source, the soft X-ray filter, and the 0.1K detector housing. This simplifies the analysis although is likely underestimated the background. The geometry used to model this setup is diagrammed in figure 2.6.

With the complete model, it is now possible to inspect the region of interest more closely. A plot of just the 40 keV region is shown in figure 2.7. This region has visible lines from ^{238}Pu, ^{239}Pu, ^{240}Pu, and ^{242}Pu above a constant Compton background. Assuming that in an optimized detector a count-rate of 100 Hz could be achieved, the axis on the left shows how many counts per pixel per day would be recorded in this region. At a count-rate of 355 counts per day in the ^{242}Pu peak it is, in theory, possible to quantify the ^{242}Pu concentration to 10 percent in roughly a single day and to 1 percent in 100 days with a single detector channel. This assumes that the source distance and strength can be optimized such that a count rate near the limit for MMC's can be achieved. The figure also shows what the spectrum would look like convolved with Gaussians of different width. The 1 keV spectrum corresponds roughly to the resolution of a typical coaxial HPGe detector. The 500 eV spectrum corresponds to the resolution of a planar HPGe detector designed for low energies. The 200 eV and 50 eV spectra show the upper limit at which quantification of ^{242}Pu is possible and what could be achieved with an optimized MMC operating in a dilution refrigerator.

The other region of interest that is often used for plutonium isotopics is the region around 100 keV. This region also contains lines from all of the major plutonium isotopes. This region is much

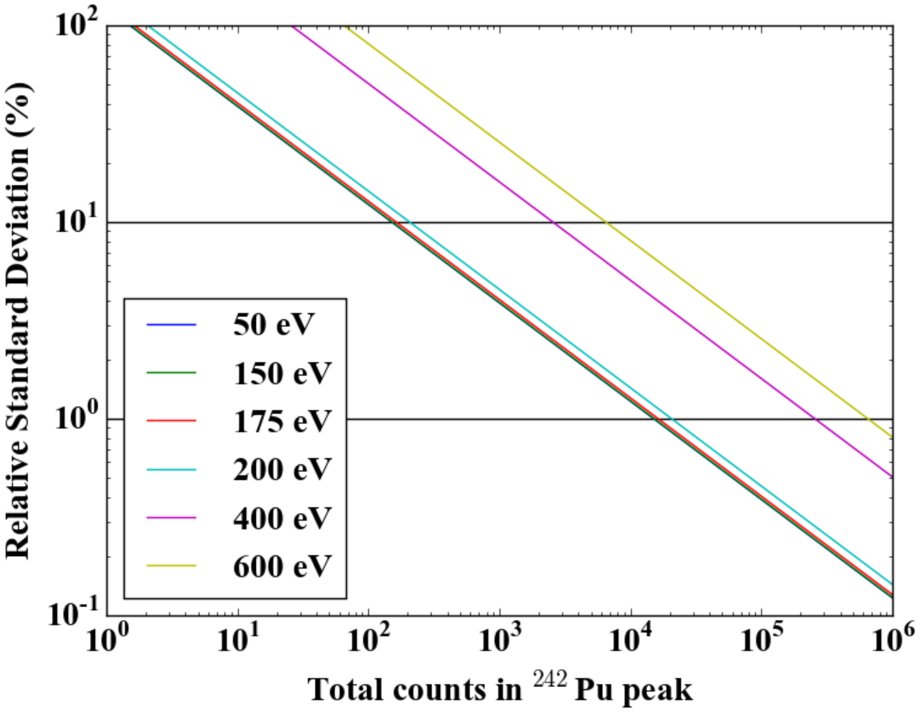

Figure 2.5: A comparison of the number of counts needed in the ^{242}Pu peak for different levels of quantification. This assumes a background rate that is 10% of the count-rate in the ^{242}Pu peak.

more challenging for the direct observation of ^{242}Pu as the line is a factor of 10 weaker. As the spectrum in figure 2.8 shows, in an idealized geometry it is still possible to observe this line. This is true in a zero-thickness plutonium sample with no plutonium self-fluorescence (ie. in an ion trap). In a thick sample the plutonium K_α X-ray fluorescence, also at 103.5 keV, will completely dominate the ^{242}Pu line.

The results of these simulations show that it should be possible to measure the ^{242}Pu line in a mixed isotope sample of plutonium with an MMC that has $<$ 200 eV FWHM energy resolution. There is one assumption that has been made so far that has not been discussed and that is that the purification of the plutonium from the americium is perfect and that no ^{241}Am in-growth has happened from the decay of ^{241}Pu. This assumption should not fundamentally preclude the measurement of ^{242}Pu in a real sample, but the count rate and added background from ^{241}Am will make the measurement more difficult. Chapters 7 and 8 will discuss this in more detail. The required quantification times for a single pixel are also not practical in a realistic scenario, but an array of 100's of pixels operating at 100 counts per second could quantify ^{242}Pu even in a small sample in a matter of hours [47].

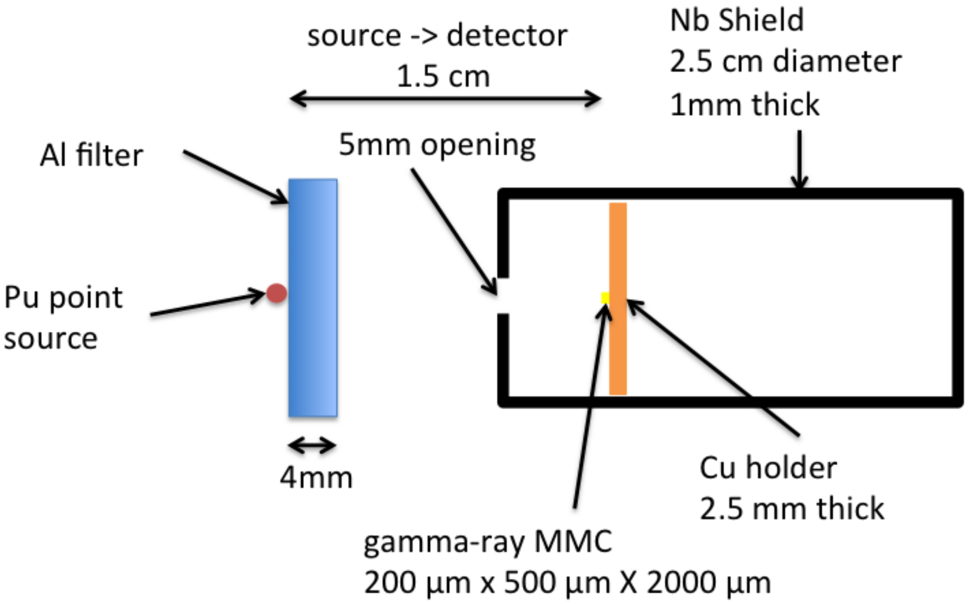

Figure 2.6: A diagram of the geometry used for the Geant4 simulations.

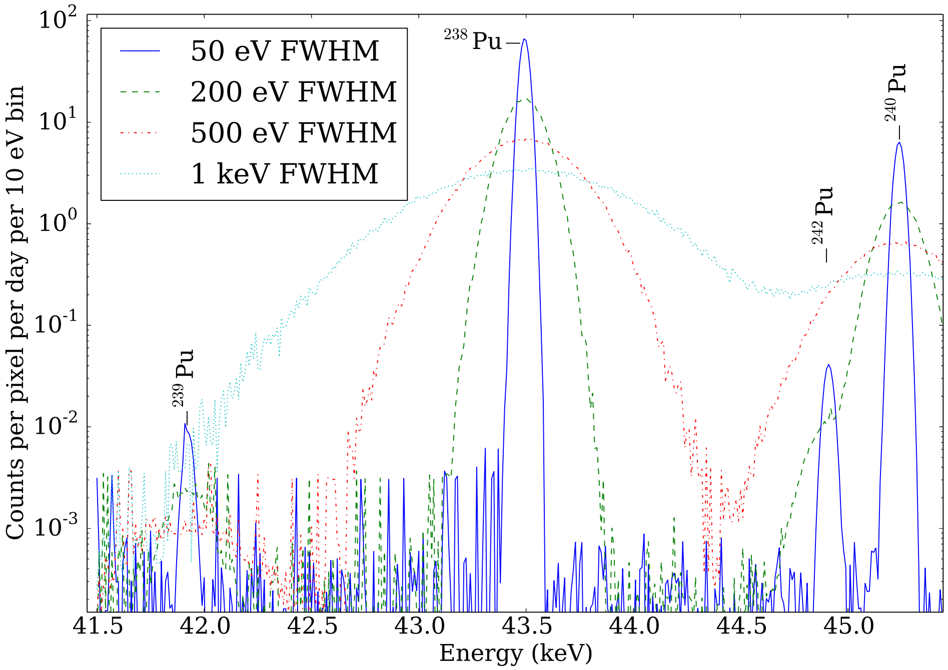

Figure 2.7: Geant4 simulation of the plutonium spectra in an MMC in the 40 keV region.

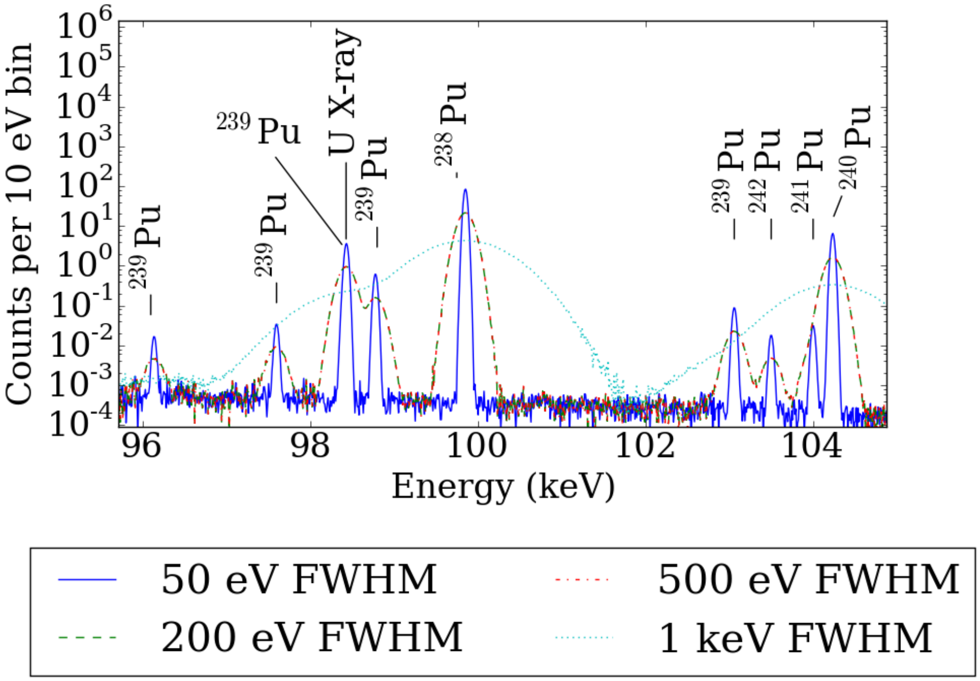

Figure 2.8: Geant4 simulation of the plutonium spectra in an MMC in the 100 keV region.

Chapter 3

MMC Theory

3.1 Calorimeter Fundamentals

This chapter discusses the physics underlying the function of MMCs. It covers the fundamental components that make up an MMC. This includes a discussion of the physics of paramagnetic systems, the selection of the host material for the paramagnetic ion, and the selection of the paramagnetic ion. In addition, it covers how gamma-ray interactions are converted into an electrical signal that can be digitized using a two-stage superconducting quantum interference device (SQUID) pre-amplifier.

The idea of cooling calorimeters to very low temperatures in order to improve their performance was first recognized in the 1930s [48]. Due to practical considerations such as cooling and low-noise amplification it was not until the 1980s that they were first proposed for use in practical experiments [49, 50, 51]. Spectroscopic calorimeters are based on the principal of measuring the change in the temperature of an absorber from photon or particle absorption. This change in temperature is defined by the relationship in eq. 3.1 where E is the energy of the particle and C is the heat capacity of the absorber.

$$\Delta T = \frac{E}{C} \tag{3.1}$$

A canonical calorimeter setup is shown in figure 3.1. In the setup, the absorber is directly connected to both a thermometer and to a cold bath via a weak thermal link. While the fundamental setup has remained the same, the absorber material and thermometer technology have changed based on the application and advancements in technology over the last 80 years. The three most prominent thermometer types that are currently used are: semiconductor thermistors (Si and neutron transmission doped Ge), superconducting transition edge sensors (TESs), and metallic magnetic calorimeters.

Semiconductor thermistors are the simplest type of cryogenic particle detector. These rely on a large change in resistivity, typically in doped silicon or neutron transmission doped germanium, for a small change in temperature [52]. These devices can be very precise, but in general have very long thermal time constants. Superconducting transition edge sensors leverage the large change in resistivity that occurs in superconductors at their critical temperature. These thermometers are significantly faster than semiconductor thermistors, especially with the implementation of electrothermal feedback [53]. While these thermometers are faster, they require good process control to produce large arrays with identical critical temperatures. In addition, the response function of pulse height as a function of deposited energy can be slightly non-linear and differs between devices and after thermal cycling. This makes building large arrays that can operate in automated fashion difficult [54].

Metallic Magnetic Calorimeters are the least mature of the three micro-calorimeter technologies currently being developed, but they have several key advantages. MMCs rely on the Curie-like behavior of a paramagnet in a weak magnetic field, i.e. that the magnetization of the paramagnet varies inversely proportional to T. In order to measure this change in magnetization it is necessary to apply a weak field and measure the change in the local field strength due to the change in magnetization. This can be done inductively using an appropriately coupled pickup loop and amplifier.

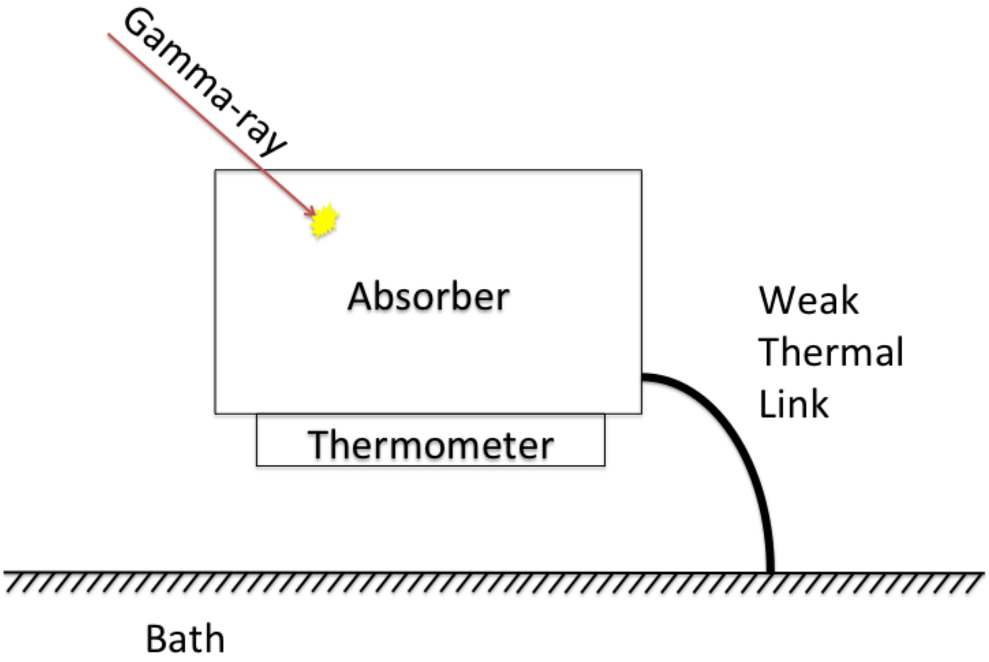

Figure 3.1: A canonical micro-calorimeter composed of an absorber, a thermometer and a weak thermal link.

In this way, a small change in temperature can be measured with a sensitive field-sensor, such as a SQUID. One of the primary advantages of MMCs is that as a result of the Curie-like behavior the response function is expected to be highly linear. This means that it is not necessary to operate the device at a specific transition temperature and that summing spectra from multiple pixels and cooldowns is straightforward.

One other advantage MMCs have over other cryogenic detector technologies is that their thermal system can be constructed entirely of normal metal conductors. This means that signal rise times can be much faster than in other micro-calorimeters, with comparable heat capacity. Ideally, this allows these devices to count at higher rates than have been possible with other technologies, but this has yet to be demonstrated in practice. Prior to the development of metallic magnetic calorimeters, paramagnetic calorimeters were used for cryogenic particle detection but semiconductors as a host material [55, 56, 57]. This limited the count rate that was possible due to the very slow spin-phonon coupling in semiconductors at cryogenic temperatures.

MMCs

Like all micro-calorimeters, MMCs consist of an absorber connected to a thermometer by a thermometer and a weak thermal link. The diagram in figure 3.2 shows a notional concept of the basic

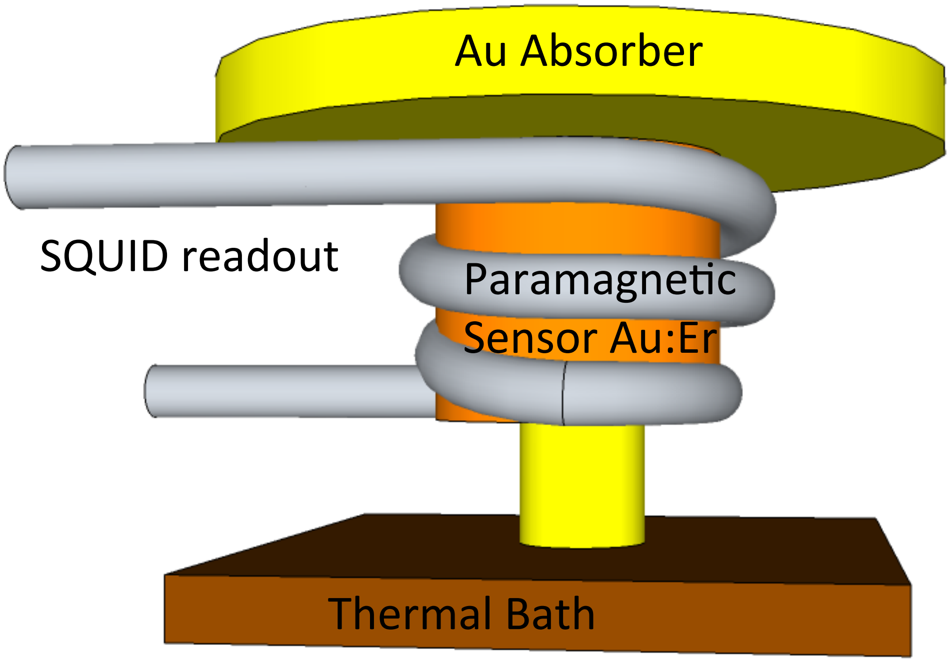

Figure 3.2: A conceptual sketch of the basic MMC components.

components of an MMC. The thermometer relies on the Zeeman splitting of electronic states in the paramagnet caused by applying a magnetic field of several milli-Tesla. This Zeeman splitting is on the order of four micro-electronvolts for the MMC used in this work. The two different states have different spin orientations. The relative population of these two states determines what the susceptibility of the paramagnet is. This relative population is a function of the temperature of the absorber. This makes it a very sensitive thermometer, as there is a large change in the relative population of these two states for a small change in temperature due to their small separation. In order to measure this change in susceptibility it is necessary to add a precise magnetic field pickup loop. In most designs in use today, including the one used in this dissertation, the same wire that is used to apply the magnetic field is used as the pickup loop. This pickup loop is inductively coupled to a two-stage SQUID amplifier the output of which is then digitized at room temperature.

The practical implementation of this design is typically done using micro-fabrication. This requires making trade-offs between the optimum magnetic coupling and complexity of micro-fabrication. The MMC used in this dissertation is based on a meander design diagrammed in figure 3.3. This design makes it possible to micro-fabricate all of the components of the MMC. In order to operate this MMC, the device is first cooled to < 50 mK, then up to 100 mA of current is frozen in the meander loop using a micro-fabricated persistent current switch. When an energetic particle hits one of the two absorbers the change in temperature causes a change in magnetization, which causes an AC current to be induced in the wire, which then flows to the input coil that is

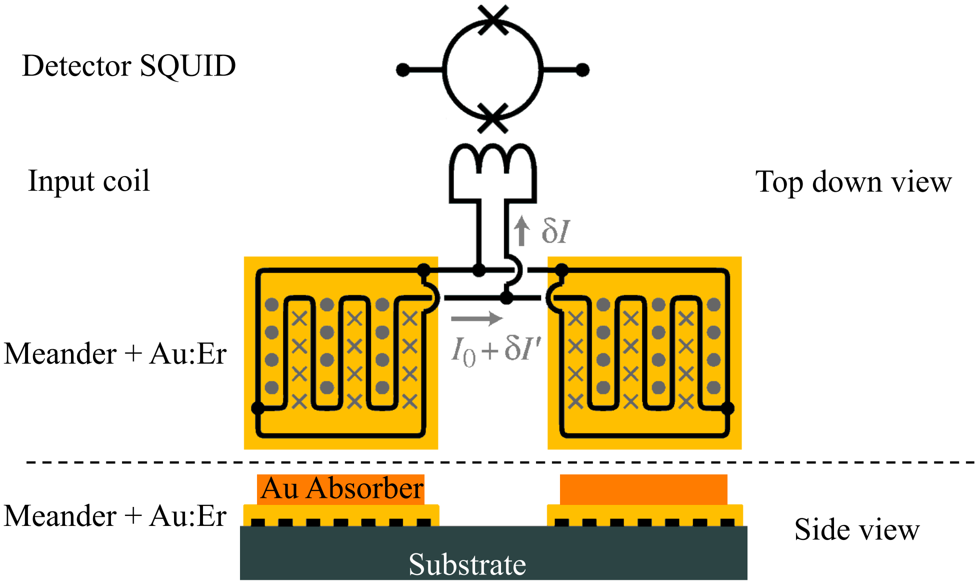

Figure 3.3: A diagram of the meander MMC geometry used in this work. Adapted from [58].

inductively coupled to the SQUID.

3.2 Selection of Host Material

Paramagnetic systems have been used for accurate thermometry for many decades in low temperature systems, as their magnetization can be ideally described as a function of temperature and fundamental constants along with material properties that can be well measured. The first magnetic micro-calorimeters used a dielectric paramagnet as a thermometer [55, 56, 57] based on this idea. These had slow intrinsic signal rise times of several milliseconds which limited their countrate [55]. In order to make the devices more practical, a group led by George Seidel proposed the use of paramagnetic ions in a metallic host [59]. Initial testing with handmade devices showed a resolution of 3.4 eV at 5.9 keV and 340 eV at 122 keV [22, 60]. Several different metallic host materials have been tried in the past including palladium, silver and gold [61, 62]. Eventually, erbium doped gold was determined to be the best choice by researchers at the University of Heidelberg. Devices in this dissertation were based on their fabrication process and therefore use the same combination of host and paramagnetic ion. Gold makes a good host material for many paramagnetic ions because these ions can exist in concentrations up to a few thousand ppm without forming separate inclusions [63].

3.3 Selection of Paramagnetic Ion

With the selection of Au as a host material, the next step is to choose a suitable paramagnetic ion. One of the disadvantages of choosing a metal with high electrical and therefore high thermal conductivity is a high free electron density in the conduction band. When a paramagnetic ion is placed into this environment, there is a significant amount of coupling that occurs between the conduction electrons and the spin of the paramagnetic ions' electrons. This coupling is known as the Ruderman-Kittel-Kasuya-Yosida (RKKY) interaction and it degrades the signal size and increases the effective heat capacity of the spin system, both of which degrade the energy resolution. It is therefore necessary to choose an ion with a small RKKY interaction. The best candidates are rare earth metals with vacancies in the 4f band [63, 64]. There is one additional criterion which goes into choosing which specific ion is best suited: nuclear spin. Nuclear spin is important because if one of the naturally occurring isotopes of the chosen ion has a non-zero spin, it will lead to hyperfine splitting of the spin states in the paramagnetic system. This will cause a similar reduction in magnetization change and increase in heat capacity. The paramagnetic ion that has been found to best meet these criteria is $^{3+}$Er. There is one downside to this choice which is that one of the naturally occurring isotopes, ^{167}Er, has a nuclear spin of $7/2^{+}$ [65]. This leads to the above mentioned hyperfine splitting. In order to minimize this effect it is necessary to enrich the Er in either ^{166}Er or ^{168}Er, which have a spin-parity of 0^{+}. The sensors used in this dissertation were produced using a Au:Er target enriched in ^{168}Er.

3.4 Absorber Selection

Micro-calorimeters have used a wide variety of absorber materials depending on the application. These include: semi-conductors, normal metals and superconductors. All three categories are potential absorbers for use in MMCs. The primary considerations are heat capacity per unit volume, atomic number and density, and ease of micro-fabrication. Common semiconductors that could be candidates include HgCdTe and Si, both have very small volumetric heat capacity and HgCdTe has relatively high Z. Neither of these can be easily micro-fabricated on top of the Au:Er sensor limiting their use for MMC arrays. Superconductors can provide the mix of small heat capacity per volume and high Z that is desirable. The lower thermal conductivity of superconductors could cause the response to have position dependence, which may be undesirable [66]. Finally, metals can have high Z and are the easiest to micro-fabricate. They have the downside that they have relatively high heat capacitance per volume limiting the absorber size. This is less of an issue at typical MMC operating temperatures of 15-40 mK where even metals have relatively small heat capacitance for volumes of < 1 mm^3. For scaling to large arrays uniform fabrication is the most important property, because of this metals were selected by researchers at the University of Heidelberg as the absorber material of choice for the hard X-ray MMCs used in this work.

After the basic choice of a metal is made, it is necessary to consider fabrication limitations as well as stopping power in the energy regime of interest. For large gamma-ray absorbers, the most common method of micro-fabrication for metallic magnetic calorimeters is electroplating. In order to get the best MMC performance, a short rise time is desirable. The reason for this will be discussed later in this chapter. In order to minimize the rise time, it is necessary to have a very pure deposition process such that the final absorber has a high purity. This further limits the options for absorbers to copper, gold, nickel, palladium, rhodium, tin, and silver [67]. Of these the best choice is gold due to its high Z, lack of magnetism, and high heat conductivity at low temperatures. The process of electroplating will be discussed in more detail in the fabrication section.

3.5 Superconducting Quantum Interference Devices

The other critical component needed to measure signals from MMCs is an amplifier based on a SQUID. These devices leverage unique properties of superconductors to amplify small changes in current or magnetic field with very low noise. These amplifiers are the most sensitive method of measuring changes in magnetic fields, so they are the best choice of amplifier for MMCs. This section will discuss the basic properties of SQUIDs and their operating principles as well as the characteristics of 2-stage SQUIDs used for measurements in this work.

Macroscopic wave functions in superconductors

Type I superconductors have the unique property that their electrons form Cooper pairs when they go through the transition from normal to superconducting [68]. These Cooper pairs condense to form a macroscopic wave function that can be described by:

$$\Psi = \Psi_0 e^{i\phi(\mathbf{r})} \tag{3.2}$$

Where Ψ^2 is equal to the Cooper pair density and $\phi(\mathbf{r})$ is the phase of the wave function. The superconducting wave function must always be single values in in a ring-like structure; this leads to quantization of the magnetic flux. When integrating over a closed path around a ring-like structure in order to determine the possible magnetic flux within the closed path, one finds that it obeys the following equation:

$$\Phi = n\frac{h}{2e} \tag{3.3}$$

In this equation h is Planck's constant, e is the elementary charge, and n is the wavenumber. This result implies that the magnetic flux within the loop must be an integer multiple of $h/2e$. This value is known as a magnetic flux quantum or ϕ_0. This unique property means that changes in the external field of $< h/2e$ are compensated by a supercurrent in the ring such that the flux inside the ring remains constant. This is the first of the two primary building blocks that make up a SQUID.

Josephson Junctions

The second fundamental building block of a SQUID is a Josephson junction. A simple Josephson junction consists of two superconductors separated by a thin insulating barrier. This barrier is thin

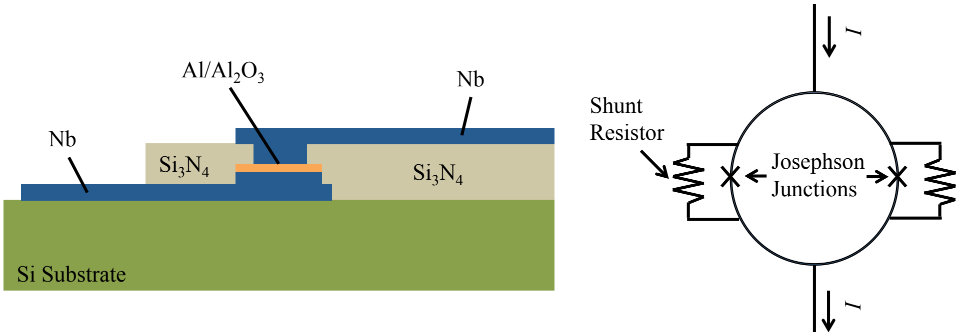

Figure 3.4: (left) Cross section of a common Josephson Junction design. (right) A diagram of a resistively shunted SQUID.

enough that it is possible for Cooper pairs to tunnel through it. This means that for small applied currents it is possible to have no voltage drop across the insulator. This ability to drive current across an insulator with no voltage drop is known as the DC Josephson effect. This effect has a limiting critical current density j_c that is a function of the tunneling conductance G_n, junction area A, and superconducting energy gap $\Delta(T)$ defined by the following equation [68]:

$$j_c = \frac{G_n}{A}\left(\frac{\pi\Delta(T)}{2e}\right)\tanh\frac{\Delta(T)}{2k_BT} \tag{3.4}$$

DC SQUIDs

These two fundamental building blocks can be combined along with resistive shunts across the Josephson contacts to create a DC SQUID in the manner shown in figure 3.4. Due to the fact that is has two Josephson contacts in parallel, the voltage becomes finite at applied currents I just above twice the critical current $I_c = j_c \cdot A$ of a single junction, assuming there is no external field. If the device is DC-biased at a current just above twice the critical current, a small increase in the external magnetic flux applied to the loop ($< \phi_0$) will change the voltage across the junction. A diagram depicting measurements of this effect can be seen in figure 3.5. One important feature of this diagram is that the voltage change as a function of flux is only linear near ($\phi = (n/2+1/4)\phi_0$). This effect can be used to convert a very small change in magnetic flux into a voltage.

The basic readout for a SQUID uses what is known as a lock-in type measurement [69]. This uses a feedback coil to supply a dc and a modulating flux. This modulating flux is of order 1/4Φ_0 and is used as a reference for the amplifier. The downside of this type of measurement is that it only has an effective bandwidth of roughly 10 kHz [70]. Signal rise times of MMCs are on the order of a few microseconds and therefore a significantly larger bandwidth would be desirable.

Reading out a single SQUID directly with room temperature electronics is not optimal because the voltage noise of the room temperature amplifier degrades the performance. The most common method of overcoming these problems is to arrange several SQUIDS in series. This gives the output a much larger voltage swing, making it easier to measure with room temperature electronics. In

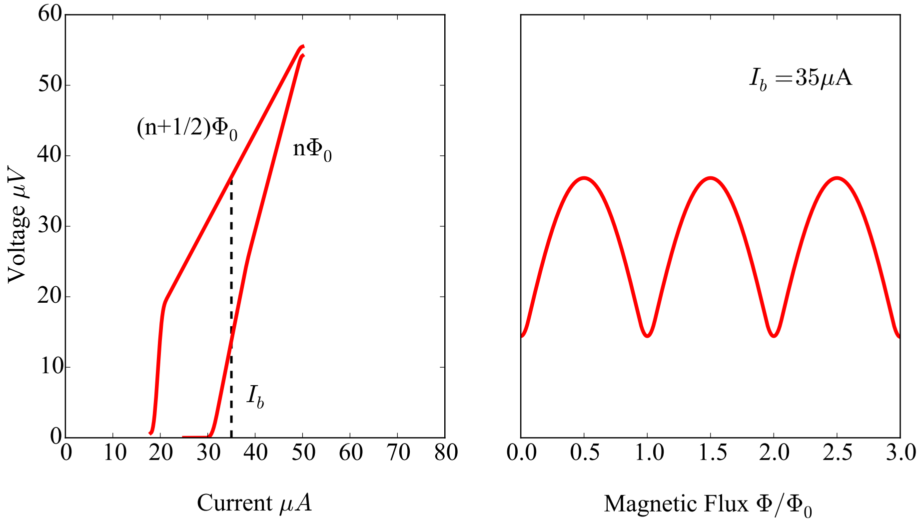

Figure 3.5: The current vs. voltage and flux vs. voltage characteristics for a DC SQUID.

addition, it also improves the signal to noise ratio in comparison to a single SQUID, because the signal increases linearly with the number of SQUIDs in series but the white noise increases as the square root of the number of SQUIDs [71]. A single array SQUID, while it can be more simply operated with room temperature electronics, is also not suitable for direct readout of MMCs as the input inductance of an array is much too large for good impedance matching with the MMC pickup loop.

The ideal readout for an MMC requires a bandwidth of close to a MHz and an input inductance of < 50 nH. This is made possible by a two-stage SQUID readout, which uses a second series array of SQUIDs to improve the bandwidth and further amplify the signal so that the limiting noise is the input SQUID noise and not the room temperature electronics [71]. A diagram showing the typical wiring for a two-stage SQUID setup used at LLNL is shown in figure 3.6. This SQUID is operated in a flux locked loop (FLL) but in a different manner than the lock-in design. With this wiring, a constant flux is maintained in the input SQUID and changes in flux at the input result in a transient current in the array SQUID pickup. The output of the array SQUID is then further amplified and integrated at room temperature. This integrated signal is connected through a resistor to the feedback in the input SQUID which cancels out the input flux. It is also possible to integrate the two-stages into a single integrated circuit, but the power dissipation in the array SQUID is often difficult to manage on the experimental platform. A two-stage SQUID setup of this type along with Magnicon FLL electronics was used for all measurements in this work.

3.6 Energy Resolution in MMCs

The energy resolution of an MMC is ideally limited only by the thermal noise in the system. In practice, additional sources of noise also contribute. In this section, the thermal noise of the MMC

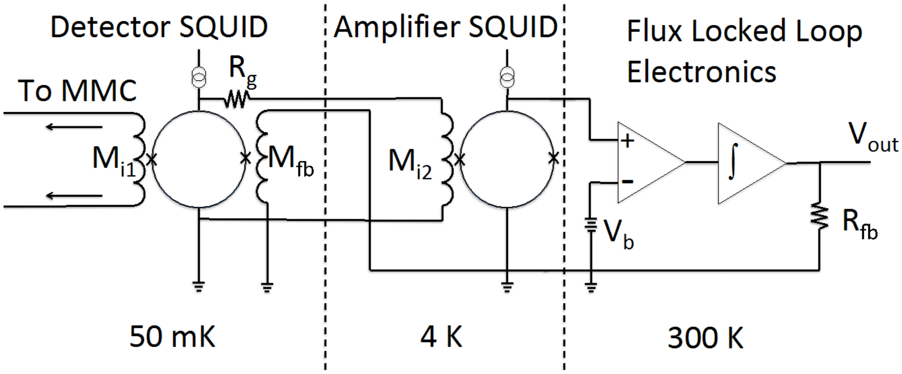

Figure 3.6: A diagram of a typical two-stage SQUID setup used in the cryostats at LLNL.

system is derived and a model of the total noise that includes the thermal noise as well as additional noise terms that are known to contribute to the detectors performance is discussed. Finally, this model will be used along with the known parameters of the MMC used for measurements in this work to estimate the expected performance of the device in the cryostat at LLNL.

Calculation of thermal noise in MMCs

Fundamental limit to energy resolution

In any system at a non-zero temperature with a thermal connection to a bath at constant temperature exhibits fluctuations in the energy content of the system due to random energy exchange with the thermal bath. These fluctuations have a standard deviation of the form

$$\sigma_E = \sqrt{k_B C T^2}, \tag{3.5}$$

where C is the heat capacity of the system, k_B is Boltzmann's constant, and T is the temperature in Kelvin. The weak thermal link between the system and the bath limits the frequency spectrum of these fluctuations. The time constant of the weak thermal link is defined by the heat capacitance of the system divided by the thermal conductance to the bath $\tau = C/G$. This implies a frequency spectrum with a single-pole roll off at $f_c = G/(2\pi C)$. In the simplest model of an interaction within the calorimeter, the energy deposition and absorber equilibration is instantaneous and the temperature will then return to the mean value with the same time constant as the noise. The time dependence of the change in calorimeter temperature after energy is deposited has the form

$$T(t, t > 0) = \frac{E}{C} e^{-t/\tau} \tag{3.6}$$

Equation 3.6 has the same frequency dependence as the noise. This means that the signal-to-noise ratio will theoretically be the same for all frequency bins. If this is the case and the noise in different bins is uncorrelated, the energy of the signal can be determined by averaging the amplitude over an arbitrary bandwidth and comparing it to the average amplitude of the background.

In this idealized model, the signal to noise ratio will improve as the square root of the bandwidth averaged over. This implies that it is possible to achieve any desired precision just by averaging over the corresponding amount of bandwidth [72].

In reality of course there are many limitations that prevent infinitely high accuracy. These come in two broad categories: effects that cause the signal to fall faster than $1/f$ or effects that cause the noise to fall slower than $1/f$. An example of the first category includes finite signal rise time, which adds a pole to the signal power spectrum and causes it to drop off at the rate of $1/f^2$ above the characteristics frequency of the rise time. The second category is comprised of effects including but not limited to amplifier, magnetic Johnson and Erbium $1/f$ noise. These effects can include both constant and frequency dependent components. All of these limit the bandwidth over which one can average the signal to improving the signal to noise ratio, and therefore cause the energy resolution of thermal detectors to be finite.

Thermal noise in a two component system

The fundamental limitations of measuring changes in temperature of a thermal system are important to understand when developing micro-calorimeters, but more complex and realistic models are needed to be able to understand the behavior of real systems. For an MMC the thermal system has two distinct components: an electronic component and a spin component. The electronic system C_e consists of free electrons in the gold absorber and gold host material while the spin system C_z consists of the Er spins in the sensor. These two systems are coupled together with a time constant for the energy transfer, which is on the order of 100 ns [63]. These two systems and the bath are coupled by two connections in the manner described in figure 3.7. The first is the connection between the electron and spin system modeled as a resistive component G_{ze} and a noise source P_{ze}. The second in the thermal connection between the electron system and the bath, also modeled as a parallel resistive component G_{eb} and a noise source P_{eb}. Using this model, it is possible to derive the noise and the fundamental thermal limit to the energy resolution in this system. This derivation follows the derivation in *Cryogenic Particle Detection*[63] with some adjustments for clarity. The energy content of the two systems can be described using the following two differential equations:

$$\dot{E}_z = C_z\dot{T}_z = -(T_z - T_e)G_{ze} + P_{ze} \tag{3.7}$$

$$\dot{E}_e = C_e\dot{T}_e = -(T_e - T_z)G_{ze} - (T_e - T_0)G_{eb} - P_{ze} + P_{eb} \tag{3.8}$$

This system of differential equations can be converted into the frequency domain using formalisms developed for circuit analysis [72]. The power spectrum of the resulting conversion is given by [63]:

$$S_E(f) = k_b C_z T^2 \left(\alpha_0 \frac{4\tau_0}{1+(2\pi f\tau_0)^2} + \alpha_1 \frac{4\tau_1}{1+(2\pi f\tau_1)^2}\right) \tag{3.9}$$

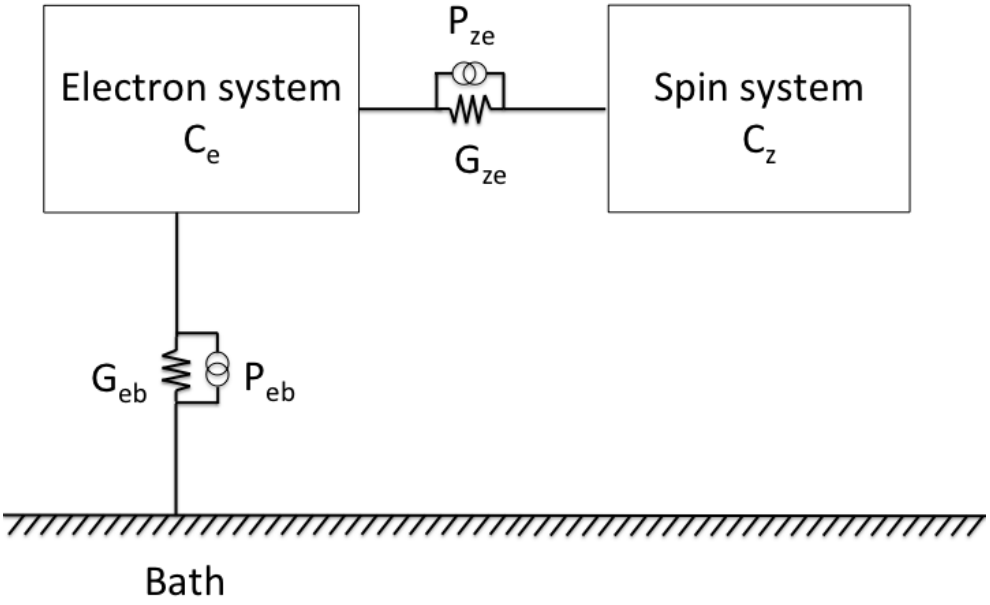

Figure 3.7: A simple thermodynamic model describing the electron and spin systems in an MMC.

The two time constants τ_0 and τ_1 have been determined by solving for the characteristic polynomial of the differential equations 3.7 and 3.8. The three parameters of the second order polynomial of the form $ax^2 + bx + c$ are:

$$a = G_{ze}G_{eb} \tag{3.10}$$

$$b = C_eG_{ze} + C_z(G_{ze} + G_{eb}) \tag{3.11}$$

$$c = C_zC_e \tag{3.12}$$

The time constants are the roots of this polynomial and can be described by the following equation:

$$\begin{aligned}\tau_{0/1} = \frac{1}{2G_{ze}G_{eb}}\Big(&C_eG_{ze} + C_z(G_{ze} + G_{eb}) \\ &\pm \sqrt{C_eG_{ze} + C_z(G_{ze} + G_{eb})^2 - 4G_{ze}G_{eb}C_zC_e}\Big)\end{aligned} \tag{3.13}$$

The two additional undefined parameters α_0 and α_1 in equation 3.9 are also in their most complete form complex functions of the polynomial parameters, but can be simplified for situations of relevance where $\tau_0 << \tau_1$ and $C_e \approx C_z$. Under these conditions, the following relations can define the two parameters:

$$\alpha_0 = \beta \tag{3.14}$$

$$\alpha_1 = 1 - \beta \tag{3.15}$$

where:

$$\beta = \frac{C_z}{C_e + C_z} \tag{3.16}$$

To convert a power spectrum to an energy resolution, it is helpful to use the concept of noise equivalent power (NEP). The NEP is the input power that is equal to the noise power at that frequency. This can be calculated using the power spectrum $S_e(f)$ of the noise and the responsivity $\tilde{p}$ of the device with the following equation:

$$\text{NEP}(f) = \frac{\langle |S_e(f)|^2 \rangle}{\tilde{p}} \tag{3.17}$$

In order to calculate the responsivity of the detector, we have to consider both electron and spin systems. In the time domain the response of this system to an instantaneous deposition of energy into the device has the form:

$$\tilde{p}(t > 0) \approx \beta(e^{-t/\tau_1} - e^{-t/\tau_0}) \tag{3.18}$$

This can be represented in the frequency domain as:

$$\tilde{p}(f) \approx \frac{\beta\tau_1}{\sqrt{(1 + (2\pi f\tau_0)^2)(1 + (2\pi f\tau_1)^2)}} \tag{3.19}$$

This equation also assumes that $\tau_1 >> \tau_0$ in order to neglect the τ_0 component of the numerator. This equation can be combined with equations 3.9 and 3.17 to calculate the NEP. The result of this equation can be written as a function of frequency of the following form:

$$\text{NEP}^2(f) = \text{NEP}_0(1 + (f/f_{eff})^2) \tag{3.20}$$

By manipulating equations 3.19 and 3.9 it is possible to arrive at the following terms for NEP_0^2 and f_{eff}.

$$\text{NEP}_0^2 = 4k_bT^2G_{eb}(1 + \frac{G_{eb}}{G_{ze}}) \tag{3.21}$$

$$f_{eff} = \frac{1}{2\pi C_e}\sqrt{G_{ze}G_{eb}\left(1 + \frac{G_{eb}}{G_{ze}}\right)} \tag{3.22}$$

Having derived a function for the NEP^2, it is possible to calculate the energy resolution. Under the assumption that optimum Wiener filtering is being used, the energy resolution is related to $\text{NEP}(f)$ using the following equation [72]:

$$\Delta E_{rms} = \left(\int_0^\infty \frac{4df}{\text{NEP}^2}\right)^{-1/2} \tag{3.23}$$

Parameter	Value
τ_0	3 μs
τ_1	1.5 ms
C_e	13.51 nJ/K^2
β	0.5
T	35 mK

Table 3.1: Parameters used to calculate thermal fluctuations.

Inserting the function for NEP^2 into this equation, it is possible arrive at the following solution:

$$\Delta E_{rms} = \sqrt{4k_b C_e T^2}\left(\frac{G_{eb}}{G_{ze}} + \left(\frac{G_{eb}}{G_{ze}}\right)^2\right)^{1/4} \tag{3.24}$$

While this equation is an interesting fundamental description of the energy resolution of an MMC that is only limited by thermal noise, it is not in terms of any observable physical parameters. It can be rewritten as a function of the ratio of the two fundamental time constants of the system τ_0 and τ_1. The resulting equation is:

$$\Delta E_{rms} = \sqrt{4k_b C_e T^2}\left(\frac{\tau_0}{\tau_1\beta(1-\beta)}\right)^{1/4} \tag{3.25}$$

Using this formula with the known physical parameters of the device used for this work, it is possible to calculate the temperature dependent thermal fluctuations of the ideal thermal system. Using the parameters in table 3.1, it is possible to calculate the energy resolution limited only by thermal fluctuations of 25 eV FWHM. The heat capacitance of the gold absorber was calculated using the molar heat capacitance and molar volume of gold from *Matter and Methods at Low Temperatures* [73] along with the known dimensions of the absorber (200 μm x 500 μm x 2000 μm). This shows that even if the temperature of the magnetic thermometer could be measured perfectly and the readout system had infinite bandwidth the resolution would still be limited. The following section will discuss a more realistic case that includes all the well-understood sources of noise and the limits in ability to measure the energy of the spin system.

3.7 A More Realistic Model of an MMC

After gaining an understanding of the fundamental limits of noise for simple calorimeters and the more complex two-body system in an MMC, it necessary to develop a more realistic model of the signal and the noise in the device. This model needs to take into account the thermal noise previously calculated, SQUID readout noise, Johnson noise in the sensor and the absorber, and how effectively the change in magnetization of the spins can be coupled to the input of the SQUID pre-amplifier. In addition to these relatively well-understood phenomena, it is typically necessary to add an additional frequency dependent term to describe low frequency noise in the MMC. This noise is generally ascribed to Erbium spin-spin interactions but in practice it is an experimentally derived term to match the observed excess noise at low frequencies.

In order to develop this model it is necessary to know the specifics of the MMC design being used. The most common type of MMC in use today uses a meander-type geometry, which is the type of device that the hard X-ray MMC developed by the University of Heidelberg that is used in this work is based on. In this geometry a superconducting meander is micro-fabricated on a Si substrate and a Au:Er paramagnet is then sputtered on top of the meander with only a thin layer of insulation in between. The meander acts as both the field coil to apply the magnetic field, which gives rise to the Zeeman splitting in the paramagnet, and the pickup loop to detect changes in the magnetic field. The current for the magnetic field is frozen into the meander prior to operation using a micro-fabricated persistent current switch.

noise in SQUIDs

For practical MMC measurements, SQUID noise is often the dominating noise term. As was discussed previously in this chapter, in a two-stage SQUID amplifier the noise in the first stage SQUID dominates all other electronic noise sources. There are two primary components to SQUID noise. One is independent of frequency or white-noise and the other is a $1/f$-type noise that increases at low frequencies. These two noise terms can be described by the following equation:

$$S_{SQUID} = S_{SQUID}^{white} + S_{SQUID}^{1/f}\frac{1}{f^n} \tag{3.26}$$

The Johnson noise of the shunt resistors dominates the SQUID white noise. The exponent n of the $1/f$ noise is typically between 0.8 and 1.4 [74]. This exponent is assumed to be 1.0 for all calculations in this dissertation. There is no clear physical understanding of what the source of this noise is, but it is theorized to be due to properties of the surface of the SQUID loop [74].

Magnetic Johnson Noise

In any system with free electrons in a normal conducting metal at non-zero temperatures there will be some thermal motion of the electrons. This thermal motion of electrons creates small fluctuating currents, which create magnetic fields, which contribute a white noise component to the magnetic flux noise. This noise is an inherent part of all MMCs due to their metallic sensor and absorber. Previous groups have calculated this effect for a meander geometry [75]. The resulting contribution to the flux noise has the form:

$$S_{\Phi,J} = \frac{2.376}{4\pi}\mu_0^2 k_b T \sigma A p (e^{-2\pi d/p} - e^{-2\pi(d+h)/p}) \tag{3.27}$$

The magnitude of this noise is a function of the area of the sensor A, the pitch of the meanders p the thickness of the Au:Er sensor d and the thickness of the absorber h. For the geometries of the MMCs used in this dissertation this noise is typically significantly smaller than the SQUID white noise. This means that it does not contribute significantly to the total energy resolution.

Erbium Ion Noise

One additional source of noise that has been observed in all MMC devices is a low-frequency noise of initially unknown origin. The known attributes of this noise are that it has a 1/f type frequency dependence, that the magnitude is independent of temperature between 30 mK and 4.2 K, and that the magnitude appears to be linearly proportional to the erbium concentration [66]. This noise is attributed to long lived magnetic states that have lifetimes of seconds. The functional form of this noise as a component of the magnetic flux noise has the form [66]:

$$S_{\Phi,Er}(f) = \mu_0^2 x \frac{N_A}{V_{mol}} G \frac{0.1\mu_B^2}{f^\eta} \tag{3.28}$$

In this equation x is the erbium concentration, 800 ppm for the design in this work, N_A is Avogadro's number and V_{mol} is the molar volume of gold $(1.02 \times 10^{-5}$ m^3/mol) and μ_B is the Bohr Magneton. The other two factors are G, which is a geometry dependent factor that will be described in more detail in the following section, and η, which is a fit parameter of the frequency dependence of the noise.

Signal Generation in a Meander

In order to determine the signal size that will be measured in the SQUID it is necessary to determine the frequency domain response of the absorber to the absorption on an energetic particle, the change in magnetization per change in temperature, the coupling of the magnetization change to the meander pickup coil, and finally the coupling from the pickup coil into the SQUID. The derivation of these functions for the meander geometry is well-understood [63]. This section gives an overview of each of these factors and discusses how the associated equations are used, along with simulations of the geometry, to calculate the expected flux in the SQUID for a given energy deposition.

Assuming the spins are non-interacting, which is known to be a valid approximation up to at least 1000 ppm [63], it is possible to simply calculate the change in the population of the two energy levels to determine the change in magnetization. For S=1/2 spins, the Zeeman splitting is of the form $E_Z = g\mu_B B$. The number of spins that change levels can be directly calculated by dividing the fraction of the energy of the incident particle that is deposited in the spin system by the energy difference of the two states. The energy difference is assumed to be the energy required to excite one spin into the higher level state. From the change in the number of spins δN in each state, the change in magnetization δm can be calculated using the following formula $\delta m = \delta N g \mu_B$. Combining this with the formula for calculating the number of spins $\delta N = \delta E / E_Z$ and the formula for E_Z, the change in magnetization reduces to $\delta m = \delta E / B$. This simple estimate is valid under the assumption that the magnetic field is constant in the volume of the Au:Er sensor and that 100 percent of the energy is transferred to the spin system. A discussion of magnetization and coupling in a more realistic system follows.

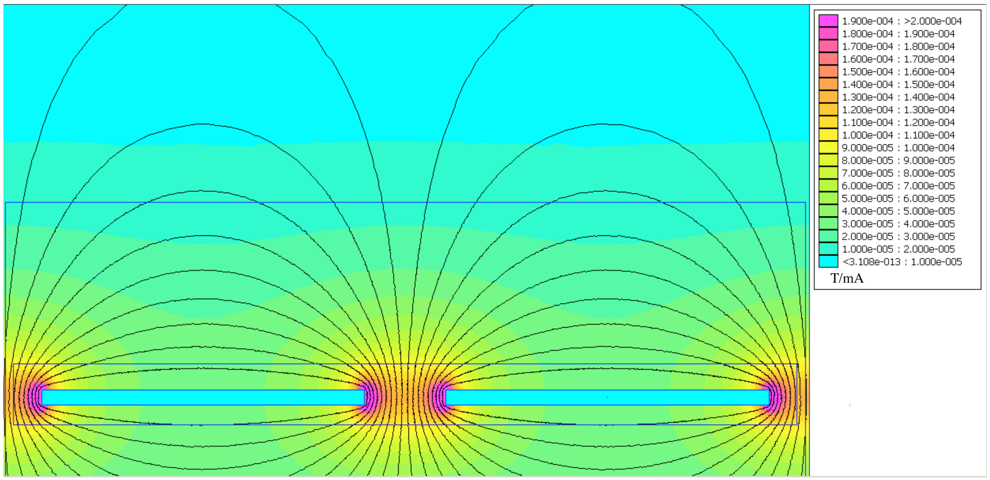

Figure 3.8: Magnetic field simulation used for the calculation of the field in a meander geometry MMC.

In order to calculate the change in magnetization for a realistic meander geometry, it is necessary to numerically integrate over the volume of the sensor due to the non-uniform magnetic field. The change in magnetization for a particular point can be described by the equation:

$$\delta M(\mathbf{r}) = \frac{\delta M(B(\mathbf{r}))}{\delta T}\frac{\delta E}{C_{tot}} \tag{3.29}$$

To determine the flux at a given point in the meander geometry, it is necessary to model the magnetic field. There are several ways to perform this calculation. For this dissertation a freely available finite element magnetics software, FEMM [76], was used due to the complex structure of the detector. While it would be desirable to do a 3-D calculation of the magnetic field from the entire meander, this is very challenging from a computational point of view. In addition, for a typical 2 mm x 0.5 mm hard X-ray pixel with a 10μm meander pitch p, the effects at the fringes are negligible. It is therefore possible to perform a simple 2-D model with reflecting boundary conditions on the two sides. A model of this sort is shown in figure 3.8. This figure also shows the calculated magnetic fields with 1 mA of current. From these magnetic field values it is possible to calculate the magnetization in each voxel and the coupling of the associated change in magnetization to the pickup coil. The change of flux in the pickup coil can be expressed as:

$$d(\delta\Phi) = \mu_0 \frac{G(\mathbf{r})}{p}\delta M(\mathbf{r}) d^3 r \tag{3.30}$$

This calculation includes the dimensionless geometry factor $G(\mathbf{r})$ that is a measure of the coupling of the magnetization change to the pickup coil as a function of the field B, the pitch p, and the field current I_f. This factor has been derived to have the following form [77]:

$$G(\mathbf{r}) = \frac{B(\mathbf{r})p}{I_f \mu_0} \tag{3.31}$$

In addition to integrating the change in flux per change in temperature by combining the above equations, it is also necessary to compute the total heat capacity. The total heat capacity is the sum of the heat capacity of electron system C_e and the heat capacity of the spin system. The heat capacity of the spin system is a function of the magnetic field because the heat capacity is due to the Zeeman splitting. This means the heat capacity of the sensor must be integrated over the volume as well. The equation for the total heat capacity is:

$$C_{tot} = C_e + \int_{V_s} c_z(B(\mathbf{r}))d^3r \tag{3.32}$$

The volumetric heat capacity has been measured as a function of magnetic field and erbium concentration has been calculated numerically and shown to match measured values [78].

The complete equation to compute the change in flux in the pickup loop for a given energy deposition takes the form:

$$\frac{\delta\Phi}{\delta E} = \int_{V_s} \mu_0 \frac{G(\mathbf{r})}{p} \frac{\delta M(B(\mathbf{r}))}{\delta T} d^3r \tag{3.33}$$

These above equations can be integrated numerically using the field data from the results of the FEMM simulation and dividing the sensor area into small enough sections that the average for the section is close to the value at a point in the middle of a section.

After calculating the change in flux in the meander it is necessary to convert that change in flux into a change in current in the input of the SQUID. With the particular superconducting gradiometric geometry used in this design, this change in current has the form [77]:

$$\delta I = \frac{\delta\Phi}{L + 2(L_i + L_W)} \tag{3.34}$$

where L is the inductance of the meander, L_i is the input inductance of the SQUID, and L_W is the inductance of the wirebonds. Finally, using this change in current and the design characteristics of the SQUID, it is possible to calculate the flux change in the SQUID for a given energy deposition using the equation:

$$\delta\Phi_S = M_{is}\delta I = \frac{M_{is}\delta\Phi}{L + 2(L_i + L_W)} \tag{3.35}$$

where M_{is} is the input sensitivity of the SQUID. Knowing the flux change in the SQUID for a given energy deposition makes it possible to compare the responsivity to measured SQUID performance characteristics and compare the contribution of SQUID noise to other noise sources in the device.

Complete Noise Model and Predictions

Section 3.6 discussed the calculation of the energy resolution of a system that was only limited by thermal noise. In this limit a detector with the characteristics shown in table 3.1 would achieve a

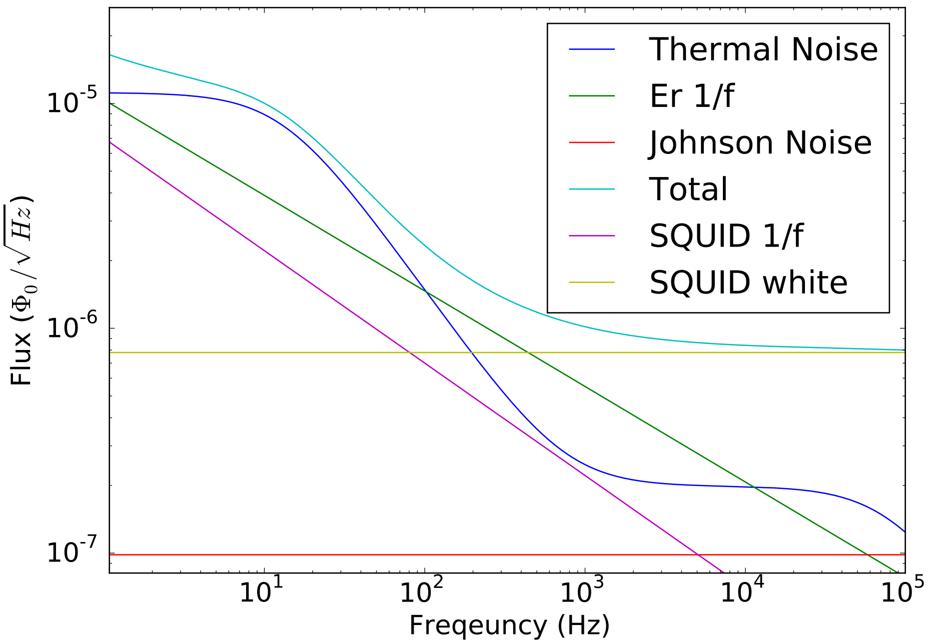

Figure 3.9: Predicted noise as function of frequency.

resolution of 26 eV FWHM at 35 mK. Now that a more complete model of the response and noise in a realistic detector has been developed, it is possible to calculate the total noise and the energy resolution based on the signal-to-noise ratio. For this calculation it is necessary to convert all the noise into a common set of units Φ_0^2/Hz. The resulting formula for the total noise has the form

$$S_{\Phi_s,tot}(f) = S_{SQ}(f) + \frac{M_{is}^2(S_{\Phi,Er}(f) + S_{\Phi,J}(f) + S_e(f)(\frac{\delta\Phi}{\beta\delta E})^2)}{(L + 2(L_i + L_W))^2}, \tag{3.36}$$

where the individual terms in 3.36 come from equations 3.26, 3.27, 3.28, 3.9, 3.33, and 3.35. Equation 3.36 allows us to compute the expected noise spectrum of the device from known MMC and SQUID characteristics. Table 3.2 lists all the known characteristics. A plot of the predicted noise spectrum in units of $\Phi_0/\sqrt{Hz}$ is shown in figure 3.9. This figure shows that for the measured parameters of our device, SQUID noise will dominate over most of the frequency spectrum.

To calculate the corresponding energy resolution, we use the NEP formalism described in equation 3.23. To convert units from Φ_0^2/Hz to eV^2/Hz, we use the unit conversion:

$$S_{E,tot}(f) = S_{\Phi_s,tot}(f)\beta^2 \left(\frac{\delta E}{\delta \Phi_s}\right)^2 \tag{3.37}$$

Using the result of this equation and the responsivity of the detector $p(f)$ calculated in equation

Parameter	Value
SQUID white noise	0.78e-6 $\Phi_0/\sqrt{Hz}$
SQUID 1/f noise	7E-6 $\Phi_0/\sqrt{Hz}$
SQUID input sensitivity (M_{is})	2.36 $\mu A/\Phi_0$
SQUID input inductance (L_i)	29 nH
Absorber heat capacity (C_e)	13.51 nJ/K^2T
Temperature	35 mK
Field current (I_f)	115 mA
Sensor height (d)	2.25 μm
Sensor area (A)	1 mm^2
Meander pitch (p)	10 μm
Meander width (w)	8 μm
Meander inductance (L)	30 nH
Erbium concentration (x)	600 ppm
Erbium 1/f	1.08e-10/f$^{0.85}$ Φ_0^2/Hz

Table 3.2: MMC parameters used for simulation of responsivity and noise.

3.19 it is then possible to calculate the energy resolution in eV using the following equation:

$$\Delta E_{FWHM} = 2\sqrt{2\ln 2}\left(\int_0^\infty \frac{p(f)^2}{S_{E,tot}(f)}\right)^{-1/2} \tag{3.38}$$

This equation assumes that an optimum Wiener filter is used such that the frequency response of the filter is perfectly matched to maximize the integrated signal to noise ratio. This filter will be discussed in more detail in chapter 6. With the values from table 3.2 it is now possible to predict an energy resolution of the device. The predicted resolution is 69 eV FWHM. This predicted result will be compared with the measured noise and energy resolution in chapter 7.

Chapter 4

MMC Fabrication

4.1 Introduction

The metallic magnetic calorimeters used in this work were fabricated at the University of Heidelberg using mostly standard micro-fabrication techniques. The gold absorber is the only unusual component as it requires the micro-fabrication of a mold for free-standing posts and electroplating 200 μm of ultra-pure gold. This final step was improved significantly as a part of this work by replacing the photoresist SU 8 with AZ 125 nXT. The MMC chip design included four gradiometric MMCs with eight total 2000 μm x 500 μm x 200 μm absorbers per chip. This chapter will discuss the general fabrication process and will go into detail about the new process for fabricating the absorber mold. The devices were fabricated on a 2" circular silicon wafers with 34 detector chips per wafer. More detailed descriptions of the fabrication process can be found in references [79, 80].

4.2 Fabrication Process

Layer 1 : First Nb layer

The first layer of Nb is used to pattern the SQUID bond pads as well as the meanders, as shown in figure 4.1. Prior to sputtering the first layer, the wafer is ion-milled in order to remove any impurities on the surface. Following this, 400 nm of Nb is sputtered onto the surface. After this, the AZ 5214E positive photoresist is spin-coated onto the surface and exposed. The photoresist is then developed and the Nb is removed using a 3:1 mixture of concentrated sulfuric acid and 30% hydrogen peroxide, commonly known as Piranha etch. Finally, the remaining photoresist is removed using DMSO.

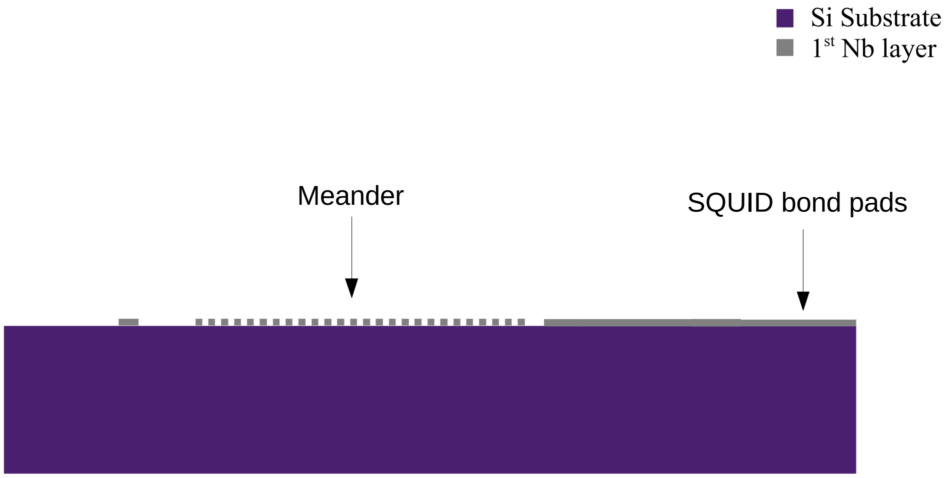

Figure 4.1: Diagram of the Nb layer for meanders and SQUID pads.

Layer 2 : SiO_2 isolation layer

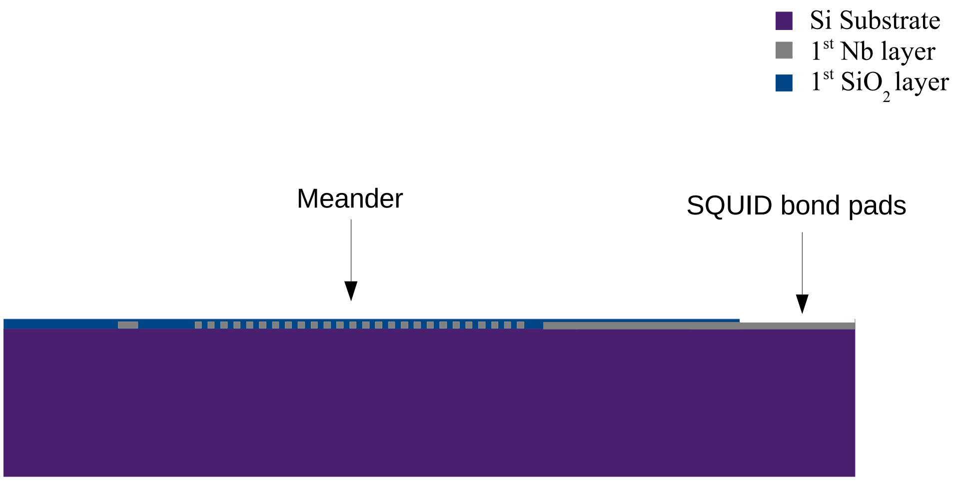

Figure 4.2: Isolation layer over the first Nb to prevent shorts.

The first isolation layer is used to electrically isolate all the meanders and connecting wires, as shown in figure 4.2. This is done using a negative photoresist process. Prior to anodization and sputtering 200 nm of SiO_2, the wafer is coated with AZ 5214E photoresist and then exposed. It is then developed, anodized, and sputtered with the bond pads and the vias remaining protected by the photoresist. Finally, the photoresist is removed using dimethyl sulfoxide (DMSO). This isolation layer is relatively thin in comparison to the thickness of the Nb layer. This is because it is desirable to have the Au:Er sensor material as close to the Nb meander as possible. This has led to reliability issues because the different conductive layers can short due to either stress caused by thermal cycling or wirebonding.

Layer 3 : Au:Pd heater layer

This layer is used for the persistent current switch, as shown in figure 4.3. Similar to the previous layer, this is done using a negative photoresist process. The AZ 5214E photoresist is coated, exposed, and developed, then the Au:Pd is sputtered onto the substrate. Prior to sputtering the Au:Pd, 5 nm of Ti is used to improve adhesion. Finally, the remaining photoresist is removed using DMSO.

Layer 4 : Second Nb layer

This layer is used for the remaining Nb wires needed for the heater as well as the Nb that acts as a magnetic shield over the SQUID lines, as shown in figure 4.4. This layer is also fabricated using a negative photoresist process with AZ 5214E. This layer is 400 nm thick.

Figure 4.3: Au:Pd layer for the persistent current switch heater.

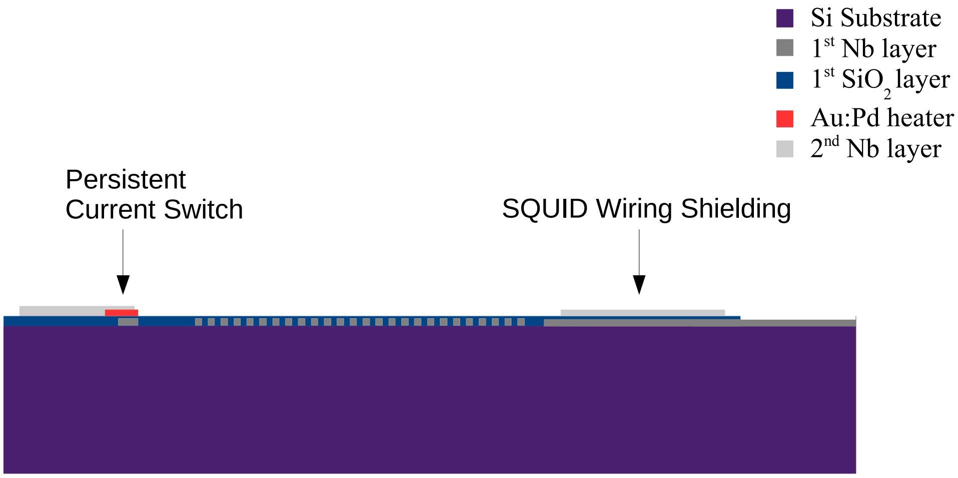

Figure 4.4: Nb layer for heater connections and SQUID wiring shielding.

Layer 5 : Second SiO_2 isolation layer

The second isolation layer is fabricated in the same manner as the first isolation layer. It is used to add an insulating layer over the 2nd Nb layer, as shown in figure 4.5. This prevents shorts between the persistent current switch wiring and the gold thermalization layer. No additional isolation is added to the area over the meanders in order to minimize the separation of the meanders from the Au:Er sensor material.

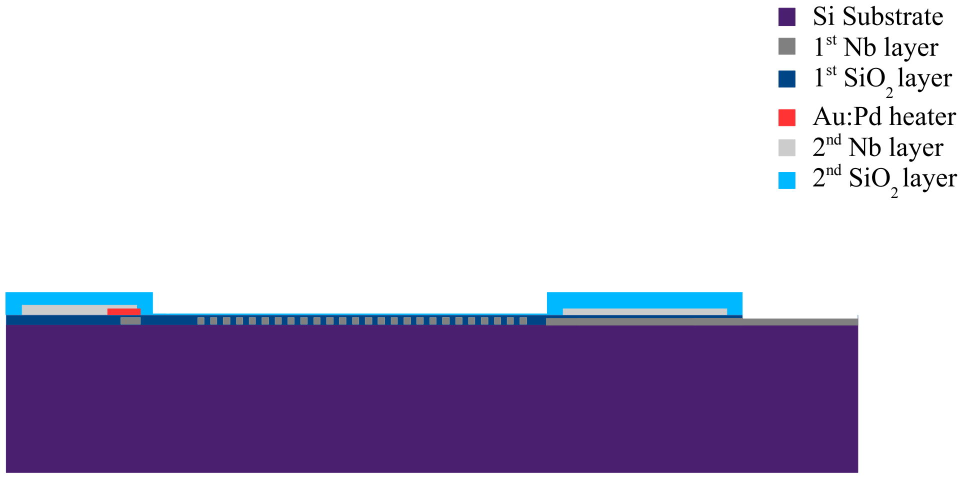

Figure 4.5: Isolation layer of SiO$_2$ to cover 2nd Nb layer.

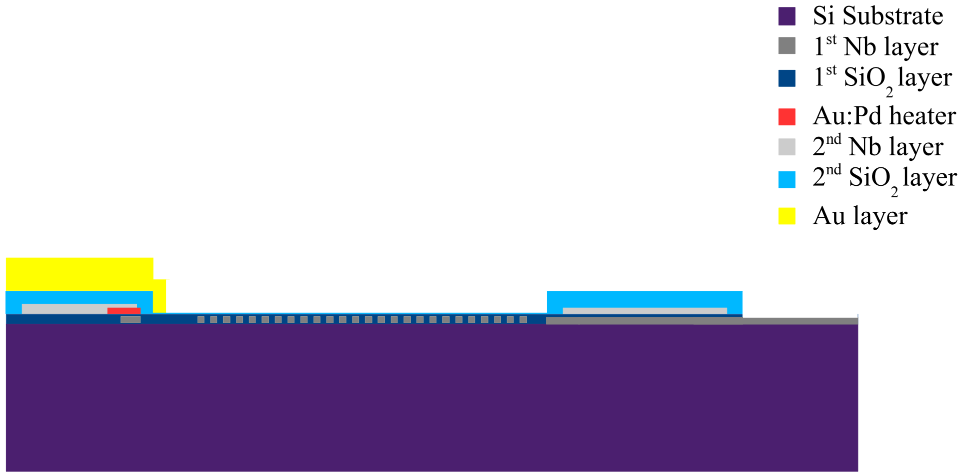

Figure 4.6: Gold layer for connecting MMC to thermal bath if desired.

Layer 6 : Au thermalization layer

This layer of gold is used to create a link from the Absorbers to a place at the edge of the chip where a connection to the thermal bath can be made, as shown in figure 4.7. The thickness and width of this layer, along with the bath temperature, defines the decay constant of the detector if gold wirebonds are used to heat-sink the MMC to the thermal bath. This layer is also patterned using negative photoresist, but due to its thickness (1 μm) the photoresist AZ 6632 is used. Before sputtering 1 μm of gold, the wafer is ion-milled to clean the surface and 2 nm of Nb is sputtered to help adhesion.

Layer 7 : Au:Er sensor

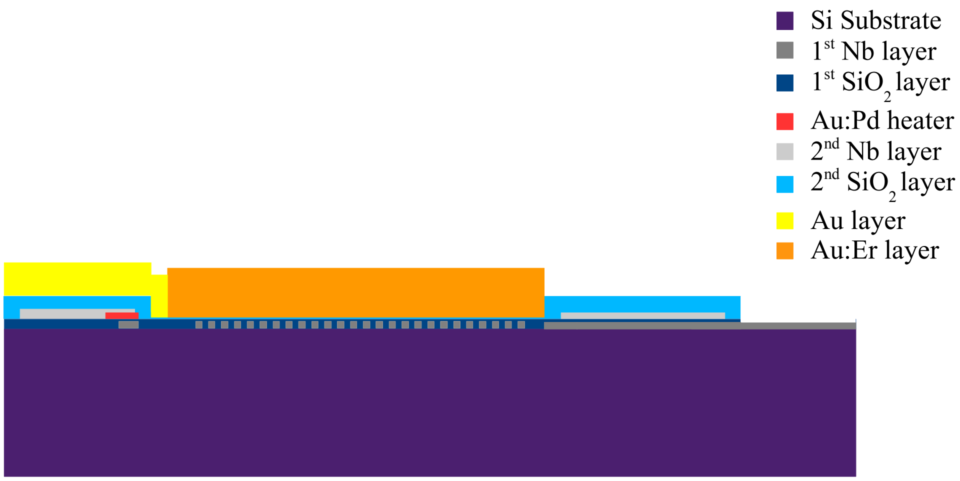

Figure 4.7: Au:Er temperature sensor material patterned over meanders.

This is the temperature sensor material that has a large change in magnetization as a function of temperature. It is patterned directly over the meanders, as shown in figure 4.7. It uses the AZ nLof 2070 photoresist and it is ion-milled beforehand. Similar to the previous layer, 2 nm of Nb is sputtered for adhesion, then 2.5 μm of Au:Er is co-sputtered at a ratio to achieve the desired Er concentration of 600 ppm. The concentration and thickness were optimized for this device by the University of Heidelberg using the model described in the previous chapter. The Au:Er target was fabricated by the University of Heidelberg using Er enriched in ^{168}Er from the National Isotope Development Center at Oak Ridge National Laboratory.

Layer 8 : Au absorber

Choice of photoresist

The final layer is electroplated Au used for the thick absorber. In order to fabricate this layer, a $>$ 200 μm thick photo-resist was needed. There are two primary candidates for electroplating compatible photo-resists: AZ 125 nXT and SU 8. SU 8 is a well-understood thick photoresist used for microfluidics and microelectromechanical systems processing. It is good for making thick structures but it has the downside that it is very difficult to remove once it has been exposed. With the tight absorber packing that is desired to achieve high fill fraction in many applications, it is common that multiple absorbers can be connected thermally to each other via the SU 8 or. It also adhered to the mask so strongly during the exposure process that the masks were sometimes destroyed in the process of separating the chip from the mask. The separation of the mask and chip also often left gaps in the mold, which resulted in multiple pixels being connected during the electroplating process.

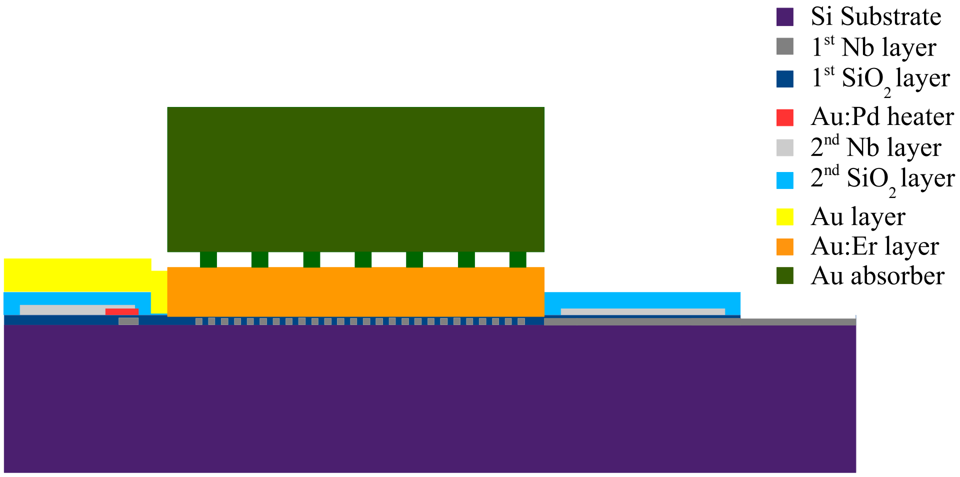

Figure 4.8: 200 μm thick electroplated gold absorber.

The alternative photoresist, AZ 125 nXT, is easier to remove but there was no well-defined process for producing 300 μm thick structures at the beginning of this dissertation. A new spin-coating process, described below, was developed for this work capable of producing 300 μm thick photoresist layers with high aspect ratio features. The final structure has the form shown in figure 4.8.

New absorber process

The process for electroplating absorbers starts by patterning a layer of AZ 5214E photoresist. This is used as a negative photoresist with only the holes for the posts left exposed. After this photoresist has been applied, the surface is ion-milled and then a seed layer of 200 nm of gold is sputtered, followed by 20 nm of Nb. This provides a clean seed Au layer protected by Nb, which is etched away before the electroplating process.

The process developed for producing thick single coat photoresists of AZ 125 nXT is based on the spin-casting process described in reference [81]. The photoresist AZ 125 nXT is first spin-coated using a single 2 s ramp to 1500 rpm for 2 s. Once the photoresist has been spin-coated, it is pre-baked for 6 hours at 105 C in a sealed container. The hot plate should be leveled to achieve maximum uniformity. Before exposing the photoresist, it is necessary to add a plastic film to protect the mask and prevent the photoresist from becoming stuck to the mask. This film is needed because it is not possible to bake sufficient solvent out of the photoresist to prevent it from sticking to the mask without also drying it so much that it cannot be developed. Finally, the photoresist is exposed to 365 nm ultraviolet light at 10 J/cm^2 using a mask for the absorber molds. The plastic film is then removed and the photoresist is developed using AZ 326 MIF. Prior to testing the electroplating process it was necessary to demonstrate that the AZ 125 nXT could form molds of the desired thickness and aspect ratio. Figure 4.9 shows a 300 μm thick test pattern on a glass slide. This demonstrated that the process could achieve an aspect ratio that was sufficient

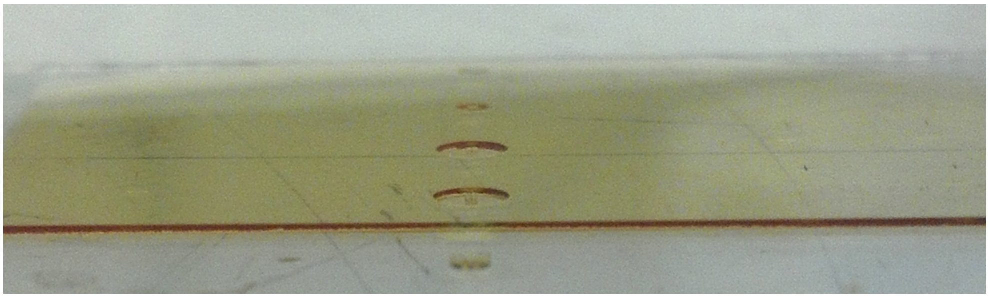

Figure 4.9: Test pattern of AZ 125 nXT on a glass slide used to demonstrate 300 μm thick photoresist process.

to keep neighboring pixels on the hard X-ray chip separated [82].

After the mold has been prepared as described, it is ion milled to clean off any remaining photoresist on top of the gold seed layer with niobium covering. After this process is completed, the Nb layer is etched away using the Piranha etching solution for up to 90 s. The etching process is quenched as soon as it is clear that the niobium layer has been fully etched through by visual inspection. The wafer is then placed in a beaker filled with deionized water. It remains in this beaker until the electroplating process is ready. Then the wafer is dried off using N_2 and it is connected to the electrode and placed in the sulfite-based electrolyte from AGC MicroVision. In order to produce the 200 μm thick absorbers a gold concentration of 17 g/L was used with a current density of 5 mA/cm^2. Using these process parameters the gold deposition rate was approximately 317 nm/min [75]. Finally, the remaining photoresist is removed by dissolving it in DMSO or acetone. After the remaining photoresist is dissolved, the wafer is diced into 34 chips for testing. A picture of an MMC that was produced using this new photoresist for the absorbers is shown in figure 4.10.

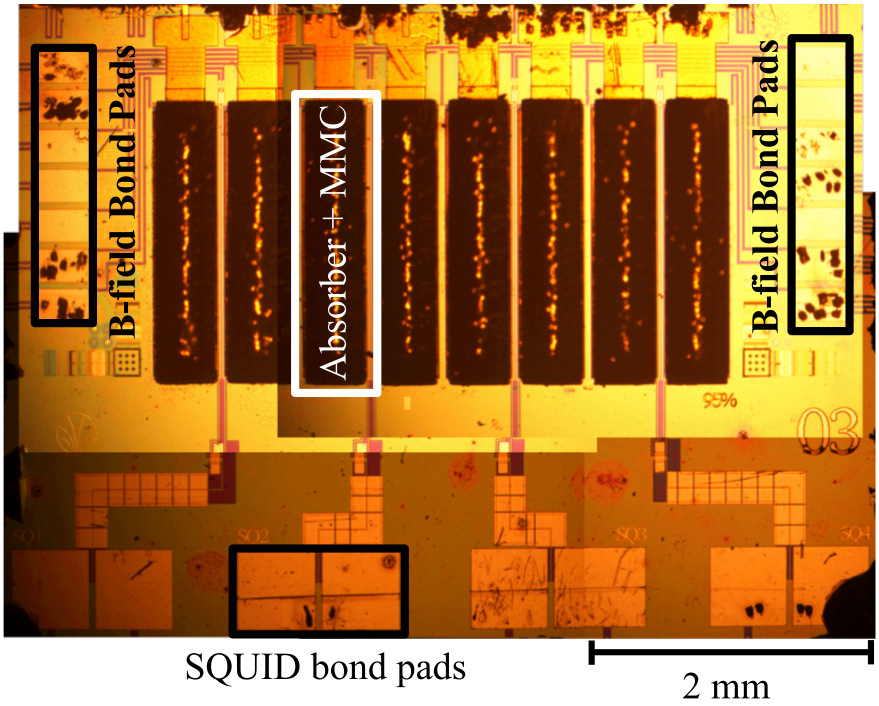

Figure 4.10: Image of an MMC fabricated using the new photoresist process developed for this work. An MMC from the same wafer was used for all measurements in this work.

Chapter 5

Experimental Apparatus

5.1 Overview

To operate MMCs with the desired sensitivity, it is necessary to cool them down to temperatures well below 100 mK. There are currently two different refrigeration technologies commonly used to reach these temperatures for bulk samples: ^{3}He/^{4}He dilution refrigeration and adiabatic demagnetization refrigeration. Both of these types of refrigeration were used in the testing of devices for this thesis, but adiabatic demagnetization refrigerators (ADRs) will be focused on because they were used for the majority of the measurements. In order to achieve the desired MMC performance, it was necessary to upgrade the ADRs at LLNL.

5.2 Cryostat Construction

Cryostats require good thermal isolation between the experimental stage and room temperature to maximize their performance. For experiments at < 100 mK it is necessary to operate the system under high vacuum to avoid thermal conduction due to gases. In addition, it is typical to have several high emmissivity layers in between 300 K and 100 mK in order to minimize the infrared heat load on the cold stage, which scales as the difference in temperature to the fourth power

$$P_{IR} \propto (T_1^4 - T_2^4).$$

In the ADR cryostat used in this work, this is accomplished by adding two additional shells that are light tight in both the visible and infra-red region. A depiction of the cryostat design is shown in figure 5.1. Either liquid cryogens or a mechanical cooler such as the pulse-tube system used in this work can be used to cool these stages to their desired temperatures. For this work a liquid cryogen based-system, which used liquid nitrogen and liquid helium, was used as the test-bed for initial development of MMC experimental techniques at LLNL. This system was not suitable for MMC operation, however, and was replaced with a liquid-cryogen-free cryostat later.

When using a pulse-tube system these stages operate at roughly 60 K and 3 K. Attached to the 3 K stage are the ADR stages and a 6.5 T superconducting magnet used to cool the experiment to millikelvin temperatures. These will be discussed in more detail later. Some of the experiments utilized a dilution refrigerator below 3 K to provide continuous cooling power. These will be discussed only briefly as they were only used for a minor portion of the testing.

Pulse-tube cooler

In order to simplify the operation of cryogenic systems, it is desirable to be able to operate them without using liquid cryogens. This makes them safer, allows them to run unattended, and makes them significantly more transportable. There have been many different technologies developed to mechanically cool cryostats to <4 K. These include GM, Joule-Thompson, Sterling cycle, and pulse-tube coolers [83]. For cryogenic detector applications, pulse-tube refrigerators are preferred, as they require no moving parts that are mechanically or electrically connected to the cryostat itself. An external rotary valve and compressor are required, but these can be isolated from the

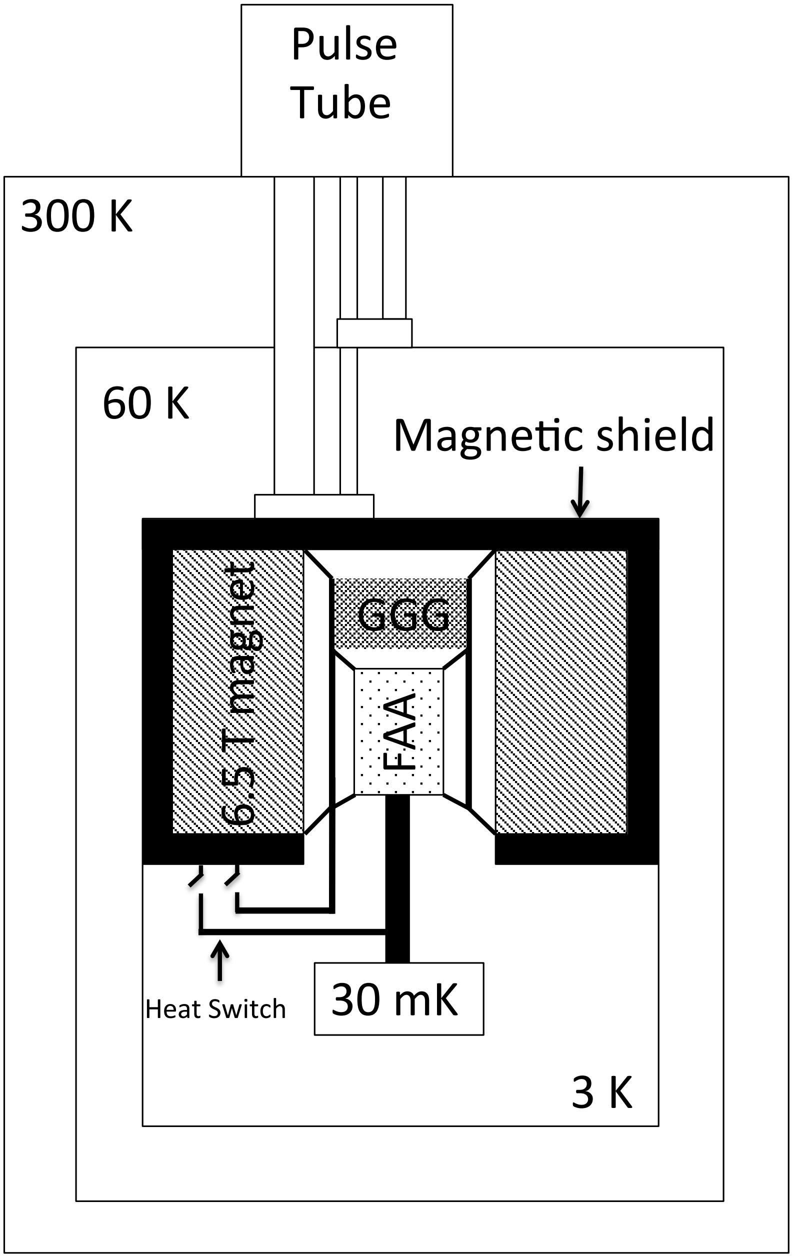

Figure 5.1: Conceptual drawing of a pulse-tube cooled two-stage ADR.

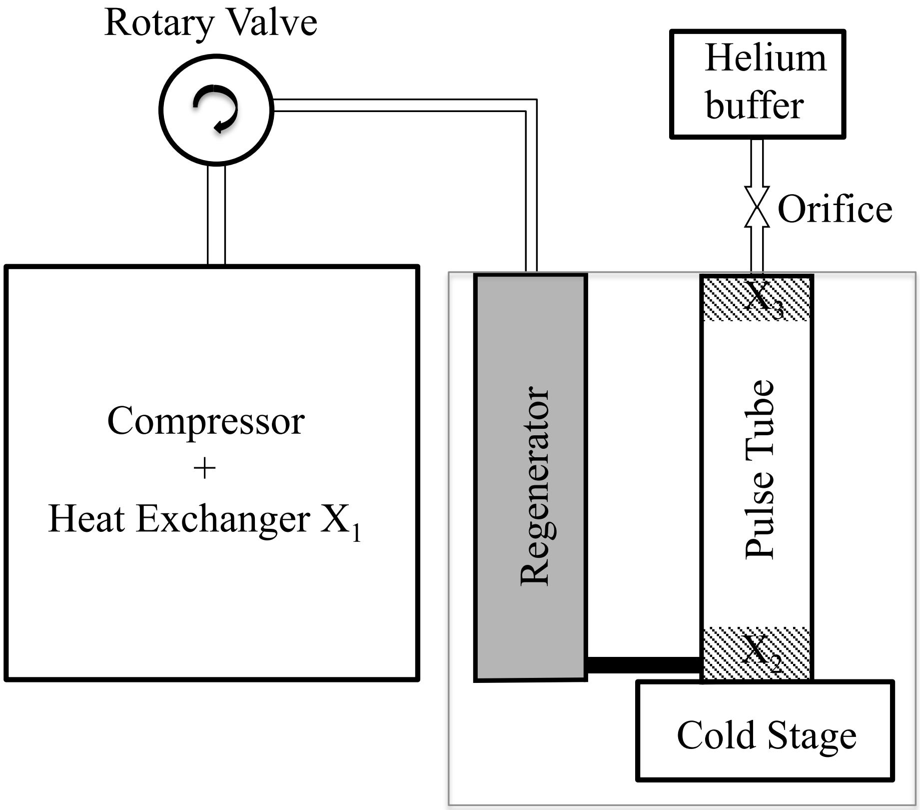

Figure 5.2: A single stage GM pulse-tube refrigerator.

cooling system to minimize microphonics and electromagnetic interference. A two-stage version of this type of cooler can be used to reach temperatures below 3 K. As this was the type of cooler used for all the measurements in this work, the fundamentals of its operation will be discussed in detail.

Theory of operation

A pulse tube cooler uses helium as a working fluid in an expansion-compression cycle. The simplest version of this is shown in Fig. 5.2. This figure shows the basic design of a pulse tube cooler. In this system, the pressure in the pulse-tube is periodically varied using the rotary valve, which alternately connects high pressure gas from the compressor and vents the high pressure in the system to the return line of the compressor. In order to achieve maximum cooling power, it is necessary to adjust the impedance of the orifice and the size of the buffer so that the pressure changes maximize the desired heat transfer. This section will describe the thermodynamic processes involved in the operation of this cooler in an idealized cycle.

The fundamental operating principal is the same as most gas cycle coolers: compression of helium in the system leads to heating and expansion leads to cooling. The two most important features of the system are the heat exchangers, where the gas has good thermal contact to the surroundings, and the regenerator - where the gas has good thermal contact to the medium, the gas has little impedance to flow, and the regenerator itself has negligible thermal conductivity [83].

The simplest description of pulse tube operation divides the pulse tube into three notionally separate mass flows of gas. This assumes that any heat due to increase of pressure in the compression space is rejected to the surroundings by heat exchanger X_1. Its temperature cycle will be ignored for this analysis. The first mass flow starts in the regenerator and passes through the heat exchanger T_L as the pressure increases. It then expands and cools in the pulse tube and returns to the heat exchanger at a lower temperature, leading to cooling. The second mass flow cycle flows from the pulse tube through heat exchanger X_2 into the buffer when the pressure increases. This compression causes heating but this heat is immediately rejected to the surroundings by X_2 before the mass flows into the buffer. As the pressure decreases in the second half of the cycle the mass flows from the buffer into the pulse tube and cools as it expands to below ambient temperature. The third flow of mass acts as a so-called "gas-piston". This mass remains in the pulse tube and transfers heat between the two other systems. All of these masses move towards the hot end during compression and towards the cold end during expansion. This leads to a net enthalpy flow and cooling. A more thorough discussion of the single stage system and the non-idealities can be found in reference [83].

Single stage pulse tube systems can only reach temperatures as low as 10.6 K [84]. In order to reach temperatures needed for high performance ADR operation of < 4.2 K it is necessary to use a two stage pulse tube system. A conceptual schematic of the two-stage pulse-tube system used for this work is shown in figure 5.3. In this setup, a second regenerator is attached to the cold end of the first regenerator. This second regenerator is then connected to a second pulse tube, which also has a heat-exchanger at each end and a buffer volume. Two-stage pulse tube coolers of this type can reach base temperatures approaching the lambda point of helium, 2.1K [83]. By separating the two stages and using ^{3}He as the working fluid of the second system, along with a superfluid vortex cooler, temperatures as low as 1.19 K have been achieved [85]. The two-stage pulse tubes used in this work were commercially available systems with optimum base temperatures of 2.7 K.

5.3 Adiabatic Demagnetization Refrigeration

Adiabatic demagnetization refrigeration is based on the reduction in the entropy of the spins in a paramagnetic material using an applied magnetic field as a source of cooling power. The base temperature that can be achieved using this technique depends on the magnetic ordering temperature of the paramagnet being used. Below this temperature the entropy at zero field drops rapidly, resulting in very little cooling power. There are many magnetic materials that can be used in ADR systems. A review of the most common ones can be found in reference [86].

In order to have sufficient time at the base temperature to make measurements, it is common to use a two-stage ADR with the first stage acting as a thermal guard. Figure 5.1 shows what this

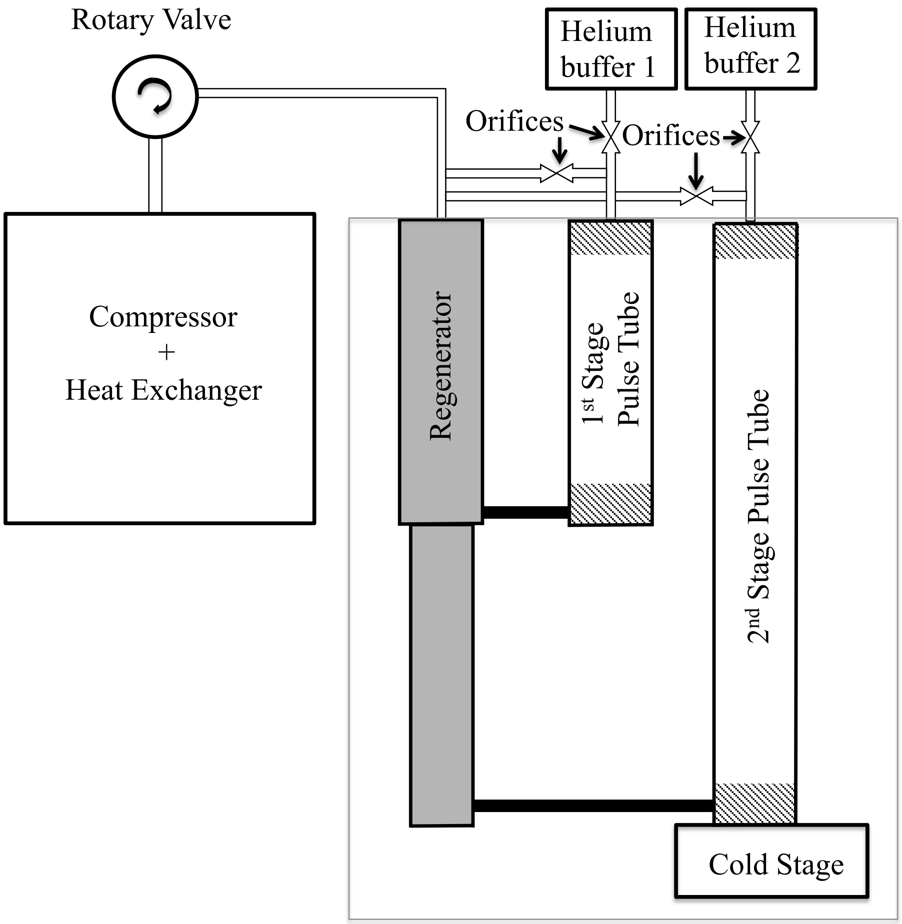

Figure 5.3: A two-stage GM pulse-tube refrigerator design. Only major adjustable orifices are shown. Additional minor orifices are common to reduce DC flow of helium.

design looks like, with the stages below 4 K connected using Kevlar strings. This ADR design originated in the early 1990's as a method to reach temperatures of < 100 mK with measurement times of 10-100 h starting at temperatures of 4 K [87, 88]. Before this development, it was necessary to pre-cool the ADR stage with a pumped ^{3}He system, otherwise the heat leak from the experimental stage to the 4 K stage would limit the measurement time to a few hours at most [87]. The two-stage ADRs used in this work are based loosely on that design, employing a GGG paramagnet as a first stage that acts as a thermal guard at 0.4 K and an FAA paramagnet for the experimental stage at 0.03 K.

Principle of magnetic cooling

Magnetic cooling uses the magnetic disorder entropy from free paramagnetic ions present in a solid for refrigeration. For common material choices, the magnetic disorder entropy is large compared to all other entropies of the system, so they can be neglected [89]. This cooling is based on two related conceptual ideas. The first is that at zero applied field as the temperature decreases the thermal energy of the system k_bT will approach the energy of the interactions between the magnetic moments μb, where b is this internal magnetic field. This will lead to an ordering of the magnetic moments. This ordering into a ferromagnetic or anti-ferromagnetic state leads to a decrease in the entropy of the system as the temperature decreases. A similar ordering and decrease in entropy is possible at higher temperature by applying an external magnetic field.

In order to understand how these two effects can be used to cool a system, it is instructive to look at a diagram of the entropy as a function of field and temperature. This requires an understanding of the magnetic entropy as a function of temperature in the paramagnetic salts. This entropy is a function of the total magnetic field and the temperature. It is also dependent on several parameters of the paramagnet, namely the spin J and the Lande factor g. It can be described using the following equations:

$$S/R = \frac{x}{2}\left(\coth\frac{x}{2} - (2J+1)\coth\frac{x(2J+1)}{2}\right) + \ln\left(\frac{\sinh\left(\frac{2J+1}{2}\right)}{\sinh(\frac{x}{2})}\right) \tag{5.1}$$

with

$$x = \frac{gB\mu_B}{k_BT} \tag{5.2}$$

The total magnetic field B can be calculated as the sum in quadrature of the internal field b and the external field B_{ext} in the following manner:

$$B = \sqrt{b^2 + B_{ext}} \tag{5.3}$$

Using this equation and measured values for g and J, it is possible determine the entropy at several different external field strengths, as shown in figure 5.4. Using this figure along with 5.1 it is straightforward to understand the ADR cooling cycle. The process starts at point 1 where the cryostat is at 3 K and the external field is 0. Then the external field is increased to 6.5 T isothermally using the superconducting magnet surrounding the paramagnetic salt pills. This brings the paramagnet to point 2. From here, the paramagnet and experimental stage are disconnected from the 3 K pre-cooling stage. This is accomplished using a heat switch shown in figure 5.1.

There are two types of heat switches employed in the cryostats used for testing. The liquid He based cryostats use a bi-stable heat switch operated using two solenoids. This has the advantage that it does not require a mechanical link between 300K and the experimental stage, but it has the disadvantage that the heat switch can sometimes cause the magnet to quench. The other alternative is a motor driven mechanical heat switch. This type has a lower likelihood of causing a magnet

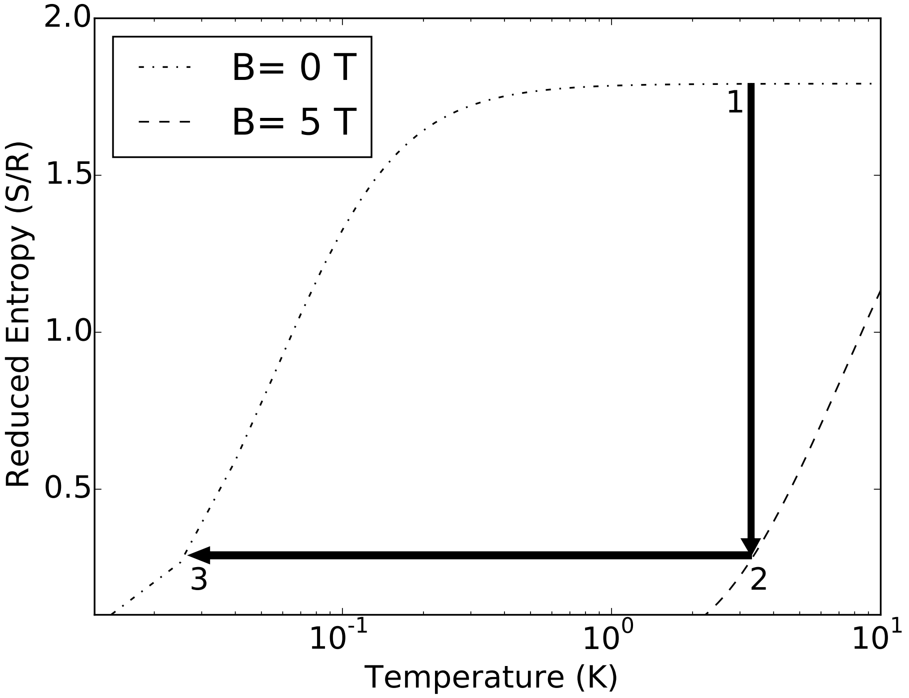

Figure 5.4: Plot of the reduced entropy of FAA as a function of temperature at zero and five Tesla.

quench, but it requires a complex mechanical coupling between the motor at 300K and the experimental stage. This mechanical linkage can heat up the experimental stage by several hundred milli-kelvin during the process of opening the heat switch. It is therefore desirable to align the stages such that as few turns are needed as possible to go from fully closed to fully open.

Once the heat switch has been opened, the magnetic field is then reduced back to 0. As the magnetic field is decreased adiabatically the paramagnet salt cools. This can be seen in figure 5.4 going from point 2 to point 3. The adiabatic process implies that entropy is constant while the magnetic field is reduced. This implies the following relation between entropy at maximum and zero external field:

$$S(B_i/T_i) = S(b/T_f) \tag{5.4}$$

Using equations 5.1 and 5.2 this equivalence can be reduced to:

$$T_f = \frac{T_i}{B_i} b$$

Where T_f is the final temperature, T_i is the initial temperature, B_i is the initial field, and b is the internal magnetic field of the paramagnet (assuming the final external field is zero). The characteristic parameters of the two salt pills are shown in table 5.1. Using these parameters, the base temperatures of the FAA and GGG are theoretically 27 mK and 222 mK, respectively.

Salt	Chemical composition	J	g	T_0 (mK)	B_0 (T)
GGG	$Gd_3Ga_5O_{12}$	7/2	2	380	0.75
FAA	$Fe(SO_4)_2NH_4$	5/2	2	26	0.05

Table 5.1: Properties of paramagnetic refrigeration salts used in this work [86].

Realistic performance of the cryogen free ADR, when wired for MMC operation, is typically 28 to 35 mK for the FAA and 375 mK for the GGG. This discrepancy can be attributed to a mix of factors, including heating while opening the heat switch, the non-negligible heat capacity of the experimental platform, resistive eddy current heating, and the thermometry and readout wiring for the MMC.

5.4 Dilution Refrigeration

The other type of refrigeration used for milli-kelvin experiments in this work is a dilution refrigerator. It leverages the unique properties of ^{3}He and ^{4}He. At temperatures below the lambda point of ^{4}He, 2.1 K in pure ^{4}He, it becomes a superfluid. At these very low temperatures, ^{3}He behaves as a Fermi liquid. Superfluid ^{4}He also has the unique property that at sufficiently low temperatures, below 850 mK, there is a limit to how much ^{3}He is miscible in ^{4}He. Below this temperature, at some limiting concentration, the ^{3}He and ^{4}He will separate into distinct phases with a layer of almost pure ^{3}He on top of a layer of ^{3}He/^{4}He mixture with an ^{3}He concentration dependent on the temperature. This mixture has an osmotic pressure of ^{3}He of $\Pi_0 = 2209$ Pa at absolute zero. This osmotic pressure means that if there is a pressure drop applied less than the osmotic pressure it is possible to drive ^{3}He into the ^{4}He. Driving ^{3}He into the ^{3}He/^{4}He requires thermal energy. This thermal energy of dilution is the source of cooling power for the base stage of the cryostat. Commercial systems of this type can commonly reach base temperatures of 9-17 mK with $10\ \mu$ W at 20 mK [90]. More details on the construction and thermodynamics of dilution refrigeration systems can be found in [83, 91]

5.5 Performance of ADRs at LLNL

MMC performance improves with reduced temperature due to the smaller heat capacitance and larger gradient in susceptibility, which leads to a larger signal and lower thermal noise. In order to achieve the resolution needed for the measurements in this work, a base temperature of < 35 mK is required. Prior to use on this project, the ADR cryostats at LLNL were designed for operation at 50 mK or higher. Initial testing was done in the liquid cryogen cooled ADRs to see if it was possible to achieve desired temperatures.

The existing magnet in the liquid ADR refrigerators was not capable of reaching fields higher than 3.6 T without quenching. At this field, the base temperature was approximately 80 mK when starting from a helium bath temperature of 4.2 K. This was slightly improved by pumping on the helium such that the starting temperature was 3.8 K and the final base temperature was 65 mK. This was still too warm for MMC operation. In order to improve the base temperature of these cryostats the existing magnet was replaced with a new 5 T magnet. This system was then tested at two different initial temperatures: 4.2 K and 2.1 K. The latter temperature was reached by pumping on the helium chamber during the demagnetization cycle. The cryostat reached a base temperature of 55 mK when starting at 4.2 K and 35 mK when starting at 2.1 K, but it was not possible to operate the ADR at this field for more than one cycle without needing to re-align the stages. This occurred due to the force on the salt pill being large enough to slightly deform the copper rod that connected it to the experimental stage. The deformation of the copper by this force led to poor performance after the first ADR cycle. More details on this problem and attempts to solve it can be found in appendix A.

Due to the unreliability of the liquid cryogen cooled ADRs, it was necessary to use the liquid cryogen free pulse-tube system. As was mentioned in the previous section, this system was capable of achieving a base temperature of 28 mK. With the MMC installed it was possible to run this system for up to 12 hours below 35 mK. Previous work using this system suffered from electronic noise problems due to the 6 kW compressor being electrically connected to the rotary valve. The solution to this and other noise issues in the pulse-tube system will be discussed later in this chapter.

5.6 MMC Operation in a Pulse Tube ADR

In order to operate MMC devices in the pulse tube ADR, it was necessary to install the appropriate cabling, design an experimental stage for MMC operation, and improve the isolation of the compressor from the cryostat. This section will discuss this work.

MMC chip carrier and platform

It was necessary to design a chip carrier to connect the MMC and SQUID to the readout and persistent current. This chip carrier needed to have good thermal heat sinking and, ideally, superconducting connections for the persistent current. In order to meet these requirements, the carrier consisted of a copper core 0.125 inches thick with a thin layer of Kapton and then a single wiring layer of gold-plated copper. In order to make the persistent current connections superconducting, the connections were covered with Pb/Sn solder which has a Tc of 7 K [92]. In addition, it is desirable to have a superconducting ground plane below the MMC and SQUID. This ground plane was made by gluing a thin sheet of niobium on top of the copper where the MMC would be attached. Figure 5.5 shows a picture of a carrier prepared for MMC installation. This chip carrier sat inside a larger superconducting magnetic shield made out of niobium as a part of the MMC platform. This design keeps the MMC well-shielded while maximizing the thermal conduction and minimizing the extra heat capacity on the experimental stage. For a more detailed discussion of the printed circuit board design see appendix D.

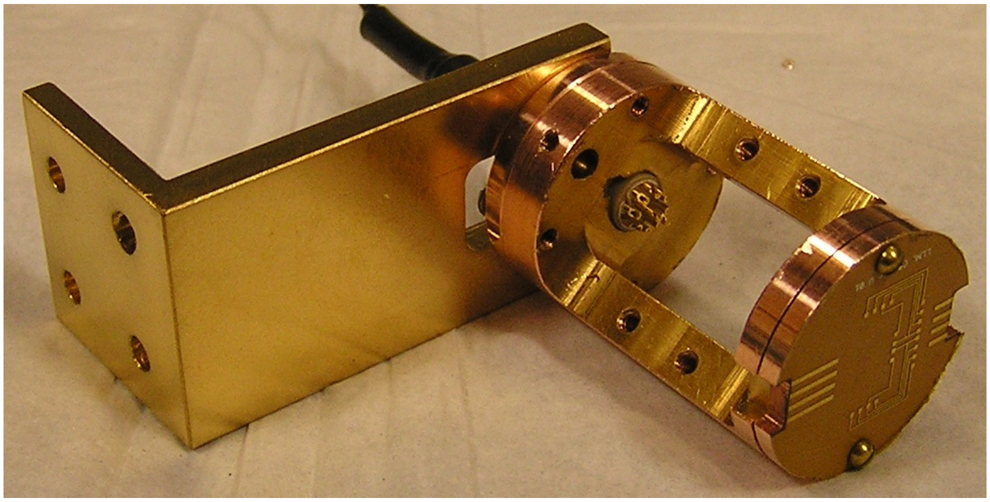

Figure 5.5: A picture of the MMC chip carrier and mechanical support prior to installing the MMC onto the chip carrier.

MMC wiring

In order to operate an MMC, it is necessary to have wiring for a two-stage SQUID and high current wiring to operate the persistent current loop. From 300 K to 3 K a commercial shielded cable made by Magnicon was used, which included wiring for the two-stage SQUIDs and current source. At 3 K the SQUID cable was connected to the standard Magnicon array SQUID package. From 3 K the wiring requirements diverged.

For the current wiring it was necessary to have all wiring below 4 K be superconducting and capable of carrying currents in excess of 200 mA without going normal and without causing excessive heating due to normal conducting interconnects. It was also desirable to be able to connect and disconnect the wiring at the experimental stage without having to remove all the cabling up to the 3 K. In order to accomplish this, an additional heat sink was added at 0.03 K and 3 K. The heat sink consisted of an oxygen free high conductivity (OFHC) copper plate with a Kapton film on top and copper traces that were tinned with Pb/Sn solder. These traces were used to connect the separate sections of wire together and were long enough that it was possible to solder one end without the other end de-soldering.

For the signal wiring it was desirable to heat sink the wire in a manner to minimize pickup of electromagnetic interference. This was done using a commercially available superconducting connector board from Star Cryoelectronics. This board had four pairs of superconducting traces that could be used to connect up to two input SQUIDs to array SQUID electronics. This heat-sink was potted in StyCast 2850FT between two gold-plated OFHC copper plates. These plates were then connected to the 1 K stage. From this connector, the wiring went straight to the MMC chip carrier.

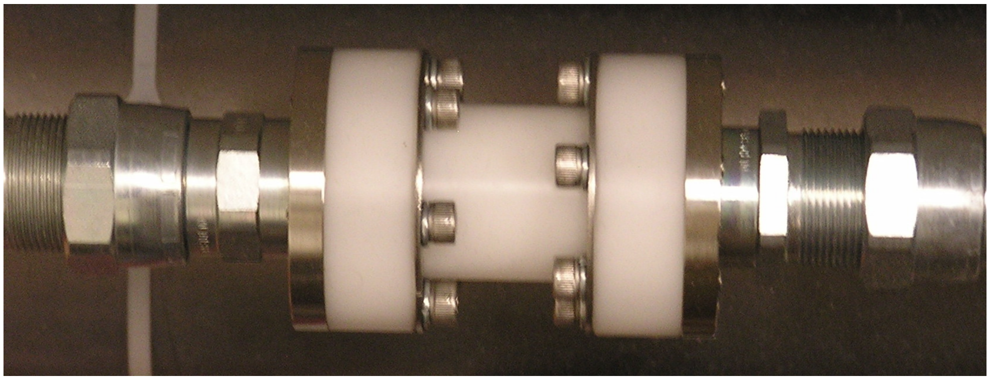

Figure 5.6: An isolator used to electrically decouple the rotary valve from the compressor.

Minimizing electromagnetic interference

SQUID amplifiers are the most sensitive magnetometers and current measurement devices used today. In addition to being able to measure small changes in magnetic field due to particle interactions, they are also sensitive to stray electromagnetic fields in the system. In order to minimize these fields, it is desirable to isolate the cryostat itself from anything that generates electromagnetic interference. Two major sources of electromagnetic interference in the MMC system are the rotary valve and compressor for the pulse-tube cooler. In the existing system both were electrically isolated, but both still induced pickup in the SQUID [33]. In addition to the electrical isolation of the rotary valve, it was also necessary to add a magnetic shield around the rotary valve. This prevented any noise from the motor used to drive the valve from reaching the SQUID. While the compressor was isolated electrically from the cryostat, it was initially still connected to the rotary valve. These connections, in the form of the large metal helium lines, effectively coupled electromagnetic interference from the compressor into the SQUID [33]. In order to eliminate this, the compressor was further electrically isolated from the rotary valve by adding isolated high pressure helium couplers directly at the output and inlet of the compressor shown in figure 5.6. After these were installed, no significant difference in noise could be measured when the compressor was on or off.

Chapter 6

Data Acquisition

6.1 Introduction

Data acquisition systems are a crucial part of any spectroscopic measurement, including those required for this thesis. Due to the fact that the MMC uses a gradiometric design the amplifier output contains both positive and negative pulses on a single channel, it was necessary to develop a custom data acquisition system. This data acquisition system required both new hardware and new software. The hardware chosen was a 4-channel 12-bit 100 MHz GaGe digitizer. This card was chosen specifically because it had a selectable input voltage range and variable acquisition rate, both of which were necessary as the optimum acquisition rate and preamplifier gain were unknown.

6.2 Data Acquisition Framework

Prior to being able to use the GaGe digitizer for MMC data acquisition, it was necessary to develop data acquisition software in order to communicate between a user interface and the hardware. One additional reason this hardware was chosen is because the existing data acquisition software was written for a data acquisition card from the same vendor. It turned out not to be possible to merely update the old data acquisition software, as the C-application programming interface (C-API) had been fundamentally changed and simplified in the intervening years. This meant that a whole new software framework would be required.

The basic requirements for a modern data acquisition framework include independent threads for acquiring, saving, and analyzing pulses as well as a user interface that is reliable and future proof. In order to achieve these goals a Python-based framework was chosen, which used ZeroMQ [93] to communicate between processes with an html-based front-end. This also made it possible to interact with the data acquisition system remotely if necessary by pointing a web browser to the appropriate port on the remote system. The source code for this framework is included in appendix C.

The fundamental building blocks of the system were classes based on the `Multiprocessing.Process` class in Python. In simplest form these classes are first initialized with an instance of a `Pipe` for commands and a `Queue` for data. Both of these objects are thread-safe, meaning that different processes can interact with them simultaneously without the need for the coder to use locking semaphores. A diagram of the basic operational theory of a process is show in 6.1. Each process loops over a function to analyze or acquire data, but between each call of that function it checks to see if it has received a command on the command pipe. If it has received a command on the pipe it then executes that command before calling the function again. Common examples of commands include "shutdown", which for simplicity is just the boolean False on the pipe; "configure" which is sent as a tuple of the command; and a configuration object which can be any python serializable object. In addition, commands can also execute any method of the class. This feature can be used, for example, to get the status or make minor configuration changes. The other major component of this core framework is a Queue. This allows the acquisition process to send data to the analysis process without having to wait for the analysis

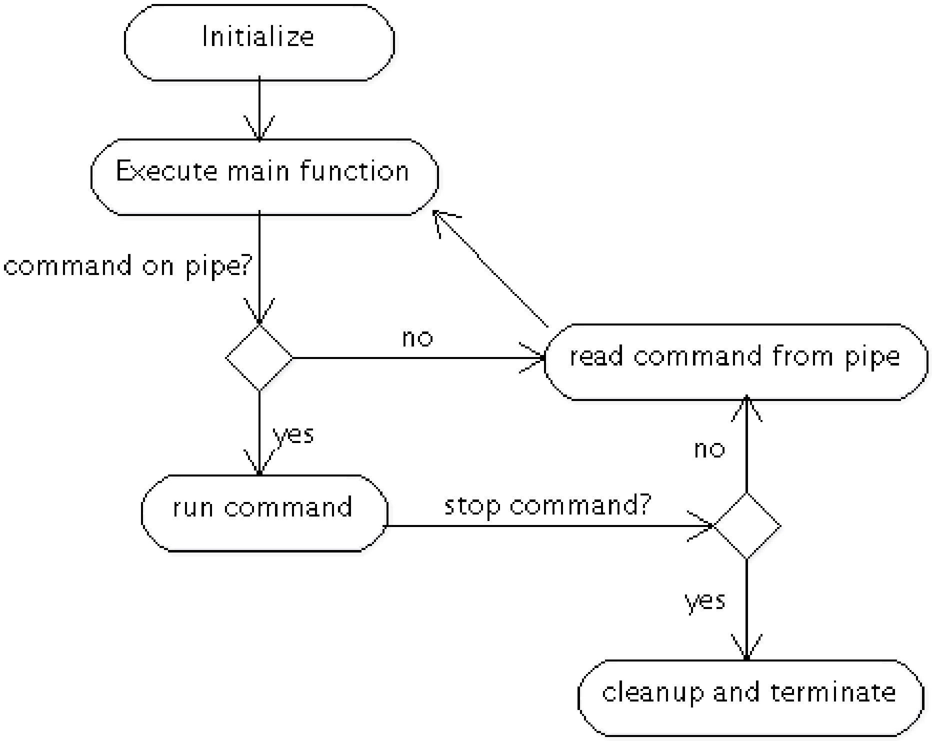

Figure 6.1: A diagram of the activity model of the core framework process.

process to finish the analysis of the previous set of data. This basic framework is sufficient for simple applications in which both processes are highly reliable and on the same machine. It also requires that all threads be initialized at the same time. This can make rapid development more challenging where it may be desirable to change one thread's behavior on the fly to fix bugs and make improvements.

In order to allow for rapid development of different aspects of the data acquisition software, an additional layer was added based on the ZeroMQ communication library [93]. This library allows for many different communication patterns, but the two that were most useful for this application were the traditional REQ-REP pattern and the PUB-SUB pattern. In REQ-REP, one thread sends a request with some data and another thread sends a reply with data. This is used for sending

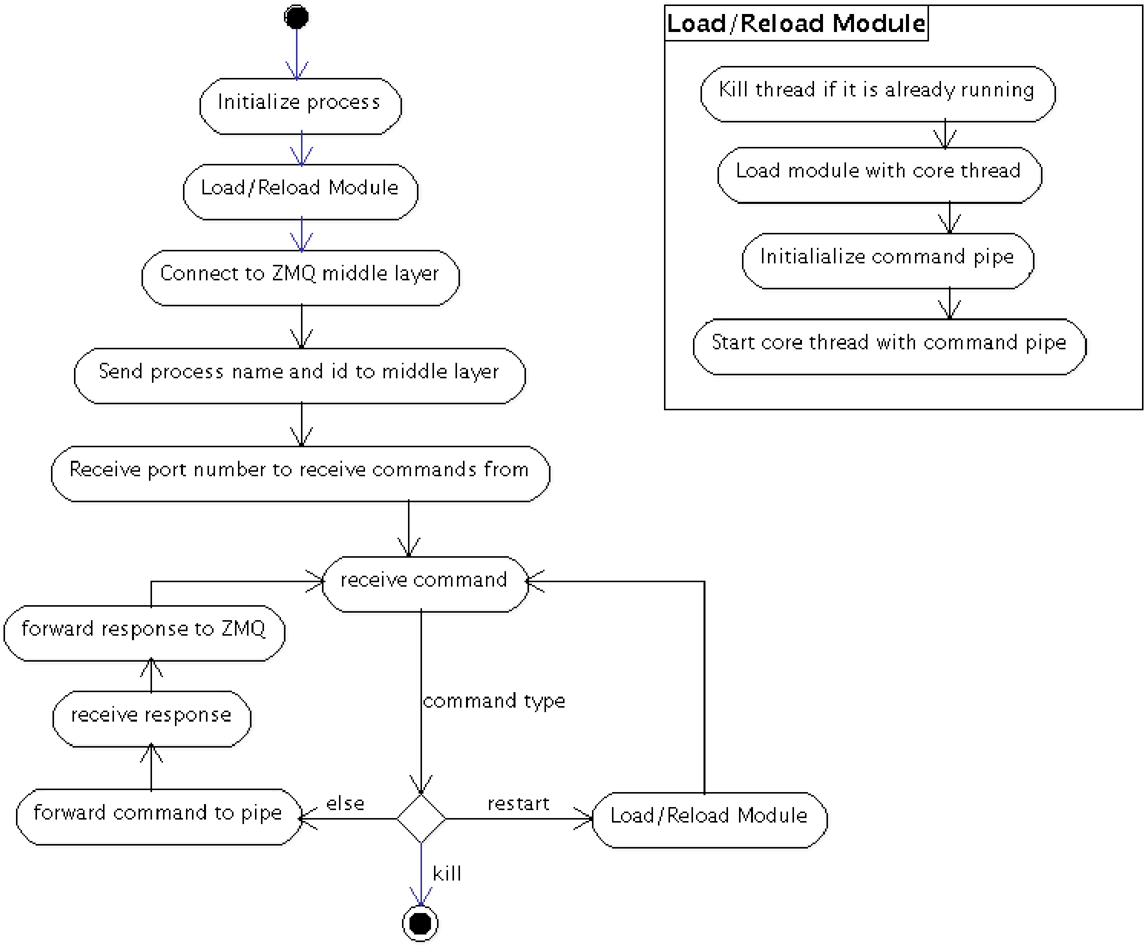

Figure 6.2: A diagram of the activity model of a ZeroMQ process.

commands and querying status. The PUB-SUB pattern involves a publisher, which sends out the same data to any subscriber. This is useful for the passing of data from the acquisition thread to an arbitrary number of analysis and saving threads. One of the most valuable aspects of this framework is that it is IP based. This means that it is possible to have different components of the framework on different machines. This feature was not required for the analysis workload in this thesis, but it makes the toolkit highly extensible for more complex problems, such as the real-time analysis of data from MMC arrays. Another valuable aspect of the ZeroMQ framework is that the threads require no specific startup order. This means that analysis packages could be added or removed from the currently running data acquisition with no impact on the core acquisition application.

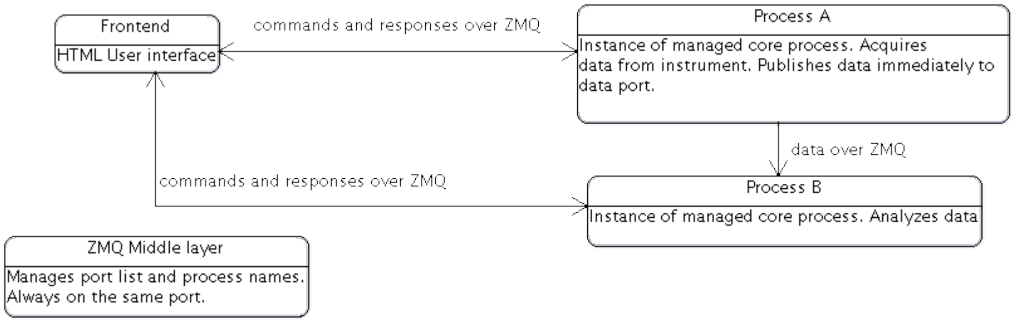

Figure 6.3: A diagram of the high level interactions between processes.

The implementation of the ZeroMQ layer consists of two primary components. The first is a middle layer process that handles the routing of commands between processes and assists in lookup of IP addresses for other processes based on their name. The second is a process that acts as the interface between the middle-layer and the core application thread described previously and diagrammed in figure 6.3. This process provides the added benefit that it makes it possible to regularly query the status of the core acquisition application and restart it if necessary. This restart process can be used for rapid development as it reloads the underlying Python code. This capability also aids in the termination of unresponsive processes that would otherwise need to be stopped manually using the operating system's task manager.

The final aspect of this data acquisition framework is the front-end, which is based on the tornado web framework. This toolkit makes it easy to write interactive web pages that respond to user events by calling Python code. One of the major advantages for this application is that it is possible to use Python code to automate the creation of repeated structures in a web-page. This is very helpful for data acquisition systems with multiple channels and triggers. This web front-end also leveraged a Javascript plotting library known as flot [94]. This makes it possible to display raw pulses to the user in the web interface.

GaGe application

Once the basic application framework was developed it was necessary to develop an application to operate the GaGe digitizer cards. This application was based on the GaGe C-API provided by the vendor. This code had to be modified slightly to be compatible with MMC data acquisition. The basic C-API read in a configuration file that, along with the basic settings for the card, also listed a total number of pulses to acquire. These pulses all had to fit in the onboard memory. After acquiring the specified number of pulses, it would return them to the C-interface and shutdown. This had to be modified to allow for continuous acquisition pulses. In addition, the provided interface had to be modified to remove a busy-wait. Without this change, at low count rates the GaGe library would consume all the processor cycles in a loop waiting for the buffer on the GaGe card to fill. With these modifications it was possible to run a basic non-interactive data acquisition.

Once this basic mode was complete, an interactive web interface to start and stop acquisitions as well as configure those acquisition parameters was added. This included configuring all four channels and eight triggers, as well as basic data acquisition parameters such as acquisition rate, pre and post trigger samples, and trigger hold-off. It was also possible to select which channels to save. As there was no information available in the API on which of the trigger thresholds was crossed, it was necessary to save all channels that may have had valid data for every trigger.

File Format

Along with the development of an application for the new digitizer cards, it was also necessary to develop a new file format due to the differences in the properties of the existing digitizers. A file format was adopted that was loosely based on the pre-existing format used for data from cryogenic detectors at LLNL. It included three basic sections: an ascii header with time and date information, an ascii copy of the configuration file used to run the acquisition, and a binary section with the raw pulses. The configuration section was based on the one specified by the GaGe API documentation. It included information relevant to the card and acquisition settings. The binary data included a 2-byte unsigned int channel number, followed by an 8-byte double formatted timestamp based off of the sample clock (Typically 2MHz), and finally an array of signed shorts representing the digitized pulse. The code used to write this file is reproduced in appendix C.

6.3 MMC Data Analysis

The analysis of MMC data uses many of the same tools that have been previously developed for nuclear pulse processing. For filtering the raw pulses there are two primary types of tools: digital filters based in the time domain and so-called optimum filters based on frequency domain analysis. The data presented in this work was processed primarily using time domain based digital filters due to the relative ease of implementation compared to the frequency filters. The exception to this were data acquired at the University of Heidelberg, where an extensive amount of work had been done to develop data acquisition and analysis tools to support the use of frequency domain based optimum Wiener filters. A comparison between the performance of these two types of filters will be shown in the results section, demonstrating that so-called optimum filters perform only marginally better than the most common digital filter and slightly worse than the cusp filter for the dataset analyzed.

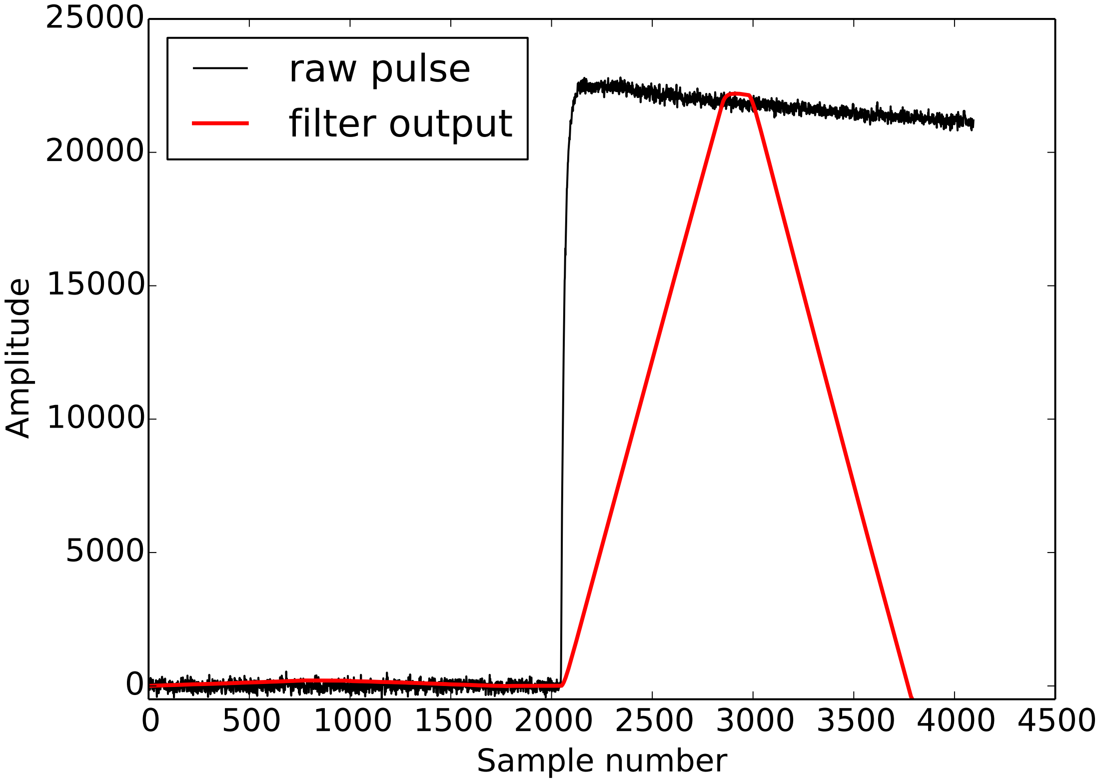

Figure 6.4: A sample raw MMC pulse and the output from a trapezoidal filter with no pole-zero correction.

Digital Filtering

The most common type of time domain digital filter used for nuclear pulse processing is known as a trapezoidal filter. It is a type of bandpass filter that can be implemented such that it only requires $\Omega(n)$ floating point operations for a signal of length n. It typically combines digital differentiator, acting as a high-pass filter, and an integrator, acting as a low-pass filter, in series. It was initially described over 40 years ago and has well understood properties [95]. The implementation used for this work is based on the implementation described by Jordanov et al.[96]. An example output of the trapezoidal filter along with the input pulse is shown in figure 6.4. This trapezoidal filter implementation is ideal because the number of loops to process the data is equivalent to the number of samples, so it could easily be implemented in a field programmable gate array in the future. Some modifications were made to optimize the resolution, including using doubles in all math with division. The code to produce this filter has been reproduced in appendix B.

All of the data used in the results was processed using a cusp filter with a gap time. Similarly to the trapezoidal filter, the cusp filter can also be implemented in a loop that is equivalent to the length of the pulse and is a combination of a differentiator and integrator. It is also included in the

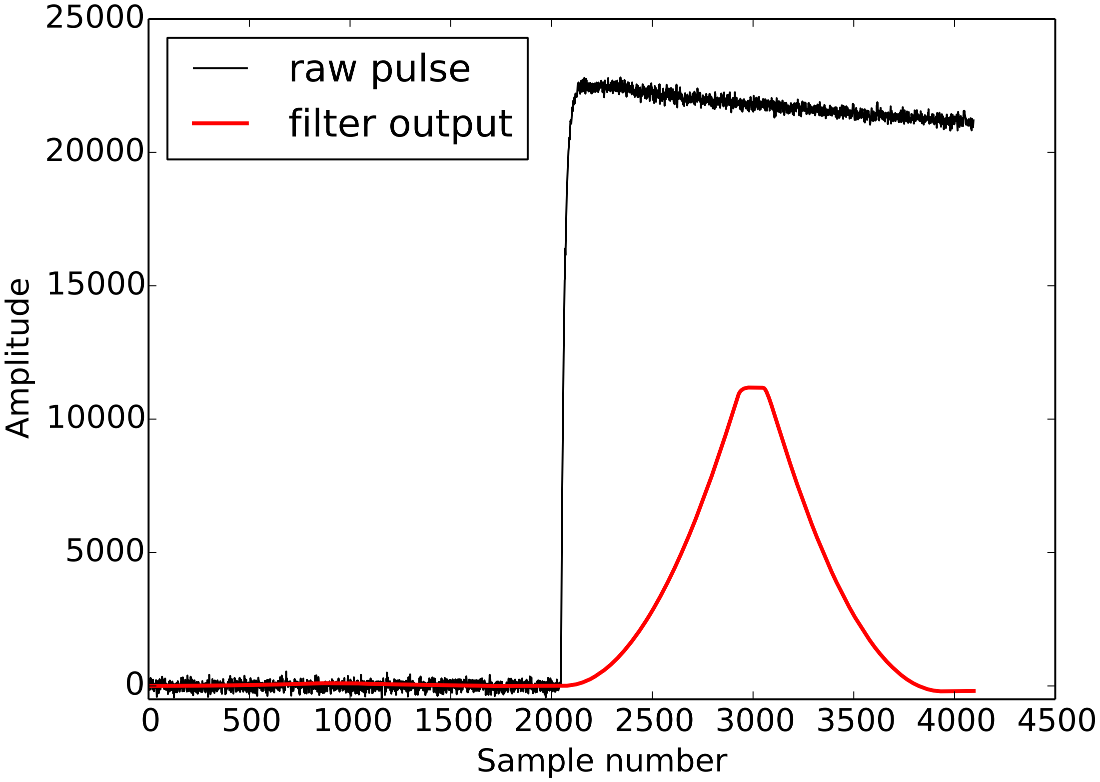

Figure 6.5: A sample raw MMC pulse and the output from a cusp filter with no pole-zero correction.

comparison of filtering techniques. It produces an output that has a cusp-like appearance, shown in 6.5. A more detailed comparison of the different filter types and their performances is provided in the results section. The code used for this filter is reproduced in B. This particular implementation with a flat-top has been previously described [96], but it is not commonly used.

The third type of digital time domain filter that was used for this work was a Gaussian-like filter. This filter approximates a classic analog Gaussian shaper that has been the standard for analog processing of nuclear data [97]. This is done using a single pole high pass filter and a 6-pole low pass filter. The output of this filter, as its name suggests, looks Gaussian in nature, which can be seen in figure 6.6. The performance of this shaper will also be compared in the results section. This filter is important for comparison because, if it works reasonably well, it could vastly simplify acquisition systems for large MMC arrays. The code used for this filter has been reproduced in appendix B.

The final filter that was used for some of this work was a Wiener optimum filter, widely used for micro-calorimetry applications [98]. This is done by first acquiring ten to fifty "characteristic" pulses and baselines. After these are acquired, each is run through a Fast Fourier Transform. This

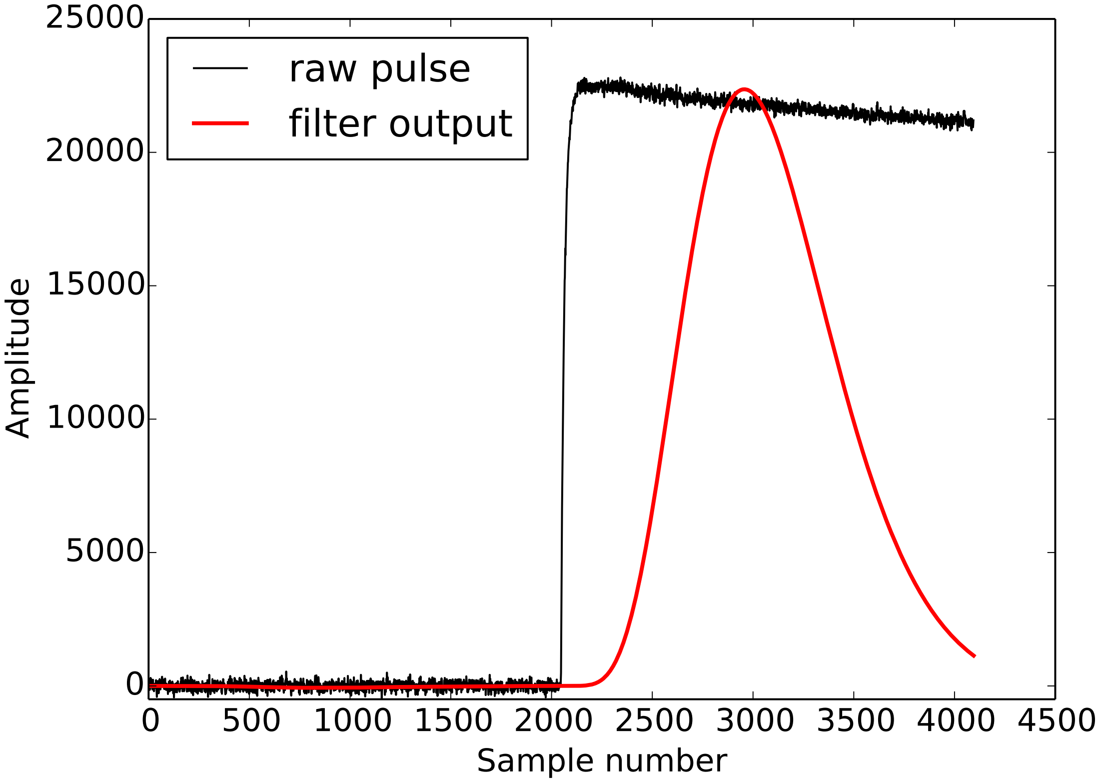

Figure 6.6: A sample raw MMC pulse and the output from a Gaussian filter.

converts the time domain information into frequency domain information. It is then possible to compare the relative magnitude of the signal to the noise in the frequency domain and compute a filter that maximizes the frequencies that have the best ratio of signal to noise. This filter is then applied to all the pulses in the acquisition. Further details of the calculation and use of this filter can be found elsewhere, as it was not used prominently in this work [98].

Linearization

One unique aspect of operating MMCs in ADRs is that, due to the fact that the optimum performance is achieved at the lowest temperature, it is desirable to run the cryostat without temperature regulation. This means that over the time of a typical acquisition of several hours, the temperature of the cryostat will change by several milli-Kelvin. This change in temperature will cause a corresponding change in pulse height. As the cryostat warms up, the signal gets smaller. A representative example of a typical scatter plot of filter output as a function time is shown in figure 6.7. In order to achieve the best possible resolution it is necessary to correct for this variation in pulse amplitude. In order to do this, two different types of windows were convolved over the events from a single peak in a spectrum: a Hanning, or raised cosine window, and a moving average window. For spectra where there was a large variation in amplitude, more than 5%, it was typically necessary to apply two corrections. The first correction was done with a broad window, roughly 500 samples wide. The second correction was done with a narrow window, typically 80 samples wide. The second correction is done for all spectra, as even temperature stabilized spectra in a dilution refrigerator show some drift in pulse amplitude over minute-long time scales. The resulting normalization curves have been plotted over the scatter plot in figure 6.8. After the normalization factor has been applied, the new flattened scatter plot can be made. This is shown in figure 6.9. After histogramming the normalized scatter plots for both windows, it was determined that the Hanning window resulted in the best energy resolution.

It is also necessary to ensure that the normalization has not skewed other portions of the spectrum. At energies below 100 keV this is not an issue. To demonstrate this, figure 6.10 shows the uranium L X-rays from a ^{242}Pu source before and after normalization using the 59.541 keV ^{241}Am gamma-ray.

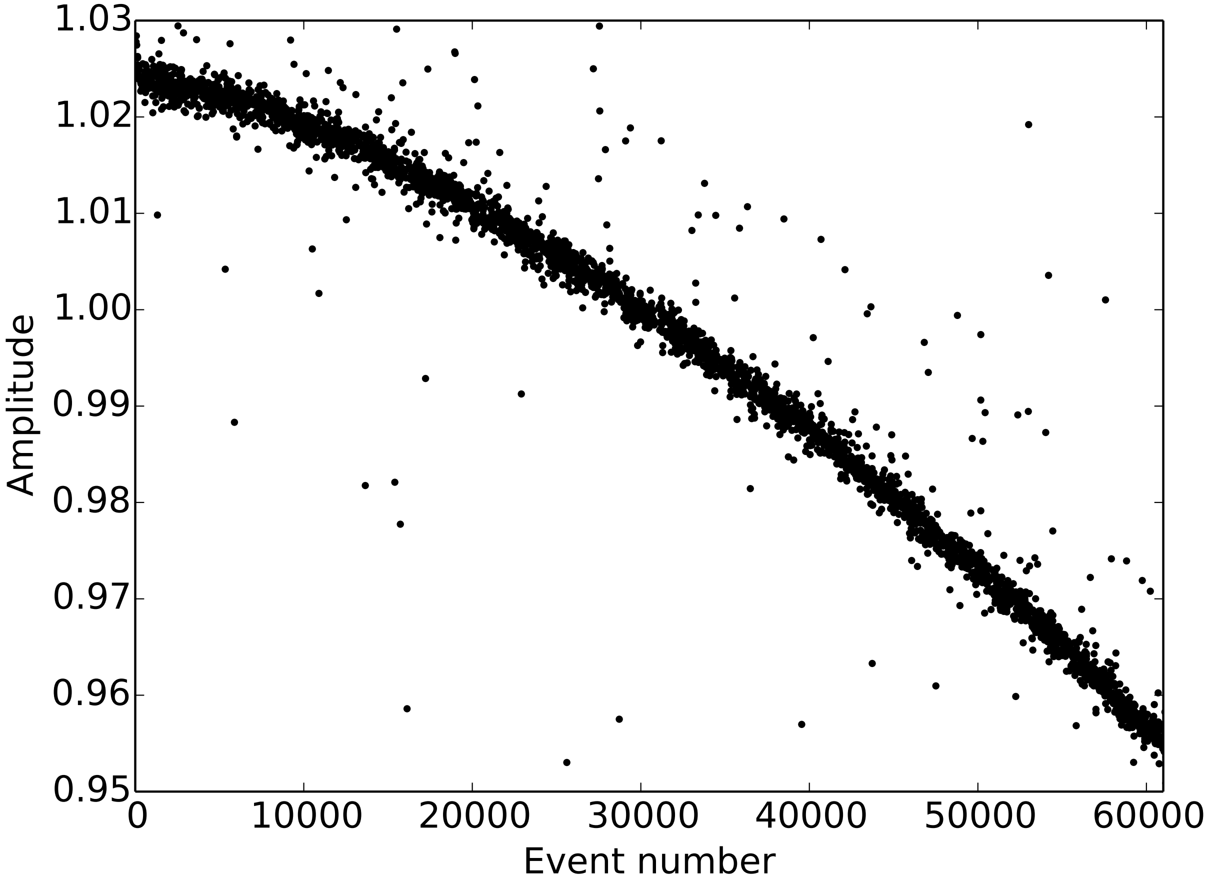

Figure 6.7: A scatter plot of filtered peak height as a function of event number showing the decrease in peak height as the cryostat warms.

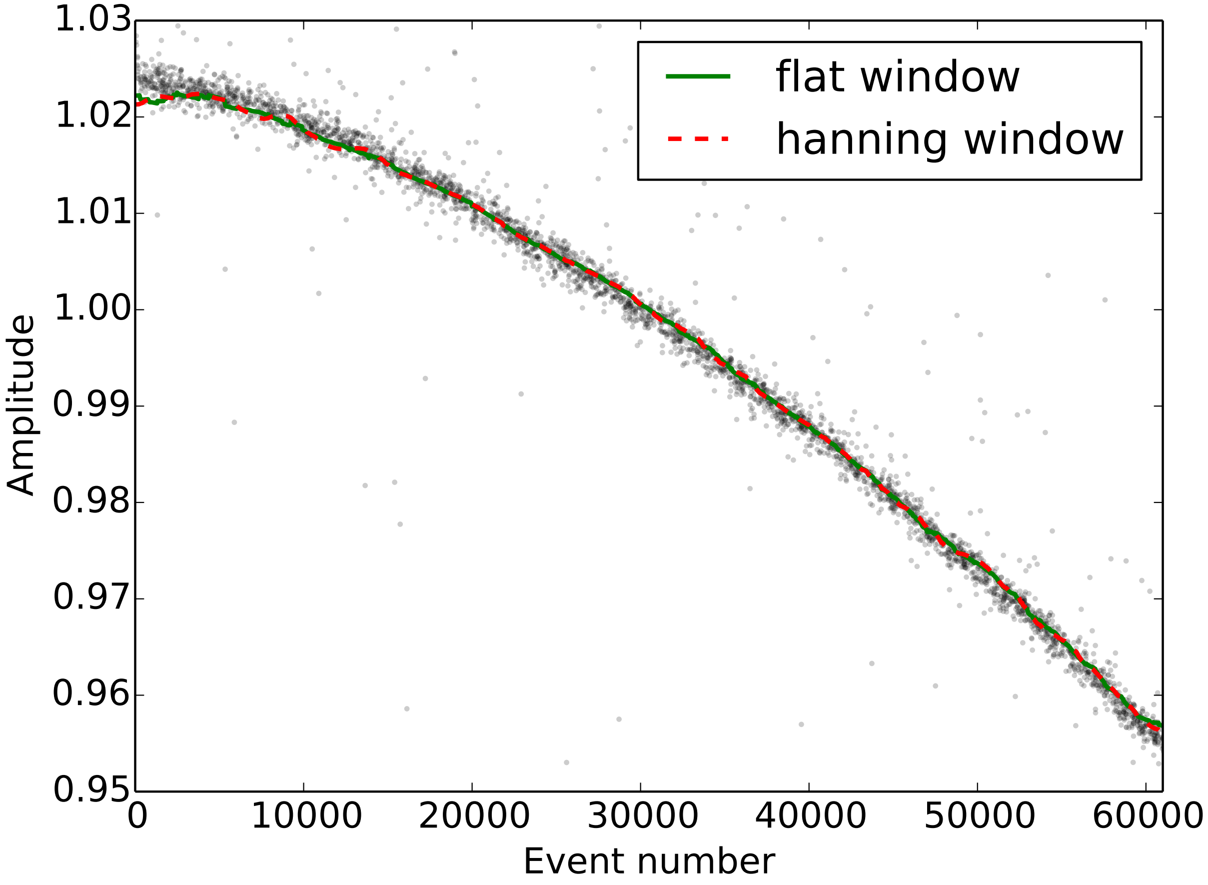

Figure 6.8: A plot of normalization curves from two different window functions overlaid on the scatter plot of peak height as a function of event number.

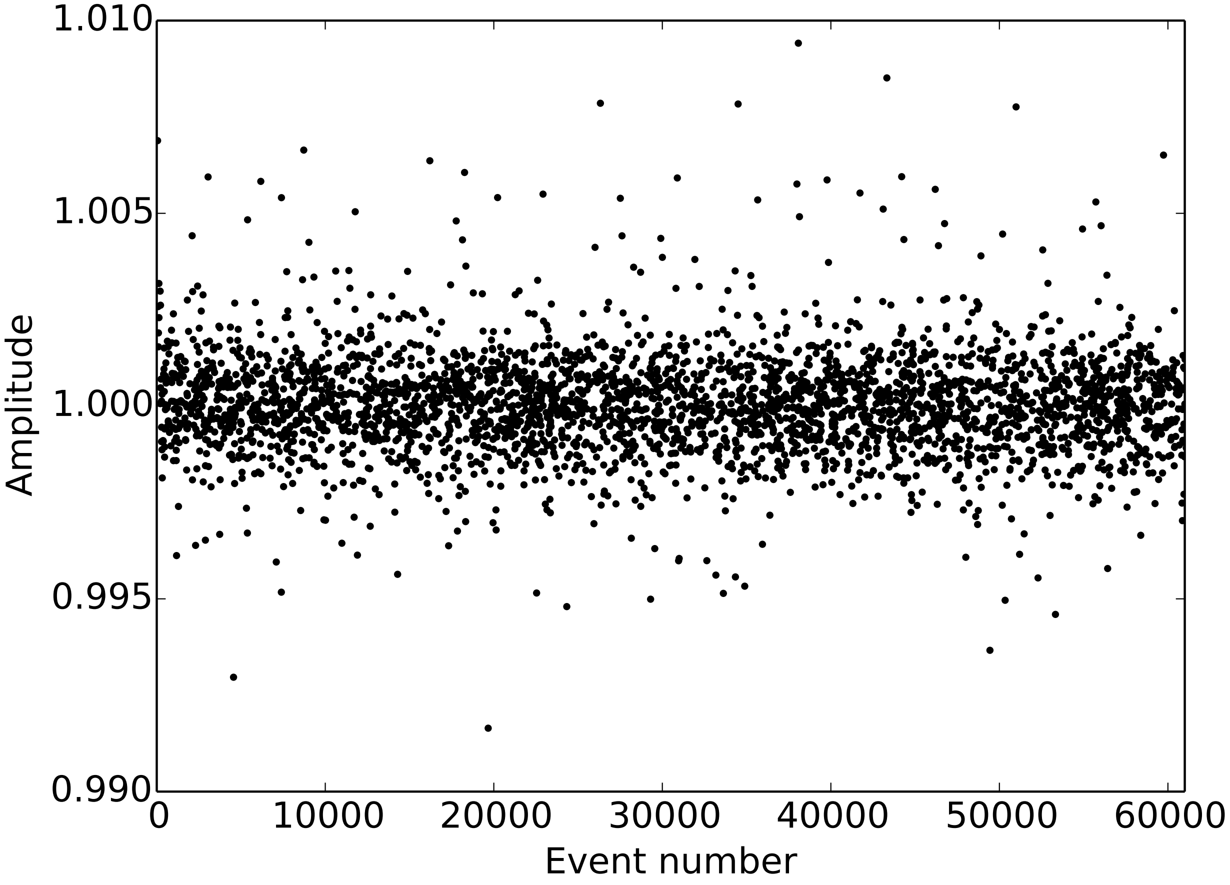

Figure 6.9: A scatter plot of filtered peak height as a function of event number after two rounds of corrections.

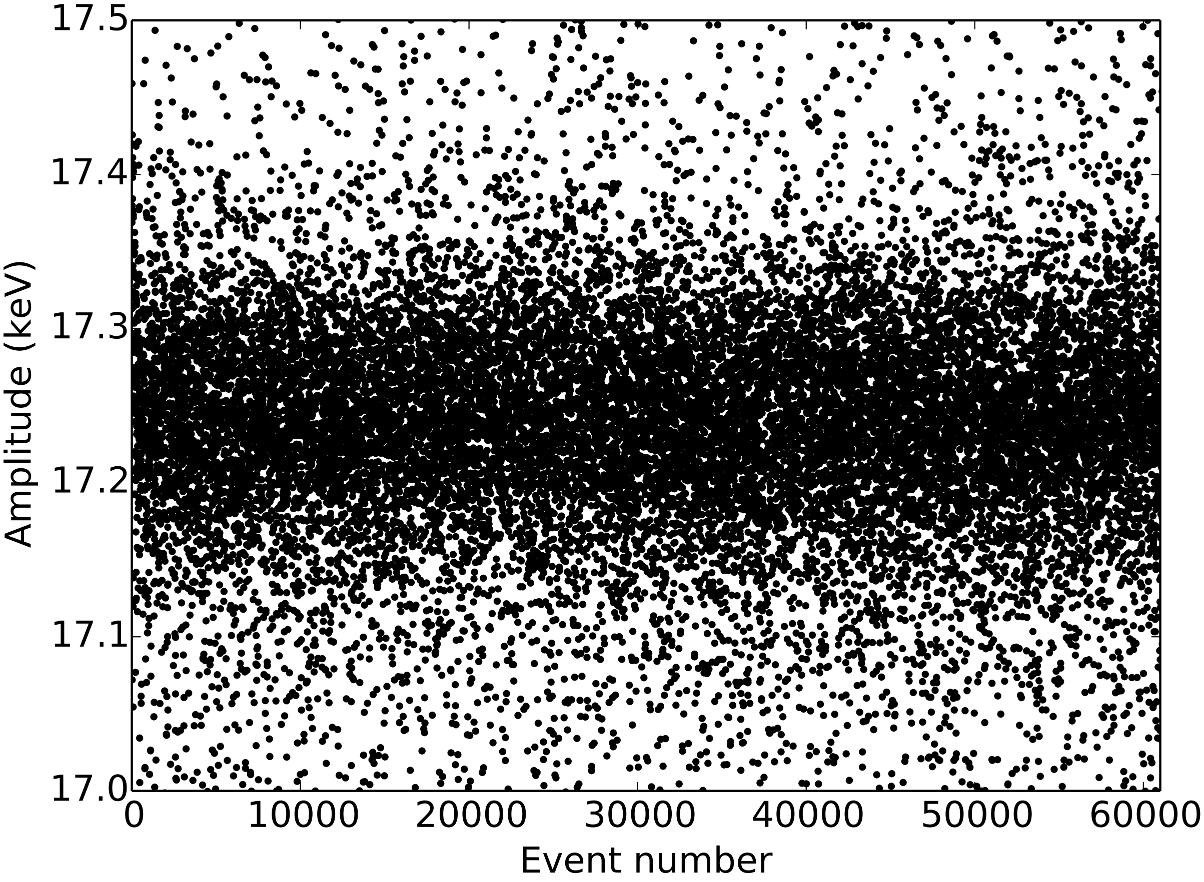

Figure 6.10: A scatter plot of event energy as a function of event number in the uranium L X-ray after two rounds of corrections applied to the 60 keV line. This shows that the X-ray lines are not distorted by the normalization procedure.

Chapter 7

Results

7.1 Introduction

In order to understand the capabilities of the gamma-ray MMC, it was necessary to first characterize it in a dilution refrigerator at the University of Heidelberg. Once that initial characterization was complete, the devices were then installed in the pulse-tube cooled ADR cryostat at LLNL described in the previous chapter and optimized for best performance. After initial optimization of the devices at LLNL, the count-rate limit, pulse uniformity, and resolution as a function of temperature were characterized. Finally, two plutonium samples were measured, one of purified ^{242}Pu and one mixed isotope sample, to determine the ability for this device to measure plutonium isotopics and combine multiple spectra.

7.2 Initial Characterization

The new gamma-ray MMCs were initially characterized by testing their performance in a pulse-tube cooled dilution refrigerator at the University of Heidelberg. This cryostat had a base temperature of 12 mK. It had a push-button cool-down system and was designed such that a single technician could disassemble it. This made it ideal for testing purposes. After leak checking the vacuum system, the system started to pump down and after approximately one hour started the pulse-tube after a sufficiently high vacuum had been achieved. Roughly 18 hours later, the pulse tube approached 3 K. As the pulse tube approached 3 K the cryostat automatically began circulating the ^{3}He/^{4}He mix between the pulse-tube and mixing chamber. This made it possible to cool the mixing chamber stage to 3K in less than two hours. At this point the cooling cycle was paused so that it was possible to measure the properties of the SQUID while the inputs were still normal. These values were compared to measurements made in a helium dipstick test at 4.2 K. After these measurements were completed, the automated cycle was resumed, the cryostat automatically began circulation of the mixture, and the cryostat cooled to its base temperature in less than 24 hours from the time that the turbo pump was started.

MMC setup

For this test, one pixel was exposed to an Am-241 source that was placed in the cryostat on the 3 K pulse-tube base plate. A picture of the configuration is shown in 7.3. In this configuration, roughly one count per second at 60 keV was expected based on the geometry. For this measurement there were two different collimators, which only allowed the source to illuminate 10 percent of the detector. A picture of the setup is shown in figure 7.2. This collimation was added to ensure that position dependent response did not degrade the resolution. The superconducting lead shield, used to block electromagnetic interference, also acted as a secondary collimator.

Pre-existing wiring was used for the persistent current and SQUID cabling. A diagram of the wiring is shown in 7.4. One important difference in this setup compared to the one at LLNL is the use of an integrated 2-stage SQUID. In this configuration, both the sensor and the array SQUID are on the same 2mm x 2mm integrated circuit. This has the advantage that there is no additional

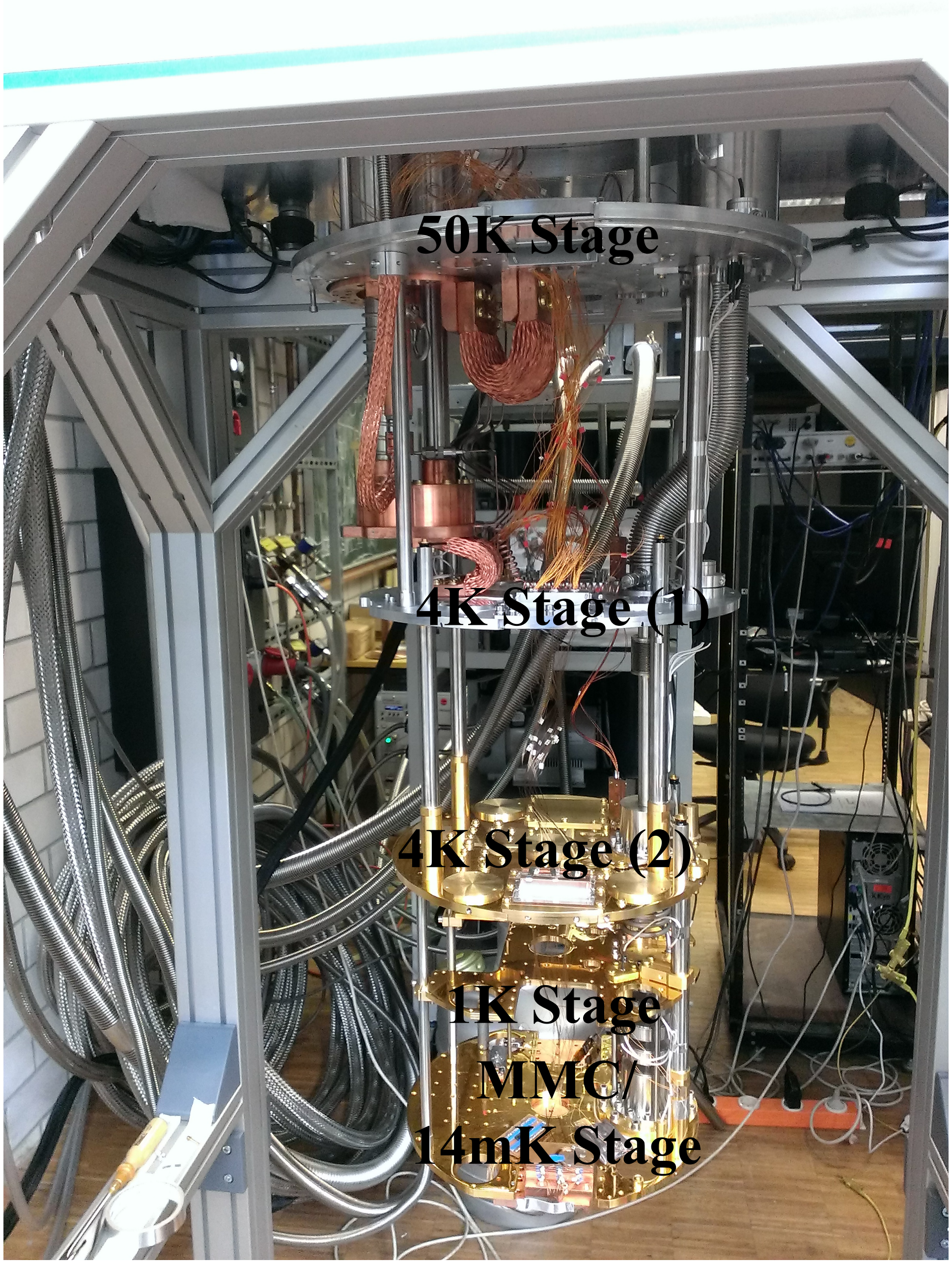

Figure 7.1: The pulse-tube cooled dilution refrigerator at the University of Heidelberg.

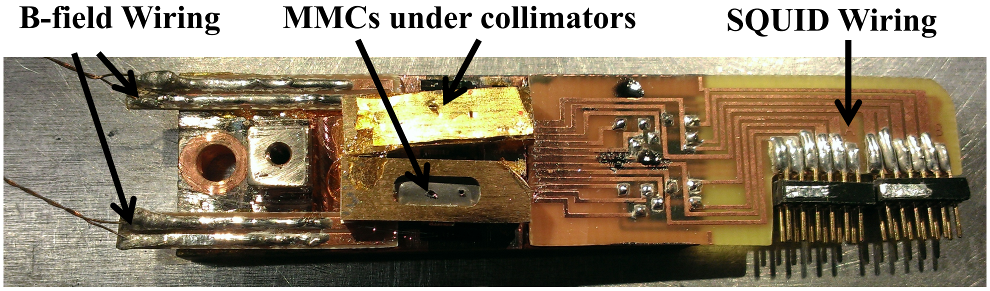

Figure 7.2: A view of the MMC experimental holder at the University of Heidelberg with two MMCs and two collimators installed.

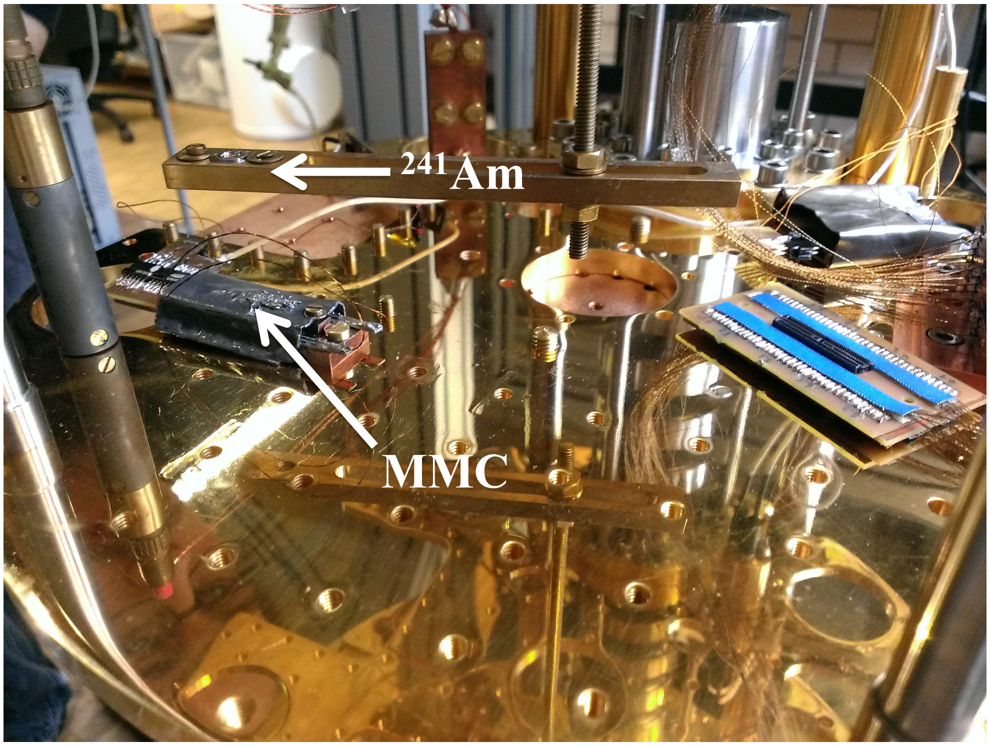

Figure 7.3: A view of the MMC experimental holder installed on the experimental stage of the pulse-tube dilution refrigerator. This shows the external lead shield as well as the ^{241}Am source installed on the 4K plate facing the collimator.

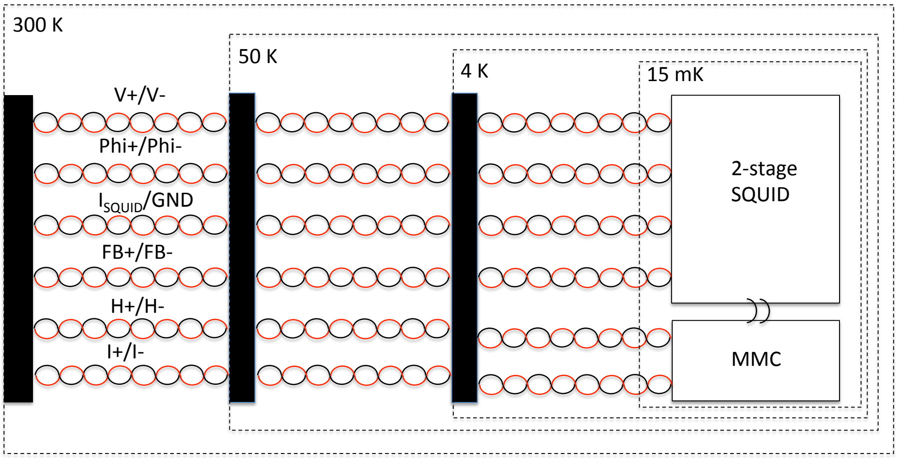

Figure 7.4: A diagram of the wiring used in the Heidelberg pulse-tube cooled dilution refrigerator.

inductance or pickup between the two stages. The downside of this configuration is that the heat dissipation makes it impractical for use in an ADR.

Results

Once the cryostat had reached its base temperature of 12 mK, it was temperature stabilized to 14 mK. Then, current was frozen into the MMC using 2 mA of heating current and 45 to 75 mA of current. Based on the pulse height of the 60 keV gammas, it was determined that the maximum current frozen in the device was approximately 45 mA. This was determined by comparing the pulse height at various different applied currents. It appeared that above 45 mA the output signal size did not significantly increase. This is likely due to excessive heating in the leads causing other parts of the chip to become normal conducting.

After the current was applied, the two-stage SQUID was tuned. Then, the output of the Magnicon preamplifier box was connected to a Stanford Research Systems (SRS) model SR560 preamplifier. This preamplifier was used to set a bandwidth limit that was roughly 1/2 that of the acquisition rate to minimize aliasing. This was typically a high pass cutoff frequency of 300 kHz with a 6 db roll-off. One of the two SRS outputs was then connected to a second SRS, which was set to bandpass mode between 10 Hz and 100 kHz. The output of the second SRS was then used to trigger the digitizer. The second output of the first SRS was connected to the digitizer.

Using this setup, baseline measurements were made of the detector performance. The primary goal was to measure the energy resolution of the device at 59.5409 keV and compare the performance of different filtering techniques described in chapter 6 with this baseline dataset.

The data acquisition system used to acquire the data was a GaGe 14-bit 100 MHz PCI digitizer with custom interface software developed at the Kirchhoff Institute for Physics for MMC data acquisition. It was triggered by splitting the input into two channels of the data acquisition card, a DC coupled channel for saving data and an AC coupled channel for triggering. The trigger was a simple level comparison set so that the fraction of noise triggers was less than 10%. This software was designed to assist in taking data suitable for analysis with an optimum filter and to perform on-line optimum filtering of the data. Prior to starting the data acquisition, the user would select 20-50 baseline pulses and 20-50 pulses from a high intensity line. These pulses would then be used to create the optimum filter. In addition, the pulse template would be used to fit all trigger events. If the events did not meet Chi-squared criteria set by the user, they would be thrown out. This software then output the raw collected pulses in binary form along with a summary of the accepted pulses in an ascii text file for plotting and further analysis. In addition to the standard University of Heidelberg pulse processing it was necessary to correct the pulse amplitude for small variations in cryostat base temperature. This was accomplished by performing a moving average window smoothing of the raw data of the strongest peak and using this smoothed function to normalize all of the pulse heights.

A plot of the 60 keV peak before and after corrections for base temperature drift is shown in figure 7.5 and the process is discussed in further detail in chapter 6. After this correction, the FWHM improved significantly from 92 to 55 eV FWHM. In addition to these corrections, it was necessary to remove some data that was initially processed incorrectly. The final result of this was a FWHM of 47.56 eV at 60 keV. Due to issues with the persistent current, this is still worse than the theoretical performance of this device at this temperature, which should be 30-40 eV, but it is still the best resolution achieved by a large X-ray MMC at this time. After the data was analyzed with the optimum filter, it was compared to the other two types of filters described in chapter 6. This was done to determine whether or not it was necessary to develop an optimum Wiener filter routine for MMC analysis at LLNL similar to the one used at the University of Heidelberg.

In order to compare the performance of the three filters, it was necessary to fit the peaks to a predicted shape. This shape is assumed to be a Gaussian with a linear background. The equation that was used to fit the peak was a Gaussian with a linear background of the form shown in equation 7.1.

$$f(x) = a + bx + c\exp\left(-\frac{(x-d)^2}{2e^2}\right) \tag{7.1}$$

In order to fit the data, the analysis package ROOT was used [99]. Within this package there is a fitting utility based on MINUIT2. This fitting utility was used along with the error calculation tool MINOS, because it provides the best error estimates. Figure 7.6 shows a comparison of the different values that were obtained for the four different filtering algorithms. The filter parameters used are shown in table 7.1. These results showed that the cusp filter was the best choice for filtering MMC data. The optimum Wiener filter should theoretically have the highest resolution, but only if the pulse shapes are uniform and the noise does not vary over the course of the acquisition. The details of the filters are described in chapter 6. The difference of the performance of all the different filters was less than 5 eV. These small differences in performance mean that when scaling this system to larger arrays, using the simple trapezoidal filter is likely the best choice. This digital filter is widely available in off-the-shelf hardware, greatly reducing the complexity required in comparison with the optimum filter, which is more traditionally used for micro-calorimetry.

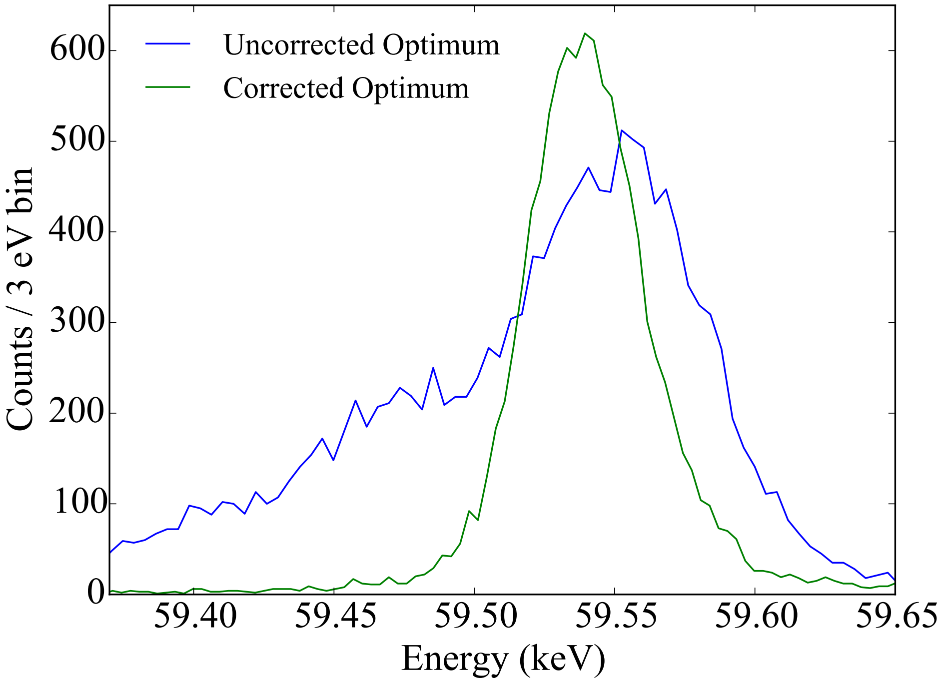

Figure 7.5: Comparison of ^{241}Am peak before and after drift corrections.

Filter	Peaking Time (μs)	Gap Time (μs)
Trapezoidal	24	2
Cusp	42	2
Gaussian	25.2	N/A

Table 7.1: Optimized values for digital filtering algorithms.

Temperature variability

The cooling power provided by a dilution refrigerator is ideally constant, but in reality it varies on timescales on the order of minutes by a few micro-Kelvin. If the current frozen in a gradiometric MMC is not evenly frozen in the two pixels or the coils themselves are not perfectly gradiometric, these small temperature variations will cause large changes in the DC output of the SQUID. In order to attempt to minimize these variations, a heater on the stage was used to regulate the temperature to 14 mK. This regulation was not ideal, as the time constants involved were long enough that it was not possible to completely eliminate the variations. This necessitated using the techniques described in chapter 6 to re-normalize the spectrum.

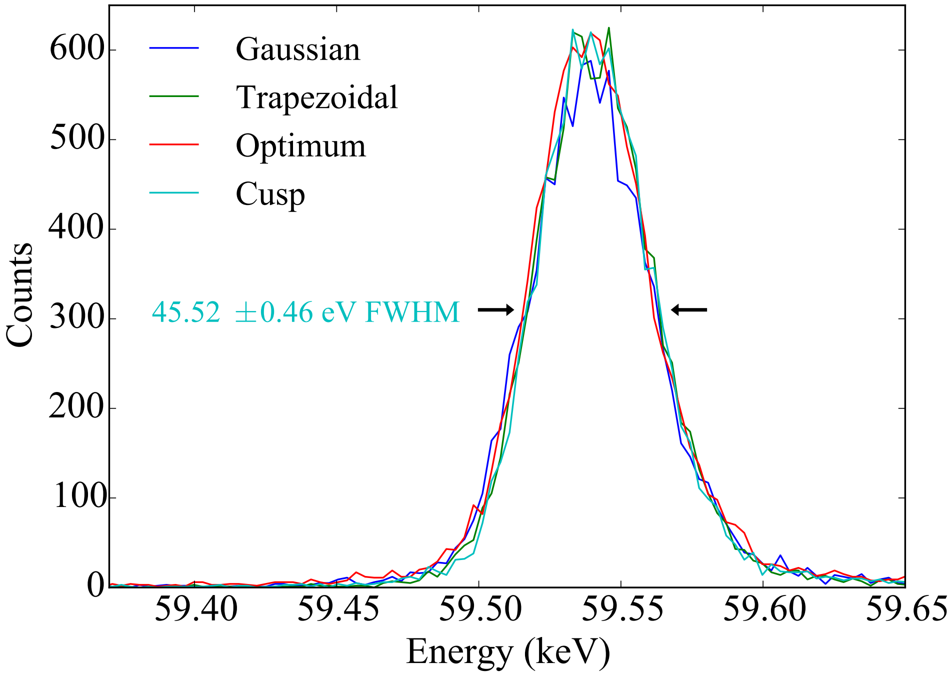

Figure 7.6: A comparison of common digital filtering techniques applied to MMC data.

X-ray spectrum from ^{241}Am

In addition to analyzing the 59.5409 keV peak from ^{241}Am, it is also possible to analyze the X-rays produced by ^{241}Am. These fall in between 12 and 27 keV. The energy calibration used was a linear fit of the ^{241}Am peak and the strongest X-ray lines. This spectrum, shown in figure 7.7, demonstrates the clear ability to separate lines spaced less than 300 eV apart and, in combination with the ^{241}Am peak, shows a clear ability to accomplish this at energies above 44.915 keV, the energy of the ^{242}Pu γ-ray that is the primary focus of this work.

7.3 Results in Cryostat at LLNL

After completing the initial characterization at the Kirchhoff Institute for Physics in Heidelberg, several of the tested devices were brought to LLNL. Due to issues with shorts between different wiring layers, only one of the devices was suitable for testing. These shorts were created during the wire-bonding of the gold thermalization layer to the copper MMC chip carrier. Due to this issue, it was not possible to use the gold wires to heat sink the device. This increased the decay time of the device from 1.5 ms at 40 mK to 16 ms at 40 mK. This has the benefit that it reduces the thermal noise contribution by a factor of 1.8, increasing the resolution by 22 eV at 40 mK. It also reduced the position dependence of the response. This is due to the fact that the metallic heat sinking was

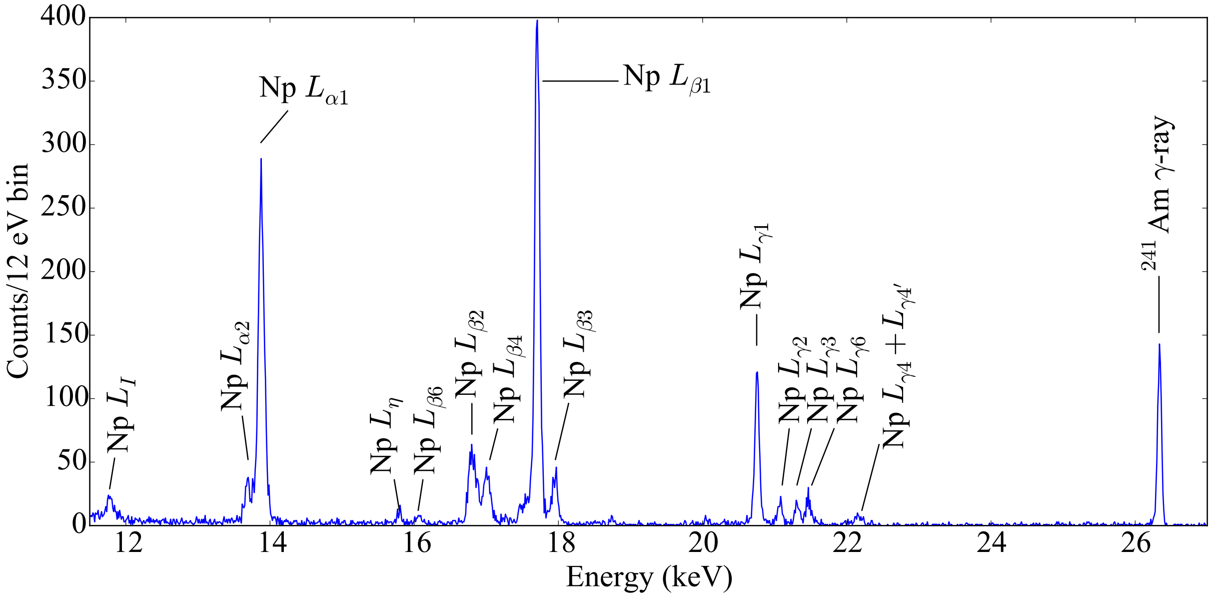

Figure 7.7: MMC X-ray spectrum from ^{241}Am taken at the University of Heidelberg.

only at one end of a rectangular device. The minimal position dependence made it possible to operate the device uncollimated. This device was installed into the cryogen free ADR described in chapter 5. This ADR is capable of reaching temperatures of 30 mK with the MMC install. In a typical cycle, a six hour measurement can be made without significant degradation in energy resolution. The mechanical design of the MMC holder is described in chapter 5. A wiring diagram of the two-stage SQUID is shown in figure 7.8. This wiring diagram differs from the one at the University of Heidelberg in that the input SQUID is next to the MMC, but the array SQUID is at 4 K. This may have reduced the usable bandwidth and increased the electronic noise in comparison to the integrated two-stage SQUID used in the dilution refrigerator. For these measurements, the MMC was installed so that it was as close to the windows of the ADR as possible, as shown in figure 7.9.

Once the cryostat was cold, it was necessary to determine the optimal parameters for the SQUID flux-locked loop operation and the data acquisition system. The first measurements were made at the maximum amplification setting of the flux-locked loop and with a data acquisition rate set such that the full waveform of the pulse could be acquired with a reasonable number of samples (16000). A diagram of the data acquisition system is shown in figure 7.10. In this setup, the SRS pre-amplifier was used to add a 6 dB single pole filter at one half of the sampling rate to ensure no high frequency signals were aliased into the data [100].

Before any optimization of the data acquisition system, the operational parameters of the flux-locked loop were varied to determine the best performance. The two primary parameters that affect performance are gain-bandwidth product and feedback resistor value. It is typically desirable to use the largest feedback resistor that is compatible with the input range of the data acquisition card,

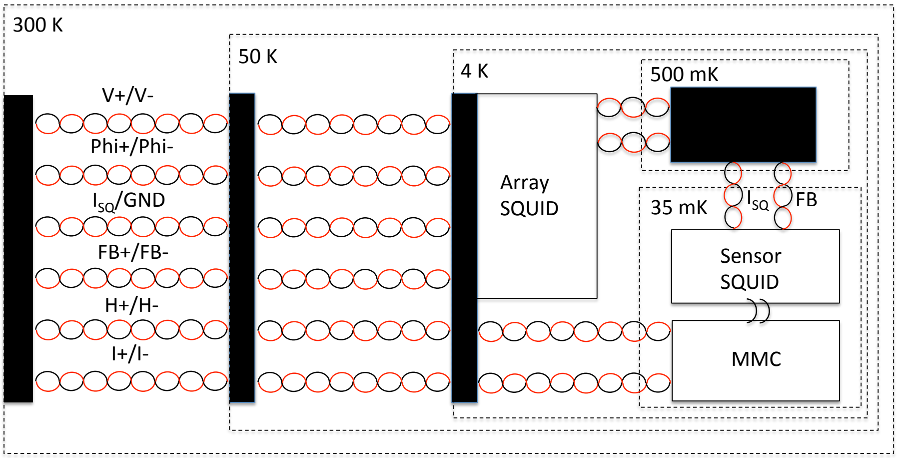

Figure 7.8: A diagram of the wiring used in the cryostat at LLNL.

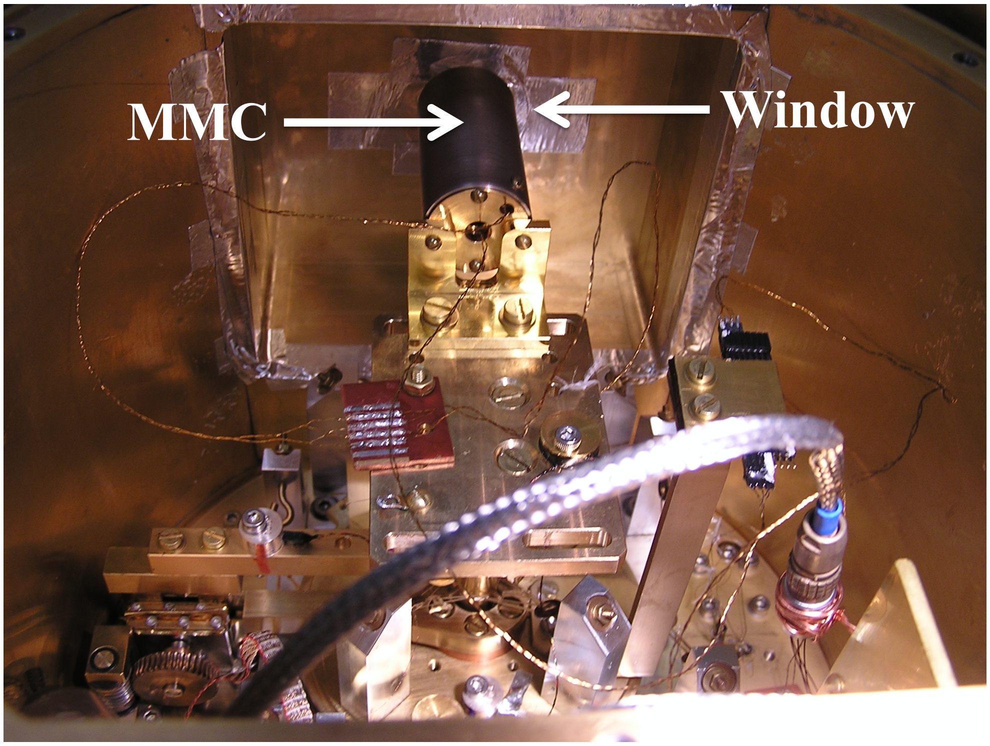

Figure 7.9: MMC installed in cryostat at LLNL for measurements of external sources.

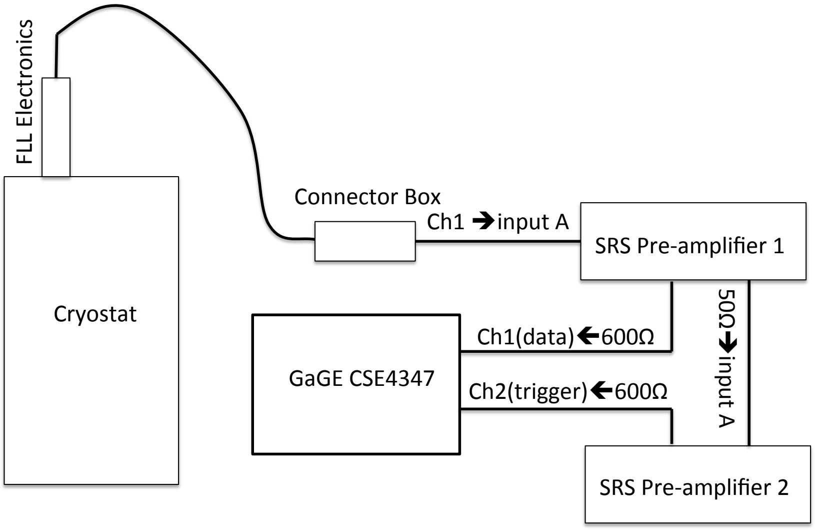

Figure 7.10: A diagram of the setup used to acquire data from the MMCs.

with the largest gain-bandwidth product that is stable to maximize the bandwidth. The relatively high operation temperature of 30-35 mK meant that it was only feasible to use the highest feedback resistor setting of 100 kOhm to have pulses that were in the range of 20-300 mV in size, which were compatible with the data acquisition system. The gain-bandwidth product was chosen by looking at the FFT of the signal from 100 kHz to 10 MHz and increasing the value until the resonance in the amplification circuit added too much noise. It was only possible to use the lowest gain-bandwidth product available in the Magnicon XXF-1 electronics of 230 MHz, because even at this value there was a significant resonance at several MHz, which could degrade performance.

Optimized spectrum in cryostat at LLNL

After optimizing the SQUID electronics, the data acquisition and filter parameters were optimized. This involved testing the MMC with the data acquisition card set at 2MHz and the digital filter peaking time adjusted from 125 microseconds to 20 milliseconds. The results of this parameter sweep are shown in figure 7.11. This measurement was done while the cryostat was at 37 mK. The best results were obtained with a peaking time of 750 microseconds. Using this optimized filter parameter for a measurement at 31 mK with a highly collimated 10 mCi ^{241}Am source roughly 30 cm away, an energy resolution of 91.3 ± 1.2 eV at 59.5409 keV was obtained. The count-rate for this measurement was approximately one count per second. This result compares favorably with

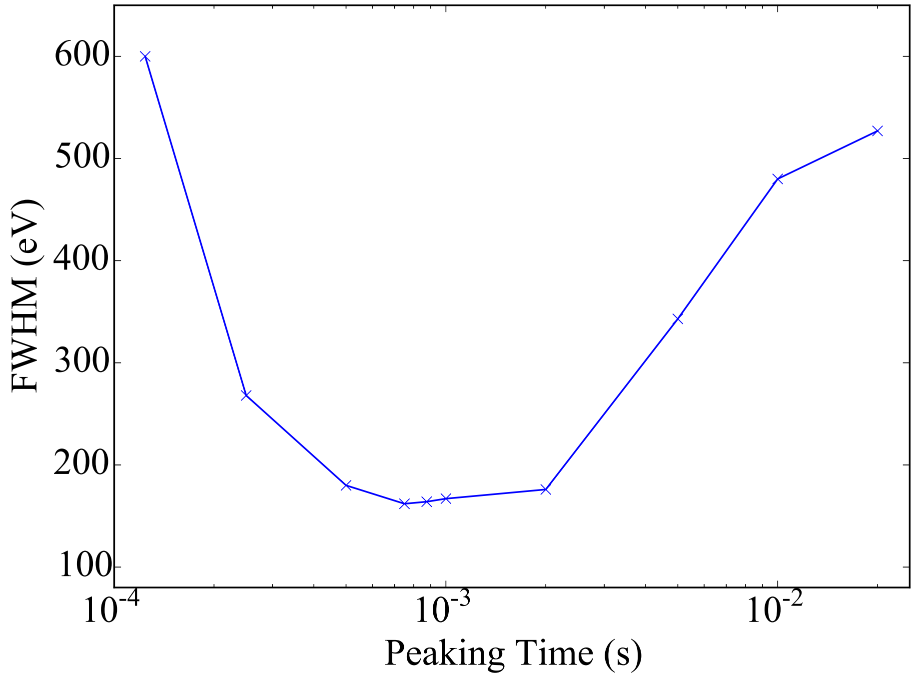

Figure 7.11: A plot of the energy resolution as a function of the peaking time of the digital cusp filter.

the performance in the dilution refrigerator at the University of Heidelberg, as it is at 2.2 times the temperature and 2.0 times poorer resolution. This is better than the linear scaling predicted by pure thermodynamic constraints. This was most likely due to the fact that the persistent current was 115 mA instead of 45 mA. The best spectrum is shown in figure 7.12. It clearly shows the ^{241}Am peak along with the two other strongest lines, both from ^{241}Am decay to ^{237}Np. This measurement was performed with diagnostic connections removed from the cryostat and all other non-essential instruments in the lab unpowered and electrically disconnected from sharing a ground with the compressor, the rotary valve, or the acquisition system (including the SR560, the SQUID electronics, and the computer with the digitizer). While this shows the ultimate achievable performance in the cryostat, it is not practical to operate it in this fashion unless a sacrifice in statistics is an acceptable trade-off for the increased resolution.

Comparison of noise model with data from LLNL cryostat

It is important not only to compare the model energy resolution with the achieved energy resolution but also to compare the individual components in so far as possible. This comparison can help to identify sources of noise that were under- or over-estimated in the model and possibly help to design future MMCs with better energy resolution. One way of doing this is measuring the noise with and without the persistent current in the MMC using a spectrum analyzer. This was done

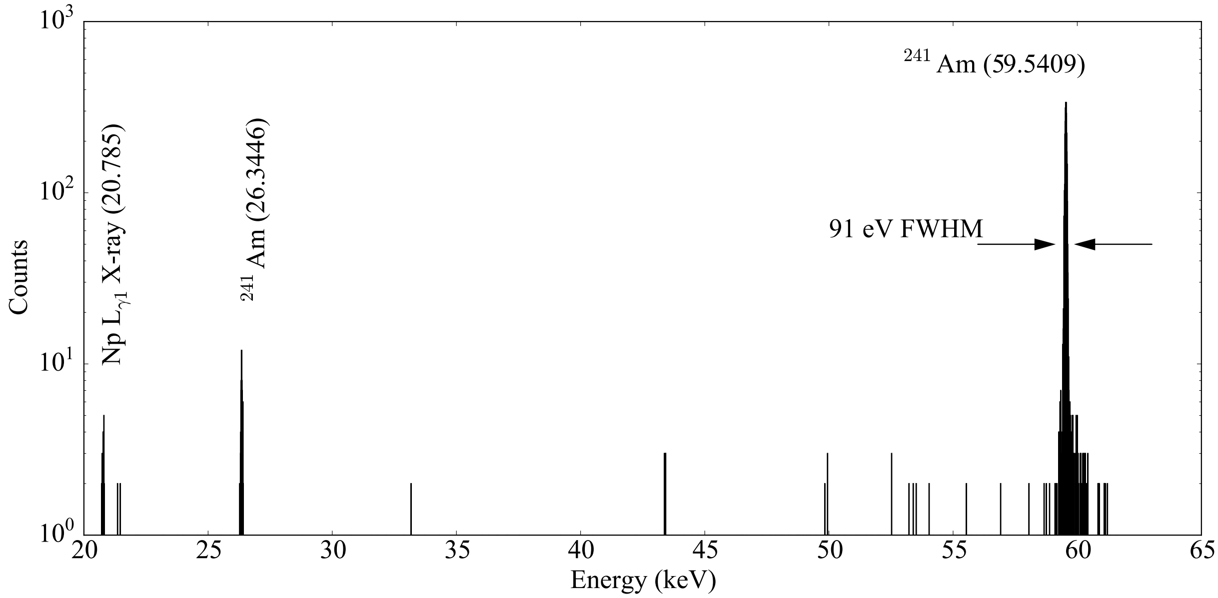

Figure 7.12: The highest resolution MMC spectrum acquired at LLNL with 91.3 eV FWHM at 59.5409 keV.

for the previous ^{241}Am measurement by taking one noise spectrum after a demagnetization cycle, prior to freezing the persistent current, and taking a second noise spectrum after a second demagnetization cycle with the persistent current frozen just prior to measurement. This requires two demagnetization cycles because the process of setting the persistent current heats up the cryostat substantially, which will affect the noise measurement. The results of this are shown in Figure 7.13. This makes it possible to determine the noise parameters of the SQUID without having to deconvolve them from the thermal and magnetic Johnson noise. The comparison shows the difference between the noise that is independent of magnetic field, the SQUID and Er $1/f$ components, and the additional thermal and magnetic Johnson noise that are added once the persistent current has been set. This can be seen more clearly by comparing the individual components of the noise model with the measured noise, as shown in figure 7.14. At frequencies above 200 Hz, the SQUID noise dominates, while at frequencies below 200 Hz the additional $1/f$ noise component from the Er ions is visible. This shows several important features. It also clearly shows the 60 Hz pickup from the AC power lines and the dominance of thermal noise at low frequencies. With the relatively good match between the model and the measured noise, it is possible to use the model to understand noise source and options to reduce them. A breakdown of the contributions of the different noise sources is shown in 7.2. This shows that thermal, Er $(1/f)$, and SQUID noise are the most significant factors in energy resolution. The thermal noise is dependent on the design, as was discussed in chapter 3. The Er $1/f$ is a function of the erbium concentration. While it is an important source of noise at temperatures of 35 mK, it is desirable, based on the model, to increase the erbium concentration because the increase in responsivity more than compensates for the in-

Source	Equation	Contribution (eV FWHM)
Er $1/f$	3.28	35.8
SQUID	3.26	29.0
Thermal	3.9	27.3
Magnetic Johnson	3.27	1.8
Total Model		69.0
Width of ^{241}Am peak		91.3

Table 7.2: Noise contributions based on University of Heidelberg MMC noise model compared with measured energy resolution. *Note: Model noise parameters do not sum in quadrature to the total model noise because the underlying terms appear in the denominator of the integral and they are frequency dependent.*

creased noise. Finally, the SQUID noise is a function of the design of the SQUID. The SQUID used for this work is the only SQUID commercially available with the combination of the input impedance and sensitivity needed for this measurement.

In addition to analyzing the sources of noise, it is also important to compare the baseline noise, ie. what is measured with the spectrum analyzer and what was modeled, with the achieved resolution. As was described in chapter 3, it is possible to use this noise spectrum and a model of the responsivity, along with an assumption of a filter that maximizes the signal to noise ratio, to predict the best energy resolution achievable with equation 3.23. This was done for both the measured noise spectrum and the noise model and compared to the best achieved energy resolution shown in table 7.2. The parameters used in the model are shown in table 3.2 and are combined with equations 3.26, 3.27, 3.28, 3.9, 3.33, 3.35, 3.36, 3.17 and 3.23 to calculate the energy resolution. The model and measured baseline noise agree well, as can be seen in the figure 7.14. There is a significant difference between these and the measured width of the ^{241}Am peak, however. This could have multiple causes. The most straightforward explanation is the presence of imperfections in the temperature drift correction. A second possible reason is that the cryostat is warmer than the thermometer readout by several mK. It would take a difference of less than 5 mK to explain the difference in performance. This would not have a drastic effect on measured noise, but it would have a significant effect on the signal size. It would be difficult to tell in the noise spectrum if this was the case, because the heat capacitance would increase but the coupling to the SQUID would decreases, resulting in little change in the measured noise spectrum.

MMC heating in tests at LLNL

Over the course of several months of taking data, it was apparent that on occasion there would be a slight downward trend in pulse-height during the first 20 seconds of data acquisition. This could be attributed to equilibration of the MMC and SQUID, as the input SQUID generates a small amount of heat through its shunt resistors. The pulse height as a function of time was fit to an exponential decay shown in figure 7.15. Based on the slope of the change in pulse amplitude as a

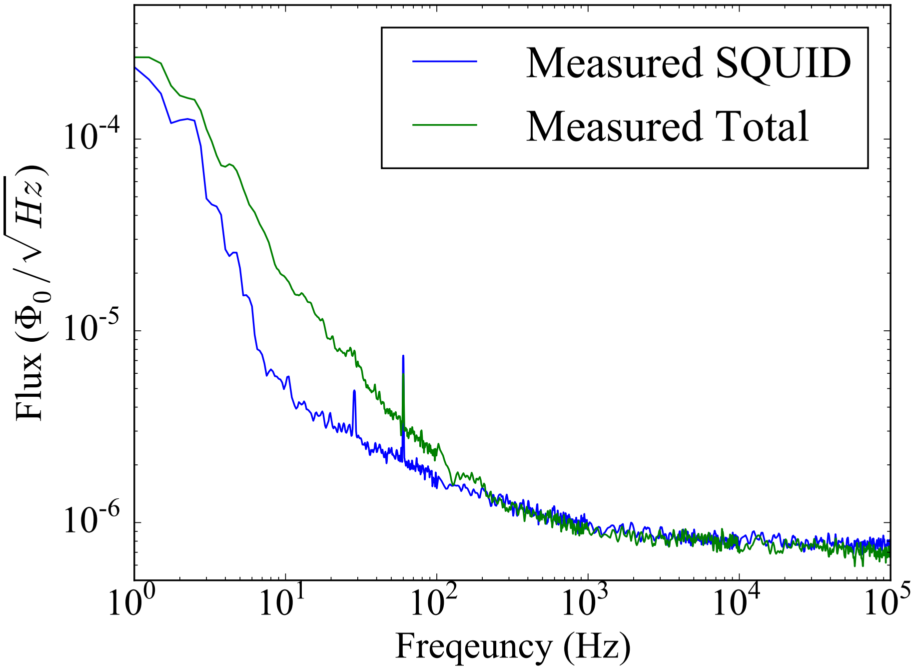

Figure 7.13: Comparison of noise with and without persistent current.

function of time and the known change in pulse amplitude as a function of temperature from [75], it is possible to calculate the starting temperature. Assuming the most likely case of 10 seconds between the SQUID being turned on and the MMC acquisition starting, this corresponds to 119 μK colder starting temperature. If there were a full minute between the power-on of the SQUID and the start of data acquisition, this would correspond to a starting temperature 1.90 mK colder. In this extreme case, it could degrade the energy resolution from increased heat capacitance and smaller signal by up to 9 eV FWHM. One possible advantage of adding a metallic thermal link is that it may eliminate this heating, but the reduced decay constant will likely have a larger negative affect, degrading the resolution by 18.1 eV FWHM from additional thermal noise.

7.4 Resolution as a Function of Count-Rate

In order to minimize the counting time required to have good enough statistics, it is desirable to count at the fastest rate possible that incurs a minimal loss in energy resolution. In order to determine the maximum possible counting with the device used at LLNL, an external 1 mCi ^{241}Am source was placed at successively closer distances to increase the observed count rate in the detector. A 10 mCi ^{241}Am source was placed at successively closer distances to the MMC starting at approximately 30 cm and ending at 10 cm, so that count rates in the detector of 2 Hz, 6 Hz, 16 Hz, 30 Hz, and 60 Hz were observed. The measurement time at each rate was adjusted so that the

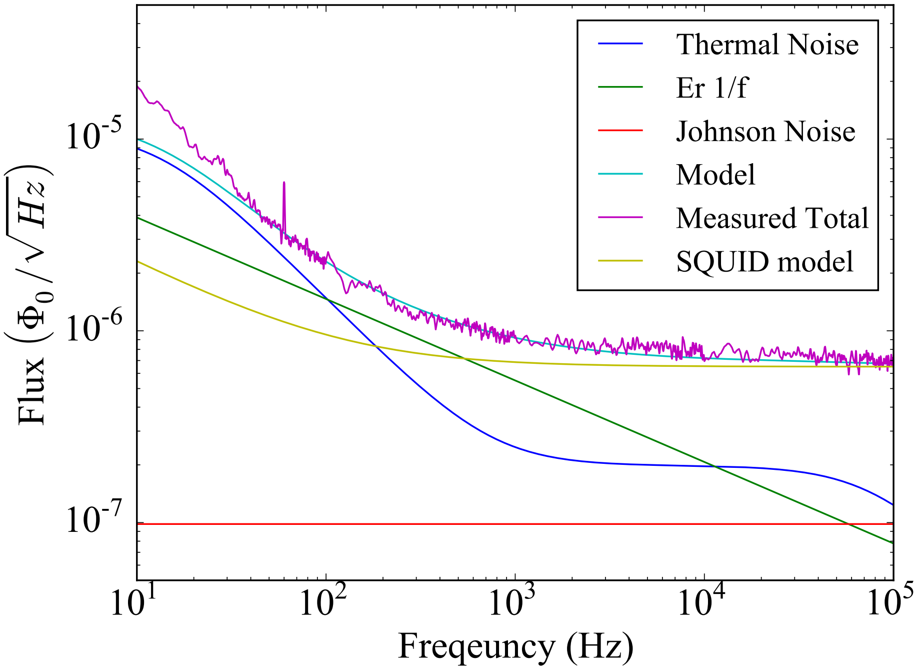

Figure 7.14: Comparison of model noise with measured noise spectrum.

total number of counts in the 59.5409 keV peak was approximately the same, roughly 3000. This allowed for a high accuracy measurement of the energy resolution while minimizing effects from temperature drift.

The resulting energy resolution as a function of count-rate is shown in figure 7.16. This shows that at all but the lowest count rate there is significant degradation in energy resolution. The primary cause of the decreased resolution is pileup. Due to the lack of metallic thermalization connections, the time constant of the thermal decay is 15.2 ± 0.1 milliseconds. This means that it takes hundreds of milliseconds for the pulse to decay back to the baseline. This results in an expected count-rate with minimal pile-up on the order of 1 Hz, in agreement with observation.

Possible count-rate improvements

There are two methods for improving the achievable count-rate for future measurements. One is to make a normal conducting thermal link. The other method is to improve the data processing to account for pileup. A combination of these techniques may allow future devices to achieve count rates of 10's to hundreds of counts per second.

Making a conductive thermal link between the absorber and the thermal bath could reduce the decay constant to roughly 1 ms without significantly impacting performance [75]. The detectors used in this work were originally designed to have conductive thermal links, but all attempts to

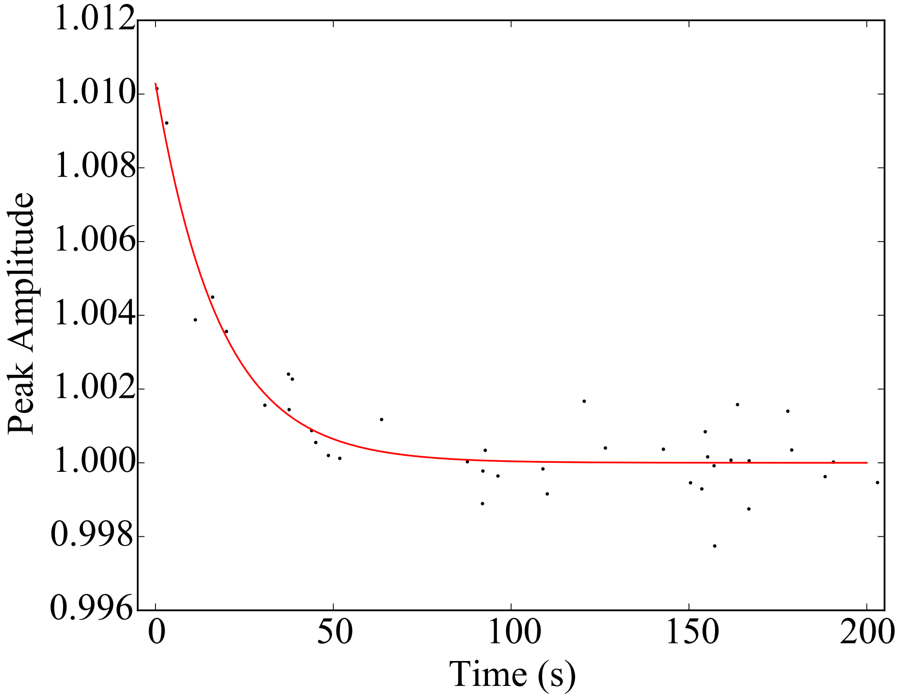

Figure 7.15: A plot of the pulse height as a function of time immediately after turning on the data acquisition system.

make this thermal link produced shorts in the devices' wiring layers, rendering them unusable. In addition, adding the thermal link would introduce a more significant position dependent response, which would likely degrade the detector performance to unacceptable levels in this cryostat. There are multiple solutions to this including operating at a lower temperature and design improvements to minimize this effect.

It may be possible to improve the tradeoff of count-rate to energy resolution by accounting for the exponential decay of the previous pulse in the pulse being measured. This has been done in the past in commercially available data acquisition systems [101]. This particular application is unique, however, because pulses in a single channel have both positive and negative polarity. Current systems are only capable of handling single polarity pulses and would have to be adapted for MMC readout.

7.5 Temperature Dependence in Energy Resolution

The energy resolution of an MMC that is dominated by thermal noise should in theory vary linearly with temperature. In reality, as the signal gets smaller other noise can reduce the performance further. Understanding this correlation is important for the design of future devices as higher operating temperatures could reduce the cost of cooling a larger future array. In addition, higher

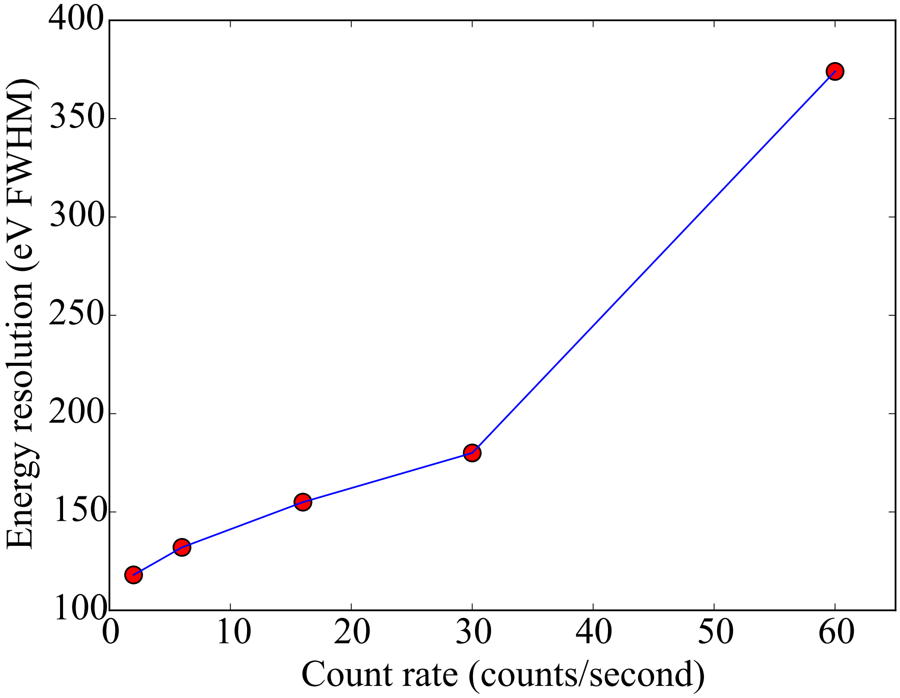

Figure 7.16: A plot of the energy resolution at 59.5409 keV as a function of count-rate.

temperatures lead to shorter decay times, so they would make it possible to operate the MMCs at higher count-rates. In order to understand this effect, the data acquisition system was left on as the cryostat at LLNL warmed from 35 to 60 mK, at which point it became difficult to discern the peak from background noise. The data was then split into five different sections and analyzed separately. In addition to this data, the data from the best run at LLNL, the best run at Heidelberg, and a run that was temperature stabilized at 40 mK at Heidelberg are plotted in figure 7.17. The error in FWHM was determined based on the fit of the peak in ROOT. This graph shows that below 50 mK the decrease in performance as a function of temperature is relatively linear, but at temperatures above 50 mK the performance starts to degrade rapidly. This sets an important limit for future system designs.

7.6 Measurements of a Pure ^{242}Pu Source

Prior to measuring a mixed isotope plutonium source, a ^{242}Pu source was prepared with minimal amounts of other plutonium isotopes. This source did have ^{241}Am such that the ratio of the line intensity of the ^{241}Am to ^{242}Pu was roughly a factor of ten. This is a first order test to demonstrate that scatter from the ^{241}Am will not obscure the ^{242}Pu. In addition, due to the fact that the source had lines from 12-110 keV it was also a useful means to determine both linearity and test the possibility of summing multiple spectra.

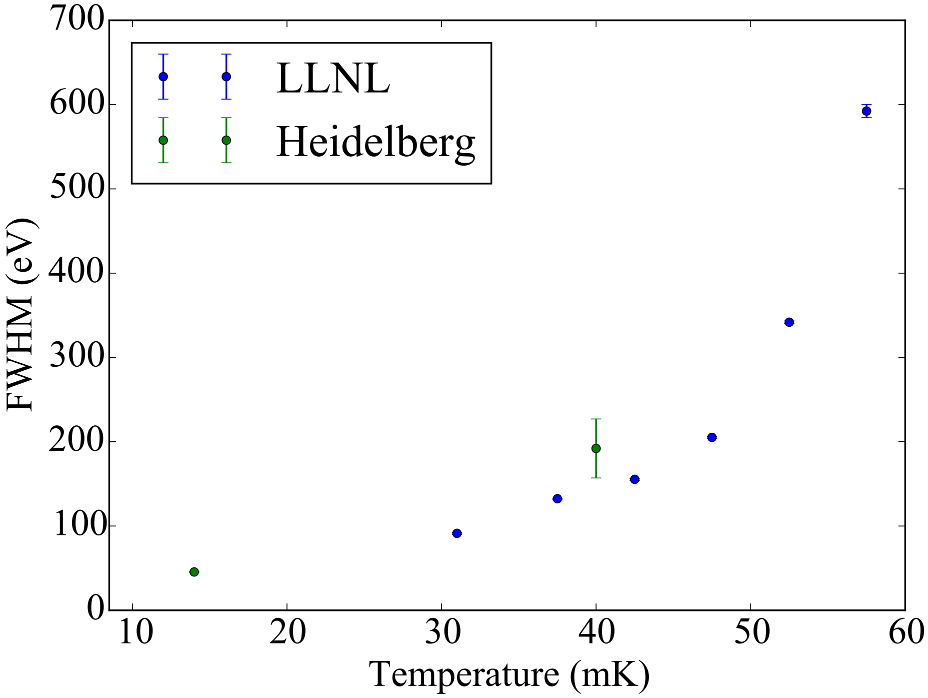

Figure 7.17: A plot of the energy resolution at 59.5409 keV as a function of temperature. The metallic thermal link used in the experiments at the University of Heidelberg result in a decay constant that is 10 times shorter. This reduces the energy resolution by 6 eV at 14 mK and by 22 eV at 40 mK.

Due to limitations in the amount of plutonium that could be used in our lab, as well as the limited amounts of isotopically separated ^{242}Pu available, the source used for this measurement was only 1 mg in size. The activity of the ^{242}Pu in the source was approximately 3.9 μCi. This low activity meant that it was necessary to install the source onto the pulse-tube base plate. Figure 7.18 shows the ^{242}Pu source installed directly in front of the MMC holder.

This source was measured over 16 days using a single gradiometric MMC with two pixels. The performance of the cryostat was such that it was only possible to run for approximately eight hours before reaching a temperature of 37 mK and needing to restart an ADR cool-down cycle. This measurement was primarily performed remotely, as both the pulse-tube refrigerator as well as the data acquisition system and SQUID control could be accessed via remote desktop. In an additional test of the reproducibility of the MMC performance, half of the measurements were taken after warming the system to 300 K and then cooling it back down to base temperature.

Prior to adding any of the spectra together, the resolution of the ^{241}Am line was measured by fitting a Gaussian with a linear background to the peak for each spectrum. Ideally, the resolution should be the same for both pixels, assuming the same amount of current gets frozen in both meanders and both are identical. However, one pixel was consistently better than the other. This is

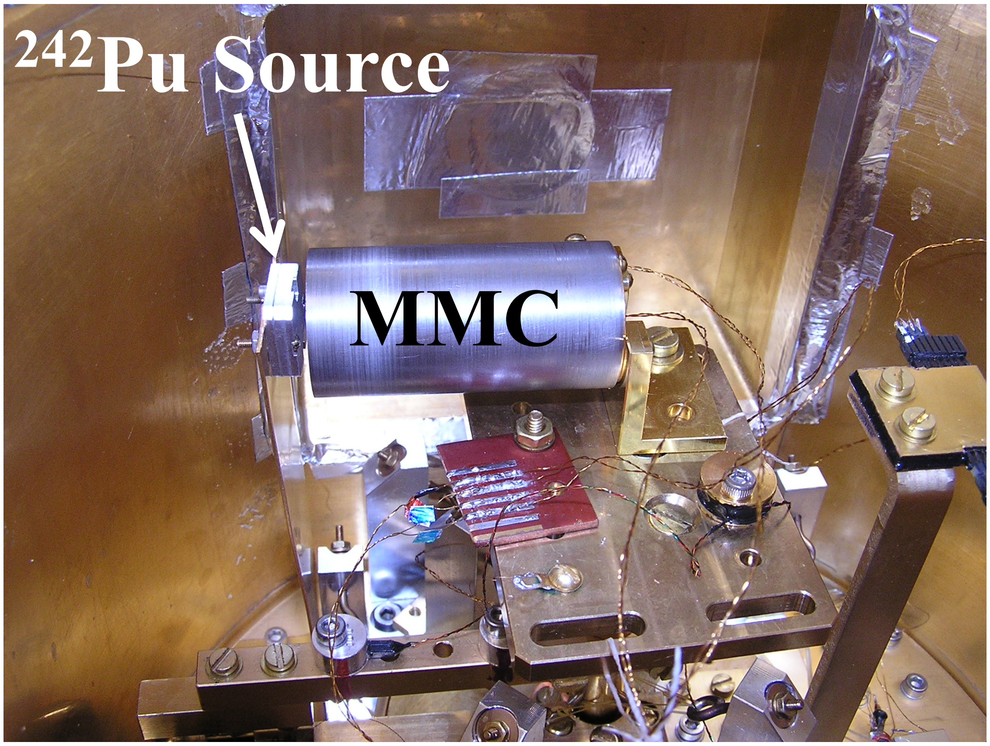

Figure 7.18: MMC installed in cryostat at LLNL for measurements of a pure ^{242}Pu source.

likely due to slight imperfections in the fabrication process that make the two pixels not perfectly identical. In addition to the resolution differing between the pixels, it also was not as good as the best single spectrum taken with an ^{241}Am source. This can be attributed to several factors. The first is that these measurements were made at a higher temperature, 35 mK vs 31 mK, due to reduced performance of the cryostat during this measurement. The second was that, due to the automated nature of these measurements, it was not possible to isolate the cryostat from external noise sources. Finally, optimizing the resolution of an individual spectrum is much simpler than optimizing the resolution of 32 spectra and it was necessary to develop a generic set of parameters that worked best for all of the spectra. The result of these three factors meant that on average the resolution was 55 eV poorer, 146 eV FWHM at 59.5409 keV. The resulting combined spectrum is shown in figure 7.19. One unique aspect of this spectrum with implications for its use in advanced safeguards concepts is the ability to see the iodine X-ray lines. This is a signature that the acid HI was used in the purification process.

7.7 Position Dependence

Previous versions of the hard X-ray MMC used for this work were known to have significant position dependence in their response. This had two primary causes. The first was that the absorber was fabricated directly on top of the sensor. This meant that the sensor started heating up before

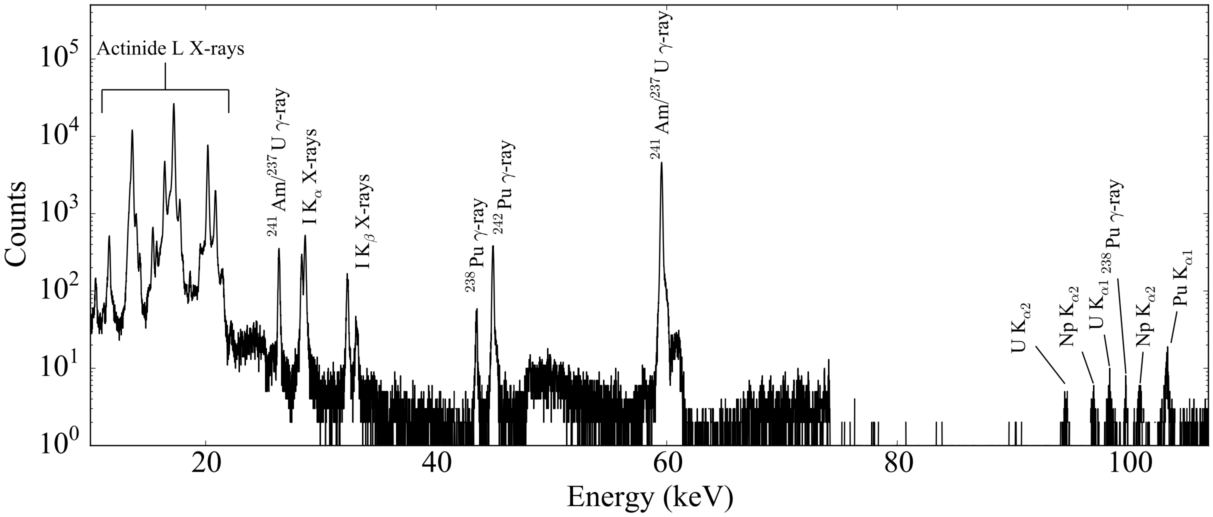

Figure 7.19: Plot of the combined spectrum from the purified ^{242}Pu source.

the temperature in the absorber equilibrated, which led to a position dependent response. The second cause was the metallic link between the thermal bath and the device. Due to the fact that this was only at one end of a rectangular device, the device response changed based on how far away the interaction was from the thermal link. The first of these issues was solved by separating the sensor from the absorber using micro-fabricated gold posts in a process described in chapter 4. The second of these issues involves a trade-off between sensor speed and uniformity, discussed previously in this chapter. Due to the fact that the resolution in typical conditions in this cryostat was close to the limit of what was needed to directly measure ^{242}Pu, 145 eV FWHM, it was not desirable to trade count-rate for resolution.

In order to determine if there was any position dependence in the response of the detector as it was configured at LLNL, 1000 pulses from the 59.5409 keV peak were plotted after being scaled to have the same filter output. Figure 7.20 shows that there is no discernible difference in pulse shape. This suggests any position dependence is very small making it possible to run this device uncollimated, significantly improving the solid angle from previous work using this device. To determine if there is a subset of outlier pulses that correspond to events that occur at the ends of the absorber and thus have a different peak shape, all of the events were fit to an exponential rise and fall of the form:

$$f(t > 0) = \beta(\exp(-t/\tau_1) - \exp(-t/\tau_0)) \tag{7.2}$$

The reduced Chi-squared was calculated for this fit for all of the pulses. The pulses that had a reduced Chi-squared in the top 25th percentile were highlighted in red in figure 7.20. There is no discernible pattern in the red pulse shapes, which is consistent with no measurable position dependence. The position dependence in the previous version of this device with a metallic link and without posts showed very distinct differences in pulse shape on the same scale [75].

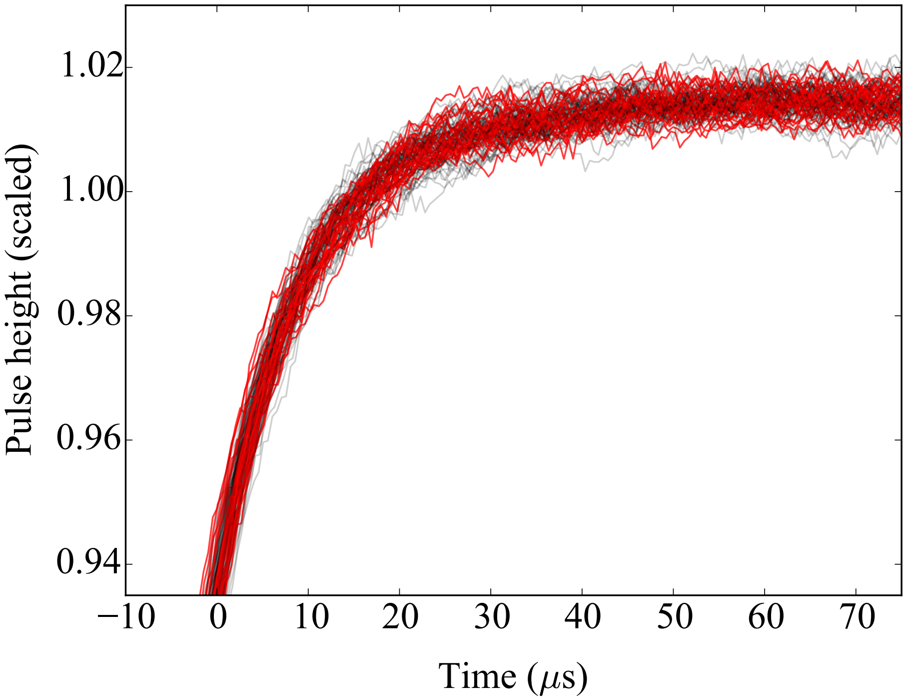

Figure 7.20: Overlay of 1000 pulses from the ^{241}Am 59.5409 keV peak showing lack of position dependence. Pulses in the top 25 % of the χ^2 distribution have been highlighted in red.

Direct sensor hits

Some photons interact in the Au:Er thermometer instead of or in addition to the absorber. These events have a very characteristic pulse shape, which can be seen in figure 7.21. These pulses, when shaped with an optimized cusp filter, have a different amplitude than the events which occur in the absorber. These pulses can be filtered out of the dataset by taking the ratio of a short trapezoidal filter and a long trapezoidal filter. By plotting the output of the two different filters for each event, we can determine what limits to set. Figure 7.22 clearly shows the three different categories of events. This ratio can be used to remove all events where the ratio is above a certain value. This can effectively remove all the direct sensor hits and most of the partial sensor hits. Partial sensor events account for approximately 10 % of all non-noise triggers in this spectrum. These events drop off in rate drastically for events where the total energy deposited is greater than 25 keV. This large rate and energy cutoff implies that theses are not multiple scatter events. One possible explanation is that these are events that occur in the thin gold thermallization strip that connects from the sensor to the edge of the chip. These events do not have a simple energy distribution, but on average they are approximately one percent lower in energy than the centroid of absorber events. The direct sensor events make up approximately 3 % of all non-noise triggers in this spectrum. These events have a centroid that is approximately 1% higher than the absorber hits. These may slightly degrade the energy resolution and add a high-energy tail. These events appear to be present for all initial

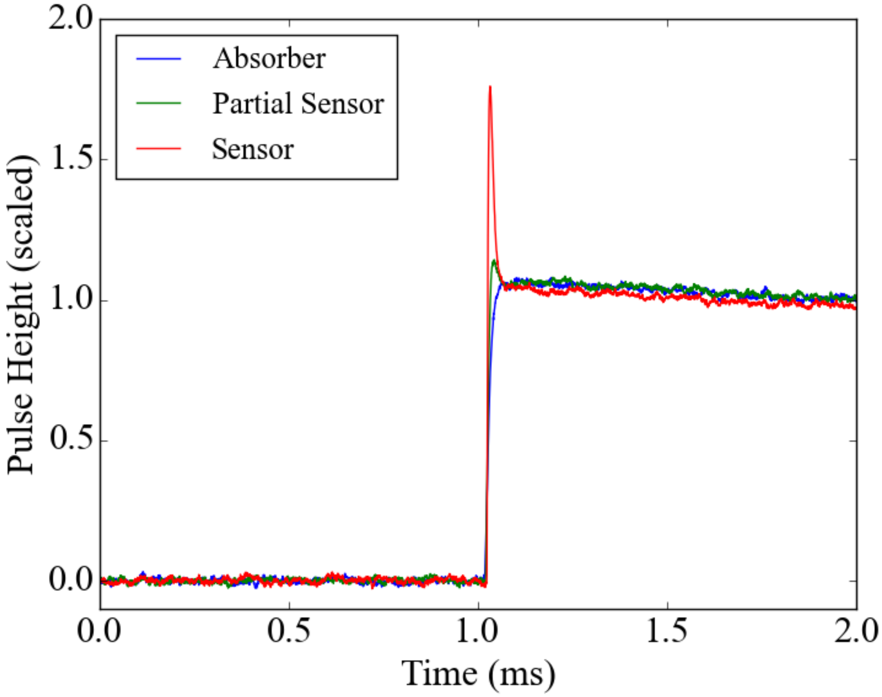

Figure 7.21: Plot of different pulse shapes observed in an MMC.

photons energies in this spectrum. The isotopic analyses in this chapter were performed before and after removing the partial and direct sensor hits on a subset of the data. Removing the sensor events did not have a significant effect on the results. As the removal of these events added another step to the analysis and there was no benefit the data presented in this dissertation do not have the sensor events removed.

7.8 Measurements of a Mixed Isotope Source

The mixed isotope plutonium source used for this work was prepared specifically for this measurement. In order to demonstrate the ability of MMCs to separate the ^{242}Pu line from the ^{240}Pu line, it was desirable to have a relatively high concentration of ^{242}Pu. In addition, it was necessary to limit the amount of ^{241}Am and ^{241}Pu, as both would contribute to a 59.5409 keV gamma-ray that in real samples could be up to a million times stronger than the ^{242}Pu. This is an important problem but not one that a single two-pixel MMC can demonstrate a solution to. To meet these requirements, 1 mg of ^{242}Pu was added to a 7 mg sample of weapons grade plutonium. The composition of the resulting material, as determined by mass spectrometry, is shown in table 7.3.

After characterizing the detector and completing initial testing showing that scatter from the ^{241}Am peak would not make measurement of the ^{242}Pu peak impossible, a mixed isotope plutonium source was measured inside the cryostat. This source was measured in the same geometry, except

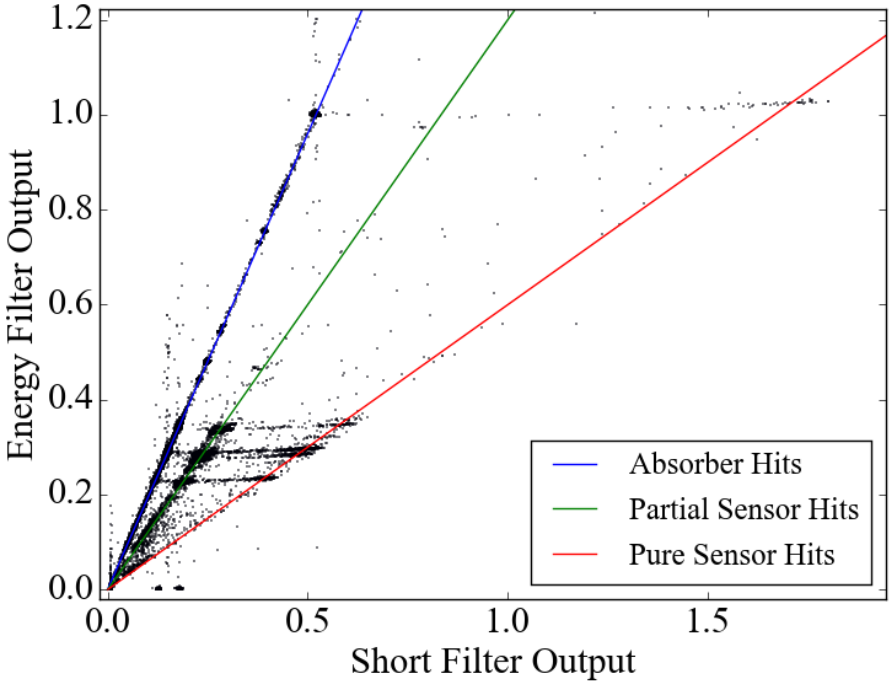

Figure 7.22: Scatter plot of short filter output vs. long energy filter output.

Isotope ratio	Value	Uncertainty (95 % Confidence Level)
^{240}Pu /^{239}Pu	0.064281	0.000085
^{242}Pu /^{239}Pu	0.12911	0.00020

Table 7.3: Results from mass spectrometry of the mixed isotope plutonium sample.

that 3.5 mm of Al was added between the source and the detector. This was added to stop most of the X-rays below 20 keV, which dominated the previous spectrum. In the ^{242}Pu spectrum, photons below 20 keV accounted for 92% of all detected photons. If the rate of the low energy photons had not been reduced for this sample, it would not be feasible to measure ^{242}Pu due to the maximum count rate of 1 cps. The 3.5 mm of Al at full theoretical density of 2.6989 g/cm^3[102] has a mass attenuation at 20 keV of 7.6E-15 and 4.75E-3 at 40 keV [103]. This reduces the X-ray rate so that the gamma-rays in the 40-60 keV region are the strongest, as can be seen in the combined spectrum in figure 7.23. A picture of the geometry is shown in figure 7.24. This source was measured over 12 days with approximately 22 hours of acquisition time per day.

HPGe measurement

In order to do a direct comparison of MMCs to the best standard technology, the mixed isotope sample was counted on a planar Ge(Li) detector. This detector had an energy resolution of 445 eV

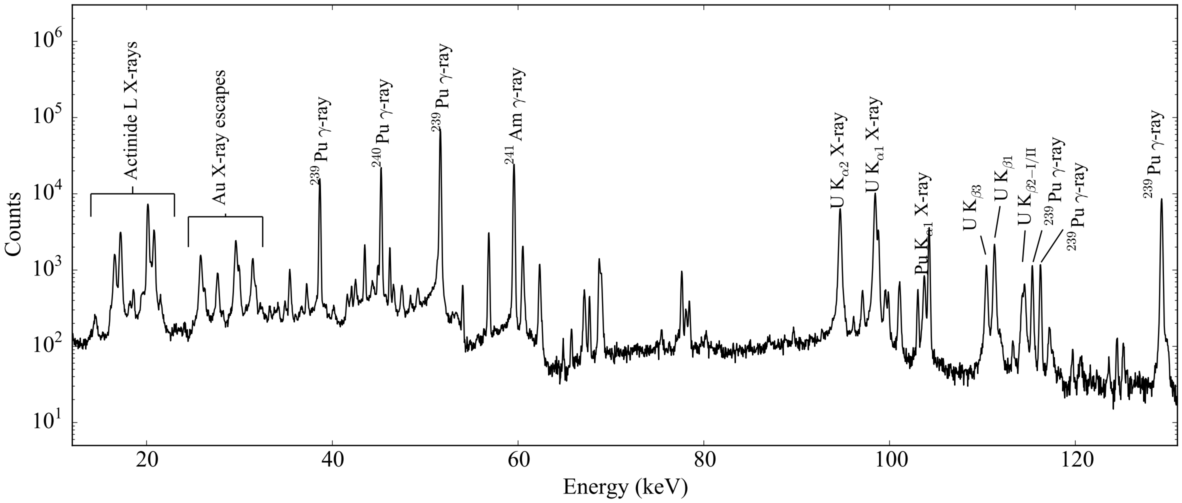

Figure 7.23: Plot of combined spectrum from a mixed isotope plutonium sample. Table 7.4 contains a list of all of the peaks and their identifications.

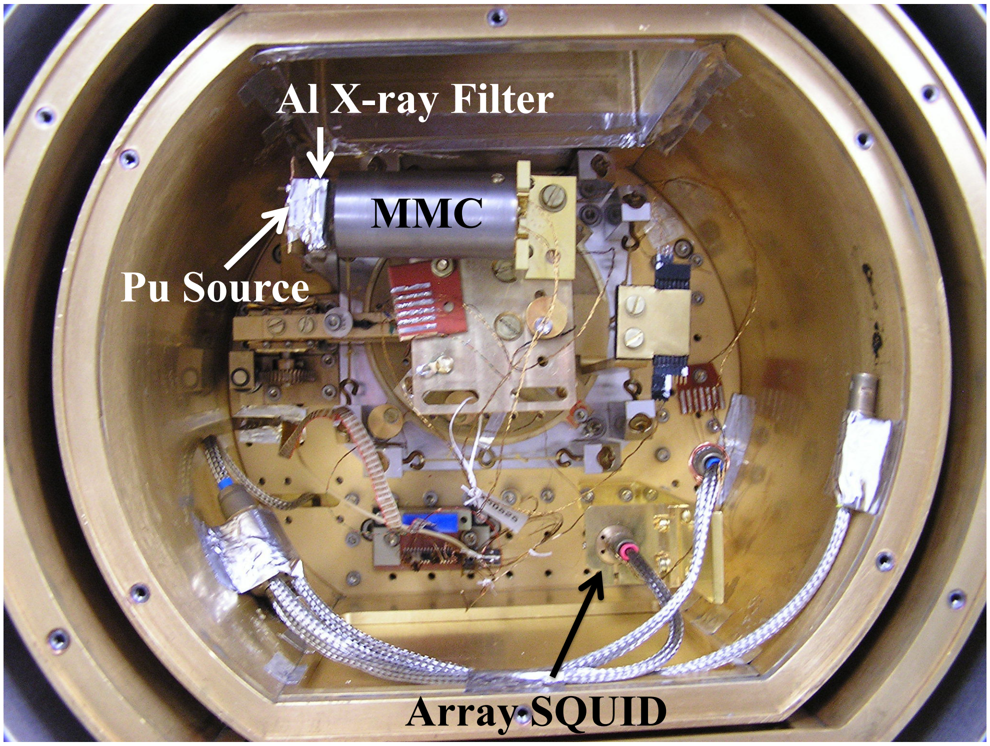

Figure 7.24: MMC installed in cryostat at LLNL for measurements of the mixed isotope plutonium source with Al X-ray filter.

FWHM at 60 keV. The mixed isotope plutonium sample was counted for 700 minutes with this detector to ensure the spectrum was not limited by statistics. The resulting spectrum from 20-600 keV has been broken up into two parts: the higher energy portion is shown in figure 7.25, the lower energy portion that overlaps with the MMC is shown in 7.29. These spectra clearly show the gamma-rays from ^{239}Pu in the 40, 100 and 300 keV regions. As discussed in chapter 1, the strongest ^{242}Pu line is in the 40 keV region. This line is centered at 44.915 keV. The region around this line is shown in figure 7.26. A plot of the expected size of the 44.915 keV line based on the known concentration from mass spectrometry and the gamma-ray branching ratio is also shown in this figure. It is possible to set an upper limit constraint on the ^{242}Pu concentration in this spectrum by tightly constraining the fitting parameters of the ^{240}Pu line next to it and fitting a Gaussian to the spectrum. Using this approach it is possible to set an upper limit on the counts in the ^{242}Pu peak of 17485. This corresponds to a ^{240}Pu /^{242}Pu ratio of 1/11. This is much smaller than the ^{240}Pu /^{242}Pu ratio in this sample of 1/2, which is already smaller than the ratio in realistic samples, typically 2 or greater.

ADR performance

The measurement of this sample using an MMC was performed using the Vericold ADR described in chapter 5. Under typical operating conditions, this cryostat would only provide 6-8 hours of usable measurement time. As described in detail in chapter 5, the two methods of improving the usable measurement time are to improve the base temperature of the pulse tube or the magnetic field. As it was not possible to safely increase the magnetic field strength without replacing the magnet, the only route available was to improve the pulse tube base temperature. The base temperature of the pulse tube is limited by the mass flow of the cryogenic working fluid, ^{4}He, in the pulse tube cold head. Increasing the pressure of the system increases the mass flow and to first order increases the cooling power. The peak pressure in the compressor limited the maximum helium pressure in the pulse tube system during the cool-down phase from 300 K to 50 K. Once the second stage of the pulse tube cools to below the base temperature of the first stage, the peak pressure of the compression cycle decreases. This makes it possible to decrease the base temperature of the pulse-tube system by increasing the pressure in the system once the second stage is below 50 K. This was accomplished by turning off the compressor briefly, adding additional ultra-pure helium via the filling port (up to 16.2 bar), and powering the compressor back on. This process must be completed before the base temperature of the pulse tube goes above the temperature of the first stage, approximately 50 K. This process improved the base temperature of the cryostat from 3.2 K to 2.7 K. This 500 mK drop in pulse-tube base temperature increased the operation time of the MMC from 6-8 hours below 35 mK to 24 hours below 35 mK. This improved measurement time was necessary to enable this measurement as it allowed for approximately three times more measurement hours per day. This shortened the time needed to reach less than four percent statistical error in the ^{242}Pu gamma-ray peak from over one month to 12 days.

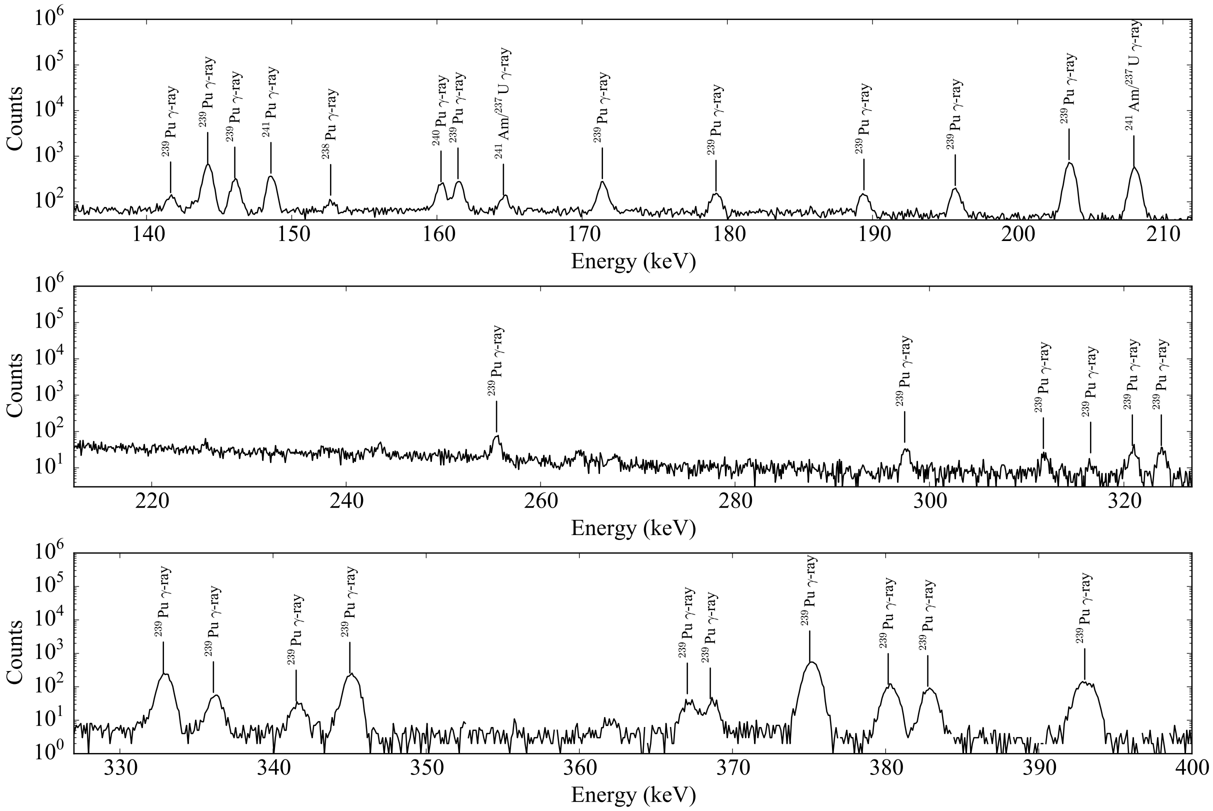

Figure 7.25: Spectrum of the 130-400 keV region of the mixed isotope plutonium source taken with a planar Ge(Li) detector.

Individual spectra

Each spectrum was analyzed individually prior to combining the 24 spectra from the 12 days of operation with two pixels. The analysis procedure was the same as that described for the previous measurements. Each set of pulses was filtered using a digital cusp algorithm with a flat top to produce a list of pulse-heights. The variation in pulse-height as a function of time was then corrected by doing a moving average fit of the 51.63 keV peak with a Hanning window 150 samples wide. By measuring the width of the 59.5409 keV peak, it was possible to check the performance of this window. This provided a measure of how well the moving average window was correcting for time-dependent variations in pulse-height, as opposed to random variations in pulse-height. The energy resolution for the 24 spectra used in the final analysis of the sample are shown in figure 7.27. From this figure it is possible to determine that pixel A had a marginally better energy resolution than pixel B, on average. The reasons for this needs further study before fabricating larger arrays. The first few spectra also have significantly poorer energy resolution. This was due to the

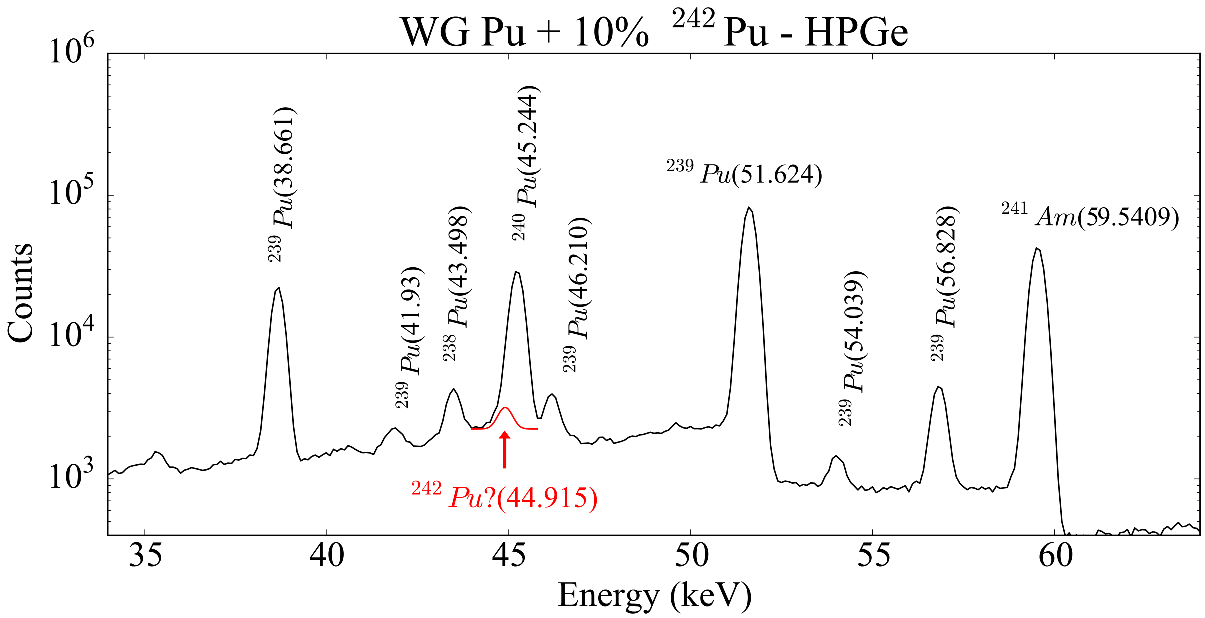

Figure 7.26: Spectrum of the 40-50 keV region of the mixed isotope plutonium source taken with a planar Ge(Li) detector.

cryostat taking several days to equilibrate at the base temperature. The data was analyzed with and without these first few spectra and it was determined that including them was preferable.

Energy dependence in responsivity

In order to determine the linearity of the two pixels PeakEasy [104] was used to fit the centroids of seven of the strongest lines for each of the pixels. The resulting fits were then used for energy calibration. Figure 7.28 shows the spectra from the two pixels, the residuals from a linear and quadratic fit, and the energy resolution. While using a quadratic term for the energy response does decrease the residuals, the uncertainty is too large to ascertain the size of this effect. This shows that for energies below 120 keV it is possible to sum multiple spectra using a simple linear fit. Also shown in figure 7.28 is the trend that higher energy gamma-rays have poorer energy resolution. This could be due to several different factors. One is that there is position dependence in a dimension in the pixel. One possibility is that there is depth dependence, as lower energy photons deposit all of their energy in the part of the absorber closest to the source. An additional possible source of added resolution is a small non-linearity in responsivity as a function of energy coupled with the pulse height normalization process. This could have an effect of a similar order of magnitude based on the calculated non-linearity in responsivity in this device from previous work of $\eta(E)/E = -5.5{\cdot}10^{-9}eV^{-1}$ at 25 mK, where the measured energy can be compared to the actual with the formula $E_m = (1+\eta(E))E$[75]. At 35 mK, the temperature of the measurement, this effect could be up to 61 eV at 129.3 keV, though quadratic fits to the measured spectra imply that

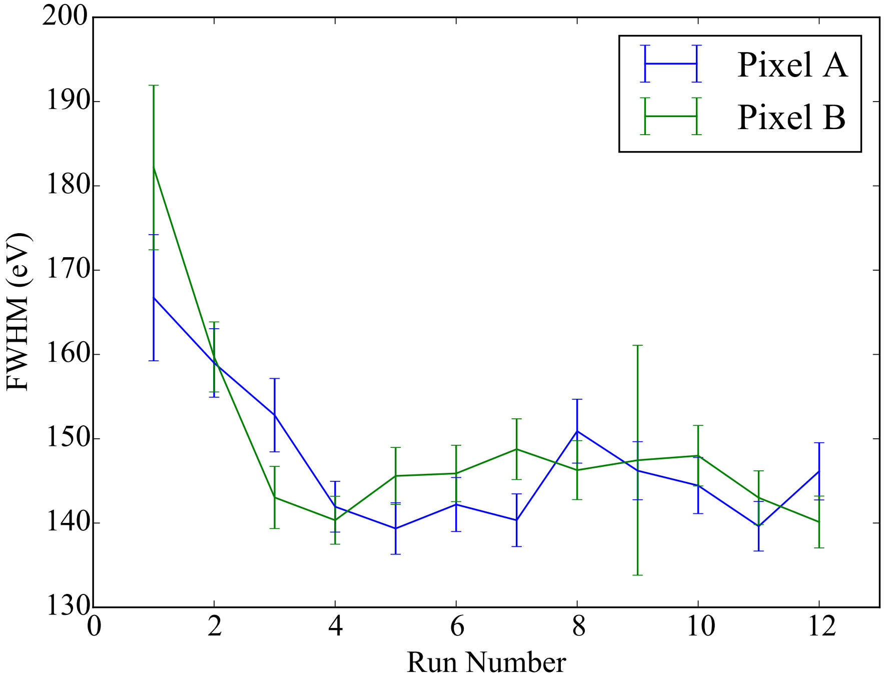

Figure 7.27: Energy resolution for the two different pixels over the 12 cool-downs used to measure the mixed isotope plutonium source.

this large of an effect is not plausible. With the available data it is not easily possible to quantify the non-linearity, but it could have a broadening effect similar to what is observed due to the pulse height normalization process.

Combined spectrum

After determining an energy calibration for the 24 spectra by doing a linear fit of the five strongest gamma-ray lines, the spectra were combined for analysis. In order to eliminate any binning problems, the filtered pulse height lists were each scaled by the fit and then combined. This meant that the final dataset for analysis was one large set of calibrated pulse heights stored as floating point numbers, which could be binned as needed. The combined spectrum is shown in figure 7.29. The first order comparison of the entire spectrum with that of the planar Ge(Li) is shown in figure 7.29. It is clearly evident that the MMC can both distinguish more closely-spaced peaks and peaks that are not discernible from background in the planar germanium detector. This is a key advantage of MMCs for detecting minor isotopes that cannot be measured by germanium detectors.

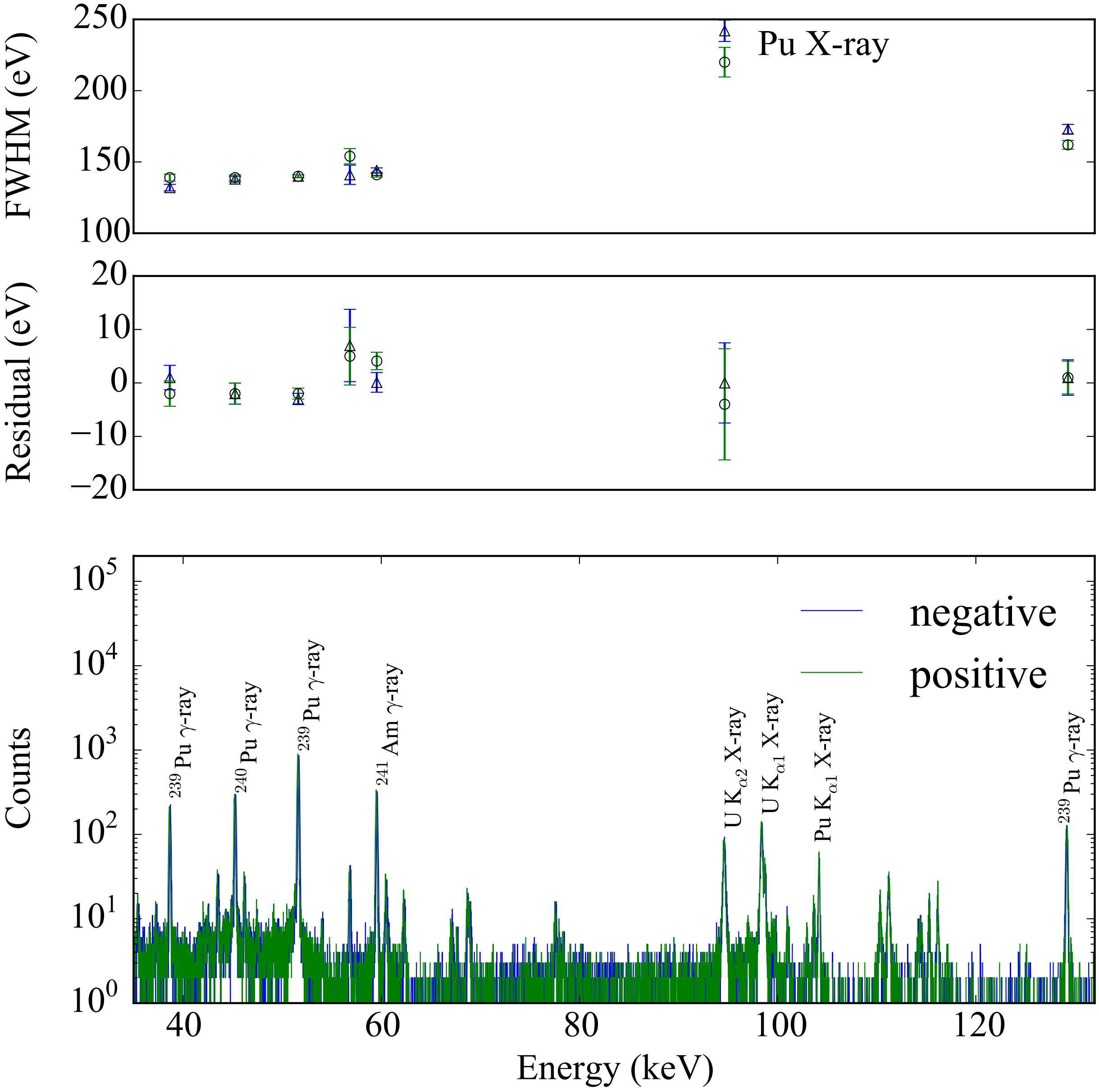

Figure 7.28: Analysis of an individual spectrum from the mixed isotope plutonium measurement showing both pixels are linear within measurement error up to 129 keV.

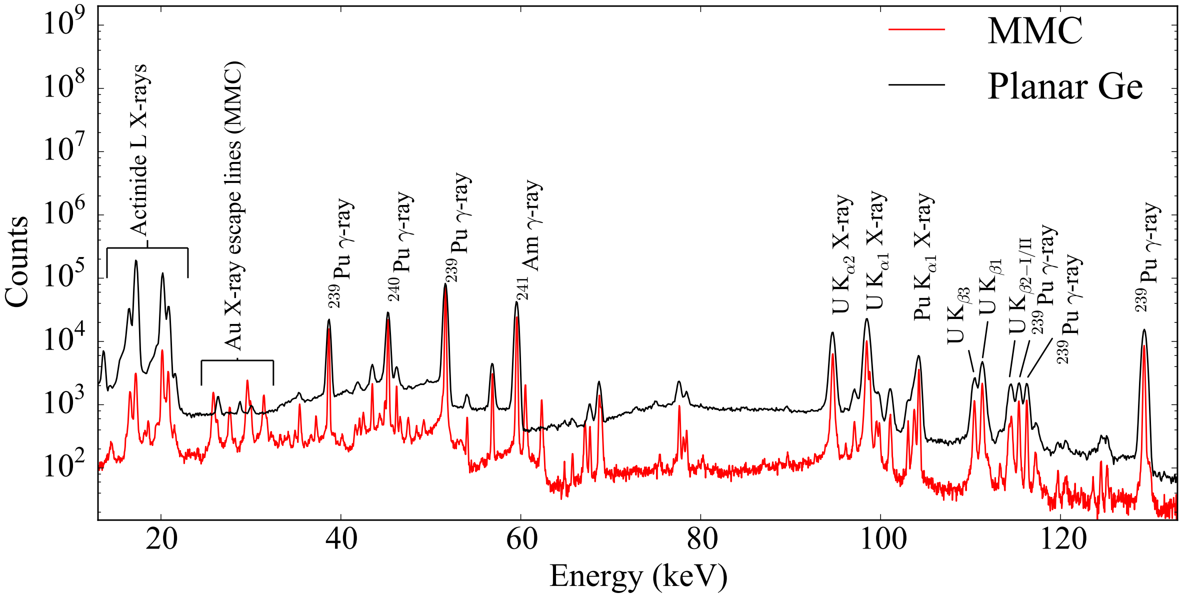

Figure 7.29: Comparison of the combined MMC spectrum with a 12 hour planar germanium spectrum of the mixed isotope plutonium source.

Identification of peaks in the combined spectrum

Prior to doing any isotopic analysis using the combined MMC spectrum, it is necessary to identify all of the peaks in the spectrum to the extent possible. This identification is necessary in order to be confident that the peaks being measured are from the desired gamma-rays and not an artifact of the detector response. The full listing of the peaks and their assignments is shown in table 7.4. All 73 peaks could be assigned to known gamma-ray and X-ray lines, indicating that there are no spectral artifacts aside from the unavoidable esape peaks.

With the clear evidence that it is possible to measure lines that cannot be measured in HPGe in comparison to background, it is now desirable to focus in where the strongest ^{242}Pu line is, in the 40-50 keV region. Figure 7.30 shows the region from 43 to 47 keV with all of the discernible gamma-rays labeled. In this spectrum, the ^{242}Pu line is immediately visible next to the much stronger ^{240}Pu line and above the background. This clearly demonstrates the ability to qualitatively see this line in a sample containing significant amounts of ^{240}Pu, which has never been shown before. In addition to the spectrum from the MMC, the Ge(Li) spectrum has been included in the same figure. This shows the stark difference in both ability to resolve closely spaced peaks and resolve peaks against background, as there are several lines that cannot be measured using the Ge(Li) detector.

The capability of directly measuring the ^{242}Pu line means that this line can now be used for isotopic analysis. This process involves calculating the peak area and efficiency and using that, along with the known branching ratios, in order to calculate the relative activity and therefore

Energy (keV measured)	Energy (keV Literature)	Difference	Identity
16.612	16.616	-0.004	Nb $K_{\alpha 1}$
17.232	17.218	0.014	U $L_{\beta 1}$
18.279	18.292	-0.013	Pu $L_{\beta 1}$
18.628	18.624	0.004	Nb $K_{\beta 1}$
20.179	20.167	0.012[2]	U $L_{\gamma 1}$
20.476	20.487	-0.011[2]	U $L_{\gamma 2}$
20.848	20.785	0.063[2]	Np $L_{\gamma 1}$
21.528	21.417	0.111	Pu $L_{\gamma 1}$
25.856	94.658[1]	0.001[2]	Au $K_{\alpha 1}$ X-ray escape
26.252	26.345	-0.093[2]	^{241}Am γ-ray
27.671	94.658[1]	0.002	Au $K_{\alpha 2}$ X-ray escape
29.63	98.434[1]	-0.001	Au $K_{\alpha 1}$ X-ray escape
29.972	98.78[1]	-0.005	Au $K_{\alpha 1}$ X-ray escape
31.446	98.434[1]	0.001	Au $K_{\alpha 2}$ X-ray escape
31.751	98.78[1]	-0.04	Au $K_{\alpha 2}$ X-ray escape
35.439	104.234[1]	0.008	Au $K_{\alpha 1}$ X-ray escape
37.259	104.234[1]	0.014	Au $K_{\alpha 2}$ X-ray escape
38.666	38.664	0.002	^{239}Pu γ-ray
41.629	110.418[1]	0.014	Au $K_{\alpha 1}$ X-ray escape
42.056	42.06	-0.004	^{239}Pu γ-ray
42.503	111.298[1]	0.008	Au $K_{\alpha 1}$ X-ray escape
43.493	43.498	-0.005	^{238}Pu γ-ray
44.326	44.4	-0.074[3]	^{227}Th γ-ray
44.911	44.915	-0.004	^{242}Pu γ-ray
45.246	45.244	0.002	^{240}Pu γ-ray
46.194	46.21	-0.016	^{239}Pu γ-ray
46.6	115.38[1]	0.023	Au $K_{\alpha 1}$ X-ray escape
47.487	116.26[1]	0.03	Au $K_{\alpha 1}$ X-ray escape
48.403	115.38[1]	0.012[3]	Au $K_{\alpha 2}$ X-ray escape
49.202	116.26[1]	-0.069[3]	Au $K_{\alpha 2}$ X-ray escape
51.624	51.629	-0.005	^{239}Pu γ-ray
54.033	54.04	-0.007	^{239}Pu γ-ray
56.836	56.828	0.008	^{239}Pu γ-ray
59.547	59.5409	0.0061	^{241}Am γ-ray
60.498	129.294[1]	0.007	Au $K_{\alpha 1}$ X-ray escape
62.312	129.294[1]	0.007	Au $K_{\alpha 2}$ X-ray escape

Table 7.4: Identification of peaks in combined mixed isotope plutonium spectrum. [1]Energy listed is that of the primary gamma-ray. [2]Measurement of peak centroid has large uncertainty due to line overlap. [3]Measurement of peak centroid has large uncertainty due to limited number of counts.

Table 7.4 continued

Energy (keV measured)	Energy (keV Literature)	Difference	Identity
64.838	64.832	0.006	^{237}U γ-ray
65.733	65.708	0.025	^{239}Pu γ-ray
67.07	66.993	0.077[2]	Au $K_{\alpha 2}$
67.185	67.25	-0.065[2]	^{234}Pa γ-ray
67.671	67.674	-0.003	^{239}Pu γ-ray
68.728	68.74	-0.012[2]	^{239}Pu γ-ray
68.947	68.806	0.141[2]	Au $K_{\alpha 1}$
75.42	144.201[1]	0.022[3]	Au $K_{\alpha 1}$ X-ray escape
77.609	77.592	0.017	^{239}Pu γ-ray
78.069	77.983	0.086[3]	Au $K_{\beta 1}$
78.416	78.43	-0.014	^{239}Pu γ-ray
89.636	89.64	-0.004[3]	^{239}Pu γ-ray
94.659	94.658	0.001	U $K_{\alpha 2}$
96.109	96.13	-0.021[3]	^{239}Pu γ-ray
97.07	97.068	0.002	Np $K_{\alpha 2}$
98.433	98.434	-0.001	U $K_{\alpha 1}$
98.766	98.78	-0.014	^{239}Pu γ-ray
99.525	99.524	0.001	Pu $K_{\alpha 2}$
99.847	99.853	-0.006	^{238}Pu γ-ray
101.056	101.057	-0.001	Np $K_{\alpha 1}$
103.029	103.06	-0.031	^{239}Pu γ-ray
103.722	103.734	-0.012	Pu $K_{\alpha 1}$
104.239	104.234	0.005	^{240}Pu γ-ray
110.419	110.418	0.001	U $K_{\beta 3}$
111.293	111.298	-0.005	U $K_{\beta 1}$
113.281	113.3	-0.019[3]	Np $K_{\beta 3}$
114.267	114.329	-0.062[2]	U $K_{\beta 2\text{-II}}$
114.537	114.556	-0.019[2]	U $K_{\beta 2\text{-I}}$
115.365	115.38	-0.015	^{239}Pu γ-ray
116.241	116.26	-0.019	^{239}Pu γ-ray
117.228	117.225	0.003	Pu $K_{\beta 1}$
119.698	119.709	-0.011[3]	^{239}Pu γ-ray
120.578	189.36[1]	0.021[3]	Au $K_{\alpha 1}$ X-ray escape
123.613	123.62	-0.007[3]	^{239}Pu γ-ray
124.487	124.51	-0.023[3]	^{239}Pu γ-ray
125.173	125.21	-0.037[3]	^{239}Pu γ-ray
129.297	129.294	0.003	^{239}Pu γ-ray

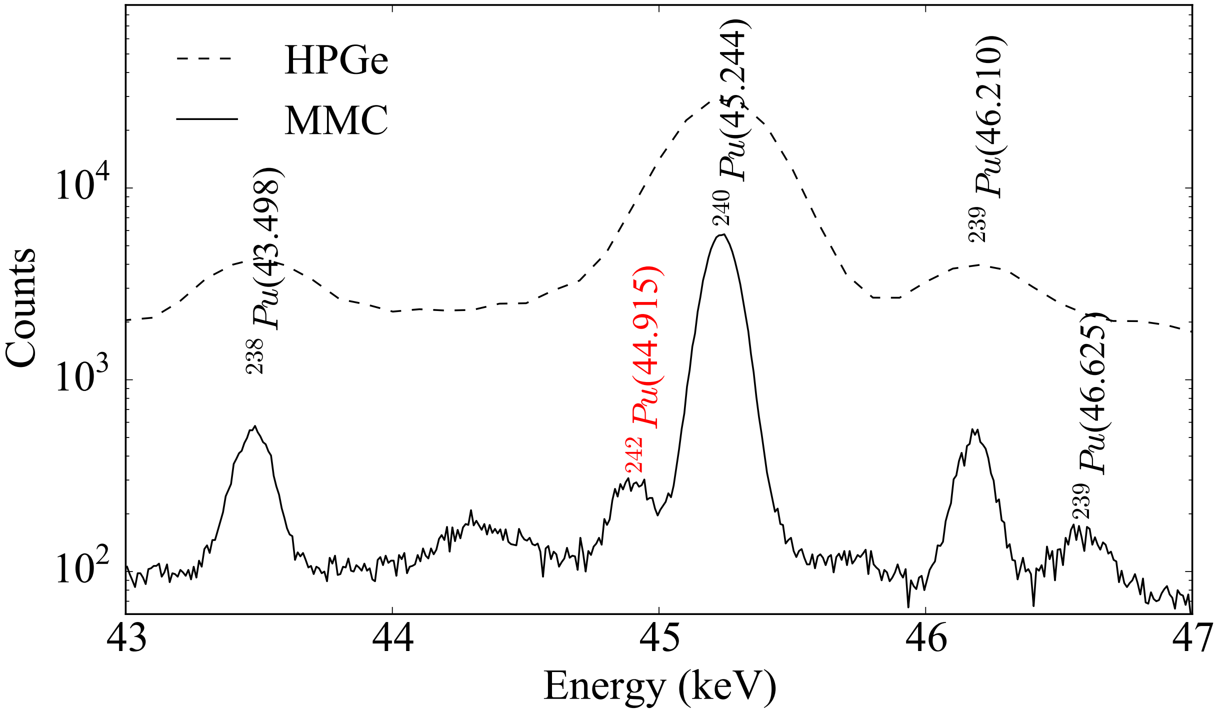

Figure 7.30: Comparison between the MMC and Ge(Li) spectrum in the 40 keV region.

the isotopic ratios of different radionuclides in a sample. There are many tools that have been developed to do this but the most widely used and flexible code is known as FRAM, which is discussed in chapter 2. In order to use FRAM to analyze the mixed isotope sample, it was necessary to change many of the default operating parameters. The most important is the addition of peaks in the 40-60 keV region and the removal of all peaks above 129 keV to make it compatible with the data from the MMC detector. A summary of the peaks used for the FRAM analysis is shown in table 7.5. It was also necessary to change many of the other additional defaults such as the shielding material type, which needed to be changed to Al.

After creating the custom parameter set, it was necessary to optimize it to work best for this specific measurement. This included replacing the default branching ratios with those available from the most recent complete evaluated nuclear structure data file archive from April 2014. This improved the performance of the analysis, but additional adjustments were required for the error on the efficiency curve to remain sufficiently small, as small changes to fits of individual peaks were prone to cause problems.

An isotopic analysis of the mixed isotope sample was performed once the parameter set had been sufficiently adjusted, such that it produced good fits for all the peaks of interest. The resulting isotopics are shown in 7.6. This table also shows the difference from the mass spectrometry results. The results from the MMC analysis show that FRAM over-predicts the ^{242}Pu and under-predicts

Isotope	peak energy (keV)	branching ratio	efficiency	activity	energy calibration
^{239}Pu	38.661	1.05E-4	Y	Y	Y
^{238}Pu	43.498	3.93E-4	N	Y	N
^{242}Pu	44.915	3.73E-4	N	Y	N
^{240}Pu	45.244	4.53E-4	Y	Y	N
^{239}Pu	46.210	7.37E-6	Y	N	N
^{239}Pu	51.624	1.05E-4	Y	N	Y
^{239}Pu	56.828	1.05E-4	N	N	N
^{241}Am	59.5409	3.59E-1	N	N	Y

Table 7.5: Information used for FRAM isotopics calculations.

Isotope	Mass spectrometry (mass %)	FRAM (mass %)	Difference (mass %)
^{239}Pu	83.75 ± 0.13	81.90 ± 0.59	-1.85
^{240}Pu	5.39 ± 0.01	5.10 ± 0.07	-0.29
^{242}Pu	10.81 ± 0.02	13.00 ± 0.61	+2.19

Table 7.6: Isotopic analysis results using FRAM.

the ^{239}Pu concentration.

The error in the direct ^{242}Pu measurement is 2.19 % absolute error in mass. This is of the same order of magnitude as errors observed with ratio-based prediction. The difference between the calculated and the actual ^{242}Pu concentration is 3.6-sigma. This is outside the bounds where counting statistics alone would cause this much error. The most likely explanation is that the efficiency curve calculated by FRAM did not match the physical parameters of the system due to the use of a thin gold absorber instead of a germanium detector. The calculated efficiency curve is shown in figure 7.31. There are several possible additional causes, including poor fits of the peaks and backgrounds used for the efficiency calculation, FRAM's inability to account for the gold K-edge in MMCs, and errors in the underlying nuclear data. These could all cause issues with the efficiency calculation, which would lead to a systematic bias in the predicted isotopics.

In order to address these issues, it was necessary to develop a custom analysis workflow. This workflow started with analysis of the spectrum in PeakEasy in order to determine peak areas and uncertainties. In addition, it was necessary to create a custom efficiency curve. The data used for this efficiency curve were from the ENDF VII.1 photo-atomic library [103]. For the self-absorption in plutonium and the aluminum X-ray filter, the total photon cross section was used (MT 501). For the gold absorber, the photoelectric cross section was used (MT 522). The relative efficiency curve was based off of a simplified version of the model used in FRAM [36]. The new efficiency curve has the form:

$$\text{Eff}(E) = C \cdot \frac{1 - exp(-\mu_{Pu} x_{Pu})}{\mu_{Pu} x_{Pu}} exp(-\mu_{Al} x_{Al})(1 - exp(-\mu_{Au} x_{Au})) \tag{7.3}$$

The first term accounts for the self-absorption in the Pu source, the second term for the trans-

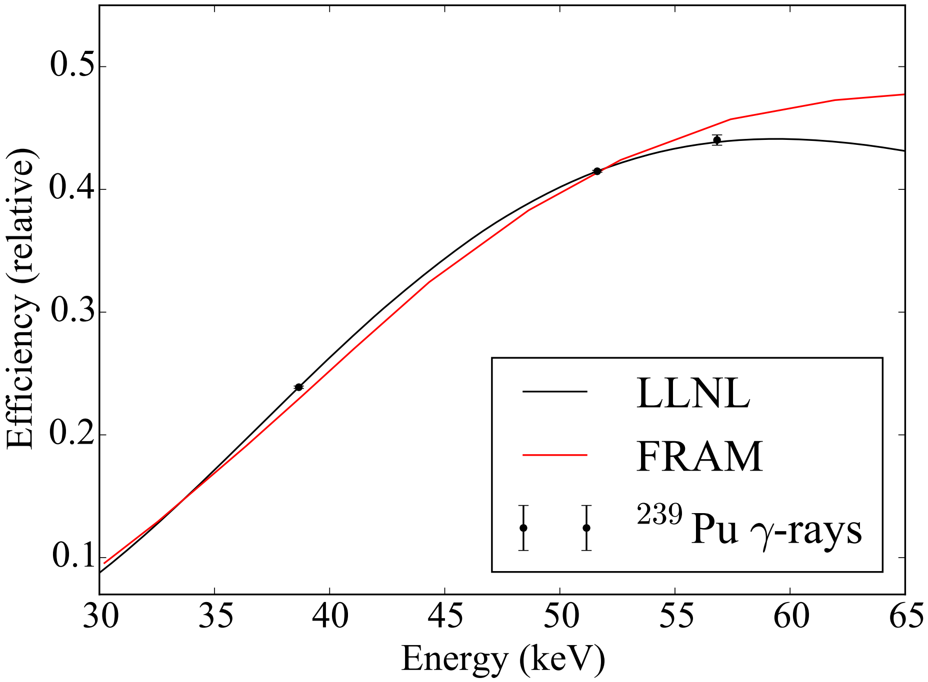

Figure 7.31: A comparison of the efficiency plot generated by FRAM for the mixed isotope plutonium source with the one calculated using ROOT.

mission of the Al filter, and the final term for the absorption in the Au absorber of the MMC. In this equation, all of the mass attenuation coefficients are energy dependent. This simple form is unlikely to be valid over a very large range of energies, but it is only necessary for it to match the form of the efficiency between 38 and 51 keV as the lines used for the analysis are all in this narrow region. ROOT was used to fit the three strongest ^{239}Pu lines in the region to this equation after normalizing them based on their relative intensities. For this fit the thickness of the Pu source x_{Pu} and the scaling factor C were the two terms that were varied. The resulting efficiency curve is shown in figure 7.31. It is clear that this curve differs from the one computed by FRAM by several percent. This is likely due to the use of the absorption cross-section for gold instead of germanium. This fit was then used to determine the efficiency at all the different peak energies used for analysis. The usage of ROOT made it possible to calculate fit uncertainties at each of the points used for analysis. These uncertainties were propagated through the rest of the analysis. After fitting the relative efficiency curve the peak areas of the ^{239}Pu, ^{240}Pu, and ^{242}Pu peaks were scaled based on the half-life of each parent nuclide, the intensity of each gamma-ray, and the detector efficiency at that energy. All of these parameters included errors which were propagated using the Python `uncertainties` package. The resulting isotopics and errors are shown in table 7.7. These results show much better agreement with the mass spectrometry results. All of the calculated ratios are within 2 sigma of the known value from mass spectrometry, which is within what is expected

Isotope	Mass spectrometry (mass %)	Predicted (mass %)	Difference (mass %)
^{239}Pu	83.75 ± 0.13	83.67 ± 0.42	-0.08
^{240}Pu	5.39 ± 0.01	5.22 ± 0.11	-0.17
^{242}Pu	10.81 ± 0.02	11.11 ± 0.42	0.30

Table 7.7: Isotopic analysis results using custom analysis routine.

given statistical fluctuations in total counts. In addition, the error for the ^{242}Pu is dominated almost purely by statistics, with the relative standard deviation of the peak area alone being 3.3%. This implies that scaling to larger arrays will improve the accuracy of these results. In the final chapter, some of the limitations when measurements are not limited by statistics will be discussed.

This measurement clearly demonstrates the ability of MMCs to directly detect gamma-rays from ^{242}Pu and use their intensity for quantitative analysis. It also showed very promising results for scaling this system to larger arrays, as it is possible to use a linear function for energy calibration with very high accuracy. In addition, it shows that MMC data can be directly used in existing plutonium isotopic analysis codes, though more work is needed to more thoroughly adapt these codes and determine any deficiencies in existing nuclear data.

Chapter 8

Conclusions

8.1 Summary

The field of Nuclear non-proliferation has a variety of challenges which could be solved by ultra-high energy resolution gamma-ray spectroscopy. Efforts to use micro-calorimeters for safeguards applications to date have been hampered by difficulties in summing spectra from multiple pixels and cooldowns. MMCs offer a possible solution to this problem, but prior to this dissertation the use of them for these applications had not been demonstrated. The successful demonstration of ^{242}Pu quantification in a mixed isotope sample shows that MMCs are a viable alternative to TESs for this type of work. In order to demonstrate this it was necessary to both collaborate with the University of Heidelberg to make improvements to the fabrication process, which helped enable an improved gamma-ray MMC design, and to construct a system at LLNL to measure samples with MMCs.

The fundamental motivation to develop ultra-high resolution gamma-ray spectrometers for non-proliferation applications is driven by two situations where current state-of-the-art spectrometers fall short. The first is when there are two peaks that are close together and one of them is much stronger than the other making it impossible to quantify the smaller peak with current systems. The second is when the Compton scatter background is so much larger than the peak that the peak cannot be discerned. One known case of the first situation is described in this dissertation, where plutonium mass quantification can be limited by the inability to measure ^{242}Pu directly. This has potential applications in nuclear safeguards, nuclear forensics, and plutonium disposition agreements. The second situation has fewer straightforward examples, but it may be of significant use to detect undeclared activities at nuclear facilities. A future system may be able to provide a viable alternative to mass spectrometry at IAEA analytical laboratories, but more understanding of isotopes of interest is required.

Prior to making any measurements of plutonium with MMCs, improvements to the gamma-ray MMC fabrication process were necessary. This is because the existing process had issues with absorber reproducibility and fabrication throughput. Both of these were caused by the same basic issue, the photoresist used for large structures, SU 8, stuck to the mask used to pattern them. It was necessary to separate the two by force, which lead to damage to the mold for the pixels and often damage to the mask. The damage to the mask was particularly problematic for fabrication as it is not financially practical to destroy a mask for each wafer of chips produced. The damage to the mold resulted in non-uniform shapes of the electroplated absorbers. This led to larger variation in the response between pixels and made it difficult to pack pixels close together without them fusing in the electroplating process. This dissertation included the development of a new process for patterning 300 μm thick AZ 125 nXT photoresist for use as a mold for the absorbers to resolve these issues. The new process made it possible to fabricate 4 gradiometric MMCs with 8 pixels closely spaced without any of the previous problems, as shown in chapter 4. In addition to the replacement of the photoresist, collaborators as the University of Heidelberg also added 7 μm tall gold posts between the Au:Er sensor and the absorber. This should reduce the position dependence in the response because it allows more time for the electron system, primarily the absorber, to equilibrate before transferring energy to the spin system, the paramagnetic Er ions.

Development of a system capable of making MMC measurements at LLNL was necessary because these measurements could not be performed at the University of Heidelberg. This is due to the fact that the sources can only be made at a facility that has access to plutonium and the ability to create custom combinations of plutonium isotopes. LLNL is one of the only facilities in the world that can create custom plutonium mixtures on demand. The development of this system included reducing the noise in the existing cryostat, installing the appropriate wiring for two-stage SQUID measurements, designing a holder for the MMC and input SQUID, and writing a data acquisition system compatible with MMC signals. Reducing the noise in the cryostat was the most critical issue as it had limited the energy resolution of previous measurements to unusable levels [33]. This was done by electrically isolating the helium lines and rotary valve from the compressor using custom made electrically isolated high-pressure helium couplings.

Two separate sets of measurements were made for this dissertation. The devices were first characterized at the University of Heidelberg and then they were brought to LLNL to measure sources of interest. The new MMC design achieved an energy resolution of 45.5 eV FWHM at 59.5409 keV in a pulse-tube cooled dilution refrigerator at the University of Heidelberg. This is the best reported energy resolution at this energy for a gamma-ray MMC. After setting this new benchmark for performance, one of the new MMCs was installed in the system at LLNL to measure a mixed isotope plutonium source. Over 12 days the two pixels recorded over 1.5 million events, 2782 ± 103 of which were attributed to ^{242}Pu. Using the data from this measurement to do isotopic analysis of the sample, the relative concentration of ^{242}Pu was determined to within 0.5% by mass. The relative uncertainty in the mass percent of ^{242}Pu was < 4 %. This is comparable to the accuracy of indirect methods for calculating ^{242}Pu, but only if the parameters used in the indirect method have been optimized using well characterized samples from the same type of reactor [43]. This measurement was limited by statistics, if the total number of counts could be increased by a factor of four the relative uncertainty would approach 2%.

An MMC system capable of determining ^{242}Pu concentration to higher precision than is possible with current non-destructive methods has many potential applications. A future system could be part of an on-line monitoring system at a reprocessing or disposition plant in order to confirm plutonium isotopics. In its present form it is already approaching the timeliness required in the field of nuclear forensics, where a measurement time of less than a week could outperform existing tools. Significantly more research and development is necessary to make this an end-user friendly tool that can make measurements for these and other applications. The remaining sections discuss some of the complications and limitations that arise when considering the further development of this system and possible solutions.

8.2 Future Development and Limitations

Measuring a more realistic sample

The measurement performed in this dissertation demonstrated the possibility to overcome one of the fundamental limitations of measuring ^{242}Pu in samples relevant to non-proliferation, but realistic samples would pose several additional challenges. The primary challenge is the presence of

^{241}Pu in similar concentrations and its two decay products, ^{241}Am and ^{237}U, both of which contribute to the gamma-ray line at 59.5409 keV produced from the excited state of ^{237}Np. Depending on the age of this sample and when chemical separation from other actinides was performed, the 59.5409 keV gamma-ray could be between one thousand and one million times stronger than the ^{242}Pu line at 44.915 keV. In comparison, the strongest line in the existing spectrum, at 51.63 keV, is only 100 times stronger than the 44.915 keV. This poses two primary challenges. The first is that it would take up to 100 times more detector days at a current proposed practical maximum count-rate of 100 counts per second in order to make the same quality measurement in the worst case scenario, assuming the count rate per pixel is the only limiting factor. It would also likely require a gram size sample. The second challenging aspect is additional background in the 45 keV region from scattered 59.5409 keV photons. The precise characterization of the full spectrum from a pure ^{241}Am source in the desired geometry would be necessary to predict the impact that this would have.

The practical counting time and acceptable error are both dependent on the specific safeguards application, but for most scenarios where an inspector is not permanently at a facility a total counting time of $<$ 4 hours and a ratio error of $<$ 2 % are desirable. In the worst case scenario described above, this would require 30,000 pixels. There are currently no methods to readout an MMC array of this size, though promising work is being done using radio-frequency (RF) SQUIDs for a multiplexed MMC readout [105]. A more common scenario in future non-proliferation measurements would be the analysis of spent fuel with a relatively long cooling time that was relatively well separated in the reprocessing process from americium. In this case, an array of just a few hundred pixels operating at 100 counts per second could quantify ^{242}Pu in a reasonable amount of time. If scatter of 59.5409 keV increases the background to intolerable levels, there are two possibilities to eliminate this problem. The first is to minimize the amount of material between the source and the detector. This will be difficult, as it is necessary to have some shielding to block X-rays below 20 keV; otherwise, they will dominate the spectrum. The other option is to improve the energy resolution of the detector. This can be done by reducing the temperature, reducing the pixel size of the individual detectors, or using an alternative absorber material with lower heat capacitance. A future MMC system, designed to operate at 100 counts per second with several hundred pixels, could make safeguards-relevant measurements in practical acquisition times.

Gamma-ray mirrors

One potential alternative for measuring very high activity samples, such as a large aqueous volume of plutonium, is to use a gamma-ray mirror that would only reflect gamma-rays between 40-50 keV. This technology has been demonstrated at energies of up to 200 keV [106], and it could significantly simplify the problem for high activity sources, as only gamma-rays in a small energy region would be transmitted to the detector. With this technology, a smaller array of approximately 50 pixels counting at 100 counts per second could be used to make measurements of the plutonium with $<$ 2 % error in ^{242}Pu concentration. This information would likely need to be combined with information from a larger high-purity germanium spectrometer to constrain the ratios of the isotopes besides ^{242}Pu.

Isotope	γ-ray energy (keV)	Intensity (γ/s/atom)	Uncertainty (γ/s/atom)	Relative error
^{242}Pu	44.915	2.185e-15	4.262e-17	1.951%
^{240}Pu	45.242	1.496e-13	3.017e-15	2.016%
^{239}Pu	51.630	2.480e-14	2.028e-16	0.818%

Table 8.1: Uncertainties in the nuclear data for the peaks used for isotopic analysis.

Isotope	Uncertainty (% RSD)	Source
^{242}Pu	3.28	peak area
^{242}Pu	1.67	branching ratio
^{239}Pu	0.676	branching ratio
^{242}Pu	0.474	half-life
^{242}Pu	0.254	efficiency
^{239}Pu	0.225	efficiency
^{239}Pu	0.158	peak area
^{240}Pu	0.105	branching ratio
^{239}Pu	0.104	half-life
^{240}Pu	0.0181	peak area
^{240}Pu	0.0115	efficiency
^{240}Pu	0.00557	half-life
Total	3.79	

Table 8.2: Sources of uncertainty in the ^{242}Pu mass percent calculation.

Limitations in nuclear data

One additional issue that was mentioned briefly in the previous chapter was that these measurements would be rapidly limited by uncertainty in the underlying nuclear data. The 1-sigma uncertainty in the intensity of the 44.915 keV peak alone is 1.951 % [107]. In order to make accurate ratio measurements of ^{242}Pu, it is desirable to know this intensity with less than 1 % uncertainty. A summary of the uncertainties in line intensities of the three gamma-rays used in this region is shown in table 8.1. Reducing these uncertainties will be important in order to make highly accurate measurements using MMCs. It may be possible to use MMCs to reduce these uncertainties by comparing measured gamma-ray intensities to mass spectrometry information and characterizing the relative efficiency of the geometry very well.

In order to understand where nuclear data uncertainties may be limiting, it is helpful to look at the different contributions to the total ^{242}Pu uncertainty. These contributions are shown in table 8.2. Unsurprisingly, the ^{242}Pu peak area dominates the uncertainty, as discussed in the previous chapter. This table makes it clear how to prioritize which error sources need to be reduced in order to reduce the uncertainty in future measurements.

8.3 Outlook for MMCs

Improving MMC count-rate capabilities

There are two primary methods for improving MMC count-rate capabilities. One is to change the design of the large sensors such that they have a stronger link to the thermal bath to reduce the thermal decay constant. The other is to develop signal processing techniques to be able to de-convolve bi-polar pileup. Both of these methods require further investigation to determine how practical each is to implement and to determine the performance trade-offs involved. The addition of a thermal link using gold wire bonds is problematic, particularly with the current design, as it likely causes non-uniformity in the response as a function of position. A proposed alternative to the gold wire bonds would be to use filled metal vias, where a hole is etched through the wafer and filled with metal to provide heat-sinking. This could make stronger and more uniform thermal links, but it would complicate the design and fabrication process significantly.

Improving the MMC design

The gamma-ray MMCs used in this work are the second version of the first MMC design for gamma-ray spectroscopy. While this design worked well enough to perform demonstration measurements for this work, more development is needed to improve the design and fabrication of gamma-ray MMCs. One major improvement that could be made in this design is going from a rectangular pixel, which was driven by a desire for spatial discrimination in one dimension, to a square, octagonal, or round pixel. In addition to changing the geometry, the thickness of the pixel could also be changed. If the peaks of interest are all below 50 keV, the detector thickness could be thinner than the current design without significant loss of detection efficiency. This thinner device would have improved energy resolution due to the smaller heat capacity. A 50 μm thick gold absorber would stop 50% of all photons at 50 keV and it would have twice the optimal energy resolution at the same temperature. Alternatively, a material with a lower heat capacitance but similar stopping power could be used. Possible candidates include gold-bismuth bilayers and superconductors such as rhenium. It will also be important to improve the reliability of the design, as the current gamma-ray MMC design has issues with isolation between different wiring layers.

Square meander or coil geometry

Various different geometries have been proposed for use in MMCs. There are two fundamentally different design categories: meander- and sandwich-based designs. To date, most designs in use have been based on the meander design. This design was described in detail in chapter 3. This design can be used in either a simple square, a rectangle such as the device used in this work, or even a hexagon. The hexagon shape is slightly more complex, but it theoretically has the best uniformity in response across the device. This uniformity may be important when the thermal link to ground is much stronger and it is important that all areas of the pixel have the same decay constant. The other geometry that was more recently developed is known as the sandwich geometry.

It was originally envisaged by S.T.P. Boyd et al.[108]. This geometry is more difficult to fabricate, particularly for devices with thick sensors needed for large absorbers, but it has far superior magnetic properties. The primary advantage of this design is that the magnetic coupling is uniform throughout the sensor volume. The improved coupling leads to a larger signal size for the same total absorber heat capacity. This design has been developed for soft X-ray spectroscopy by the University of Heidelberg, who have successfully demonstrated a device with 2.0 eV FWHM at 5.9 keV [21].

Arrays and multiplexing

Arrays of several hundred pixels are needed in order to make high-accuracy measurements in realistic samples. It is currently conceivable with modern large dilution refrigerators to have sufficient cooling power to support wiring for tens of channels using two-stage SQUIDs. It may be possible to extend this to hundreds of channels by properly selecting wiring materials and being extremely careful to minimize crosstalk, but it would be a major engineering challenge as it would require a minimum of 6 wires per channel. This option is likely only practical up to 50 channels or 100 total pixels. For arrays of more than 100 pixels, it is necessary to use some form of multiplexing where multiple channels are read out over a single or greatly reduced number of wires [109]. There are two common types of multiplexing used by the low temperature detector community: time-division and frequency-division multiplexing. Time-division multiplexing uses a series of analog switches at low temperature to read out one detector at a time. It continuously cycles through all the detectors, and then the signal from each is reconstructed at room temperature by syncing the switching signal with the different output signals. This is limited in bandwidth by the rate at which it is possible to switch between different channels at low temperature. Current systems use a switching frequency of 1 MHz and a multiplexing ratio of 8, leading to an effective sample rate of 125 kHz [110]. This is significantly slower than what is desirable for use with MMCs. The other type of multiplexing is frequency division multiplexing. In this multiplexing system, each pixel is part of a resonant circuit with a different resonant frequency and the signal from each channel is up-mixed on a different carrier frequency [111]. All of the different channels are then sent on the same coaxial cable to room temperature. This type of multiplexing has been used to achieve multiplexing ratios of 7, but it has also been traditionally limited in bandwidth to < 10 kHz [112]. Recent work at the University of Heidelberg has shown a potential solution for a type frequency multiplexing with a carrier that is at several GHz [105] utilizing dissipation-less RF biased SQUIDs. This work shows promise for multiplexing SQUIDs with MHz bandwidth. All of the multiplexing technologies currently in use, including the recent developments at the University of Heidelberg, would likely reduce the MMC performance. The magnitude of this reduction requires further study when choosing a multiplexing solution for MMCs. There are trade-offs between complexity, cost of cooling, maximum count rate, multiplexing ratio, and impact on MMC resolution that would require detailed study to select the best choice for a future system.

8.4 Future Research Efforts

This chapter covered a summary of the work and a look at future applications, the limitations of current MMC systems, and how to solve those limitations. MMC systems today at LLNL are still in the research and development phase, and additional work is needed before attempting to build the hundred-plus pixel system discussed above. The next stage of this effort should include design of a new gamma-ray MMC that has a thermal decay constant of ≤ 1 ms and whether changes to the meander geometry are needed to minimize cross-talk between neighboring channels and improve reliability. This next stage of research is needed to drive the design decisions that need to be made in order to construct a one hundred channel-plus system. This dissertation has demonstrated that the use of MMCs is a credible approach to ultra-high energy resolution gamma-ray measurements for nuclear non-proliferation applications.

Appendix A

Improving ADR Performance

Adiabatic demagnetization refrigerators cooled with liquid cryogens potentially provide the lowest noise environment for MMC measurements. Unlike pulse-tube cooled systems the only source of electronic noise is from the magnet used for temperature regulation. By operating the cryostat unregulated it is possible to also eliminate this source of noise. This makes it possible to make measurements with only the MMC electrically connected to the cryostat. In order to further minimize any external noise the pre-amplifier and flux-locked loop electronics can be operated on battery power within a faraday cage. Finally, the data acquisition system can be outside of the faraday cage connected via a BNC cable. The ability to make these very low noise measurements is why it is desirable to use a system cooled with liquid cryogens for initial testing of MMCs. This was not possible in this work due to the inability to reliably achieve the temperatures necessary for high performance MMC operation. This appendix details the efforts to solve this problem and the potential solutions.

The existing magnets which were installed in the ADR cryostats at LLNL were originally designed to be able to achieve a maximum magnetic field density of 5 T. Due to degradation of the epoxy used to hold the magnet wirings in place initial testing of the magnets for this work demonstrated that it was impractical to operate the system above 4 T without risking a magnet quench. These magnets had a large Permendur 49 magnetic shield. This shield greatly reduced the magnetic field in the experimental volume as it has a high saturation field of approximately 2.4 T [113]. This shield placed constraints on the size of the replacement magnet. In addition, the existing wiring was not suitable for operation at currents of higher than 25 A. These two factors constrained the replacement magnet to a maximum field of 5 T. This is a 25% improvement in field strength that should provide a significant reduction in base temperature to less than 40 mK. This would provide sufficiently low temperatures to test existing MMC designs from the University of Heidelberg.

Installation of the new 5 T magnet required disassembling the cryostat and removing the paramagnetic salts prior to installing the new magnet. After the new magnet was installed it was necessary to center the salts in the bore of the magnet as well as possible. This is necessary because the peak field in the magnet is actually in the center of the magnet at the edge of the bore. Paramagnets will preferentially center themselves in the region of highest field. This results in both axial and tangential forces on the salts. These forces were calculated using FEMM [76] simulations of the magnet bore. The axial forces are the largest, on the order of 10's of pounds. The tangential forces are ideally zero if the magnet is perfectly centered, but increase to approximately ten pounds of force on the salt pills when they touch the walls of the bore. These forces scale with the field strength so these forces are also significantly larger with the 5 T magnet. The result is that when operated at full field even after both re-aligning the salt pills and re-tensioning the Kevlar strings such that the stage themselves cannot be easily torqued there is still permanent deformation in the oxygen free high conductivity copper rod that connects the salt pills to the experimental stages. Over the course of a single cycle this typically does not lead to a conductive touch, but it is not possible to cycle the magnet to full field a second time without the pill touching the wall of the magnet. Due to the fact that the magnet itself is at 4 K, or higher due to eddy current heating, if the salt pill is in contact with the wall the performance of the ADR is greatly reduced.

Figure A.1: A picture of the 3D printed ring designed to keep the salt pill from making conductive contact with the magnet wall.

One attempt was made to minimize the movement of the salt pill by adding a non-conductive centering ring which provided minimal contact to the pill, ideally none at zero field, but as the field increased it would prevent the pill from getting far enough away from the center of the bore to deform. This centering ring was made out of ABS plastic using a 3D printer, as it was not clear whether or not this technique would prevent the deformation and it was desirable to have a part that could be quickly and cheaply tested. A picture of the centering ring is shown in figure A.1. This ring has five points where the salt pill can touch that are as fine as possible in order to minimize the thermal conduction.

This ring was installed on the end of the magnet as shown in figure A.2 and the salt pill was centered such that it did not touch any of the five points at room temperature. This solution was tested by running several ADR cycles. At first it seemed to provide the desired solution, the base temperature was 42-45 mK. The hold time below 50 mK was reduced to 6 hours or so which would be sufficient for demonstration measurements and could be improved by replacing the ring with a similar design made out of a material with a much lower thermal conductivity. After approximately 6 ADR cycles, however, the conductive touch returned. This is likely due to the direction of forces

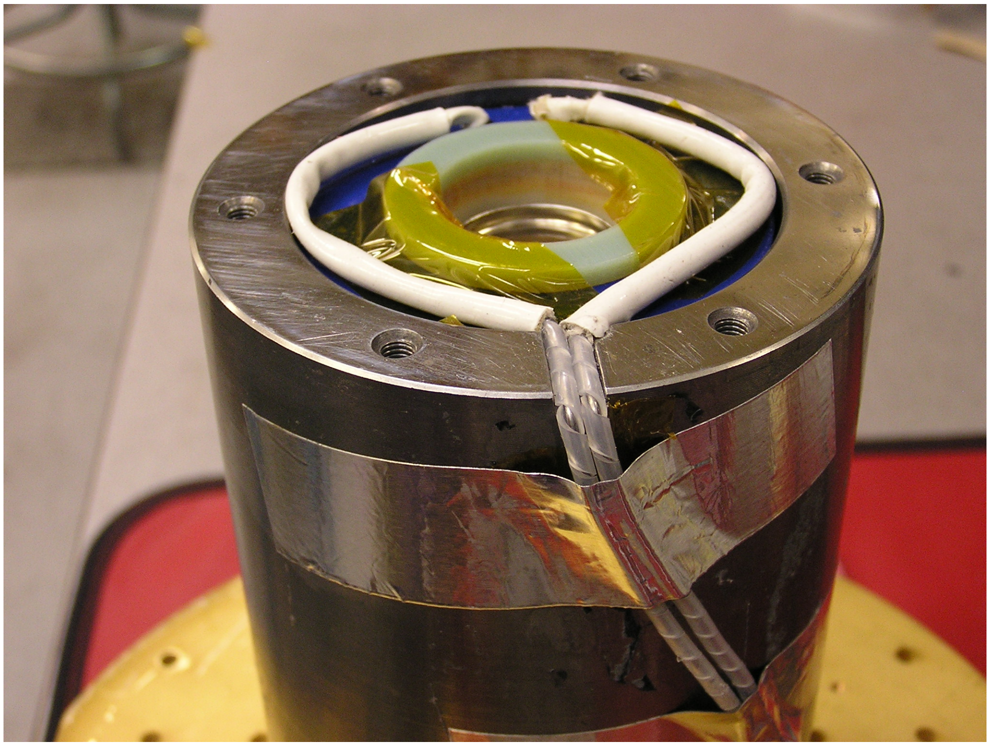

Figure A.2: A picture of the 3D printed ring installed at the bottom of the magnet.

on the FAA. As shown in figure A.3 the forces are oriented such that the ring does not prevent deformation of the copper rod. It was not possible to 3D print a version that would meet the tolerance requirements to prevent the FAA from touching at the other end.

The results of this testing made it clear that it would be necessary to make more drastic design changes in order for this system to operate routinely at 5 T. These design changes were outside the scope of this work. The two strategies considered were suspending the salt pill at the bottom end and stiffening the copper rod with a tube made out of a much stiffer metal. The latter was chosen as it would be simpler to retrofit existing cryostats and would provide a more reversible solution if it did not work. This required that a new GGG salt pill be fabricated, as the bore in the center of the current one was not large enough to accommodate the tube around the copper rod connecting the FAA to the experimental stage.

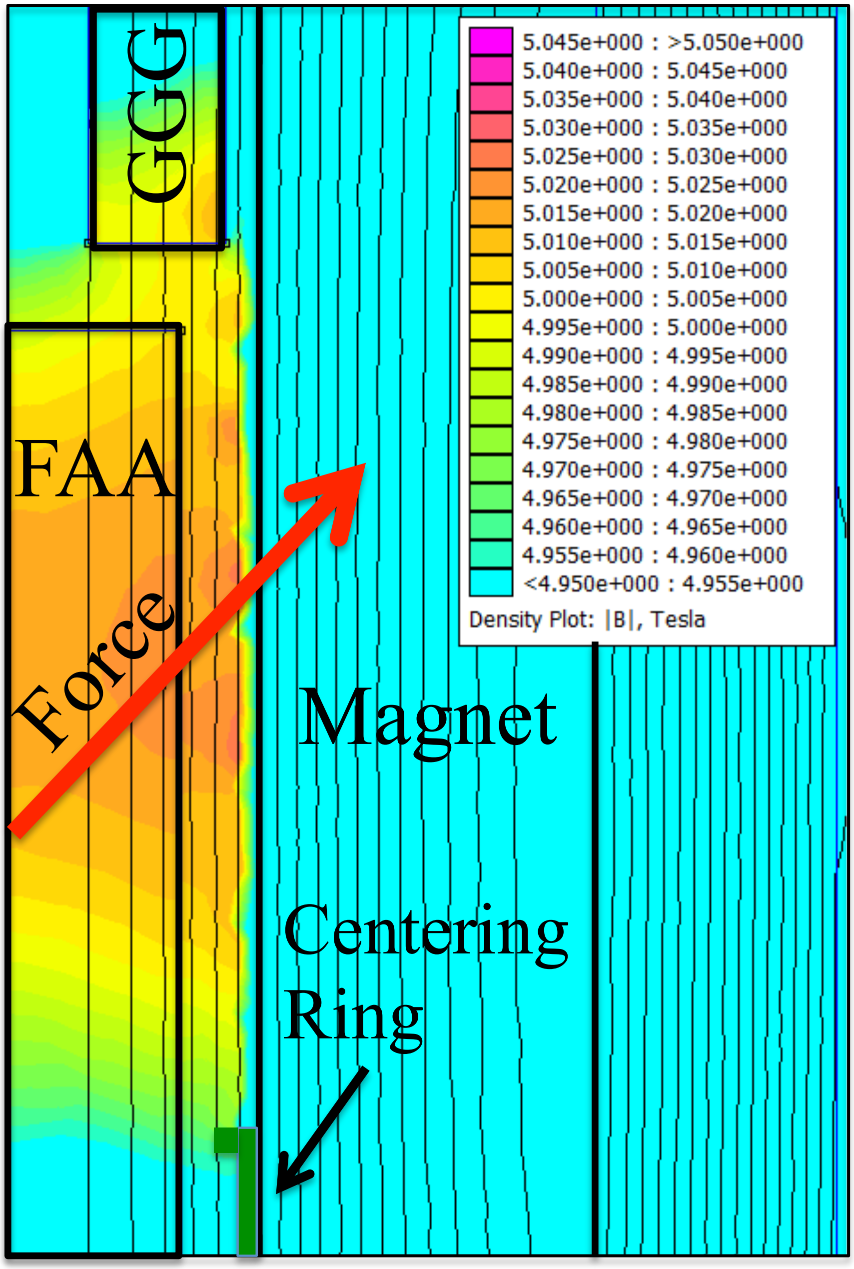

Figure A.3: A plot of the magnetic field inside the magnet with the salt pills inside showing the direction of the force on the FAA pill.

Appendix B

Digital Filtering Algorithms

The algorithms used for the first two digital filtering in this work were based on descriptions in reference [96]. The C implementations are included below. The gaussian filter is based on concepts described in [114].

B.1 Trapezoidal Filter

```
#include <stdio.h>
/***
 * Trapezoidal filter function for use with python high level
 * analysis and C binary data reader tools. Implementation is
 * based on lecture notes given by Valentin Jordanov.
 *
 * @author: Cameron Bates
 */

//These are needed unless you compiling in c99 mode
#ifndef TRUE
#define TRUE 1
#endif

#ifndef FALSE
#define FALSE 0
#endif


// defines a sample delay length must be greater than peaking + gap
#ifndef MAX_DELAY
#define MAX_DELAY 16384
#endif


double trapfilter(int *pulse, int peaking, int gap, int M, int len,
                  int len_in, double N, int bl, int pol) {
/***
 * primary function inputs are as follows
 * int *pulse: array containing raw pulse(this will be replaced by the
               filtered pulse)
 * int peaking: peaking time in samples of the trapezoidal filter
 * int gap: gap time in samples of the trapezoidal filter
 * int M: Decay correction factor ~ decay constant in samples
 * int len: actual length of the raw pulse
 * int len_in: shortened length of the raw pulse(improves speed)
 * double N: decay correction parameter 2. Set this to 0 and M to 1 to
 *           remove decay correction. Otherwise this should be 1
 *
 * This function returns the max of the trapezoidal filter output.
 */
```

```
// Initialize both delay buffers k-peaking. m- peaking + gap
int delayk_buffer[MAX_DELAY];
int delayk_index ;
int shiftk ; //peaking time
long datak_out; //delayed output
int delaym_buffer[MAX_DELAY];
int delaym_index ;
int shiftm; //peaking time + gap time
long datam_in; //input data
long datam_out; //delayed output

//output of shaper
double slowshaperout;

//clear delay buffers
int i = 0;
for (i = 0; i < MAX_DELAY; i++){
           delayk_buffer[i] = 0;
           delaym_buffer[i] = 0;
}
delayk_index = 0;
shiftk = peaking;
delaym_index = 0;
shiftm = peaking + gap;
if (len_in < len){
  len = len_in;
}

//initialize variables for trapezoidal filter
int n = 0;
i = 0;
double max = 0;
double accum1 = 0;
double accum2 = 0;
double adder2out;
double adder3out;
int input;

while (i < len ){
    input = (pulse[i] - bl) * pol;


    //peaking time delay
    datak_out = delayk_buffer[delayk_index];
    delayk_buffer[delayk_index] = input;
    delayk_index++;
    if (delayk_index >= shiftk) delayk_index = 0;

    // input to second delay stage is output of
```

```
        // first minus input (moving average 1)
        datam_in = input - datak_out;

        datam_out = delaym_buffer[delaym_index];
        delaym_buffer[delaym_index] = datam_in;
        delaym_index++;
        if (delaym_index >= shiftm) delaym_index = 0;

        // subtraction of second stage output from
        // first delay output (moving average 2)
        adder2out = datam_in - datam_out;
        // first accumulator
        accum1 += adder2out;
        //decay correction
        adder3out = adder2out*M + accum1*N;
        //second accumulator
        accum2 += adder3out;
        //shaper output (scaled by peaking time)
        slowshaperout = accum2/(double)peaking;

        //determines max of the slow shaper output
        if (slowshaperout > max){
            max = slowshaperout;
        }
        // This can be used to see what the shaper output is
        pulse[i] = slowshaperout;
        i++;

    }
    return max;
}
```

B.2 Cusp Filter

```
#include <stdio.h>
/***
 * Cusp filter function for use with python high level
 * analysis and C binary data reader tools.
 *
 * @author: Cameron Bates
 *
 *
 */

//These are needed unless you compiling in c99 mode
#ifndef TRUE
#define TRUE 1
#endif

#ifndef FALSE
```

```
#define FALSE 0
#endif

// defines a sample delay length must be greater than peaking + gap
#ifndef MAX_DELAY
#define MAX_DELAY 8000
#endif

double cuspfilter(int *pulse, int peaking, int gap, int M, int len,
                  int len_in, double N, int bl, int pol) {
/***
 * primary function inputs are as follows
 * int *pulse: array containing raw pulse(this will be replaced
              by the filetered pulse)
 * int peaking: peaking time in samples of the cusp filter
 * int gap: gap time in samples of the cusp filter
 * int M: Decay correction factor ~ decay constant in samples
 * int len: actual length of the raw pulse
 * int len_in: shortened length of the raw pulse(improves speed)
 *
 * This function returns the max of the cusp filter output.
 */


        // Initialize both delay buffers k-peaking. m-- peaking + gap
        int delayk_buffer[MAX_DELAY];
        int delayk_index ;
        int shiftk ; //peaking time
        long datak_out; //delayed output
        int delaym_buffer[MAX_DELAY];
        int delaym_index ;
        int shiftm; //peaking time + gap time
        long datam_in; //input data
        long datam_out; //delayed output

    int delaykm_buffer[MAX_DELAY*2];
    int delaykm_index ;
    int shiftkm ; //2*peaking +gap
    long datakm_out; //delayed output

    //output of shaper
    double slowshaperout;

    //clear delay buffers
    int i = 0;
    for (i = 0; i < MAX_DELAY; i++){
               delayk_buffer[i] = 0;
               delaym_buffer[i] = 0;
               delaykm_buffer[i] = 0;
    }
```

```
delayk_index = 0;
shiftk = peaking;

delaym_index = 0;
shiftm = peaking + gap;

delaykm_index = 0;
shiftkm = shiftk + shiftm;

if (len_in < len){len = len_in;}

//initialize variables for cusp filter
int n = 0;
i = 0;
double max = 0;
long p;
long p_old = 0;
long accum1 = 0;
long accum2 = 0;
long adder2out;
long adder3out;
int input;

while (i < len ){
    input = (pulse[i] − bl) ∗ pol;

    //first delay
    datak_out = delayk_buffer[delayk_index];
    delayk_buffer[delayk_index] = input;
    delayk_index++;
    if (delayk_index >= shiftk) delayk_index = 0;


    //second delay
    datam_in = input;
    datam_out = delaym_buffer[delaym_index];
    delaym_buffer[delaym_index] = datam_in;
    delaym_index++;
    if (delaym_index >= shiftm) delaym_index = 0;

    //third delay
    datakm_out = delaykm_buffer[delaykm_index];
    delaykm_buffer[delaykm_index] = input;
    delaykm_index++;
    if (delaykm_index >= shiftkm) delaykm_index = 0;


    // cusp filter algorithm with flat top
    p = p_old + input − datak_out + datam_out − datakm_out;
```

```
        p_old = p;

        adder2out = input + p − (datak_out + datam_out)∗shiftk
                  − datam_out + datakm_out;
        accum1 += adder2out;

        adder3out = adder2out∗M + accum1 ∗ N;
        accum2 += adder3out;

        // output corrected for peaking time^2
        slowshaperout = (double)accum2/(double)peaking/(double)peaking;

        //determination of max
        if (slowshaperout > max){
            max = slowshaperout;
        }

        pulse[i] = slowshaperout;
        i++;
    }

    return max;
}
```

B.3 Gaussian Filter

```
#include <stdio.h>
#include <math.h>
/∗∗∗
 ∗ Gaussian filter based on fortran code converted to C
 ∗
 ∗ @author: Cameron Bates
 ∗/

//These are needed unless you compiling in c99 mode
#ifndef TRUE
#define TRUE 1
#endif

#ifndef FALSE
#define FALSE 0
#endif


// defines a maximum sample length
#ifndef MAX_DELAY
#define MAX_DELAY 16384
#endif

#define N_POLES 6
```

```
double gaussfilter(int *pulse, double peaking, int len,
                   int len_in, double N, int bl, int pol) {
/***
 * primary function inputs are as follows
 * int *pulse: array containing raw pulse(this will be
               replaced by the filetered pulse)
 * int peaking: peaking time in samples of the trapezoidal filter
 * int len: actual length of the raw pulse
 * int len_in: shortened length of the raw pulse(improves speed)
 * double N: pole-zero correction factor
 *
 * This function returns the max of the gaussian filter output.
 */
    //    Gain=1/(n_poles**n_poles*exp(-n_poles)/n_poles!)
    double gain = 6.22575;

    // Time constant = tc samples REAL tc
    double tc = peaking;
    //C Pole zero correction = pz samples REAL pz
    double pz = N;
    int i, j;
    double a0, a1, b1;
    double y[MAX_DELAY], z[MAX_DELAY];
    //C Read input data DO i = 0, n - 1
    //READ( 5, * ) t( i ), x( i ) ENDDO
    if (len_in < len){
      len = len_in;
    }

    b1 = exp( -1.0 / tc );
    a0 = (1.0 + b1) / 2.0;
    a1 = - (1.0 + b1) / 2.0;
    y[0] = 0;
    pulse[0] = pulse[0] - bl;
    for (i= 1; i < len ; ++i) {
      pulse[i] = (pulse[i] - bl) * pol;
      y[i]= b1*y[i-1] + a0 * pulse[i] + a1 *
            pulse[i-1] + pulse[i-1]/pz;
    }

    //n-pole low pass filter
    //b1 = EXP( -1.0 / tc )
    a0 = 1.0 - b1;
    for(j = 0; j< N_POLES; ++j) {
      for (i= 1; i < len ; ++i) {
        z[i] = b1 * z[i - 1] + a0 * y[i];
      }
      for (i= 1; i < len ; ++i) {
```

```
        y[i] = z[i];
      }
    }
    double max = 0;
    for (i= 0; i < len ; ++i) {
      if (z[i]/peaking*gain > max) {
        max = z[i]/peaking*gain;
      }
      pulse[i] = z[i]*gain;
    }
    return max;
}
```

Appendix C

Data Acquisition Software

As a part of this work an acquisition framework, described in chapter 6 was developed. The source code for the principle components of this framework are included in this appendix. The readme for the acquisition code is included below.

C.1 Readme

A threaded acquisition code for python

This package has two distinct components: a base set of tools in `core.py` for building multi-threaded applications that use pipes for communication and queues for sharing data and a set of tools in `zmqcore.py` and `zmqmiddle.py` that wraps this in a ZeroMQ communication layer. This communication layer makes it possible for startup and shutdown of threads to be completely independent. It also supports restarting crashed threads though this functionality currently only works on linux.

The acquisition server

The server provides information to facilitate control and communication between disparate processes. It is possible to connect to the server to request backend application information from port 5555 by sending the python object ("list"). The server returns a list of application names and ports as a python object. These ports provide the direct interface to applications. The primary interaction methods are broken into two groups: command and control. Control functions are predefined and include: reload, kill, and status. Reload kills and reimports the process and configures it with the current configuration. The kill control function kills the process and the ZeroMQ interface process. The status control function asks the process for a heartbeat response which the ZeroMQ layer forwards to the underlying thread. If the underlying process is not responding the ZeroMQ layer can kill or restart it. The command category calls a function on the underlying process and can include data that will then be forwarded to the application. The application can then return anything from a simple success value to an arbitrary python object. The only predefined command is the configure command. This calls the configuration command on the underling process and stores the configuration object in the ZeroMQ layer to use in case the module needs to be restarted and re-configured.

The core thread

There is only one required function that a user has to implement after inheriting the AProcess class: execute. This is the primary acquisition/analysis loop that should run continuously, but busy waiting should be avoided if possible. The three additional methods are: initialize, which is called once when the process is started; stop, which is called once before the process is killed; and configure, which is called on reload and can be called to configure the application. It is recommended that the user use a separate ZeroMQ PUB-SUB or PUSH-PULL communication pattern to send raw data from one process to another.

C.2 Core Acquisition Thread

```
"""
This multithreaded acquisition code has two main process types DAQ
and Analysis. DAQ threads are designed to post data to a queue while
Analysis threads pull data from a queue by default. Both types of threads
have command pipes that allows for execution of functions synchronously with
readout.

@author: Cameron Bates
email: cameron.r.bates at gmail.com

"""
from __future__ import print_function, division

from multiprocessing import Process, Queue, Pipe
import time


class AProcess(Process):
    def __init__(self, dqueues=[], cmdpipe=None):
        if dqueues is not []:
            self.queue = []
            for i in range(len(dqueues)):
                self.queue.append(dqueues[i])
        if cmdpipe is not None:
            self.cmdpipe = cmdpipe
        else:
            self.cmdpipe = None
        Process.__init__(self)

    def run(self):
        self.running = True
        self.initialize()
        while True:
            if self.running is False:
                break
            if self.running is True:
                self.execute()
            if self.running is not True and self.running is not False:
                if not isinstance(self.running, str):
                    arg = self.running[1]
                    # print "argument: ", arg
                    self.running = self.running[0]
                else:
                    arg = None
                try:
                    fmethod = getattr(self, self.running)
                except:
                    print("call : ", self.running, " failed")
```

```
                    pass
                else:
                    if arg is not None:
                        returnval = fmethod(arg)
                    else:
                        returnval = fmethod()
                    if returnval is not None:
                        self.cmdpipe.send(returnval)
                self.running = True
            if self.cmdpipe is not None:
                poll = self.cmdpipe.poll()
            else:
                poll = None
            if poll:
                self.running = self.cmdpipe.recv()
        self.stop()

    def initialize(self):
        '''
        This will be run when the thread is started but before the
        acquisition/analysis loop starts.
        '''
        pass

    def execute(self):
        '''
        this is the main acquire or analyze function it must be overridden to
        do something useful.
        '''
        pass

    def stop(self):
        '''
        This function to be overridden handles any termination deletion calculation etc
        required by the user prior to the thread quitting
        '''
        #self.queue.close()

        pass

    def status(self):
        'This must return true if the process is working and false if it is broken'
        return True


class DAQ(AProcess):
    '''
    Basic data acquisition class to be subclassed. Acquire data method should
    be overridden and should return data or None
    '''
```

```
    def execute(self):
        '''
        method to put data from acquiredata method onto data queue checks if
        None is returned. This does not need to be overridden.
        '''
        data = self.acquiredata()
        if data is not None:
            self.queue[0].put(data)

    def acquiredata(self):
        '''
        Primary data acquisition loop returns data of any type if successfull
        or None if not
        '''
        return 1


class Analysis(AProcess):
    '''
    Basic data analysis class to be subclassed. Has an analyze data method
    that does does work on self.data and then saves the result. It also has
    an example retrieve data method that can be used to retrieve data by the
    main loop to get data for plotting for example.
    '''
    def initialize(self):
        self.sm = 0

    def execute(self):
        '''
        Analysis class primary method this is called repeatedly to retrieve
        data from the queue and analyze it using analyzedata.
        '''
        try:
            self.data = self.queue[0].get(1)
            #print self.data
        except:
            pass
        #print data
        else:
            self.analyzedata()

    def analyzedata(self):
        '''
        This method should be overridden to analyze that data contained in
        self.data.
        '''
        self.sm = self.data + self.sm

    def retrievedata(self):
        '''
```

```
        A function like this can be used to return data to the main analysis
        thread.
        '''
        return self.sm

if __name__ == '__main__':
    '''
    Example main for a simple application that runs for 10 seconds prints out
    the number of times the daq and analysis threads were called and then
    exits.
    '''
    cmdpipein1, cmdpipeout1 = Pipe()
    cmdpipein2, cmdpipeout2 = Pipe()

    dataqueue = Queue()
    D = DAQ((dataqueue, ), cmdpipeout1)
    A = Analysis((dataqueue, ), cmdpipeout2)
    D.start()
    A.start()
    time.sleep(10)
    cmdpipein2.send("retrievedata")
    while not cmdpipein2.poll():
        pass
    hist = cmdpipein2.recv()
    print(hist)
    cmdpipein1.send(False)
    cmdpipein2.send(False)
    D.terminate()
    A.terminate()
```

C.3 ZeroMQ Wrapper of Core Thread

```
from __future__ import print_function, division
import zmq
from multiprocessing import Pipe, Process
import os
import time


class zmqprocess(Process):
    def __init__(self, modulename):
        # no ZMQ STUFF HERE!
        super(zmqprocess, self).__init__()
        self.modulename = modulename
        self.loaded = False

    def load_reload_module(self):
        if self.loaded is True:
            self.mod = reload(self.mod)
            del self.process
```

```
        else:
            self.mod = __import__(self.modulename)
        self.loaded = True
        stuff = dir(self.mod)
        localprocessname = [item for item in stuff if "PDA" in item][0]
        localprocess = getattr(self.mod, localprocessname)
        self.pipe, process_pipe = Pipe()
        self.process = localprocess([], process_pipe)
        self.process.start()

    def configure(self):
        if self.config is not None:
            self.pipe.send(['configure', self.config])

    def run(self):
        self.context = zmq.Context()
        self.load_reload_module()
        self.transportsocket = self.context.socket(zmq.REQ)
        self.transportsocket.connect("tcp://localhost:5555")
        self.transportsocket.send_pyobj(("port", os.getpid(), self.modulename))
        self.addr = self.transportsocket.recv_pyobj()
        self.socket = self.context.socket(zmq.REP)
        self.socket.bind("tcp://*:"+str(self.addr))
        self.config = None
        while True:
            # TODO get messages + send heartbeat in a separate thread
            message = self.socket.recv_pyobj()
            if len(message) == 2:
                message_type, message_data = message
                if message_type == "control":
                    if message_data == "reload":
                        if self.process.is_alive():
                            self.pipe.send(False)
                            time.sleep(0.5)
                            #self.process.join()
                            self.process.terminate()
                        else:
                            self.process.terminate()
                        self.load_reload_module()
                        self.socket.send_pyobj("success")
                        self.configure()
                    elif message_data == "kill":
                        self.process.terminate()
                        self.socket.send_pyobj("success")
                        self.transportsocket.send_pyobj(('remove', self.addr))
                        break
                    elif message_data == "status":
                        self.pipe.send("status")
                        status = None
                        if self.pipe.poll(2):
```

```
                            status = self.pipe.recv()
                        if status:
                            self.socket.send_pyobj("alive")
                        else:
                            self.socket.send_pyobj("dead")
                if message_type == "command":
                    if len(message_data) == 2:
                        command, data = message_data
                        if command == "configure":
                            self.config = data
                            self.configure()
                            self.socket.send_pyobj("success")
                        else:
                            if command[0] != '_':
                                self.pipe.send([command, data])
                                if self.pipe.poll(2):
                                    status = self.pipe.recv()
                                    self.socket.send_pyobj(status)
                                else:
                                    self.socket.send_pyobj('Fail')
                            else:
                                self.socket.send_pyobj('Fail -illegal command')

            else:
                self.socket.send_pyobj("Fail")
```

C.4 ZeroMQ Server Layer

```
from __future__ import print_function, division

import zmq


def router():
    pids = []
    portnum = 8000
    context = zmq.Context()
    repsocket = context.socket(zmq.REP)
    repsocket.bind("tcp://*:5555")
    while True:
        message = repsocket.recv_pyobj()
        if len(message) == 3:
            request, pid, name = message
            if "port" == request:
                pids.append([pid, portnum, name])
                repsocket.send_pyobj(portnum)
                portnum = portnum + 1
        elif len(message) == 2:
            message, port = message
            if "remove" == message:
```

```
                for index, item in enumerate(pids):
                    p, pn, nm = item
                    if pn == port:
                        rm = index
                        break
                pids.pop(rm)
                repsocket.send_pyobj(True)
        elif isinstance(message, str):
            if message == 'shutdown':
                print("SHUTTING DOWN ALL THREADS!")
                repsocket.send_pyobj(True)
                for pid, portnum, name in pids:
                    socket = context.socket(zmq.REQ)
                    socket.connect('tcp://localhost:'+str(portnum))
                    socket.send_pyobj(('control', 'kill'))
                break
            elif message == 'list':
                repsocket.send_pyobj(pids)
            elif message == 'name':
                repsocket.send_pyobj("zmqmiddle")


def startup():
    context = zmq.Context()
    socket = context.socket(zmq.REQ)

    socket.connect("tcp://localhost:5555")
    poll = zmq.Poller()
    poll.register(socket, zmq.POLLIN)
    socket.send_pyobj('name')
    socks = dict(poll.poll(1000))  # set timeout to 1s
    if socks.get(socket) == zmq.POLLIN:
        reply = socket.recv_pyobj()
        if "zmqmiddle" != reply:
            raise Exception('error', 'something already operating on 5555')
    else:
        socket.setsockopt(zmq.LINGER, 0)
        socket.close()
        poll.unregister(socket)
        print("no server found creating one...")
        from multiprocessing import Process
        p = Process(target=router)
        p.start()
```

C.5 Common Tools for ZeroMQ Threads

```
from __future__ import print_function, division
import zmq
```

```
def zmq_recv_timeout(socket):
    poll = zmq.Poller()
    poll.register(socket, zmq.POLLIN)
    socks = dict(poll.poll(5000))  # set timeout to 5000s
    if socks.get(socket) == zmq.POLLIN:
        reply = socket.recv_pyobj()
    else:
        socket.setsockopt(zmq.LINGER, 0)
        socket.close()
        reply = None
    return reply


def getport(pname):
        context = zmq.Context()
        repasocket = context.socket(zmq.REQ)
        repasocket.connect("tcp://localhost:5555")
        repasocket.send_pyobj('list')
        message = repasocket.recv_pyobj()
        if len(message) > 0:
            for item in message:
                pid, portnum, name = item
                if name == pname:
                    break
        return portnum
```

C.6 Raw Data Writer

```
// Reliable Replacement File Format
#include <stdio.h>
#include <stdlib.h>
#include <time.h>
#include <Python.h>
#include <numpy/arrayobject.h>


#define RRFF_Version 1

FILE * datafile;

int write_header_C(char* datafilename, char* inifilename,int len){
    time_t rawtime;
    struct tm * timeinfo;
    long lSize;
    char * buffer;
    size_t result;
    FILE * pFile;
/////////////////////////////////////////////////////////////////
    // Buffer inifile into memory to go into header
    pFile = fopen ( inifilename , "rb" );
```

```
    if (pFile==NULL) {fputs ("File error",stderr); exit (1);}

    // obtain file size:
    fseek (pFile , 0 , SEEK_END);
    lSize = ftell (pFile);
    rewind (pFile);

    // allocate memory to contain the whole file:
    buffer = (char*) malloc (sizeof(char)*lSize);
    if (buffer == NULL) {fputs ("Memory error",stderr); exit (2);}

    // copy the file into the buffer:
    result = fread (buffer,1,lSize,pFile);
    if (result != lSize) {fputs ("Reading error",stderr); exit (3);}
/////////////////////////////////////////////////////////////////////

    datafile = fopen(datafilename,"wb");
    fprintf(datafile,"Header version: %d \n",RRFF_Version);

    time ( &rawtime );
    timeinfo = localtime ( &rawtime );
    fprintf(datafile,"date/time: %s",asctime (timeinfo));
    fprintf(datafile,"Total number of pulses: 0\n");
    fprintf(datafile,"Total acquisition time(s): 0\n");
    //copy the inifile into the header
    fwrite(buffer,1,lSize,datafile);
    //Plaintext description of binary data
    fprintf(datafile,"Binary data is an %d byte channel",sizeof(int));
    fprintf(datafile,"followed by a %d byte timestamp and",sizeof(double));
    fprintf(datafile,"%d %d byte values\n",len,sizeof(short));
    fprintf(datafile,"---End of ASCII formatted data---\n");
    free(buffer);
    return 0;
};

int write_pulse_C(int channel, double timestamp, short *data, int len){
    fwrite(&channel,sizeof(int),1,datafile);
    fwrite(&timestamp,sizeof(double),1,datafile);
    fwrite(data,sizeof(short),len,datafile);
    return 0;
};

int close_file_C(){
    fclose(datafile);
    return 0;
};

PyObject *write_header(PyObject *self, PyObject * args) {
        char* datfile;
    char* inifile;
```

```
    int len;
    PyArg_ParseTuple(args,"ssi",&datfile,&inifile,&len);
    write_header_C(datfile,inifile,len);
    Py_INCREF(Py_None);
    return Py_None;
};

PyObject *write_pulse(PyObject *self, PyObject * args) {
    PyArrayObject *adcarray;
    int channel;
    double timestamp;
    PyArg_ParseTuple(args,"idO",&channel,&timestamp,&adcarray);
    write_pulse_C(channel,timestamp,(short *)adcarray->data,adcarray->dimensions[0]);
    Py_INCREF(Py_None);
    return Py_None;
};

PyObject *close_file(PyObject *self, PyObject * args) {
    //PyArg_ParseTuple(args,"idO",&channel,&timestamp,&adcarray);
    close_file_C();
    Py_INCREF(Py_None);
    return Py_None;
};


static PyMethodDef RRFFmethods[] = {
        {"write_header", (PyCFunction)write_header, METH_VARARGS, ""},
    {"write_pulse", (PyCFunction)write_pulse, METH_VARARGS, ""},
    {"close_file", (PyCFunction)close_file, METH_VARARGS, ""},
        {NULL,NULL}
};

PyMODINIT_FUNC initRRFF(void) {
        (void) Py_InitModule("RRFF", RRFFmethods);
        import_array();
};


int write_header_C(char* datafilename, char* inifilename,int len);
int write_pulse_C(short channel, double timestamp, short *data, int len);
```

Appendix D

MMC Printed Circuit Board Preparation

In order to readout an MMC it is necessary to wirebond the MMC to a SQUID and wirebond both devices to readout pads, which can have wires soldered to them. In addition, the MMC and SQUID require as much magnetic shielding as possible in order to minimize external noise. Finally both chips need to have good thermal heat-sinking. This is important for the SQUID as it dissipates power in the resistors and this can cause undesirable heating of the MMC chip if the SQUID is not well heat sunk since the two are thermally connected via the wirebonds. It is also important for the MMC, especially when not using additional gold wirebonds to heat sink each pixel, because the responsivity changes as a function of the chip temperature and variations due to insufficient heat-sinking could degrade the resolution. Finally, it is desirable to have the conductive pathway between 4 K and the MMC that is used for the persistent current to be entirely superconducting so there is no runaway heating when freezing current in the MMC. This section will discuss the solutions to these problems that were employed for this work.

D.1 Printed Circuit Board Design

Circuit board choice

Typical printed circuit boards are produced by etching copper that is laminated to FR-4. This fiberglass material is good for electronics fabrication because it is self-extinguishing. At low temperatures, however, it has very low heat conduction. This is a problem for MMC operation because good heat-sinking is necessary to keep both the MMC and the input SQUID at the lowest possible temperature. In order to get around this problem it is necessary to choose an alternative circuit board design to connect both heat-sink and connect MMC and SQUID. Based on previous work at LLNL a design based on a 1/8" copper sheet with a polyimide laminate and an etched copper wiring layer on top of that was chosen. This only allows for a single wiring layer but has excellent heat conduction.

Wiring design

The MMC and SQUID are both designed to be connected using aluminum wirebonds. These are bare wires commonly used to connect integrated circuits. The wires that are used for connecting the electronics at room temperature and 4 K are superconducting NbTi filaments in a CuNi matrix. This is not conducive for wirebonding and is typically connected with Pb-Sn solder to a metal pad. The printed circuit board is needed as the bridge between a pad for soldering and a pad for wirebonding. This printed circuit board needs wiring that can accommodate both the MMC and the SQUID and is compatible with different MMC orientations. This drove a design that would be simple and flexible. The resulting circuit layout is shown in figure D.1. As shown in the figure the SQUID is connected at the bottom. There are two sets of unconnected pads near the top for connecting the MMC. These are designed to allow for any desired combination of four connections to the MMC by using wirebonds as jumpers between the two different pads. The connector pads at the ends of the printed circuit board were originally designed for use with right angle connectors.

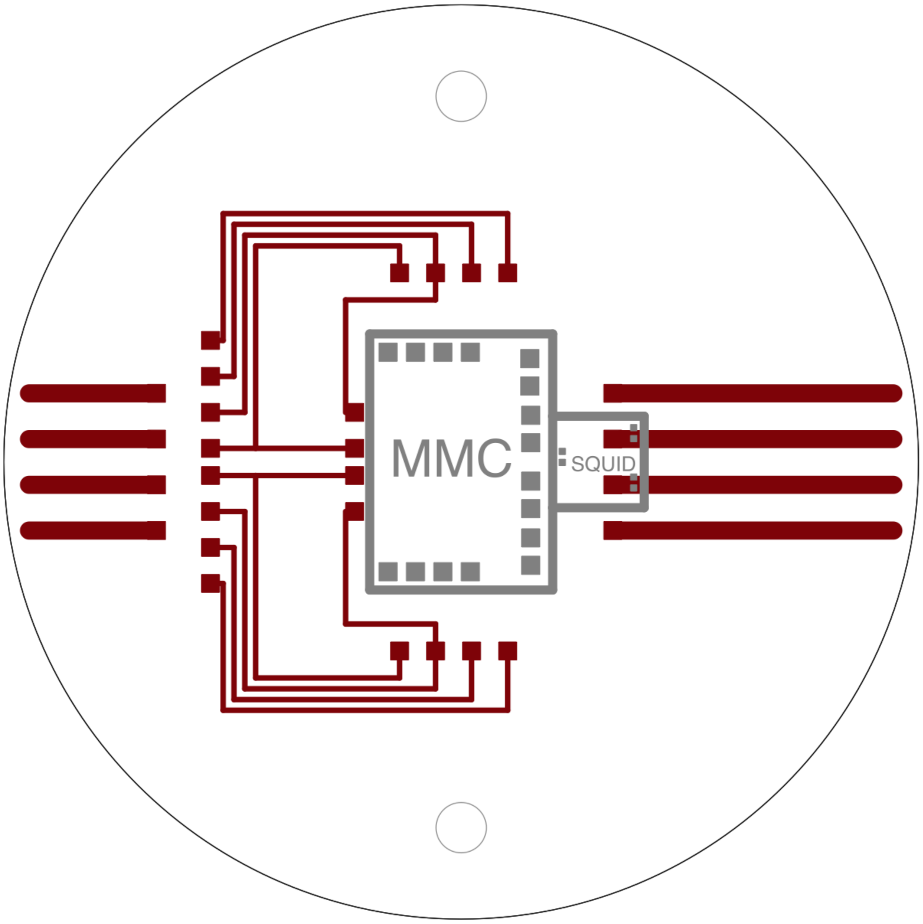

Figure D.1: Printed circuit board layout with SQUID and University of Heidelberg MMC positioning denoted.

These electrical connections turned out to be unreliable when cycled between room temperature and 4 K. In order to improve the reliability of the wiring the connectors were replaced with wires soldered directly to the pad and then epoxied into place to remove the stress from the solder joint.

D.2 Preparation of Chip Holder for MMC

In order to prepare the printed circuit board for the MMC is it necessary to mill out the area where the MMC and SQUID are attached so that the wirebond pads are at the same level. In addition, it is necessary to add a superconducting layer underneath the MMC and SQUID in order to minimize the influence of external magnetic fields on them. After the printed circuit board had been milled appropriately a thin sheet of 1/16" thick niobium was epoxied into the milled area to provide the superconducting layer. The MMC and SQUID were then epoxied to this niobium sheet. The steps

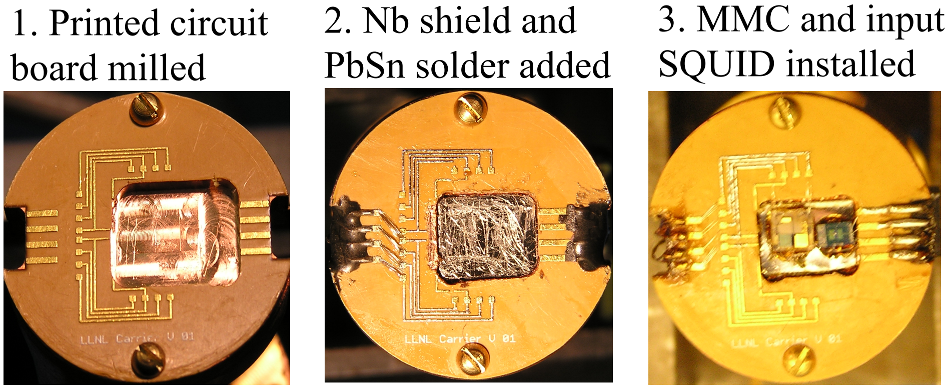

1. Printed circuit board milled

2. Nb shield and PbSn solder added

3. MMC and input SQUID installed

Figure D.2: Printed circuit board preparation and MMC installation.

for this process are shown in figure D.2.

D.3 Persistent Current Wiring

One unique aspect of MMC operation in comparison with other cryogenic detectors is the necessity for 100 mA wiring for the current that will be frozen in the persistent current loop. It takes hundreds of milliseconds to set the persistent current switch with the current methods. While setting the persistent current switch it is essential that all of the wiring below 4 K remains superconducting so that there is not excessive heating of the 1 K or 0.1 K stage. It is also desirable to be able to disconnect the wiring at 0.1 K so that the MMC can be removed without removing all the wiring. This was accomplished using a piece of copper coated in polyimide with etched copper on top similar to the printed circuit board but with just 4 strips of copper covered in PbSn solder as a connector and heatsink. These strips were long enough such that it is possible to solder wires at one end without accidentally de-soldering the other end. Superconducting NbTi wires in a CuNi matrix were used to connect the persistent current switch wiring from 4 K to the 0.1 K heat-sink and NbTi wires in a Cu matrix were used to connect the wires from the 0.1 K heat-sink to the MMC printed circuit board.

Initial tests with this wiring showed that while it was possible to freeze current into the MMC with this method there was still excessive heating. The experimental stage would rapidly heat up to over 100 mK when currents over 10 mA were applied. Using a 4-wire measurement of the resistance of the MMC printed circuit board it was determined that the gold-plated copper traces on the printed circuit board were the cause of the heating. This was remedied by adding PbSn solder to the traces everywhere except the bond-pads. This made the traces superconducting and made it possible to run up to 200 mA of current to the experimental stage at 35 mK with less than 1 mK in temperature rise over 10 s.

D.4 Future Printed Circuit Board Design Alternatives

The printed circuit board design chosen for this work was based on previous experience at LLNL in designing printed circuit boards for low temperature operation. This method worked well but had the disadvantage that it required specialized printed circuit board manufacturing, which increased the costs by an order of magnitude. One possible alternative is to use a standard 2-layer printed circuit board. Instead of using both layers for wiring the layer on the bottom side of the board is a single plane used for heat-sinking and the etched copper on the top side of the board has sections for wiring and sections for heat-sinking. The heat-sinking portions on the top side of the board are linked to the plane on the bottom side using via's. This should provide similar thermal performance at much lower cost. This has the disadvantage that it would be necessary to wirebond from the printed circuit board to the MMC which will be at different heights, but this is can be done with existing wirebonding machines at LLNL.

Bibliography

[1] G. T. Seaborg. The plutonium story. Technical Report LBL-13492, Lawrence Berkeley National Laboratory, 1981.

[2] F. J. Gavin. *Nuclear Statecraft*. Cornell University Press, 2012.

[3] U. G. Assembly. Establishment of a commission to deal with the problems raised by the discovery of atomic energy, January 1946.

[4] D. E. Lilienthal, C. I. Barnard, C. A. Thomas, J. R. Oppenheimer, and H. A. Winne. The acheson-lilienthal report: Report on the international control of atomic energy. Technical report, U.S. Government, 1946.

[5] K. Bird and M. J. Sherwin. *American Prometheus*. Vintage Books, 2006.

[6] D. Fischer. History of the international atomic energy agency : the first forty years. Technical report, International Atomic Energy Agency, 1997.

[7] K. J. Moody, I. D. Hutcheon, and P. M. Grant. *Nuclear Forensic Analysis*. CRC Press, 2005.

[8] R. Mowatt-larssen. Al qaeda weapons of mass destruction threat: hype or reality? Technical report, Harvard Kennedy School, 2010.

[9] World nuclear power reactors & uranium requirements, Accessed: Sept. 29 2014.

[10] Z. Mian, A. Meerburg, and F. von Hippel. Scope and verification of a fissile material (cutoff) treaty. In *Conference on Disarmament*, 2009.

[11] J. Doyle. *Nuclear Safeguards, Security and Nonproliferation: Achieving Security with Technology and Policy*. Butterworth-Heinemann, 2008.

[12] J. C. Mark. Explosive properties of reactor-grade plutonium. *Science and Global Security*, 4(1):111–128, 1993.

[13] T. Uckan, J. March-Leuba, D. Powell, and M. Wright. Blend down monitoring system fissile mass flow monitor implementation at the electrochemical plant, zelenogorsk, russia. Technical report, Oak Ridge National Laboratory, 2005.

[14] M. May, R. Abedin-Zadeh, D. Barr, A. Carnesale, P. E. Coyle, J. Davis, W. Dorland, W. Dunlop, S. Fetter, A. Glaser, I. D. Hutcheon, F. Slakey, and B. Tannenbaum. Nuclear forensics role, state of the art, and program needs. Technical report, American Physical Society and the American Association for the Advancement of Science, 2008.

[15] F. J. Low. Low-temperature germanium bolometer. *J. Opt. Soc. Am.*, 51(11):1300–1304, Nov 1961.

[16] S. Moseley, R. Kelley, R. Schoelkopf, and A. Szymkowiak. Advances toward high spectral resolution quantum x-ray calorimetry. *IEEE TNS*, 35(1):59–64, 1988.

[17] A. Alessandrello, J. Beeman, C. Brofferio, O. Cremonesi, E. Fiorini, A. Giuliani, E. Haller, A. Monfardini, A. Nucciotti, M. Pavan, G. Pessina, E. Previtali, and L. Zanotti. High energy resolution bolometers for nuclear physics and x-ray spectroscopy. *Physical Review Letters*, 82(3):513–515, 1999.

[18] M. F. Cunningham, J. Ullom, T. Miyazaki, S. Labov, J. Clarke, T. Lanting, A. Lee, P. Richards, J. Yoon, and H. Spieler. High-resolution operation of frequency-multiplexed transition-edge photon sensors. *Applied Physics Letters*, 81(1):159–161, 2002.

[19] B. Zink, J. Ullom, J. Beall, K. Irwin, W. Doriese, W. Duncan, L. Ferreira, G. Hilton, R. Horansky, C. Reintsema, and L. Vale. Array-compatible transition-edge sensor microcalorimeter γ-ray detection with 42 ev energy resolution at 103 kev. *Applied Physics Letters*, 89(12):124101, 2006.

[20] A. Fleishmann, L. Gastaldo, S. Kempf, A. Kirsch, A. Pabinger, J.-P. P. C. Pies, P. Ranitzsch, S. Schäfer, F. Seggern, T. Wolf, C. Enss, and G. Seidel. Metallic magnetic calorimeters. *AIP Conf. Proc.*, 1185:571–578, 2009.

[21] C. Pies, S. Schaefer, S. Heuser, S. Kempf, A. Pabinger, J.-P. Porst, P. Ranitsch, N. Foerster, D. Hengstler, A. Kampkoetter, T. Wolf, L. Gastaldo, A. Fleischmann, and C. Enss. maxs: Microcalorimeter arrays for high-resolution x-ray spectroscopy at gsi/fair. *J. Low Temp. Phys.*, 167:269, 2012.

[22] A. Fleischmann, M. Link, T. Daniyarov, H. Rotzinger, C. Enss, and G. Seidel. Metallic magnetic calorimeters (mmc): detectors for high-resolution x-ray spectroscopy. *Nuclear Instruments and Methods in Physics Research Section A: Accelerators, Spectrometers, Detectors and Associated Equipment*, 520(1-3):27 – 31, 2004. Proceedings of the 10th International Workshop on Low Temperature Detectors.

[23] M. Loidl, E. Leblanc, J. Bouchard, T. Branger, N. Coron, J. Leblanc, P. de Marcillac, H. Rotzinger, T. Daniyarov, M. Linck, A. Fleischmann, and C. Enss. High-energy resolution x-ray, gamma and electron spectroscopy with cryogenic detectors. *Applied Radiation and Isotopes*, 60(2-4):363 – 368, 2004. Proceedings of the 14th International Conference on Radionuclide Metrology and its Applications, {ICRM} 2003.

[24] M. Loidl, E. Leblanc, T. Branger, H. Rotzinger, T. Daniyarov, M. Linck, A. Fleischmann, and C. Enss. Feasibility study of absolute activity measurement with metallic magnetic microcalorimeters. *Nuclear Instruments and Methods in Physics Research Section A: Accelerators, Spectrometers, Detectors and Associated Equipment*, 520(1-3):73 – 75, 2004. Proceedings of the 10th International Workshop on Low Temperature Detectors.

[25] H. Rotzinger, J. Adams, S. Bandler, J. Beyer, H. Eguchi, E. Figueroa-Feliciano, W. Hsieh, G. Seidel, and T. Stevenson. Performance of micro-fabricated magnetic calorimeters arrays for x-ray spectroscopy. *Journal of Low Temperature Physics*, 151(1-2):351–356, 2008.

[26] D. Reilly, N. Ensslin, H. S. Jr., and S. Kreiner. *Passive Nondestructive Assay of Nuclear Materials*. National Technical Information Service, 1991.

[27] IAEA. Nuclear fuel cycle simulation system (vista). Technical Report IAEA-TECDOC-1535, Nuclear Fuel Cycle and Materials Section, 2007.

[28] J. McKibben, D. Chostner, and E. Orebaugh. Plutonium-uranium separation in the purex process using mixtures of hydroxylamine nitrate and ferrous sulfamate. Technical report, Savannah River Lab, 1983.

[29] International Atomic Energy Agency. Iaea safeguards glossary. Technical report, International Atomic Energy Agency, 2001.

[30] F. Dalnoki-Veress, M. Pomper, S. Lieggi, C. McCombie, and N. Chapman. Rethinking spent fuel management in south korea. Technical report, James Martin Center for Nonproliferation Studies, 2013.

[31] The Government of the United States of America and the Government of the Russian Federetion. Agreement between the government of the united states of america and the government of the russian federation concerning the management and disposition of plutonium designated as no longer required for defense purposes and related cooperation, 2000.

[32] UNIDIR. A fissile material cut-off treaty understanding the critical issues. Technical report, United Nations Institute for Disarmamanet Research, 2010.

[33] J. Dryer. *Development of Superconducting High-Resolution Gamma-Ray Spectrometers for Nuclear Safeguards*. PhD thesis, University of California, Berkeley, 2012.

[34] D. Vo. Personal communication, 2014.

[35] R. Gunnink and W. Ruhter. Multiple group analysis (mga): A gamma-ray spectrum analysis code for determining plutonium isotopic abundances. Technical report, Lawrence Livermore National Laboratory, 1990.

[36] T. Sampson, T. Kelley, and D. Vo. Application guide to gamma-ray isotopic analysis using the fram software. Technical Report LA-14018, Los Alamos National Laboratory, 2003.

[37] M. Loidl, E. Leblanc, M. Rodrigues, J. Bouchard, B. Censier, T. Branger, and D. Lacour. Metallic magnetic calorimeters for absolute activity measurement. *Journal of Low Temperature Physics*, 151(3-4):1055–1060, 2008.

[38] E. B. Norman, E. Browne, H. A. Shugart, T. H. Joshi, and R. B. Firestone. Evidence against correlations between nuclear decay rates and earth-sun distance. *Astroparticle Physics*, 31(2):135 – 137, 2009.

[39] S. Agostinelli, J. Allison, K. Amako, J. Apostolakis, H. Araujo, P. Arce, M. Asai, D. Axen, S. Banerjee, G. Barrand, F. Behner, L. Bellagamba, J. Boudreau, L. Broglia, A. Brunengo, H. Burkhardt, S. Chauvie, J. Chuma, R. Chytracek, G. Cooperman, G. Cosmo, P. Degtyarenko, A. Dell'Acqua, G. Depaola, D. Dietrich, R. Enami, A. Feliciello, C. Ferguson, H. Fesefeldt, G. Folger, F. Foppiano, A. Forti, S. Garelli, S. Giani, R. Giannitrapani, D. Gibin, J. G. Cadenas, I. Gonzlez, G. G. Abril, G. Greeniaus, W. Greiner, V. Grichine, A. Grossheim, S. Guatelli, P. Gumplinger, R. Hamatsu, K. Hashimoto, H. Hasui, A. Heikkinen, A. Howard, V. Ivanchenko, A. Johnson, F. Jones, J. Kallenbach, N. Kanaya, M. Kawabata, Y. Kawabata, M. Kawaguti, S. Kelner, P. Kent, A. Kimura, T. Kodama, R. Kokoulin, M. Kossov, H. Kurashige, E. Lamanna, T. Lampén, V. Lara, V. Lefebure, F. Lei, M. Liendl, W. Lockman, F. Longo, S. Magni, M. Maire, E. Medernach, K. Minamimoto, P. M. de Freitas, Y. Morita, K. Murakami, M. Nagamatu, R. Nartallo, P. Nieminen, T. Nishimura, K. Ohtsubo, M. Okamura, S. O'Neale, Y. Oohata, K. Paech, J. Perl, A. Pfeiffer, M. Pia, F. Ranjard, A. Rybin, S. Sadilov, E. D. Salvo, G. Santin, T. Sasaki, N. Savvas, Y. Sawada, S. Scherer, S. Sei, V. Sirotenko, D. Smith, N. Starkov, H. Stoecker, J. Sulkimo, M. Takahata, S. Tanaka, E. Tcherniaev, E. S. Tehrani, M. Tropeano, P. Truscott, H. Uno, L. Urban, P. Urban, M. Verderi, A. Walkden, W. Wander, H. Weber, J. Wellisch, T. Wenaus, D. Williams, D. Wright, T. Yamada, H. Yoshida, and D. Zschiesche. Geant4 a simulation toolkit. *Nuclear Instruments and Methods in Physics Research Section A: Accelerators, Spectrometers, Detectors and Associated Equipment*, 506(3):250 – 303, 2003.

[40] J. Allison, K. Amako, J. Apostolakis, H. Araujo, P. Dubois, M. Asai, G. Barrand, R. Capra, S. Chauvie, R. Chytracek, G. A. P. Cirrone, G. Cooperman, G. Cosmo, G. Cuttone, G. G. Daquino, M. Donszelmann, M. Dressel, G. Folger, F. Foppiano, J. Generowicz, V. Grichine, S. Guatelli, P. Gumplinger, A. Heikkinen, I. Hrivnacova, A. Howard, S. Incerti, V. Ivanchenko, T. Johnson, F. Jones, T. Koi, R. Kokoulin, M. Kossov, H. Kurashige, V. Lara, S. Larsson, F. Lei, O. Link, F. Longo, M. Maire, A. Mantero, B. Mascialino, I. McLaren, P. Lorenzo, K. Minamimoto, K. Murakami, P. Nieminen, L. Pandola, S. Parlati, L. Peralta, J. Perl, A. Pfeiffer, M. Pia, A. Ribon, P. Rodrigues, G. Russo, S. Sadilov, G. Santin, T. Sasaki, D. Smith, N. Starkov, S. Tanaka, E. Tcherniaev, B. Tome, A. Trindade, P. Truscott, L. Urban, M. Verderi, A. Walkden, J. P. Wellisch, D. Williams, D. Wright, and H. Yoshida. Geant4 developments and applications. *Nuclear Science, IEEE Transactions on*, 53(1):270–278, Feb 2006.

[41] Y. Akovali. Nuclear data sheets for a = 242. *Nuclear Data Sheets*, 96(1):177 – 239, 2002.

[42] R. Gunnink. Use of isotope correlation techniques to determine ^{242}pu abundance. In *Nuclear Materials Management*, volume 9, 1980.

[43] G. Bignan, W. Ruhter, H. Ottmar, A. Schubert, and C. Zimmerman. Plutonium isotopic determination by gamma spectometry: Recommendations for the ^{242}pu content evaluation using a new algorithm. *ESARDA BULLETIN*, 28:1–6, 1998.

[44] G. Zschornack. *Handbook of X-Ray Data*. Springer, 2007.

[45] P. L. Ryder. Theoretical analysis of statistical limitations to the accuracy and spectral resolution in energy dispersive x-ray analysis. In *Proceedings of the Workshop on Analytical Electron Microscopy*, volume 1 of *Scanning Electron Microscopy*, March 1977.

[46] O. Drury, S. Terracol, and S. Friedrich. Quantifying the benefits of ultrahigh energy resolution for gamma ray spectrometry. *phy. stat. sol. c*, 2:1468–1479, 2005.

[47] S. Ali, S. F. Terracol, I. D. Hau, O. B. Drury, and S. Friedrich. The possibility of direct ^{242}pu with cryogenic gamma-ray spectrometers pu detection. In *46th Annual Meeting of the Institute of Nuclear Materials Management (INMM)*, 2005.

[48] F. Simon. Application of low temperature calorimetry to radioactive measurements. *Nature*, 135:763, May 1935.

[49] S. H. Moseley, J. C. Mather, and D. McCammon. Thermal detectors as x-ray spectrometers. *Journal of Applied Physics*, 56(5):1257–1262, 1984.

[50] E. Fiorini and T. Niinikoski. Low-temperature calorimetry for rare decays. *Nuclear Instruments and Methods in Physics Research*, 224(1–2):83 – 88, 1984.

[51] M. W. Goodman and E. Witten. Detectability of certain dark-matter candidates. *Phys. Rev. D*, 31:3059–3063, Jun 1985.

[52] D. McCammon. Semiconductor thermistors. In C. Enss, editor, *Cryogenic Particle Detection*, volume 99 of *Topics in Applied Physics*, pages 35–62. Springer Berlin Heidelberg, 2005.

[53] K. Irwin and G. Hilton. Transition-edge sensors. In C. Enss, editor, *Cryogenic Particle Detection*, volume 99 of *Topics in Applied Physics*, pages 63–150. Springer Berlin Heidelberg, 2005.

[54] S. Bandler, E. Figueroa-Feliciano, N. Iyomoto, R. Kelley, C. Kilbourne, K. Murphy, F. Porter, T. Saab, and J. Sadleir. Non-linear effects in transition edge sensors for x-ray detection. *Nuclear Instruments and Methods in Physics Research Section A: Accelerators, Spectrometers, Detectors and Associated Equipment*, 559(2):817 – 819, 2006. Proceedings of the 11th International Workshop on Low Temperature Detectors LTD-11 11th International Workshop on Low Temperature Detectors.

[55] T. Fausch, M. Buhler, and E. Umlauf. Signal rise time of the magnetic bolometer. *Journal of Low Temperature Physics*, 93:703–708, 1993.

[56] M. Bühler, E. Umlauf, and J. Mather. Noise of a bolometer with vanishing self-heating. *Nuclear Instruments and Methods in Physics Research Section A: Accelerators, Spectrometers, Detectors and Associated Equipment*, 346(1–2):225 – 229, 1994.

[57] M. Bühler and E. Umlauf. The noise of the magnetic bolometer. *Journal of Low Temperature Physics*, 93(3-4):697–702, 1993.

[58] A. Fleischmann. Cryogenic particle detectors. In *Cryocourse 2012*, 2012.

[59] S. R. Bandler, C. Enss, R. E. Lanou, H. J. Marls, T. More, F. S. Porter, and G. M. Seldel. Metallic magnetic bolometers for particle detection. *Journal of Low Temperature Physics*, 93:709–714, 1993.

[60] J. S. Adams, S. R. Bandler, C. Enss, A. Fleischmann, Y. H. Huang, Y. H. Kim, J. Schoenefeld, G. M. Seidel, and R. Weis. Magnetic calorimeters for x-ray and gamma-ray detection. In *X-Ray and Gamma-Ray Instrumentation for Astronomy XI*, volume 4140, pages 445–451, 2000.

[61] B. Klemme, M. Adriaans, P. Day, D. Sergatskov, T. Aselage, and R. Duncan. Pdmn and pdfe: New materials for temperature measurement near 2 k. *Journal of low temperature physics*, 116(1-2):133–146, 1999.

[62] C. Enss, A. Fleischmann, T. Görlach, Y. H. Kim, G. M. Seidel, and H. F. Braun. Thermalization of magnetic calorimeters. *AIP Conference Proceedings*, 605(1):71–74, 2002.

[63] A. Fleischmann, C. Enss, and G. Seidel. Metallic magnetic calorimeters. In C. Enss, editor, *Cryogenic Particle Detection*, volume 99 of *Topics in Applied Physics*, pages 151–216. Springer Berlin Heidelberg, 2005.

[64] A. Freeman. Energy band structure, indirect exchange interactions and magnetic ordering. In R. Elliott, editor, *Magnetic Properties of Rare Earth Metals*, pages 245–333. Springer US, 1972.

[65] C. M. Baglin. Nuclear data sheets for a = 167. *Nuclear Data Sheets*, 90(3):431 – 644, 2000.

[66] J. Porst. *High-Resolution Metallic Magnetic Calorimeters for β-Spectroscopy on ^{187}Rhenium and Position Resolved X-Ray Spectroscopy*. PhD thesis, University of Heidelberg, Germany, 2011.

[67] Technic Inc., Accessed: Sept. 29 2014.

[68] T. V. Duzer and C. Turner. *Principles of Superconducting Devices and Circuits*. Elsevier, 1981.

[69] J. Clarke, W. Goubau, and M. Ketchen. Tunnel junction dc squid: Fabrication, operation, and performance. *Journal of Low Temperature Physics*, 25(1-2):99–144, 1976.

[70] W. Jenks, S. Sadeghi, and J. P. Wikswo Jr. Squids for nondestructive evaluation. *Journal of Physics D: Applied Physics*, 30(3):293, 1997.

[71] R. Welty and J. Martinis. Two-stage integrated squid amplifier with series array output. *Applied Superconductivity, IEEE Transactions on*, 3(1):2605–2608, March 1993.

[72] D. McCammon. Thermal equilibrium calorimeters - an introduction. In C. Enss, editor, *Cryogenic Particle Detection*, volume 99 of *Topics in Applied Physics*, pages 1–34. Springer Berlin Heidelberg, 2005.

[73] F. Pobell. Refrigeration by adiabatic nuclear demagnetization. In *Matter and Methods at Low Temperatures*, pages 215–258. Springer Berlin Heidelberg, 2007.

[74] S. M. Anton, J. S. Birenbaum, S. R. O'Kelley, V. Bolkhovsky, D. A. Braje, G. Fitch, M. Neeley, G. C. Hilton, H.-M. Cho, K. D. Irwin, F. C. Wellstood, W. D. Oliver, A. Shnirman, and J. Clarke. Magnetic flux noise in dc squids: Temperature and geometry dependence. *Phys. Rev. Lett.*, 110:147002, Apr 2013.

[75] C. Pies. *maXs-200: Entwicklung und Charakterisierung eines Röntgendetektors basierend auf magnetischen Kalorimetern für die hochauflösende Spektroskopie hochgeladener Ionen*. PhD thesis, Ruprecht-Karls-Universität Heidelberg, 2012.

[76] D. Meeker. Finite element method magnetics, version 4.2, Accessed: Nov 5, 2014.

[77] A. Burck. Entwicklung großflächiger magnetischer kalorimeter zur energieaufgelösten detektion von röntgenquanten und hochenergetischen teilchen. Master's thesis, Ruprecht-Karls-Universität Heidelberg, 2004.

[78] C. Enss, A. Fleischmann, K. Horst, J. Schönefeld, J. Sollner, J. Adams, Y. Huang, Y. Kim, and G. Seidel. Metallic magnetic calorimeters for particle detection. *Journal of Low Temperature Physics*, 121(3-4):137–176, 2000.

[79] C. Pies. Entwicklung eines detektor-arrays basierend auf magnetischen kalorimetern für die hochaufgelöste röntgenspektroskopie an hochgeladenen ionen. Master's thesis, University of Heidelberg, 2008.

[80] A. Burck. *Entwicklung großflächiger mikrostrukturierter magnetischer Kalorimeter mit Au:Er- und Ag:Er-Sensoren für den energieaufgelösten Nachweis von Röntgenquanten und hochenergetischen Teilchen*. PhD thesis, University of Heidelberg, 2008.

[81] M. Staab, F. Greiner, M. Schlosser, and H. Schlaak. Applications of novel high-aspect-ratio ultrathick uv photoresist for microelectroplating. *Microelectromechanical Systems, Journal of*, 20(4):794–796, Aug 2011.

[82] C. Bates, C. Pies, S. Kempf, L. Gastaldo, A. Fleischmann, C. Enss, and S. Friedrich. Development of mmc gamma detectors for nuclear analysis. *Journal of Low Temperature Physics*, 176(5-6):631–636, 2014.

[83] A. de Waele. Basic operation of cryocoolers and related thermal machines. *Journal of Low Temperature Physics*, 164(5-6):179–236, 2011.

[84] Z. Gan, W. Dong, L. Qiu, X. Zhang, H. Sun, Y. He, and R. Radebaugh. A single-stage gm-type pulse tube cryocooler operating at 10.6 k. *Cryogenics*, 49(5):198 – 201, 2009.

[85] I. A. Tanaeva, A. T. A. M. de Waele, U. Lindemann, N. Jiang, and G. Thummes. The superfluid vortex cooler. *Journal of Applied Physics*, 98(3):–, 2005.

[86] P. Wikus, G. Burghart, and E. Figueroa-Feliciano. Optimum operating regimes of common paramagnetic refrigerants. *Cryogenics*, 51(9):555 – 558, 2011.

[87] C. Hagmann and P. Richards. Two-stage magnetic refrigerator for astronomical applications with reservoir temperatures above 4 k. *Cryogenics*, 34(3):221 – 226, 1994.

[88] G. W. Wilson and P. T. Timbie. Construction techniques for adiabatic demagnetization refrigerators using ferric ammonium alum. *Cryogenics*, 39(4):319 – 322, 1999.

[89] F. Pobell. Refrigeration by adiabatic demagnetization of a paramagnetic salt. In *Matter and Methods at Low Temperatures*, pages 203–213. Springer Berlin Heidelberg, 2007.

[90] Janis Research Company, LLC, Accessed: Dec 11, 2014.

[91] F. Pobell. The 3he-4he dilution refrigerator. In *Matter and Methods at Low Temperatures*, pages 149–189. Springer Berlin Heidelberg, 2007.

[92] F. Pobell. Thermal contact and thermal isolation. In *Matter and Methods at Low Temperatures*, pages 95–114. Springer Berlin Heidelberg, 2007.

[93] iMatix Corporation. Zeromq, Accessed: Dec 12, 2014.

[94] D. Schnur. flot, Accessed: Dec 10, 2014.

[95] V. Radeka. Optimum signal-processing for pulse-amplitude spectrometry in the presence of high-rate effects and noise. *Nuclear Science, IEEE Transactions on*, 15(3):455–470, June 1968.

[96] V. T. Jordanov and G. F. Knoll. Digital synthesis of pulse shapes in real time for high resolution radiation spectroscopy. *Nuclear Instruments and Methods in Physics Research Section A: Accelerators, Spectrometers, Detectors and Associated Equipment*, 345(2):337 – 345, 1994.

[97] G. F. Knoll. *Radiation Detection and Measurement*. Wiley, 2010.

[98] A. Szymkowiak, R. Kelley, S. Moseley, and C. Stahle. Signal processing for microcalorimeters. *Journal of Low Temperature Physics*, 93(3-4):281–285, 1993.

[99] R. Brun and F. Rademakers. {ROOT} - an object oriented data analysis framework. *Nuclear Instruments and Methods in Physics Research Section A: Accelerators, Spectrometers, Detectors and Associated Equipment*, 389(1-2):81 – 86, 1997. New Computing Techniques in Physics Research V.

[100] C. Shannon. Communication in the presence of noise. *Proceedings of the IRE*, 37(1):10–21, Jan 1949.

[101] P. A. B. Scoullar, C. C. McLean, and R. J. Evans. Real time pulse pile-up recovery in a high throughput digital pulse processor. In *AIP Conference Proceedings*, volume 1412, Dec 2011.

[102] R. M. Jr, C. Gesh, R. Pagh, R. Rucker, and R. W. III. Compendium of material composition data for radiation transport modeling. Technical report, Pacific Northwest National Laboratory, 2011.

[103] M. Chadwick, M. Herman, P. Obložinský, M. Dunn, Y. Danon, A. Kahler, D. Smith, B. Pritychenko, G. Arbanas, R. Arcilla, R. Brewer, D. Brown, R. Capote, A. Carlson, Y. Cho, H. Derrien, K. Guber, G. Hale, S. Hoblit, S. Holloway, T. Johnson, T. Kawano, B. Kiedrowski, H. Kim, S. Kunieda, N. Larson, L. Leal, J. Lestone, R. Little, E. McCutchan, R. MacFarlane, M. MacInnes, C. Mattoon, R. McKnight, S. Mughabghab, G. Nobre, G. Palmiotti, A. Palumbo, M. Pigni, V. Pronyaev, R. Sayer, A. Sonzogni, N. Summers, P. Talou, I. Thompson, A. Trkov, R. Vogt, S. van der Marck, A. Wallner, M. White, D. Wiarda, and P. Young. Endf/b-vii.1 nuclear data for science and technology: Cross sections, covariances, fission product yields and decay data. *Nuclear Data Sheets*, 112(12):2887 – 2996, 2011. Special Issue on ENDF/B-VII.1 Library.

[104] B. Rooney and P. Felsher, Accessed: Dec 10, 2014.

[105] S. Kempf, M. Wegner, L. Gastaldo, A. Fleischmann, and C. Enss. Multiplexed readout of mmc detector arrays using non-hysteretic rf-squids. *Journal of Low Temperature Physics*, 176(3-4):426–432, 2014.

[106] Y. Ogasaka, T. Iwahara, T. Miyazawa, Y. Fukaya, N. Sasaki, K. Tamura, Y. Kanou, H. Kunieda, and K. Yamashita. Characterization of pt/c multilayer at 200 kev soft gamma-ray. In *Optics for EUV, X-Ray, and Gamma-Ray Astronomy III*, volume 6688, pages 66880S–66880S–8. SPIE, 2007.

[107] F. Chukreev, V. Makarenko, and M. Martin. Nuclear data sheets for a = 238. *Nuclear Data Sheets*, 97(1):129 – 240, 2002.

[108] S. T. P. Boyd and R. H. Cantor. Microcalorimeter magnetic sensor geometries using superconducting elements. *AIP Conference Proceedings*, 1185(1):595–598, 2009.

[109] M. Kiviranta, H. Seppä, J. van der Kuur, and P. de Korte. Squid-based readout schemes for microcalorimeter arrays. *AIP Conference Proceedings*, 605(1):295–300, 2002.

[110] J. A. Chervenak, K. D. Irwin, E. N. Grossman, J. M. Martinis, C. D. Reintsema, and M. E. Huber. Superconducting multiplexer for arrays of transition edge sensors. *Applied Physics Letters*, 74(26):4043–4045, 1999.

[111] J. van der Kuur, P. de Korte, P. de Groene, N. Baars, M. Lubbers, and M. Kiviranta. Implementation of frequency domain multiplexing in imaging arrays of microcalorimeters. *Nuclear Instruments and Methods in Physics Research Section A: Accelerators, Spectrometers, Detectors and Associated Equipment*, 520(1-3):551 – 554, 2004. Proceedings of the 10th International Workshop on Low Temperature Detectors.

[112] J. van der Kuur, J. Beyer, D. Boersma, M. Bruin, L. Gottardi, R. den Hartog, H. Hoevers, R. Hou, M. Kiviranta, P. J. de Korte, and B.-J. van Leeuwen. Progress on frequency-domain multiplexing development for high count rate x-ray microcalorimeters. *AIP Conference Proceedings*, 1185(1):245–248, 2009.

[113] G. Elmen. Magnetic alloys of iron nickel, and cobalt. *American Institute of Electrical Engineers, Transactions of the*, 54(12):1292–1299, Dec 1935.

[114] W. H. Press. *Numerical Recipes: The Art of Scientific Computing*. Cambridge University Press, 2007.